AD-A194 111 LINEAR THYRATRON(U) SPECTRA TECHNOLOGY INC BELLEVUE WA 1/3
M J KUSHNER ET AL. 31 JUL 87 AFWAL-TR-87-2080
F33615-84-C-2474

UNCLASSIFIED F/G 9/1 NL

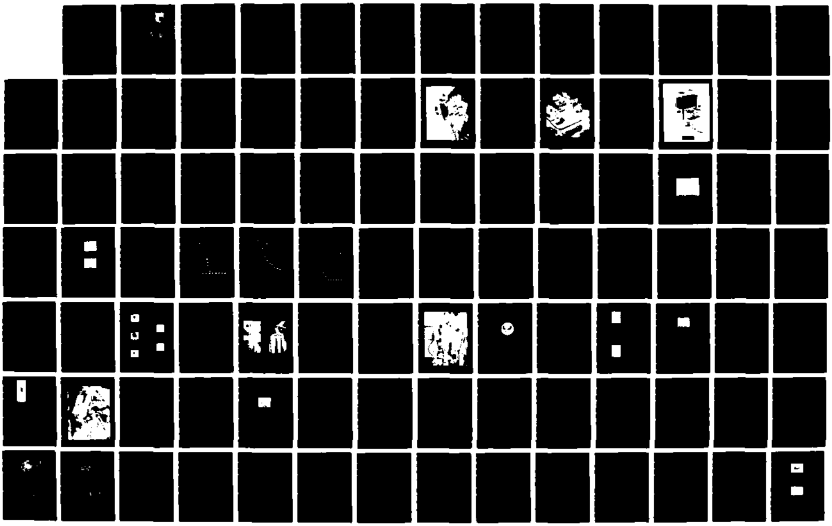

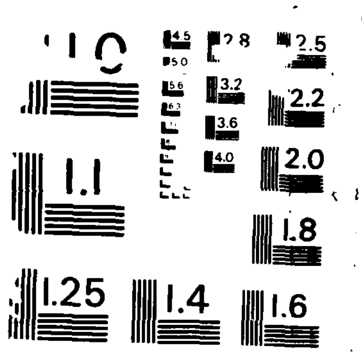

MICROCOPY RESOLUTION TEST CHART
NATIONAL BUREAU OF STANDARDS-1963-A

AFWAL-TR-87-2080

LINEAR THYRATRON

Mark J. Kushner/M. von Dadelszen
Principle Investigators

SPECTRA TECHNOLOGY, INC.
2755 Northup Way
Bellevue, Washington 98004

31 July 1987

Final Report for Period 1984 to 1987

Approved for public release; distibution unlimited

AERO PROPULSION LABORATORY
Air Force Wright Aeronautical Laboratories
Air Force Systems Command
Wright-Patterson Air Force Base, Ohio 45433-6563

NOTICE

When Government drawings, specifications, or other data are used for any purpose other than in connection with a definitely related Government procurement operation, the United States Government thereby incurs no responsibility nor any obligation whatsoever; and the fact that the Government may have formulated, furnished, or in any way supplied the said drawings, specifications, or other data, is not to be regarded by implication or otherwise as in any manner licensing the holder or any other person or corporation, or conveying any rights or permission to manufacture, use, or sell any patented invention that may in any way be related thereto.

This report has been reviewed by the Information Office and is releasable to the National Technical Information Service (NTIS). At NTIS, it will be available to the general public, including foreign nations.

This technical report has been reviewed and is approved for publication.

PETER BLETZINGER
Power Components Branch
Aerospace Power Division
Aero Propulsion Laboratory

PAUL R. BERTHEAUD, Chief
Power Components Branch
Aerospace Power Division
Aero Propulsion Laboratory

FOR THE COMMANDER

WILLIAM A. SEWARD, Lt Col, USAF
Deputy Director
Aerospace Power Division
Aero Propulsion Laboratory

"If your address has changed, if you wish to be removed from our mailing list, or if the addressee is no longer employed by your organization please notify AFWAL/POOC, WPAFB, OH 45433-6563 to help us maintain a current mailing list."

Copies of this report should not be returned unless return is required by security considerations, contractual obligations, or notice on a specific document.

UNCLASSIFIED

SECURITY CLASSIFICATION OF THIS PAGE

REPORT DOCUMENTATION PAGE

1a. REPORT SECURITY CLASSIFICATION: UNCLASSIFIED

1b. RESTRICTIVE MARKINGS: N/A

2a. SECURITY CLASSIFICATION AUTHORITY: N/A

2b. DECLASSIFICATION/DOWNGRADING SCHEDULE: N/A

3. DISTRIBUTION/AVAILABILITY OF REPORT: Approved for public release; Distribution unlimited

4. PERFORMING ORGANIZATION REPORT NUMBER(S):

5. MONITORING ORGANIZATION REPORT NUMBER(S): AFWAL-TR-87-2080

6a. NAME OF PERFORMING ORGANIZATION: Spectra Technology

6b. OFFICE SYMBOL (If applicable):

7a. NAME OF MONITORING ORGANIZATION: Aero Propulsion Laboratory (AFWAL/POOC) AF Wright Aeronautical Labs.

6c. ADDRESS (City, State and ZIP Code): 2755 Northup Way Bellevue WA 98004

7b. ADDRESS (City, State and ZIP Code): Wright-Patterson AFB OH 45433-6563

8a. NAME OF FUNDING/SPONSORING ORGANIZATION: AFWAL

8b. OFFICE SYMBOL (If applicable): POOC-3

9. PROCUREMENT INSTRUMENT IDENTIFICATION NUMBER: F33615-84-C-2474

8c. ADDRESS (City, State and ZIP Code): Wright-Patterson AFB OH 45433-6563

10. SOURCE OF FUNDING NOS.

PROGRAM ELEMENT NO.	PROJECT NO.	TASK NO.	WORK UNIT NO.
63221C	1D01	00	05

11. TITLE (Include Security Classification): Linear Thyratron

12. PERSONAL AUTHOR(S): Mark J. Kushner, Michael von Dadelzson

13a. TYPE OF REPORT: Final

13b. TIME COVERED: FROM 1984 TO 1987

14. DATE OF REPORT (Yr., Mo., Day): 1987 July 31

15. PAGE COUNT: 232

16. SUPPLEMENTARY NOTATION

17. COSATI CODES

FIELD	GROUP	SUB. GR.
20	09	
09	03	

18. SUBJECT TERMS (Continue on reverse if necessary and identify by block number): Thyratron, High Power, Discharge Model

19. ABSTRACT (Continue on reverse if necessary and identify by block number)

A linear configuration thyratron was investigated experimentally and theoretically. Advantages of this configuration are lower inductance and the capability of increasing current capability by increasing the length of the device without increasing current density or inductance. The experimental device used a 10-cm-long dispenser type cathode a baffled grid and an auxiliary grid. Several modifications were made improving vacuum quality, voltage-standoff or switching speed. The discharge volume could be analyzed using several viewing ports. Using the auxiliary grid, the discharge ignited uniformly over the whole length of the device, proving the linear concept. The distribution of th electron density was measured time resolved using Hook spectroscopy. The data were in good agreement with a numerical code using a spatial grid and time resolved solutions of the Poisson equation. The elctrons were represented with normalized spatial densities ("macro-electrons") and their motion calculated using Monte Carlo techniques and the appropriate elastic and inelastic collision cross sections.

20. DISTRIBUTION/AVAILABILITY OF ABSTRACT: UNCLASSIFIED/UNLIMITED ☒ SAME AS RPT ☐ DTIC USERS ☐

21. ABSTRACT SECURITY CLASSIFICATION: UNCLASSIFIED

22a. NAME OF RESPONSIBLE INDIVIDUAL: PETER BLETZINGER

22b. TELEPHONE NUMBER (Include Area Code): 513 255-2923

22c. OFFICE SYMBOL: AFWAL/POOC-3

DD FORM 1473, 83 APR EDITION OF 1 JAN 73 IS OBSOLETE.

UNCLASSIFIED

SECURITY CLASSIFICATION OF THIS PAGE

TABLE OF CONTENTS

TABLE OF CONTENTS (CONTINUED)

TABLE OF CONTENTS (CONTINUED)

LIST OF FIGURES

LIST OF FIGURES

LIST OF FIGURES

LIST OF FIGURES (CONTINUED)

LIST OF FIGURES (CONTINUED)

LIST OF FIGURES (CONTINUED)

LIST OF TABLES

Section 1
INTRODUCTION

Future electrical pulse power systems for civilian and military applications have requirements that exceed our present technology, particularly as pertains to high repetition rate, high-voltage, and high-current switches. Although the details of those requirements vary over a large parameter space, a large fraction of the requirements would be met by an electrical switch operating at ≥100 kV, ≥100 kA, $\geq 10^{12} A\text{-}s^{-1}$, and with a repetition rate of >100 Hz. The linear thyratron is a candidate to satisfy these requirements. As its name implies, the Linear Thyratron (LT) is a gas discharge switch built in a linear geometry as opposed to the cylindrical geometry used with commercially available devices. Scaling cylindrical thyratrons to higher currents by increasing the diameter of the cathode has had limited success because of the inability to uniformly utilize the entire cathode surface. Scaling cylindrical thyratrons in this manner increases their inductance (thereby decreasing dI/dt) and increases the geometrical mismatch between the switch and stripline modulators. The LT, though, is conceptually scalable to arbitrarily large currents by lengthening the thyratron in the axial dimension while not changing the characteristic gap dimensions or the distance between any spot on the cathode and the control grid slot, the critical dimensions which determine the switching properties. The inherently low inductance of the linear geometry also makes the LT more attractive to obtain high values of dI/dt. The LT has been developed with the goal to demonstrate proof of principle, high-voltage scaling, and the ability to scale in length (i.e., scale in current).

The concept of the linear thyratron resulted from inadequacies of commercial cylindrical thyratrons. These inadequacies became apparent when switching fast discharge excimer lasers. These lasers typically have pulse power requirements of 10-50 kV and 10-50 kA. The pulse widths are typically 100-300 ns and rate of current rise $\geq 10^{12} A\text{-}s^{-1}$. These parameters equal or exceed the specifications of commercial thyratrons and, therefore, demanded a

new switch. Discharge excimer lasers and their pulse forming networks are also built in a linear geometry. A low inductance switch which mates these two linear components should also have a linear geometry, as shown in Figure 1-1. These performance and geometrical considerations led to the development of the linear thyratron.

An additional consideration is thyratron lifetime. When used as a switch for excimer lasers, conventional cylindrical thyratrons equipped with oxide cathodes have a lifetime of $\approx 10^7$ pulses. Autopsies of failed thyratrons showed that arcing had occurred and that most of the oxide cathode material had eroded from the cathode vanes. To increase the lifetime of commercial thyratrons, we must reduce the value of dI/dt and peak current that the thyratron must switch. Magnetic pulse compression is a technique that can limit dI/dt in the switch, and its use has extended thyratron life for these conditions to 10^8 shots (References 1,2). However, magnetic pulse compression addresses only the symptoms and not the limitations of thyratrons in fast, high current discharge circuits. Therefore, the LT must not only improve upon the single pulse and geometrical specifications cited above but it must also have long lifetimes. Therefore, the LT must use a cathode that is less susceptible to damage from the higher performance specifications.

In 1981, Spectra Technology, Inc. (STI) and Impulse Engineering began a joint effort to develop the linear thyratron. Impulse Engineering fabricated the prototype experimental linear thyratron and delivered it to STI in May 1983. Figure 1-2 shows a schematic of the prototype linear thyratron, and a photograph of the prototype device appears in Figure 1-3. Our design was based on a structural concept that can be linearly scaled and that does not involve oven-fired, sealed-off fabrication methods. Permanent ceramic-to-metal seals in thyratron construction are subject to thermally induced stress, which restricts the maximum scale dimensions of the tube and prevents the use of an elongated (linear) geometry. High vacuum is obtained in the prototype LT by using an O-ring sealed chamber that incorporates either Pyrex or ceramic insulators for high-voltage holdoff. A gas flow supply and exhaust system is used, which eliminates the need for a hydrogen reservoir and

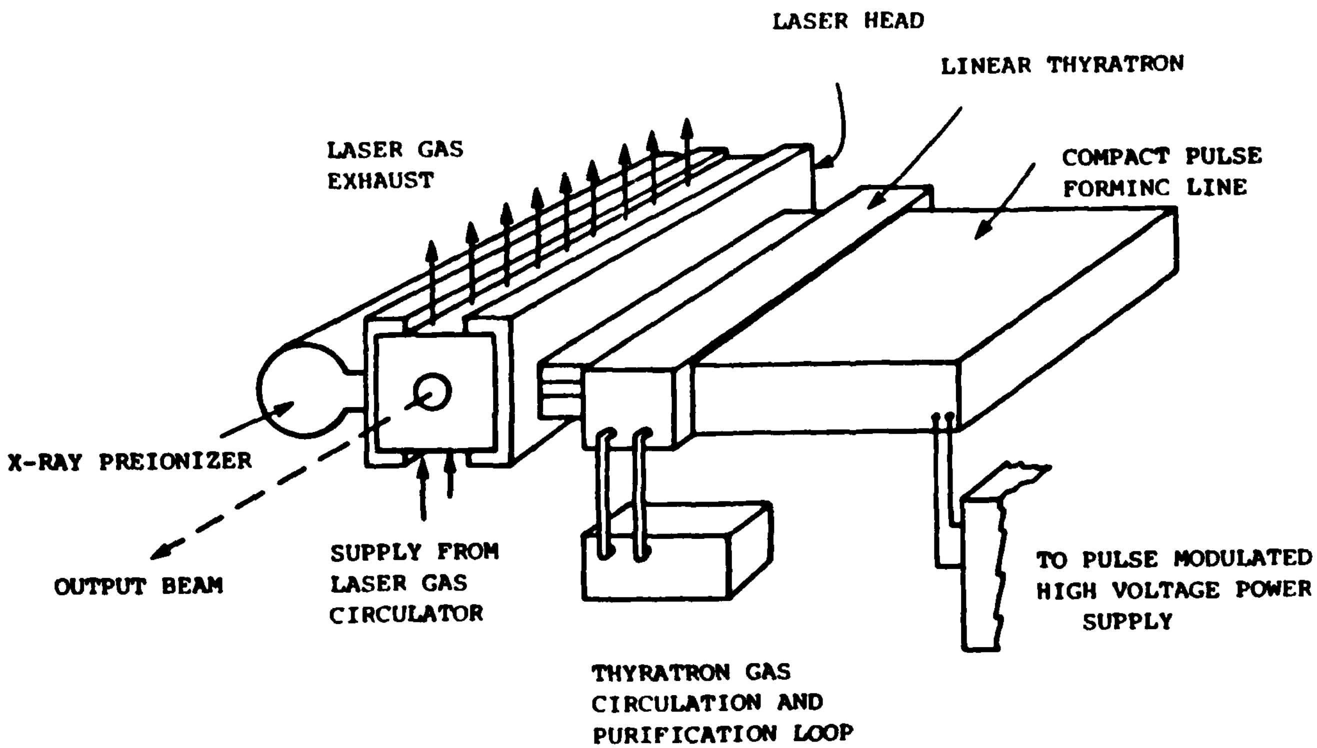

81 05426

Figure 1-1. Schematic of Example Large-Scale Discharge Laser Assembly Using New Linear Thyratron Switch.

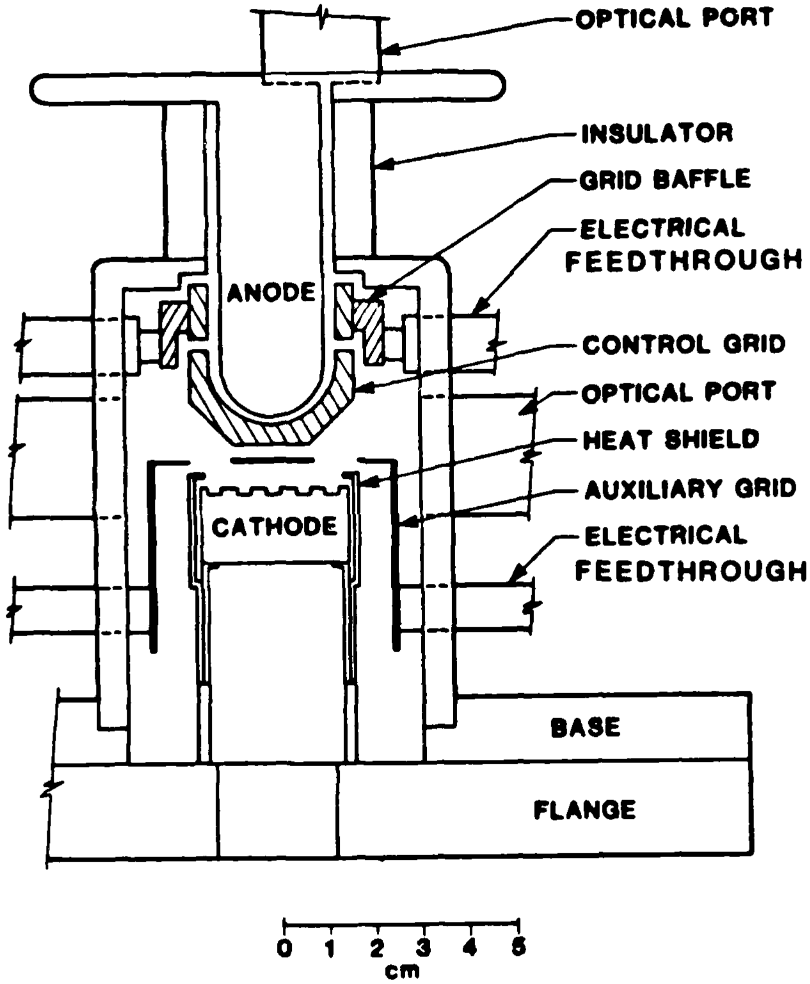

85 09442

Figure 1-2. Schematic of Prototype Linear Thyratron.

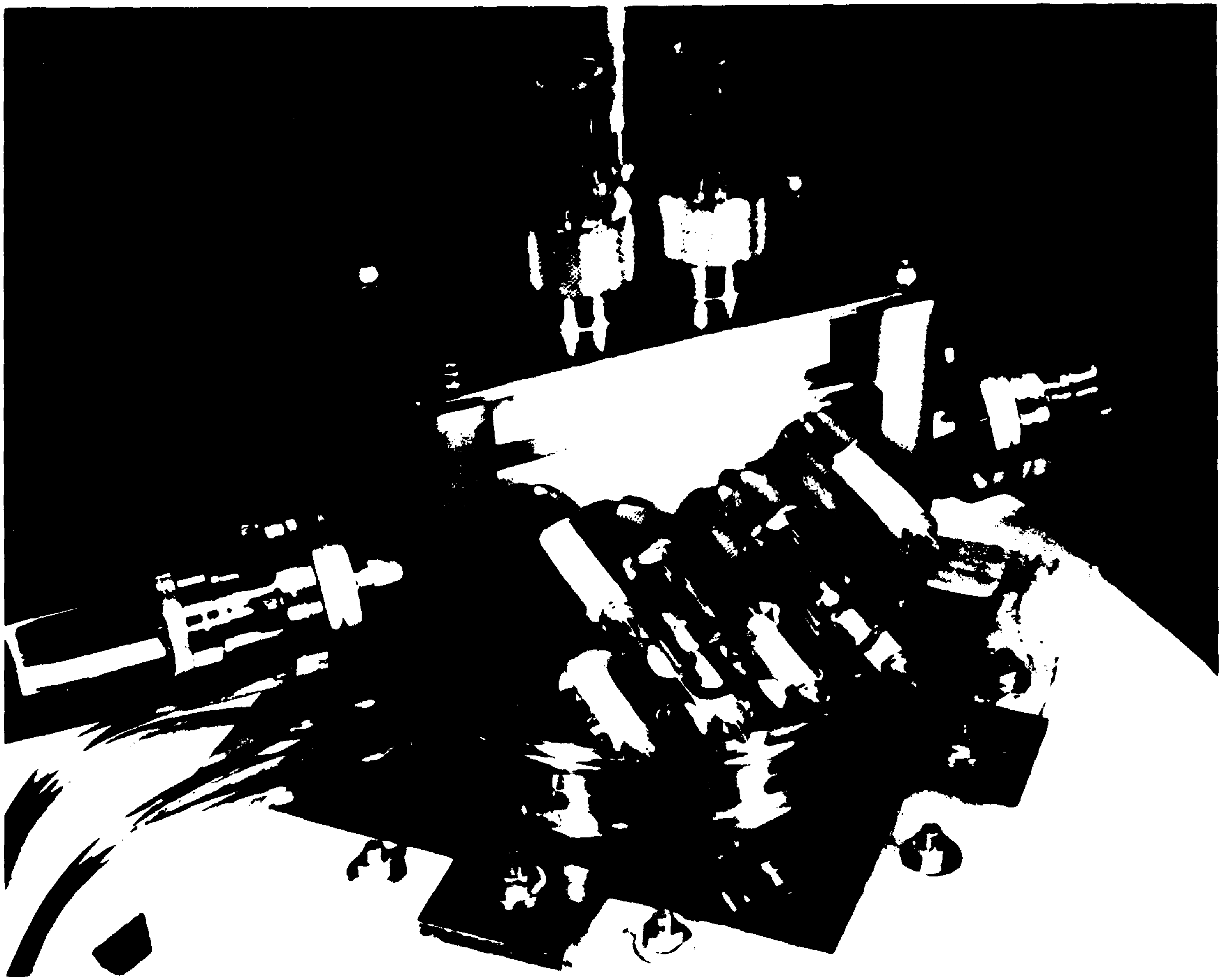

Figure 1-3. Photograph of the Prototype Linear Thyratron as Delivered to STI by Impulse Electronics.

allows the use of other gases such as helium and neon. The prototype linear thyratron is fitted with a dispenser cathode which, when operated at room temperature (i.e., with no cathode heater power), yields current densities >100 A/cm^2. These cathodes are less susceptible to cathode arcing from high dI/dt and high peak current switching than are oxide cathodes (References 3-11). During experiments described in this report, the LT was operated with the cathode surface facing down without "flaking" off any cathode material. The prototype experimental thyratron was also equipped with optical ports that permit direct viewing of the cathode-control grid space and the anode-control grid space. These ports allow quantitative time-resolved spectroscopic and interferometric diagnostic techniques to be used to measure plasma properties during the formation, conduction, and recovery stages of thyratron operation.

The anode structure penetrates the thyratron body and is surrounded by the control grid. This anode structure is similar to that of an earlier experimental 100 kV single-stage thyratron investigated by Mancebo (Reference 12). The control grid-anode assembly is 10 cm long. There are control grid slots on either side of the control grid. The grid slot area is large enough to pass in excess of 10 kA while keeping the current density in the grid aperture region below 1 to 2 kA/cm^2, the generally accepted quenching limit for microsecond-long discharges. An auxiliary grid is positioned below the control grid. The dispenser cathode is 3 cm wide by 10 cm long. The total surface area of the slotted cathode is ≈80 cm^2. The maximum expected current density at room temperature at the time of design was 5 kA (Reference 9). This value was exceeded during the studies reported here. Except for the high-voltage insulator (Pyrex), and the auxiliary grid (molybdenum), the entire thyratron structure is stainless steel.

Our initial electrical characterization of the linear thyratron was performed with the configuration shown in Figures 1-2 and 1-3. During the studies reported here, the LT was modified three times. The first modification was to improve the design of the auxiliary grid and to increase the size of the optical ports, as shown in Figure 1-4. The second modification was to change the internal configuration of the control grid and

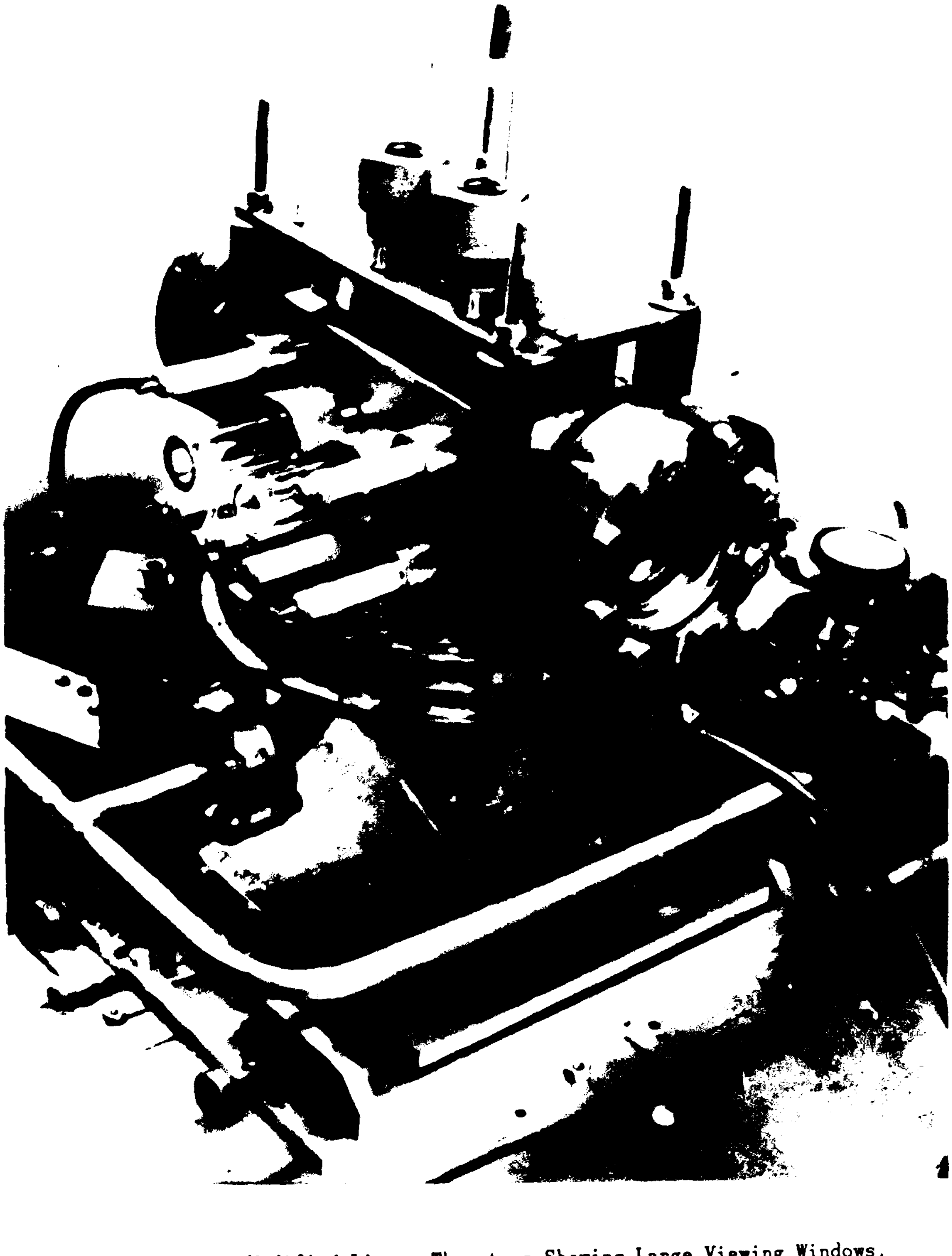

Figure 1-4. Modified Linear Thyratron Showing Large Viewing Windows.

anode in order to improve its high-voltage performance. The final external modifications of the LT are shown in Figure 1-5.

The linear thyratron research and development program performed by STI and summarised in this report is called the Phase II program. The intent of the program was to further our fundamental understanding of the plasma processes and scaling potential of the LT and to demonstrate that improved understanding by modifying the LT to operate at voltages of ≤ 100 kV. The investigations consisted of electrically and spectroscopically characterizing the LT, and developing a first-principles plasma simulation model for the LT to apply to subsequent design tasks. In brief summary, the following program goals were met:

- The LT was electrically characterized by measuring the pertinent voltage, current, and timing parameters.

- The operating requirement to obtain uniform and simultaneous cathode coverage was confirmed by observing plasma emission.

- Excited state densities in the thyratron plasma were measured using hook spectroscopy. The measurements were used to guide subsequent modifications of the LT.

- A plasma simulation model was developed, validated, and applied to the design of modifications of the LT.

- The maximum current capacity of the dispenser cathode was measured over a wide parameter space.

- The design requirements for a 100-kV linear thyratron were defined and two designs of an advanced linear thyratron were performed.

- The LT was modified to switch higher voltages and was successfully operated at voltages ≤ 95 kV.

- Further modifications allowed simultaneous switching of 60 kV at 3kHz with dI/dt $>10^{11}$ A/s.

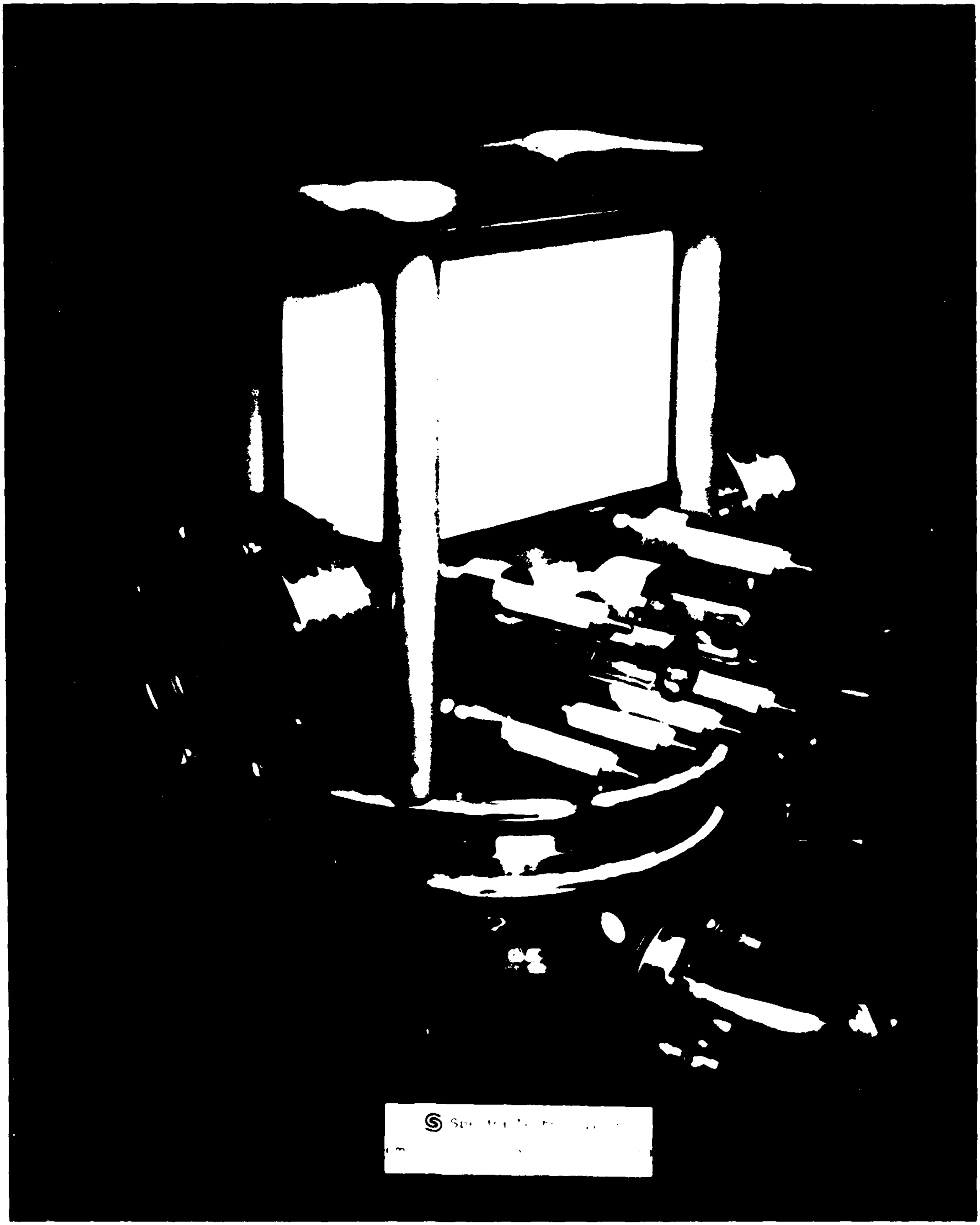

Figure 1-5: Final Modified Linear Thyratron.

REFERENCES

1. I. Smilanski, S. Byron, and T. Burkes, "Electrical Excitation of an XeCl Laser Using Magnetic Pulse Compression," Appl. Phys. Lett. 40: XXX, (1982)

2. R. Petr, J. Zumdieck, J. Demboski, I. Smilanski, J. Ewing, and R. Center, "Magnetic Pulse Compression for Copper Vapor Lasers," 4th IEEE Pulsed Power Conference, IEEE Cat. 83CH1908-3, New York, 1983, pp. 236-241,

3. MSNW and Impulse Electronics, Long-Life High-Current Thyratrons for Fast Discharge Lasers, Final Report, Contract AFWAL-TR-84-2003, March 1984.

4. D. Turnquist, T. Lynch, S. Merz, and N. Reinhardt, "Development of Instant-Start Thyratrons," IEEE 14th Pulse Power Modulator Symposium, New York, 1980, pp. 46-53.

5. D. Fleisher, D. Turnquist, S. Goldberg, and N. Reinhardt, "The Plasma-Heated Thyratron," IEEE Trans. Electron Devices ED-26: 1444 (1979)

6. S. Friedman, R. Petr, J. McGowan, and J. O'Connell, "Instant-Start Cathodes for High Average Power Hydrogen Thyratrons," IEEE 15th Pulse Power Modulator Symposium, New York, 1982, pp. 127-132.

7. EG&G, LANL Laser Isotope Seperation Program and NSWC High Voltage-Low Inductance Hydrogen Thyratron Program, Final Report, DOE Contract EN-77-C-04-4047, 1982.

8. EG&G, Research Studies for Cathode and Grid Elements for Superpower Switches, Final Report, DOD Contract DA 36-039-SC-85338, 1962.

9. R. Petr and M. Gundersen, "Field Emission Cathodes for High Power Beams," Lasers and Particle Beams 1: 207 (1983)

10. S. Schneider, private communication, 1984.

11. J.L. Cronin, "Modern Dispenser Cathodes," IEE Proc. 128: 19 (1981)

12. L. Mancebo, "100-kV Thyratron Without Gradient Grids," IEEE Trans. Elect. Dev. ED-18: 920 (1971)

Section 2

SUMMARY OF PHASE I LINEAR THYRATRON CHARACTERIZATION

In this section, the electrical characterization of the prototype linear thyratron during Phase I will be summarized. These activities are discussed in detail in the Phase I Final Report (Reference 1).

The linear thyratron tube was connected to a gas handling system, shown schematically in Figure 2-1. During a test, the thyratron was backfilled with the operating gas to the desired pressure through a cold trap and valved off. It was not necessary to flow gas if the thyratron was operated with its dispenser cathode at room temperature; however, with a hot cathode (900°C) the gas purity degraded, resulting in the high-voltage holdoff of the thyratron decreasing. A flow rate of a few sccm was sufficient to maintain the maximum high- voltage holdoff. The test circuit used for the Phase I measurements is shown schematically in Figure 2-2. The control grid breakdown voltage versus tube pressure for different values of the auxiliary grid current is shown in Figure 2-3. Typical voltage and current waveforms for the control grid are shown in Figure 2-4.

The performance specifications obtained for the prototype linear thyratron during Phase I are summarized in Table 2-1. The results in this table are for operation with a hot cathode (900°C). The working gas during Phase I was neon. At a pressure of 100 μm (0.1 Torr), the thyratron could be operated with anode voltages up to 15 kV at a gas pressure of 100 μm and with an anode voltage fall time of ≈200 ns. At the high gas pressure of 500 μm (0.5 Torr), the anode voltage fall time decreased to 100 ns, but high-voltage holdoff also decreased to 5 kV. Generally the tube pre-fired by flashing along the insulator from the thyratron body-insulator-control grid triple point illustrated in Figure 2-5. The flashover propapagated to the top section of the anode.

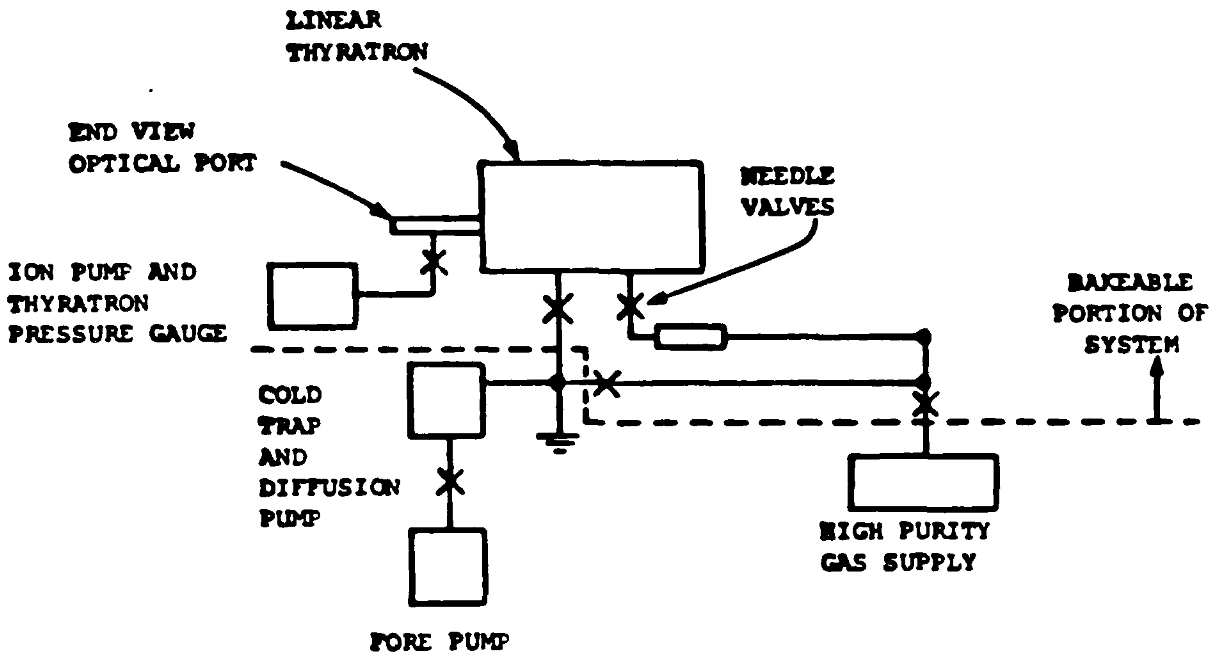

Figure 2-1. Schematic of Gas Handling System.

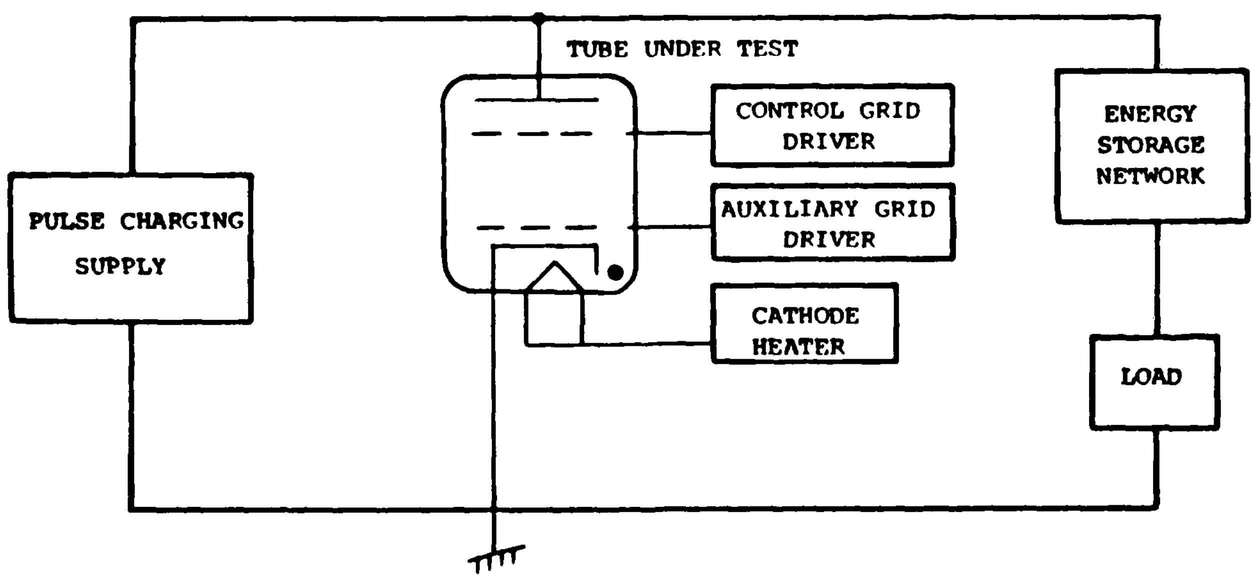

84 08901

Figure 2-2. Schematic of Linear Thyratron Electrical System.

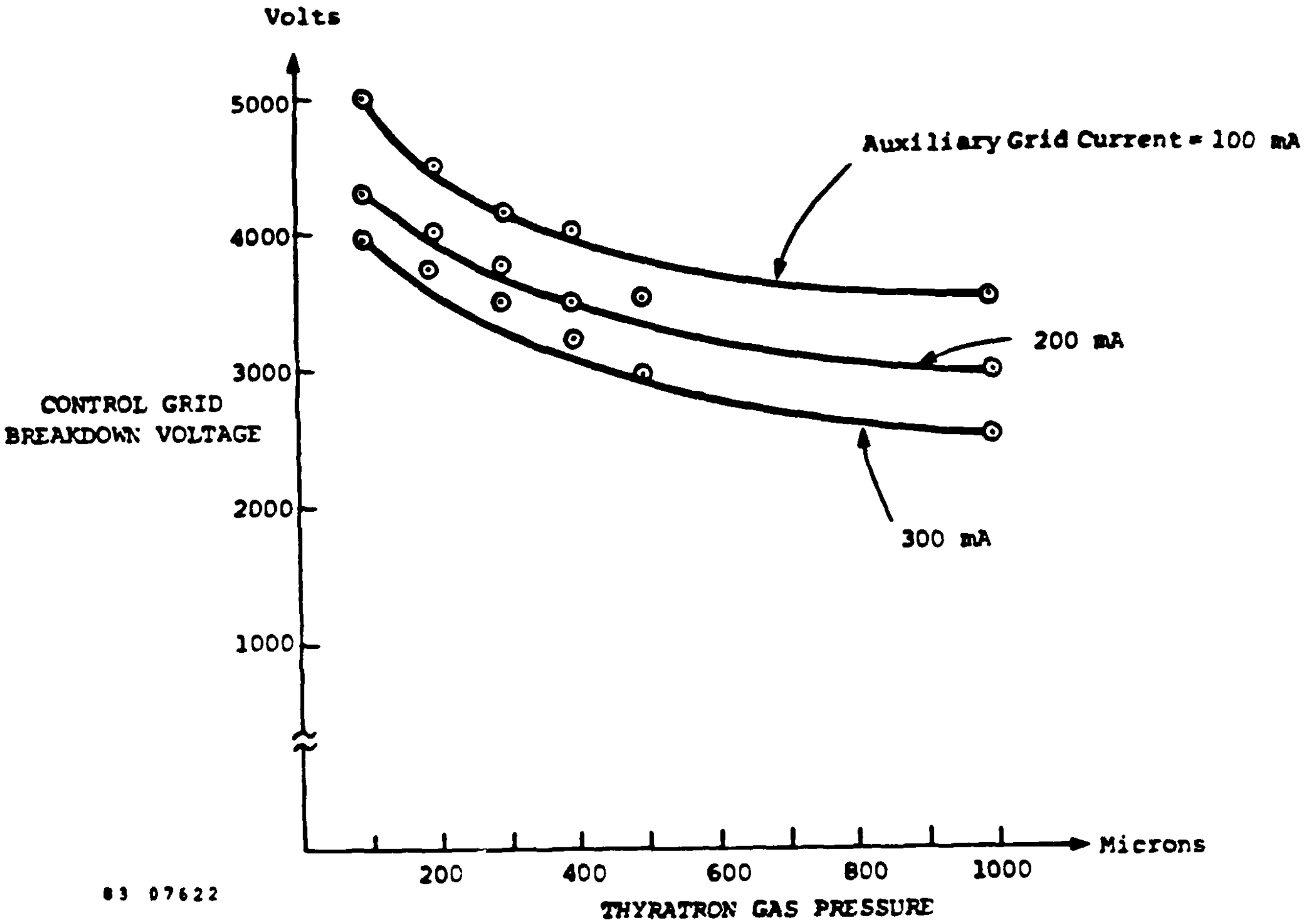

Figure 2-3. Control Grid Breakdown Voltage vs. Tube Pressure for Different Auxiliary Grid Current Settings. No applied anode voltage.

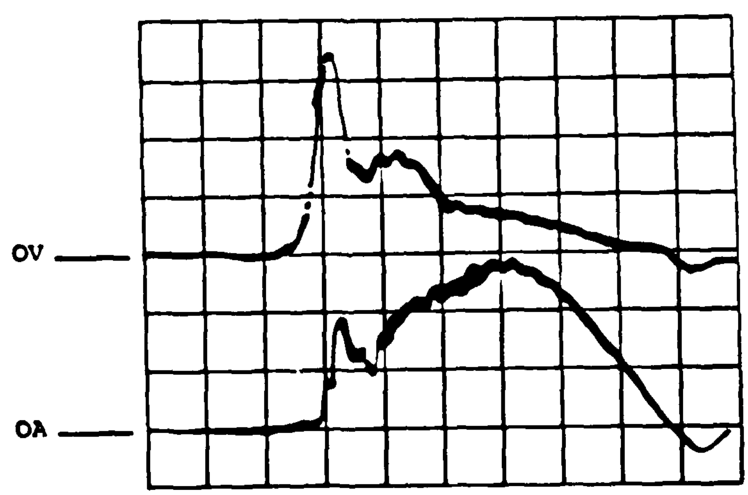

Figure 2-4. Typical Control Grid Voltage and Current

Top: Grid voltage 1 kV/div
Bottom: Grid current 10 A/div
Horizontal: 100 nsec/div
No applied anode voltage.

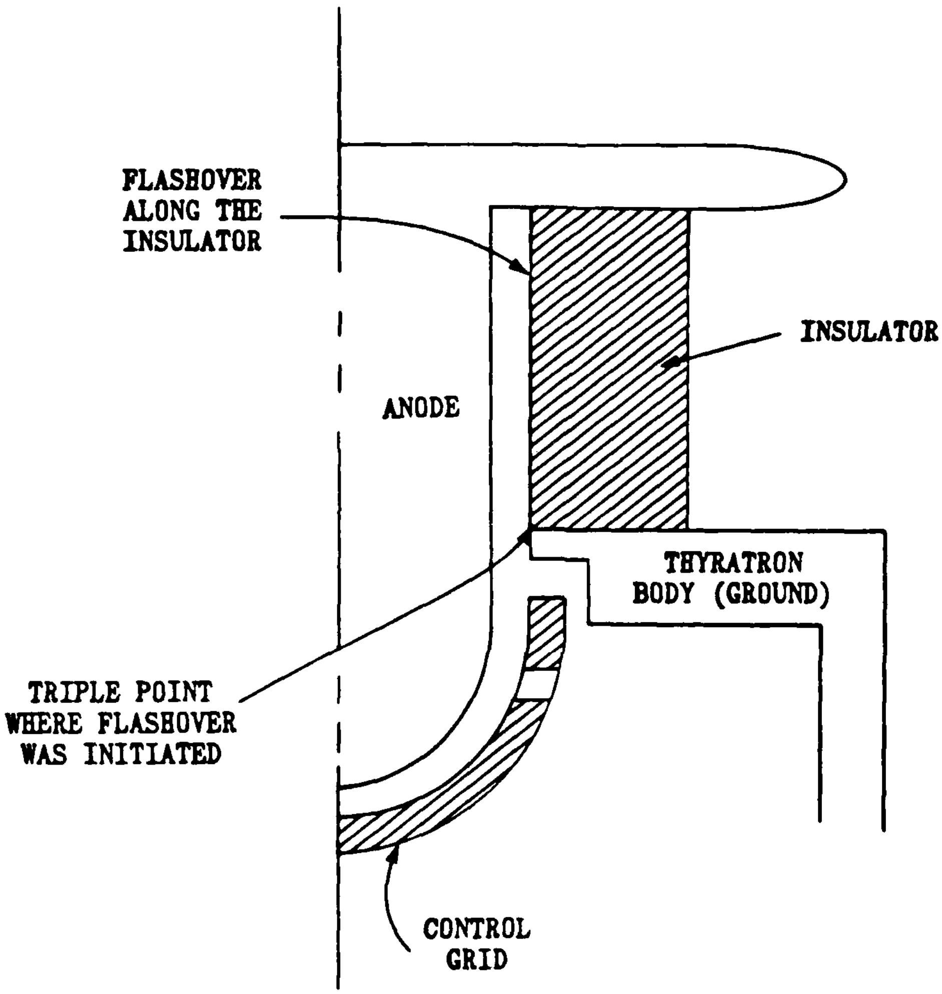

Figure 2-5. Anode-Insulator-Ground Triple Point where Flashover was Initiated.

10962

The performance specifications obtained for the prototype linear thyratron during Phase I operation with an unheated cathode (≈20°C) are summarized in Table 2-2. Similar voltage holdoff was obtained at 500 μm as with the hot cathode. The anode voltage fall time, though, was ≈50 ns when operating cold, as compared to 100 ns when operating with a hot cathode. A typical commutation waveform with a cold cathode appears in Figure 2-6.

We were encouraged to find that the discharge plasma appeared to light up uniformly along the length of the thyratron for both a hot and cold cathode. This uniform discharge spreading was, however, very sensitive to using a dc current between the auxiliary grid and the cathode. In the absence of the dc current, the spatial distributions of the discharge in both the cathode-control grid gap and the control grid-anode gap were not uniform. If the discharge in the lower grid sections favored one end of the tube, the grid-anode plasma also appeared to be localized to that end of the tube. This qualitative demonstration of uniform cathode coverage was particularly encouraging because it implied that length scaling of the LT may be possible.

A structural failure in the linear thyratron prevented further characterization during Phase I. Subsequent characterization and development was delayed until Phase II.

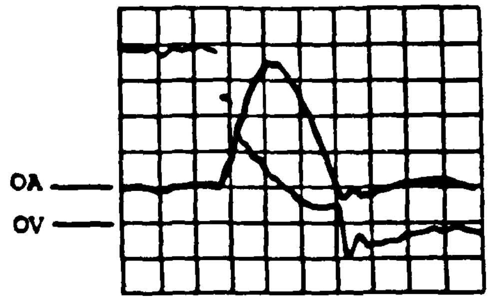

Left: Anode voltage 1 kV/div
Right: Anode current 200 A/div
Horizontal: 50 nsec/div

Gas pressure: 500 microns neon
Cathode temperature: 20°C
Auxiliary grid current: 100 mA

8E 11004

Figure 2-6. Thyratron Commutation Waveforms with a Cold Cathode.

Table 2-1

PHASE I LT SWITCHING CHARACTERISTICS FOR HOT CATHODE

Gas	Neon
Pressure	100 μm
Cathode Temperature	900°C
Peak Anode Voltage	15 kV
Peak Discharge Current	2 kA
Discharge Current Duration	120 ns FWHM
Anode Fall Time	200 ns
Auxiliary Grid Current	100 mA

Table 2-2

PHASE I LT SWITCHING CHARACTERISTICS FOR COLD CATHODE

Gas	Neon
Pressure	500 μm
Cathode Temperature	20°C
Peak Anode Voltage	5 kV
Peak Discharge Current	700 A
Discharge Current Duration	120 ns FWHM
Anode Fall Time	<50 ns
Auxiliary Grid Current	100 mA

REFERENCES

1. Spectra Technology and Impulse Electronics, Long-Life High-Current Thyratrons for Fast Discharge Lasers, Final Report, Contract AFWAL-TR-84-2003, March 1984.

Section 3

PHASE II: LINEAR THYRATRON ELECTRICAL CHARACTERIZATION

3.1 INTRODUCTION

A critical requirement for the development of the linear thyratron is the necessity that the discharge cover the cathode uniformly and simultaneously. We qualitatively observed during Phase I that the thyratron appeared to turn on uniformly along its entire length. An objective of Phase II was to confirm this through unambiguous measurements. In Phase II, we also desired to study the effects of different gases on thyratron operation and to determine the performance characteristics of a cold dispenser cathode. Since the diagnostic ports in the linear thyratron permit direct observation of the temporal and spatial behavior of the plasma, optical diagnostics could be applied to the thyratron to achieve these ends.

In this section, the electrical characterization of the prototype linear thyratron will be discussed. The grid drivers and pulse charging circuits will be briefly described. This description is followed by a discussion of measurements of the uniformity of cathode coverage and of the uniformity of the discharge within the grid-anode gap. Various other electrical parameters were also measured, such as anode delay time and voltage delay time.

3.2 ELECTRICAL DRIVE EQUIPMENT

The electrical drivers for the linear thyratron were upgraded for Phase II from those used in Phase I. This equipment included an auxiliary grid driver, a control grid driver, and a pulse charging power supply. The two grid drivers are separate to allow them to be independently timed. The charging supply is pulsed in order to reduce the time the thyratron must hold off high voltage. This reduces the likelihood of pre-fires, insulation failure, corona, and other problems associated with high-voltage holdoff.

Both the control grid and auxiliary grid drivers provide a maximum of 5 kV open circuit and 20 A short circuit in 5 μs pulses at 5 Hz. This peak power amplitude can be adjusted with a variac controller. We have provided the ability to pulse the auxiliary grid (in addition to having a dc simmer current) because pulsing appears to enhance cathode utilization, especially with cold dispenser cathodes (Reference 1). The pulse charging power supply charges a 20-nF storage bank up to 25 kV in 3 μs at a maximum repetition rate of 5 Hz. Figure 3-1 shows a schematic and V-I trace for the pulse charge power supply.

3.3 GENERAL DISCUSSION OF THYRATRON PERFORMANCE

The prototype linear thyratron is a tetrode and has a slotted, sintered barium titanate dispenser cathode with dimensions 3 cm X 10 cm (see Figure 1-2). The cathode was furnished by Sprectramat, Inc. The effective surface area of the slotted cathode is approximately 80 cm^2. The thyratron body is made of stainless steel and is sealed with fluorocarbon O-rings. An external gas handling system is used (base pressure 5×10^{-8} Torr), thereby enabling the use of a variety of gases at a selection of gas pressures. The high-voltage insulator is made of Pyrex in a racetrack configuration and is 3.4 cm high. The auxiliary grid is made of molybdenum, and the control grid and anode are made of stainless steel. The thyratron is equipped with a pair of 2.5-cm-diameter optical ports on either side of the cathode looking perpendicularly into the cathode-control grid space, and a pair viewing the control grid-anode gap. There are also optical ports on either end of the thyratron. These ports originally had a viewing diameter of 2 cm (see Figure 1-3). The windows were later enlarged to provide a viewing diameter of 6 cm, which provided optical access to the entire cathode-control grid space (see Figure 1-4).

The thyratron is typically operated in either hydrogen or helium. The performance of the thyratron was qualitatively the same when using either of the gases; voltage fall time, maximum cathode current, and dI/dt were similar. The exception was with high-voltage holdoff and maximum switching

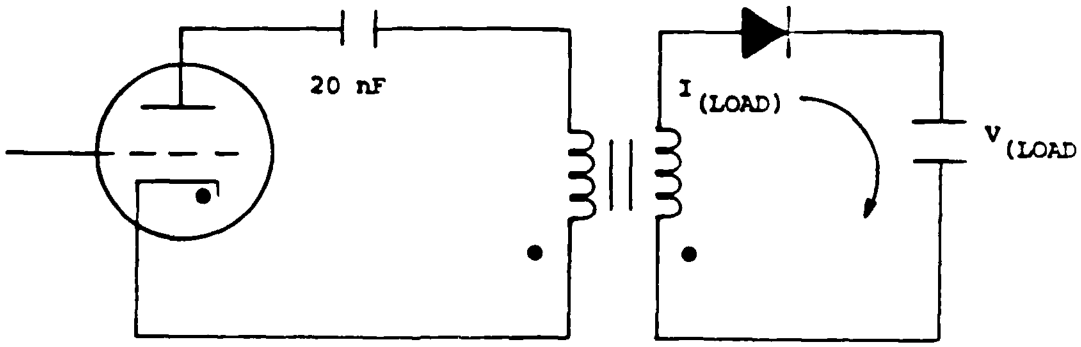

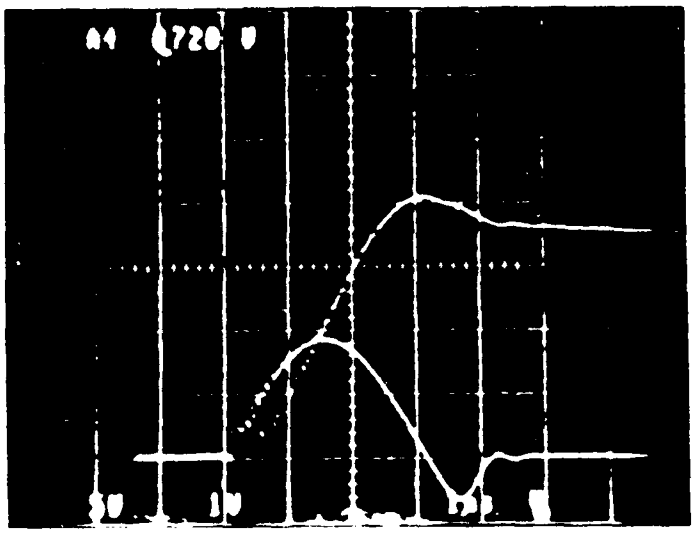

85 09106

TOP TRACE: $V_{(LOAD)}$ 5 kV/DIV

BOTTOM TRACE: $I_{(LOAD)}$ 100 A/DIV

1 μs/DIV

Figure 3-1. Schematic and I-V Trace for Pulse Charge Power Supply.

voltage. At a given gas pressure, the maximum holdoff and switching voltage was higher in helium than in hydrogen, a consequence of the more favorable Paschen curve for helium compared to hydrogen. Holdoff in the linear thyratron was limited to 25 kV by field emission at a gas-metal-insulator triple point, resulting in insulator flashover. This limiting voltage occurred at 1.5 Torr in He and 0.6 Torr in H_2. The field emission problem was subsequently corrected during modification of the linear thyratron. Holdoff and switching at 95 kV were obtained with the modified thyratron, as described in Section 8.

The prototype linear thyratron has separately switched 25 kV, 10 kA, and a maximum dI/dt of 1.3×10^{11} A-s^{-1}. The latter two values were obtained at different pulse lengths, although we did not attempt to optimize all parameters at all pulse lengths. The high current limit was obtained with a pulse duration of ≈40 μs with a dI/dt of 2×10^{9} A-s^{-1}, while the high dI/dt limit was obtained with a pulse duration of ≈120 ns and a maximum current of 4.8 kA. These parameters equal or exceed those for commercially available thyratrons (Reference 2). The cited current ratings will increase in proportion to an increase in the length of the cathode.

The cathode was typically operated without auxiliary heating. We obtained nearly the same performance when operating the cathode hot (800°C) or at room temperature. Current densities in excess of 150 A-cm^{-2} were obtained with both a hot and cold cathode, indicating that the emission mechanism for this cathode is not dominantly thermal (Reference 3). When operating with a hot cathode, the anode voltage fall time is longer and the jitter is worse than when operating with a cold cathode. The jitter, normally about 5 ns when operating cold, increased to 20-30 ns when operating with a hot cathode.

The current and voltage traces for the thyratron operating in 1.8 Torr of helium appear in Figure 3-2. The inductive component of the voltage has been removed by computer processing (Reference 4). The thyratron switched 20 nF charged to 9 kV into a 0.5 Ω load. The cathode was not heated. The peak current was 4.8 kA with a maximum dI/dt = 1.3×10^{11} A-s^{-1}. The

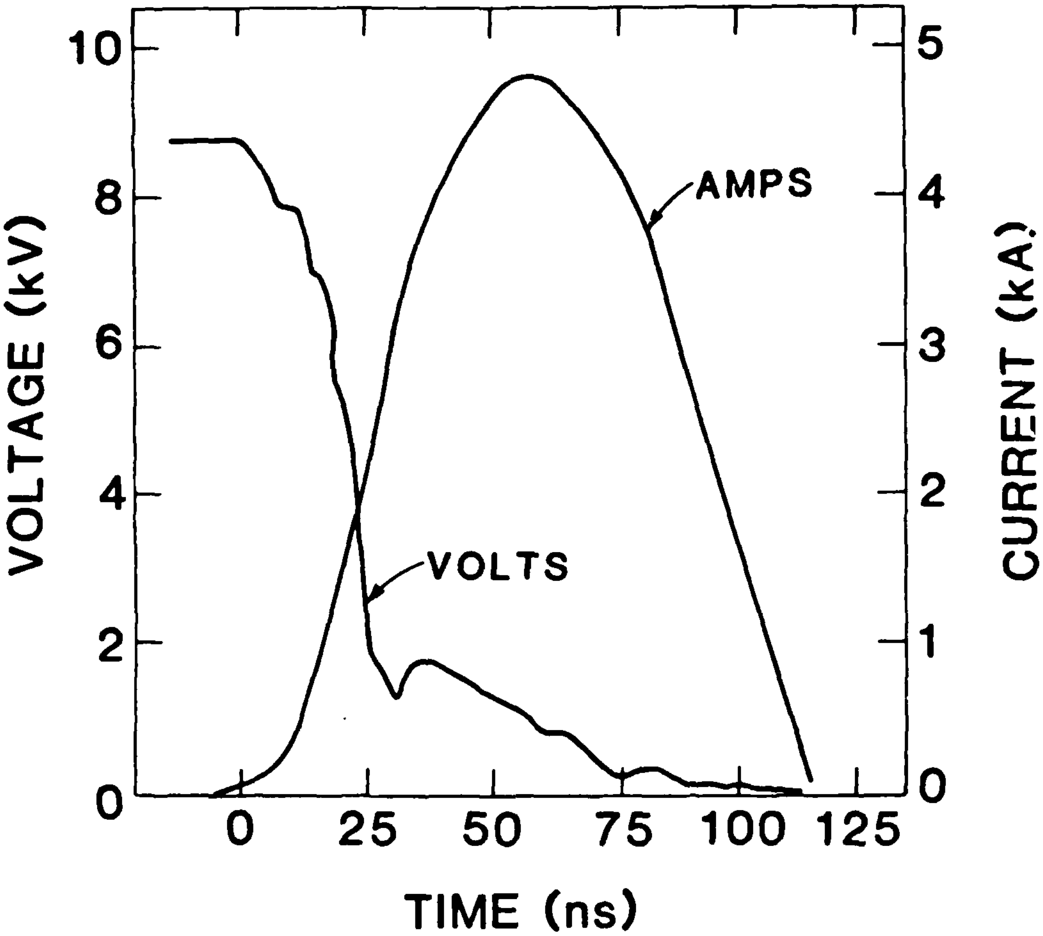

86 10739

Figure 3-2. Current and Voltage for the Linear Thyratron Operating in He at 1.2 Torr. The inductive component of voltage has been removed from the trace.

thyratron commutation appears to occur in two stages: 0-25 ns and 25-75 ns. The thyratron resistance at the end of the first stage is 0.2 Ω and after the second stage is 0.025 Ω. These parameters represent the best short-pulse performance.

3.4 DISCHARGE SIMULTANEITY

Parameters of interest to scaling the linear thyratron are (1) whether the discharge spreads uniformly across the cathode and (2) length of time required for the discharge to fill the cathode space. To determine the uniformity of the spread of the discharge across the cathode, the following method was used. Two shielded photo-multiplier tubes (PMT) were set up to view the cathode-grid space through separate view ports at far ends of the cathode (see Figure 1-4). Black tubes approximately 50 cm long were installed between the observation ports and the PMTs to insure that the PMTs viewed separate regions of the discharge. In this configuration, the PMTs viewed a region approximately 1.5 cm wide, separated by about 10 cm. Emission from the discharge was viewed while using only a neutral density filtering. Therefore, the wavelength response of the measurement was that of the photomultiplier tube (1P28). Simultaneity of discharge coverage was correlated with the simultaneity of the pulsed plasma emission. The rise time of the PMT was less than 5 ns, and the responses of the two PMTs were calibrated relative to each other by viewing the same portion of the discharge from opposite sides of the thyratron.

The uniformity of the spread of the discharge was determined by the time delay and magnitude of the pulsed plasma emission viewed by the PMTs. Examples of the emission measured by the PMTs are shown in the data presented in Figure 3-3. For these examples, both the auxiliary grid (G1) and the control grid (G2) were simultaneously pulsed and the cathode was unheated. No voltage was applied to the anode nor was there a simmer current sustained between the auxiliary grid and the cathode. Emission from the discharge in H_2 at a pressure of 420 μm appears in Figure 3-3a and shows a significant delay between opposite ends of the cathode. The emission in Figure 3-2b for 600 μm

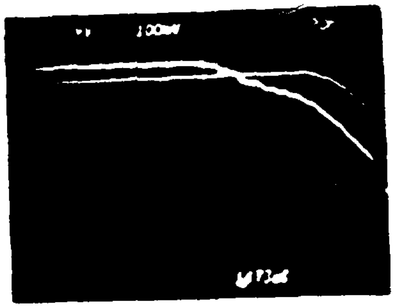

(a) 420 μms

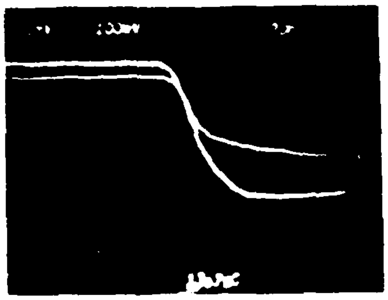

(b) 600 μms

85 09212

(20 ns/div)

Figure 3-3. PMT Signals from Different Locations in Thyratron for Auxiliary Grid Breakdown in H_2 (a) 420 μms, (b) 600 μms.

H_2 shows almost no delay. These results are summarised in Figure 3-4. For pressures greater than 500 μm, discharge coverage is simultaneous. For pressures less than 500 μm, there is a transition region where the delay increases with decreasing pressure. This transition region is only about 100 μm wide. For pressures less than 400 μm, the grid-cathode region appears to randomly light up along the length of the cathode. Improvements for the simultaneity of discharge coverage were obtained when a dc simmer current was sustained between the cathode and auxiliary grid. The simmer current was ≈100 mA (a few mA/cm^2 of cathode area). As shown in Figure 3-4, with the dc simmer current, the simultaneity of discharge coverage over the cathode remained at its minimum value (approximately 5 ns) to the lowest pressure examined (200 μm).

Similar measurements for discharge simultaneity were performed when using helium as the working gas. The time delay between pulse plasma emission from opposite ends of the grid-cathode region is plotted in Figure 3-5. For these measurements 5 kV was applied to the anode and was switched by the thyratron. When using a cold cathode and a dc simmer current (20 mA, ≈0.4 mA/cm^2), the discharge over the cathode was both uniform and simultaneous for the pressure range 750 μm - 3 Torr. When operating without a dc simmer current and with a hot cathode, simultaneity was not obtained over the same pressure range. A dc simmer current could not be used simultaneously with a heated cathode because of the tendency to pre-fire. Pre-firing was not a problem when using a heated cathode or a dc simmer current separately.

Having confirmed that the discharge covers the cathode simultaneously, a similar study was performed for the discharge between the control grid and anode. The emission from the discharge in this region was observed through the two optical ports in the top of the linear thyratron. These results are plotted in Figures 3-6a and 3-6b for H_2 and He, respectively. With H_2, simultaneity of the discharge between opposite ends of the anode improves with increasing operating pressure. Above 600 μm, with either hot or cold cathodes, the discharge is uniform and simultaneous. This simultaneity extends to 400 μm when operating with a cold cathode and with a dc simmer

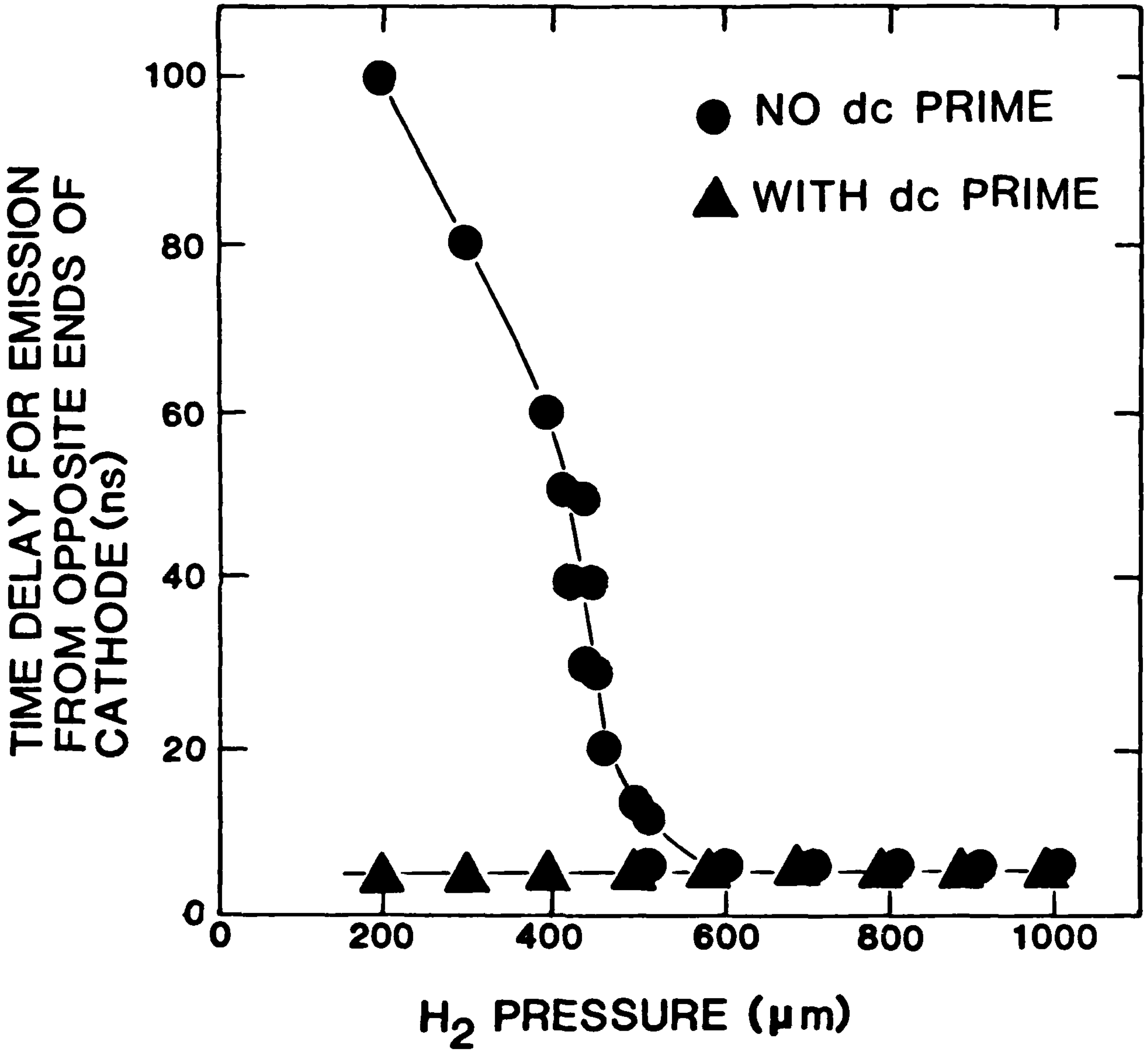

86 10738

Figure 3-4. Time Delay for Plasma Emission from Opposite Ends of the Cathode with and without a dc Simmer Current as a Function of Hydrogen Pressure.

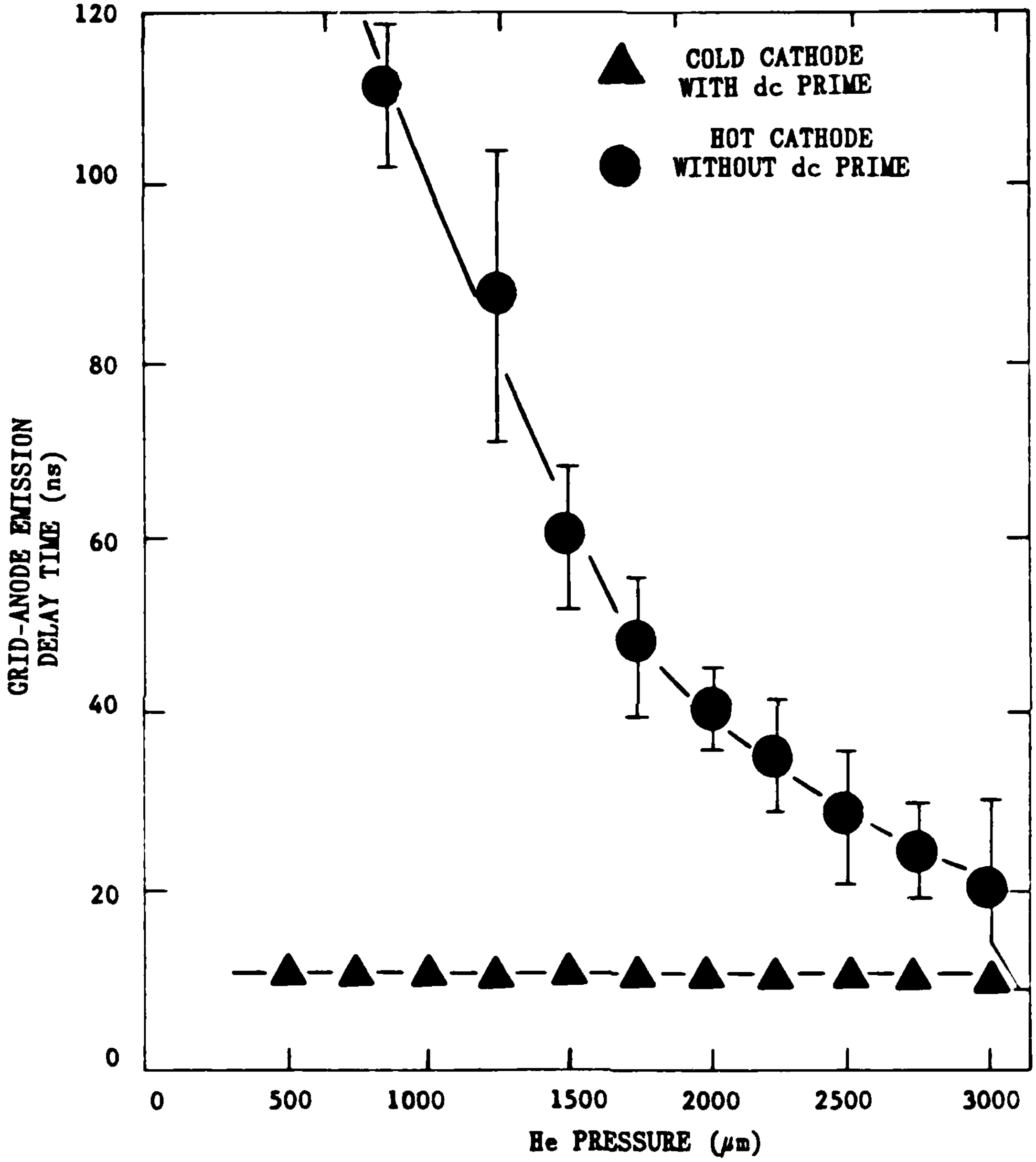

Figure 3-5. Time Delay for Plasma Emission from Opposite Ends of the Cathode for Operation in Helium for an Unheated Cathode with a dc Simmer Current and a Hot Cathode Without a dc Simmer Current. The Anode was charged to 5 kV.

10963

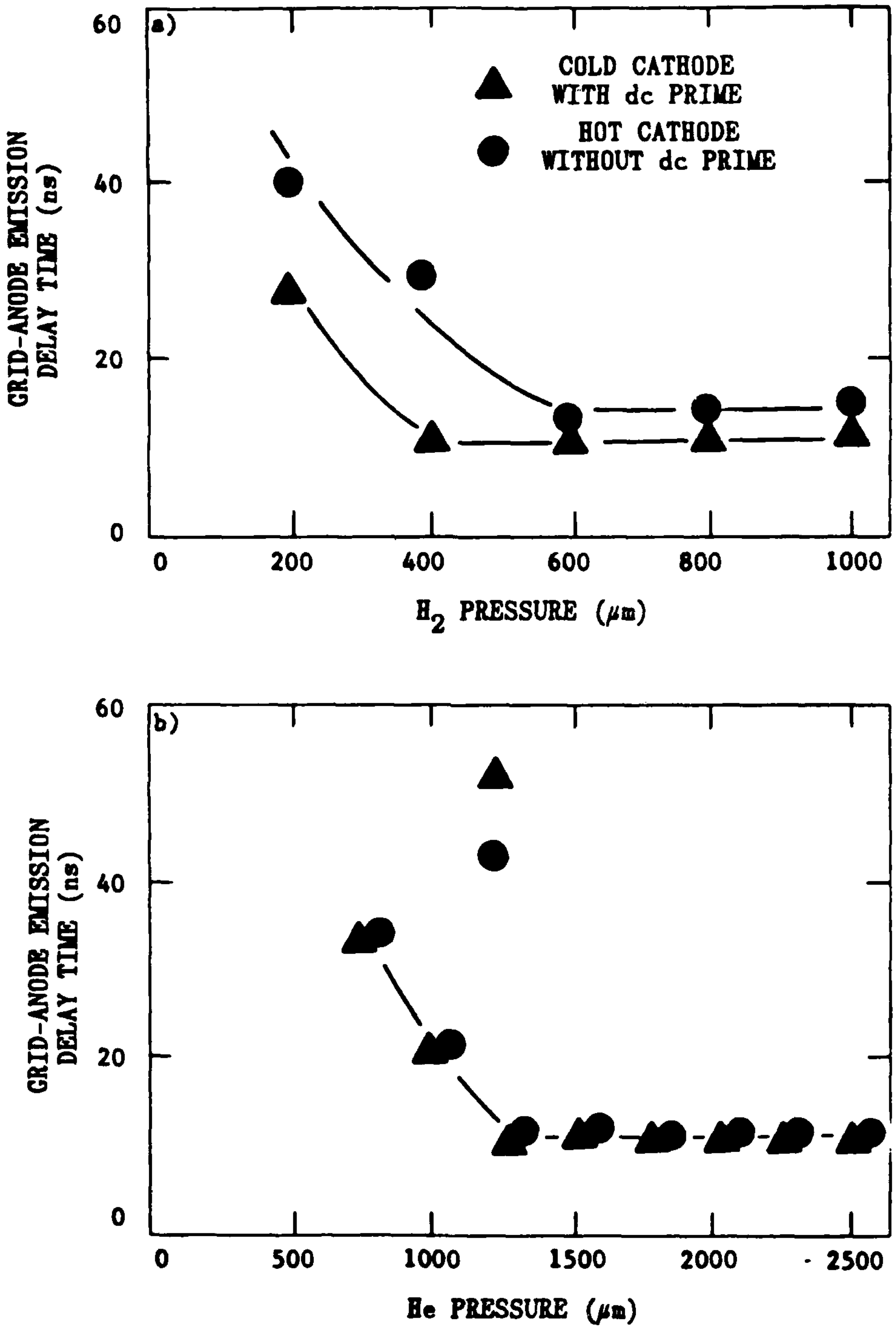

Figure 3-6. Time Delay for Plasma Emission from Opposite Ends of the Grid Anode Gap (a) Hydrogen, (b) Helium.

86 10964

current of 100 mA. Unlike the data obtained for simultaneity in the cathode region, which is maintained to pressures below 200 μm, the simultaneity between the control grid and anode is lost at pressures lower than 400 μm for the cold cathode and 600 μm for the hot cathode. Note, however, that the dc simmer on the auxiliary grid became erratic at these low pressures. For He, there is no differentiation in the simultaneity between hot and cold cathodes. In each case, simultaneity is obtained for pressures greater or equal to 1100 μm.

Another parameter of interest is the delay between discharge formation for the grid-cathode region as compared to the control grid-anode region, generally referred to as the anode delay time. This delay was measured by observing emission from both a side window and a window on top of the linear thyratron. These results are plotted in Figure 3-7 for He and H_2 with both a hot and cold cathode. The turn-on delay between opposite ends of the thyratron for the grid-cathode space and the grid-anode space also are plotted. The hot cathode measurements were made without a dc simmer current, due to the tendency towards pre-fire for those conditions, while the cold cathode measurements were made with 100 mA of dc simmer current. For helium, the anode delay time decreases from 250 ns at 500 μm to 80 ns at 2500 μm. For hydrogen, the anode delay time decreases from 120 ns at 300 μm to 50 ns at 800 μm. At the higher pressures, the residual anode delay times for hydrogen and helium are approximately 50 ns and 80 ns, respectively. Figure 3-7 shows that the grid-anode discharge simultaneity for both H_2 and He is within 10 ns when the anode delay time is minimum, which also corresponds to the minimum delay in grid-cathode discharge simultaneity.

From the results plotted in Figure 3-7, we can correlate the simultaneity of anode discharge spreading with the anode delay time. For operation with H_2, the anode delay (unheated cathode) is less than 50 ns except for pressures $\lesssim$300 μm when the dc simmer current becomes erratic. When operating with a heated cathode, however, the anode delay time is less than 50 ns only at pressures above 500 μm. The grid-cathode space takes more than 50 ns to uniformly break down only for pressures below 500 μm, which is the

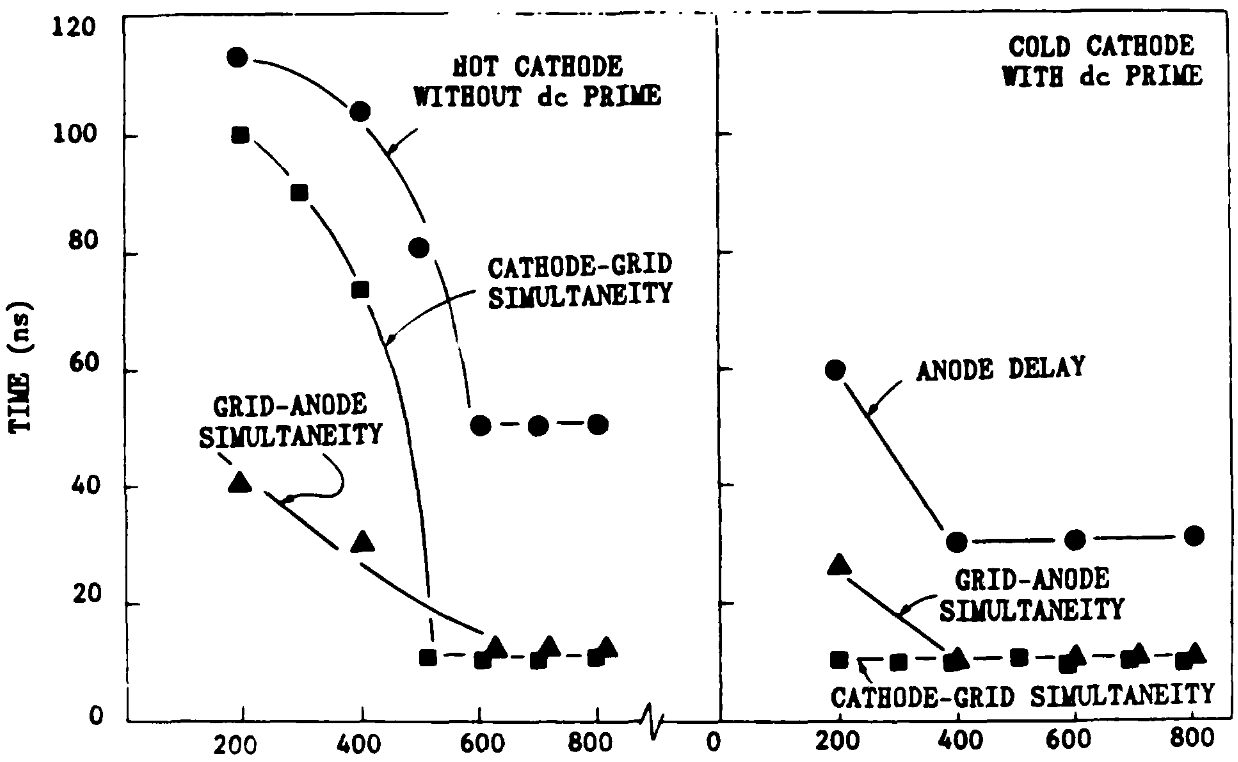

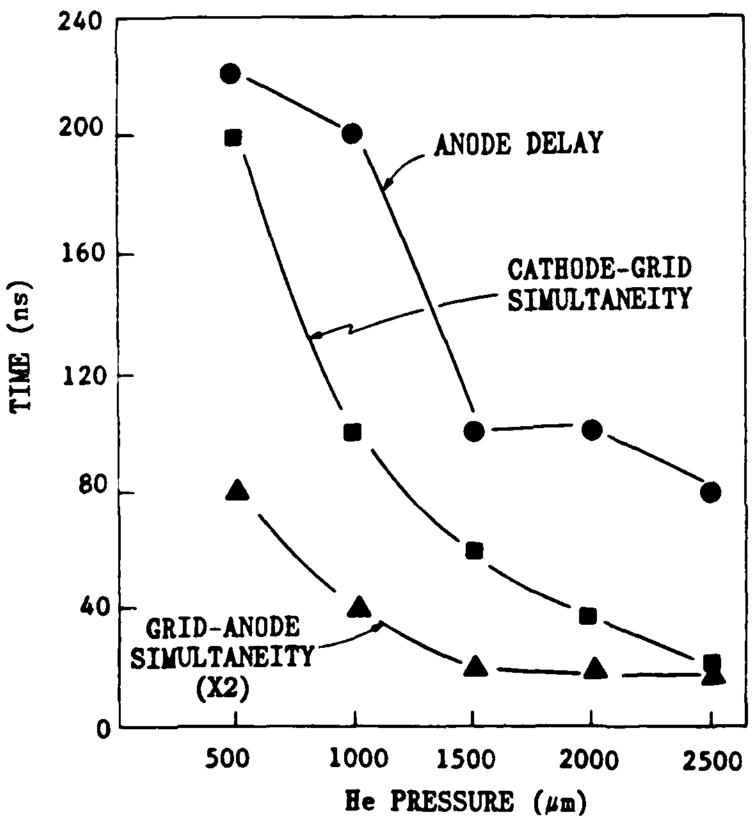

Figure 3-7. Relationship Between Anode Delay Grid-Anode Simultaneity and Cathode-Grid Simultaneity for Operation in H_2 (a) and (b) and He (c).

point where the anode turn-on time exceeds a nominal 10-ns delay time. It appears that if the time required for the discharge to uniformly cover the cathode exceeds the anode delay time (the time between triggering and anode voltage collapse), the grid-anode space will not fill with discharge simultaneously.

A similar correlation applies to helium. At high pressure (2500 μm), the anode delay time is nominally 80-100 ns. Below 1250 μm, the time required for the cathode region to uniformly light exceeds 100 ns. This pressure is the transition point below which anode simultaneity exceeds the nominal 10 ns delay time. From these observations, we can again conclude that the grid-anode space will fill with discharge simultaneously (within 10 ns) if the time required for the discharge to completely fill the grid-cathode space does not exceed the anode delay. The dc simmer current minimises the time for the grid-cathode region to uniformly fill (with high density pulsed plasma), thereby insuring that the grid-anode turn-on delay will also be a minimum.

3.5 ELECTRICAL CHARACTERIZATION

High-voltage holdoff capability of the linear thyratron was measured by applying a half-sinusoidal voltage, measuring 2 μs FWHM, to the anode for a variety of pressures in H_2 and He. For these measurements, the grids were not driven and the cathode was cold. The results are plotted in Figure 3-8. The holdoff voltage increased with decreasing pressure (i.e., P•D product) as expected since we are operating on the left-hand side of the Paschen curve. Breakdown for these conditions occurred in the control grid-cathode gap and presumably through the control grid slot, although the slot could not be directly observed during breakdown. The same upper limit in holdoff voltage, 25 kV, was measured in both H_2 and He. Breakdown at these points did not occur in the gap as with the Paschen-like data, but rather as flashover across the Pyrex high voltage insulator. This breakdown could be visually observed through the translucent insulator. We interpret these data as having reached a field emission limit at the triple point between the gas, insulator, and metal body of the thyratron. Electric field enhancement is sufficiently high

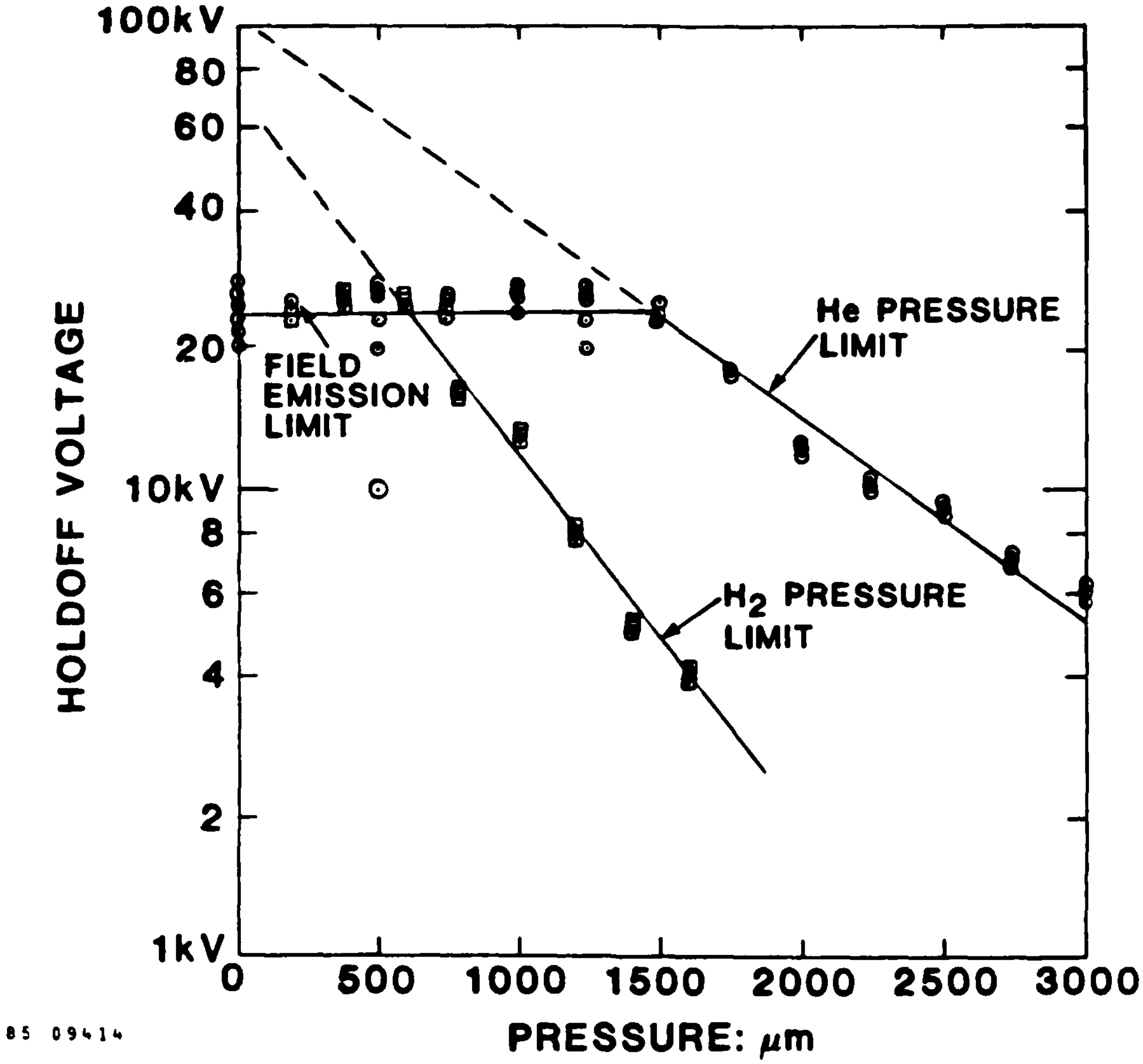

Figure 3-8. Holdoff Voltage for the Linear Thyratron in He and H_2.

that field emission of electron occurs, thereby inducing breakdown. This effect is a function predominately of geometry and is to first order independent of the operating gas, as confirmed by our measurements.

The upper limit to holdoff voltage in the linear thyratron can, in principle, be extended. Mancebo demonstrated that holdoff in thyratrons is dominately limited by field emission (Reference 5). By paying careful attention to the shape of the electrodes in his device, making sure to round edges to limit local electrode fields to less than 10^6 V/cm, Mancebo demonstrated reliable holdoff to 100 kV. The holdoff voltage data in Figure 3-8 is interesting when it is extrapolated beyond the field-emission limit for a thyratron in which field emission had been eliminated by careful contouring of all edges. The extrapolation indicates that for our present gap spacing of 200 mil and a pressure of ≈100 μm, the holdoff voltage would be ≈100 kV in He and ≈70 kV in H_2. By reducing the gap to ≈75 mils, we could expect to operate at 100 kV with a 300-μm pressure in helium, and possibly that high in voltage with hydrogen at a lower pressure.

Anode voltage fall time in the linear thyratron was measured as a function of H_2 pressure and is plotted for operation with hot and cold cathodes in Figure 3-9. When operating with an unheated cathode, a dc simmer current was used to reduce jitter, whereas the hot cathode results were obtained without a dc simmer current. When operating with a hot cathode, the anode fall time is longer than when operating with a cold cathode, an effect we attribute to the absence of the dc simmer current. The minimum current rise time for the thyratron in this configuration is approximately 80 ns. The circuit inductance is ≈180 nH, making this current rise time the inductively limited value.

The voltage fall time is longer than desired and indicates that the resistance of the thyratron is relatively high. To determine the source of the high impedance, we compared the relative voltage drops between the anode and cathode and between the grids and the cathode. These results are summarized in Figures 3-10 and 3-11. Figure 3-10 is a typical trace for

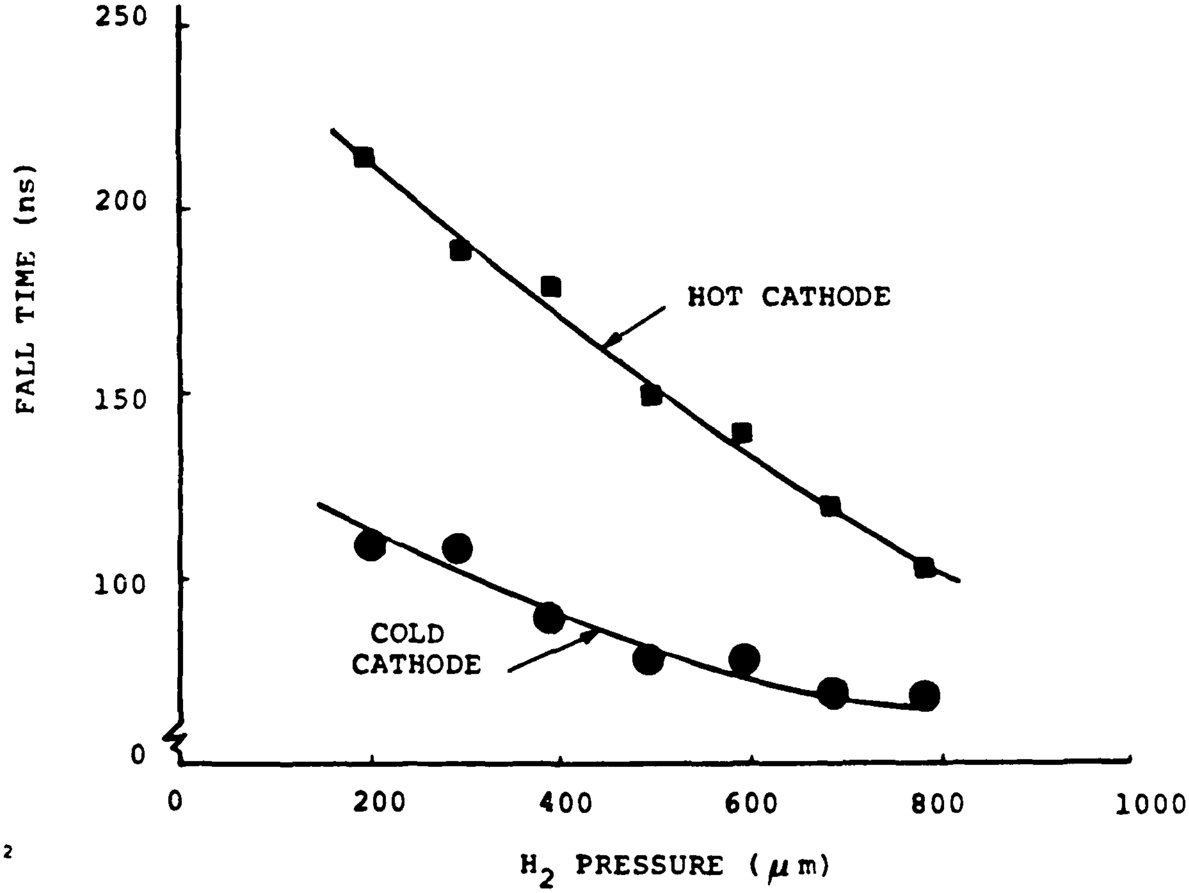

85 09162

Figure 3-9. Anode Fall Time With Hot and Cold Cathodes for Anode Voltage of 6 kV.

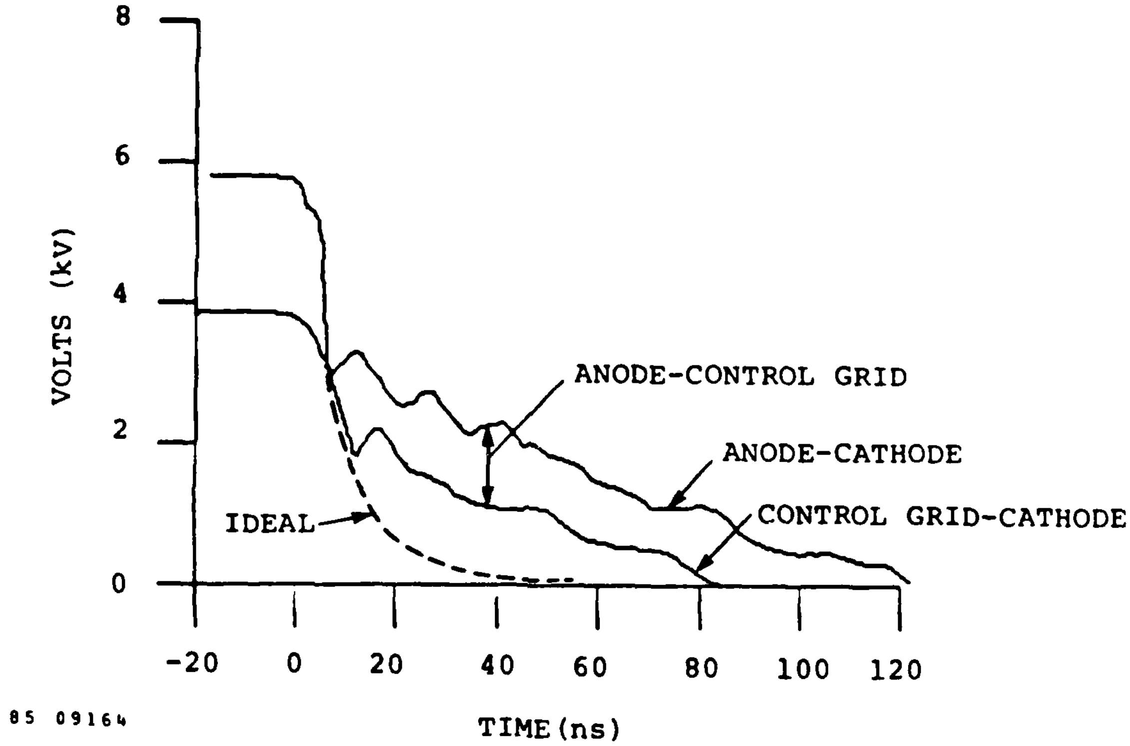

Figure 3-10. Typical Voltage Traces (H_2 500 μm) Indicating Large Voltage Drop Between Control Grid and Cathode.

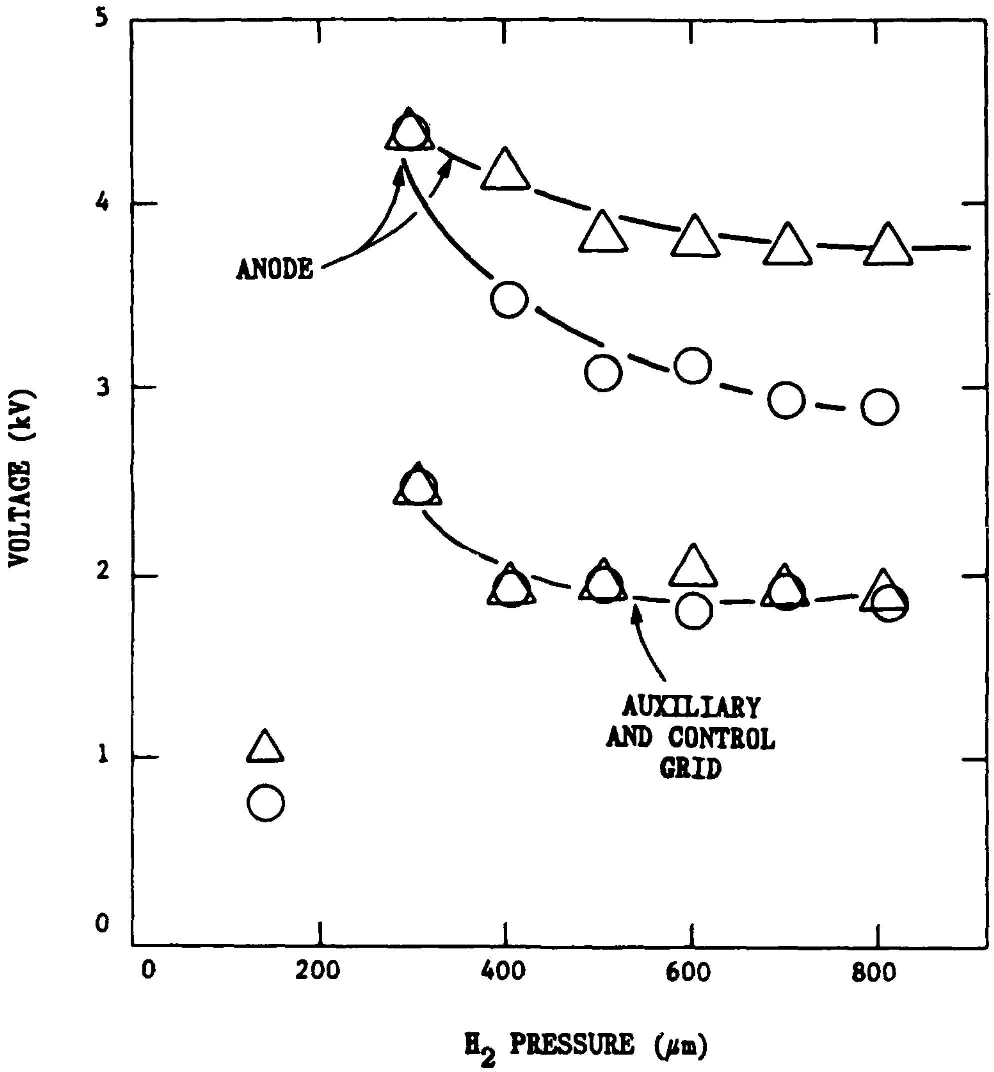

Figure 3-11. Voltage 20 ns After Breakdown.

86 10967

voltage between (a) the anode and cathode and (b) the control grid and cathode, showing that approximately half the tube voltage during the first 80 ns of conduction is dropped between the control grid and the cathode. The anode and control grid voltages 20 ns after breakdown are plotted in Figure 3-11 as a function of gas pressure in H_2. The control grid and auxiliary grid voltages are nearly equal at this time, indicating that the large voltage drop discussed above is between the auxiliary grid and cathode.

The large voltage drop between the auxiliary grid and cathode during commutation, and the relatively poor high-voltage holdoff with a hot cathode can be attributed to the control and auxiliary grid designs. The grid configurations are shown schematically in Figure 1-2. The auxiliary grid slot is relatively narrow. Once breakdown occurs, the small auxiliary grid slot restricts the flow of current, perhaps even quenching in the slot, thereby requiring higher voltages to sustain current to the anode. The consequences of this "first iteration" design are discussed further below.

3.6 AUXILIARY GRID MODIFICATIONS

In the design of the auxiliary grid in the prototye linear thyratron, most of the cathode was shielded from the control grid. Two narrow slots directly below the control grid slots provided the conduction path from the cathode. The flow of current was restricted and, as a result, the plasma appeared resistive. This configuration proved unacceptable because the high voltage sustained between the control grid and cathode during conduction promoted discharge attachment to the thyratron sidewalls, conductors at the cathode potential. Discharge flowing in this manner increased the difficulty of interpreting experimental results and led to inconsistencies between experiment and theory.

The first indication that electron emission was not limited to the cathode was obtained from measurements of excited-atom densities in the discharge plasma (see Section 4). We found that highest excited-state densities were located near the thyratron walls rather than at the cathode.

Open shutter photographs of the discharge through the end viewports collaborated the spectroscopic measurements. Photographs illustrating this errant plasma emission appear in Figure 3-12. In the first sequence of photos (Figures 3-12a,b,c), emission is recorded from a discharge in 2000 μm of He operating with a hot cathode. In Figure 3-12a, only the auxiliary grid was pulsed with no anode voltage; in Figure 3-12b, the auxiliary and control grids were pulsed with no anode voltage; and in Figure 3-12c, only the control grid was pulsed with no anode voltage. When only the auxiliary grid is pulsed, or when both the auxiliary and control grids are pulsed, it appears that the discharge is emanating from the sidewalls of the thyratron. Relatively little emission appears to come directly from the cathode. (Remember that the stainless steel sidewalls are at cathode potential.) When only the control grid is pulsed, the discharge appears to flow dominantly from the cathode and through the slot in the auxiliary grid. These results demonstrate that the anomalous emission from the sidewalls is not a result of cathode material having been deposited there. These conditions were modeled with the plasma simulation code LINTHY2D to determine whether electron emission from the sidewalls would account for our observations. In summary, results from the calculations confirmed our hypothesis. The calculations are discussed in detail in Section 4.

More evidence for the anomalous electron emission described above appears in Figures 3-12d,e. These are open shutter photographs of emission from the discharge with voltage on the anode. In Figure 3-12d, both the auxiliary and control grids are pulsed, whereas in Figure 3-12e only the control grid is pulsed. When both grids are pulsed, emission appears to come dominantly from the auxiliary grid-control grid gap, indicating that current is not preferentially coming from the cathode. More emission is observed in the auxiliary grid-cathode space only for the case where the control grid alone is pulsed. Thus, even with anode potential present, the location where the "cathode" discharge strikes is determined by the P•D product of the initial conditions.

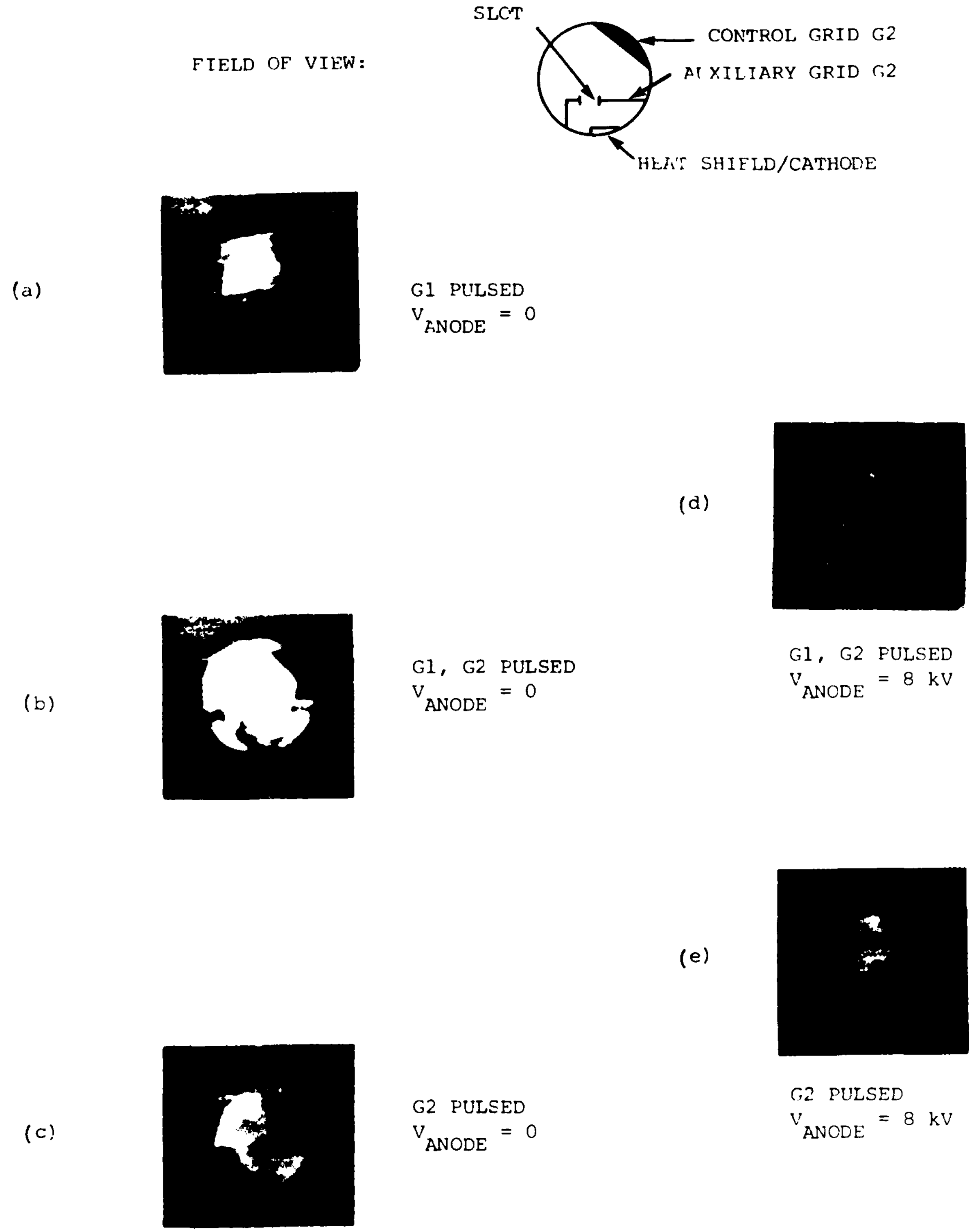

85 09415

Figure 3-12. Open Shutter Photographs of Emission from Linear Thyratron (hot cathode, He, 2000 μm)

When the linear thyratron was opened for physical examination of the internal surfaces, additional evidence of errant discharge behavior was obtained. It was apparent that the discharge had attached to the thyratron sidewall by the presence of arc marks on the steel. These arc marks are shown in Figure 3-13. Pitting occurred on the cathode heat shield as well.

Based on the discussion above, we would argue that "better" operation is obtained when only the control grid is pulsed. This argument is based on the fact that current appears to flow from the correct surfaces when only the control grid is pulsed. However, we have already shown that uniform and simultaneous discharge formation over the length of the thyratron, as well as low jitter, can only be obtained by pulsing the auxiliary grid. These observations motivated us to consider modification of the grid structures. Various auxiliary grid configurations were considered and modeled. We decided to bend the auxiliary grid vertically away from the cathode, thereby exposing more cathode to the control grid. This modification was designed to steer the discharge to the cathode and keep it from attaching to the body of the thyratron. Figure 3-14 shows the old auxiliary grid geometry and the modified version that we incorporated.

During this modification, the thyratron body also was modified to accept larger end flanges, which enables mounting of larger windows to view the entire cathode-control grid gap. Figure 3-15 indicates the field of view with the new windows compared to that of the old ones. A photograph of the linear thyratron with the larger viewports appears as Figure 3-16. Figure 3-17 is an open-shutter picture of the discharge with the new arrangement, confirming that the new auxiliary grid successfully shielded the sidewall from the discharge, and the cathode is being fully utilized.

With the larger viewports and modified auxiliary grids, framing camera photography of the plasma emission was repeated and we confirmed that the walls of the thyratron were no longer acting as a cathode. Once this physical modification in the thyratron was made and verified, the pulse forming network (PFN) was modified. This modification was intended to allow an

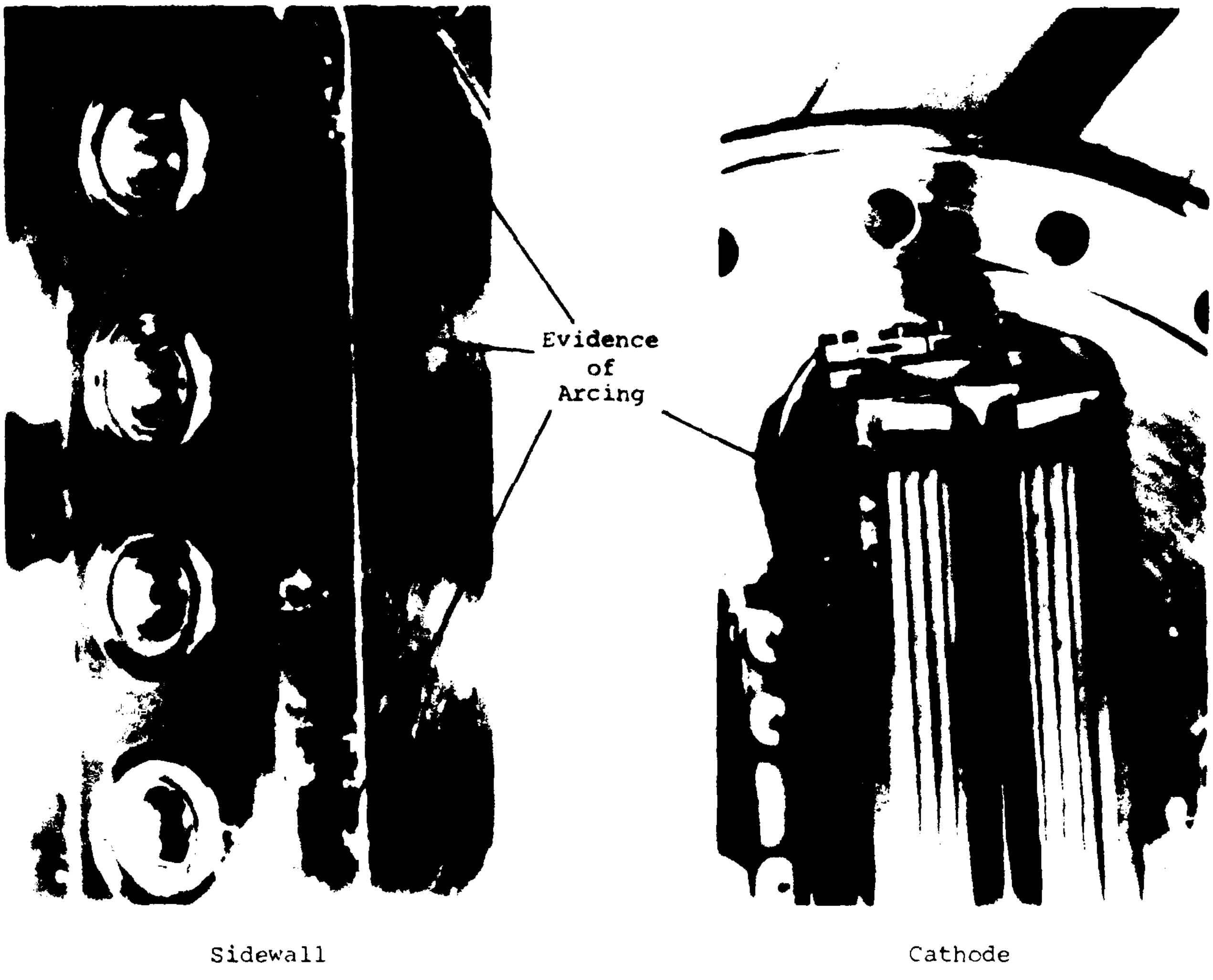

Figure 3-13. Photograph Showing Arcing on the Thyratron Sidewall and on the Cathode Heat Shield.

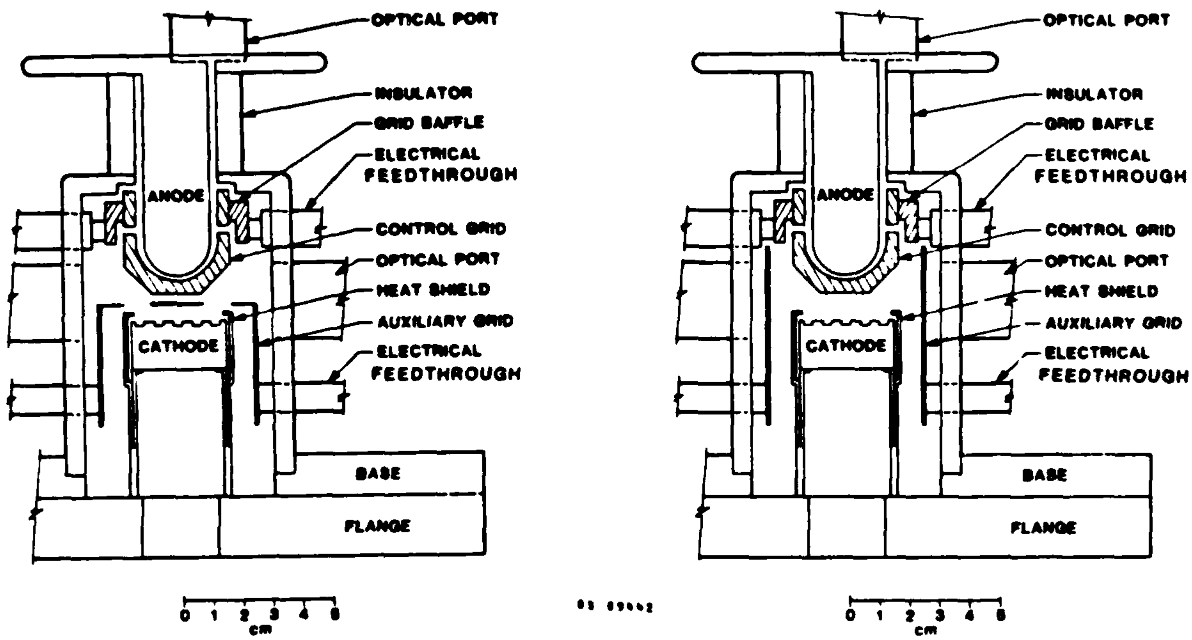

Old Auxiliary Grid Geometry:
Grid Shielded the Cathode

Modified Auxiliary Grid Geometry:
Grid Shields the Sidewalls,
Cathode is now Exposed.

Figure 3-14. Comparison of the Old Auxiliary Gird Geometry with the New, Modified Version.

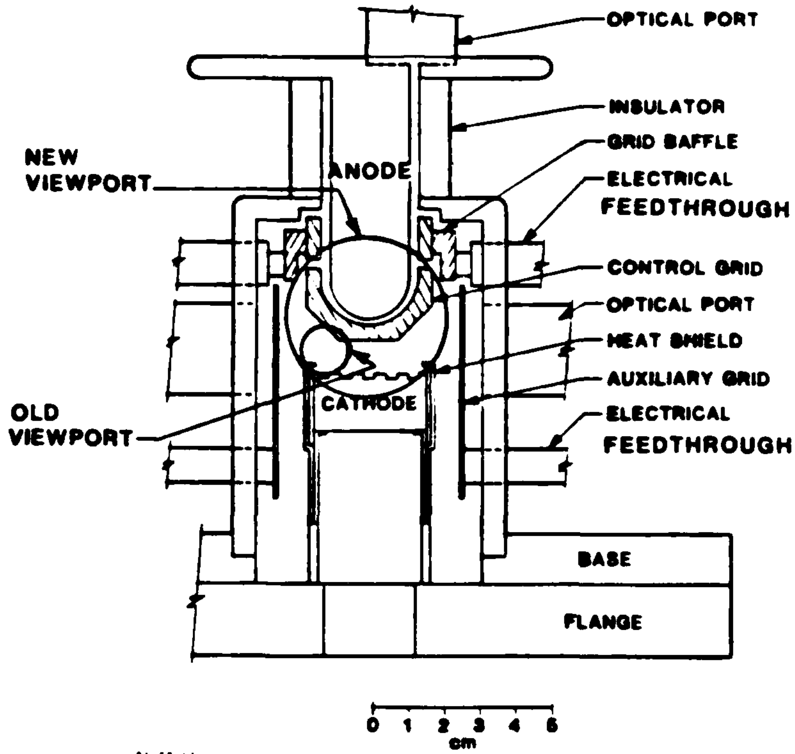

Figure 3-15. Field of View of New Viewport Compared to the Old One.

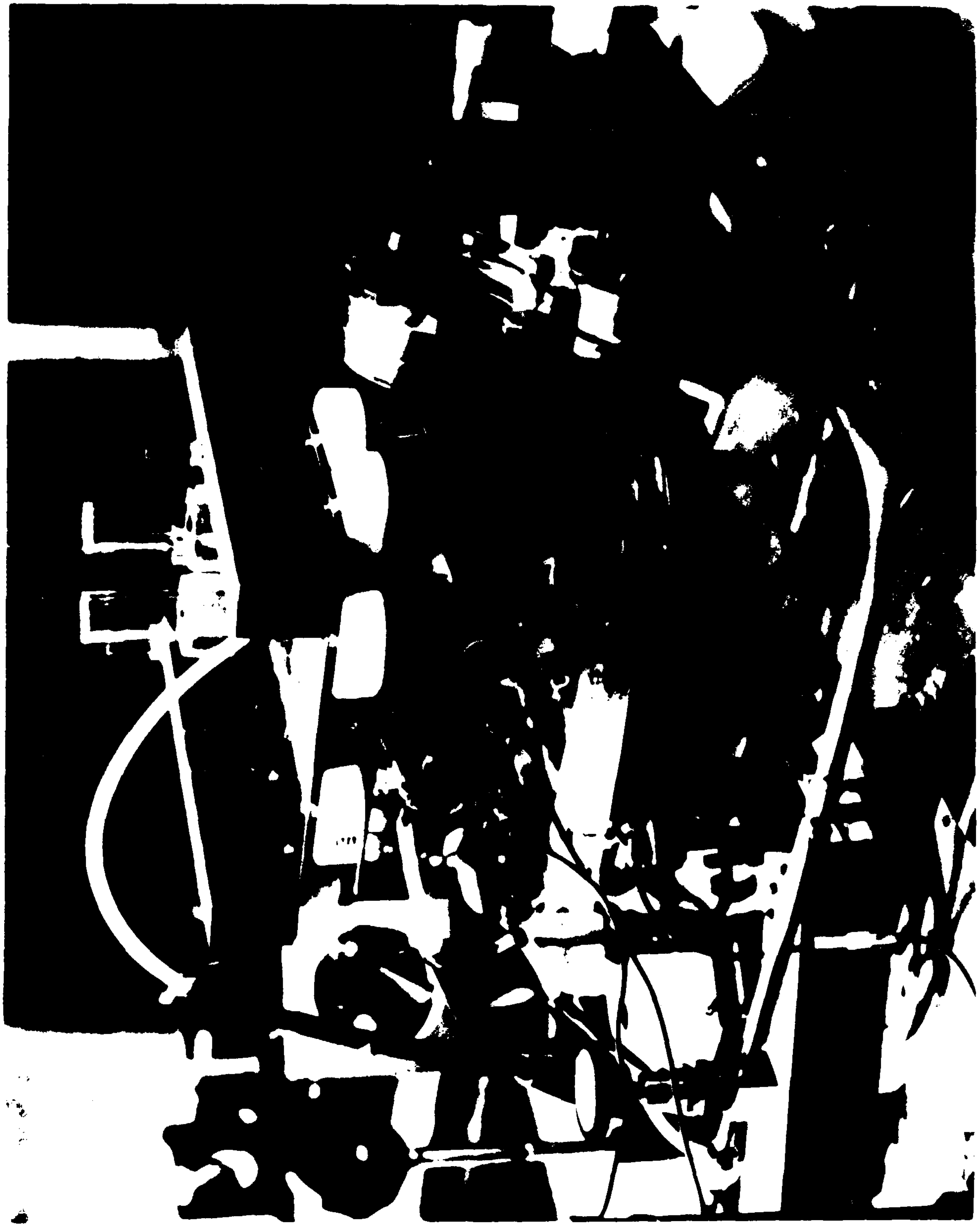

Figure 3-16. Linear Thyratron with Large Viewports Installed.

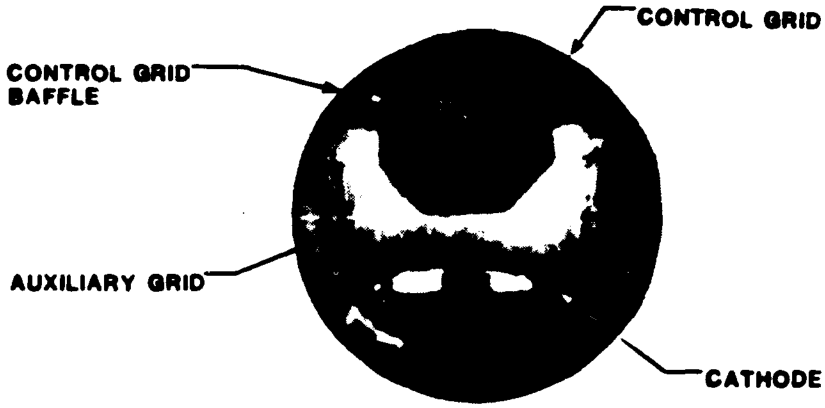

86 11005

Figure 3-17. Open-Shutter Picture of Linear Thyratrons Operating in Helium.

increase in both the current and the dI/dt obtained from the thyratron and to confirm that the previously measured values were, in fact, inductively limited. The physical layout of the PFN current return path was made more compact and the current transformer that had previously been used to measure current was replaced with an in-line current viewing resistor (CVR). These modifications reduced the inductance of the thyratron discharge circuit by greater than half (180 nH → 75 nH). Concurrent with these modifications, the load resistor in the PFN was reduced from 2 Ω to 0.5 Ω. Current and voltage traces with the old high inductance and the new low inductance geometries are shown in Figure 3-18. The peak current is approxmiately 3200 A with an initial dI/dt of 8×10^{10} A/s. This is an improvement over the values obtained in the high inductance geometry of 1200 A and 1.2×10^{10} A/s, also shown in Figure 3-18 for otherwise identical conditions. The dimensions of the slotted cathode are 3 × 10 cm, yielding an effective current density of 100 A/cm^2 in the low inductance geometry. Taking into consideration the addition area of the slots, the normalized current density is approximately 50 A/cm^2. Anode voltage initially falls rapidly from its 8 kV peak value to ≈4 kV in about 10 ns, then decays to a few hundred volts in 60 ns. The shorter voltage fall time indicates a lower plasma resistance plasma with the new grid configuration.

Due to the low switching voltage in the previous examples, we felt that the current was still inductively limited, and that the cold emission capability of the cathode had not been reached. To further increase the current, the load resistor was shorted out. The current and voltage traces for operation with the shorted load resistor are shown in Figure 3-19. The peak current is 5000 A with a dI/dt of 1.25×10^{11} A/s. The effective current density of the cathode is 160 A/cm^2.

• CURRENT LIMITED BY LOW ANODE VOLTAGE (INSULATOR FLASHOVER)

V 2 kV/δ

OV

I 200 A/δ

OA

• 50 ns/δ

V 2 kV/δ

I 800 A/δ

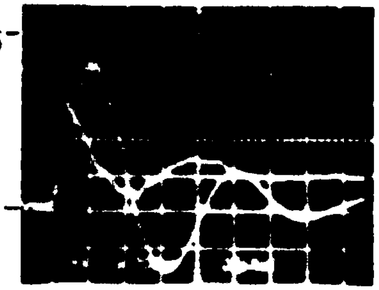

HIGH INDUCTANCE GEOMETRY

- $R_L = 2\Omega$
- I_p = 1200 A (dI/dt = 12 GA/s)

LOW INDUCTANCE GEOMETRY

- $R_L = 0.5\Omega$
- I_p = 3200 A (dI/dt = 80 GA/s)

85 09541

Figure 3-18. Linear Thyratron Voltage and Current Waveforms for High Inductance and Low Inductance Geometries for Operation in He at 1.2 Torr with an Unheated Cathode.

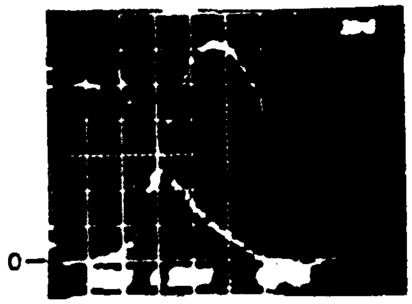

86 10991

Left: ANODE VOLTAGE 2 kV/div
Right: CURRENT 800 A/div
Horizontal: 20 ns/div
Cold Cathode (20 °C)
1.5 Torr Helium

Figure 3-19. Linear Thyratron Commutation Waveforms with Shorted Load Resistor for Operation in He at 1.5 Torr with an Unheated Cathode.

REFERENCES

1. Private conversation, R. Petr (STI) with S. Levy and S. Schneider (ERADCOM), June 1984.

2. D. Turnquist, R. Caristi, S. Friedman, S. Merz, R. Plante, and N. Reinhardt, IEEE Trans. Plasma Sci. PS-8: 185 (1980)

3. R.A. Petr and M. Gundersen, Lasers and Particle Beams 1: 207 (1983)

4. M.J. Kushner, W.D. Kimura, and S.R. Byron, J. Appl. Phys. 58: 1744 (1985)

5. L. Mancebo, "100-kV Thyratron Without Gradient Grids," IEEE Trans. Elect. Dev. ED-18: 920-924, October 1971.

Section 4
LINEAR THYRATRON OPTICAL CHARACTERIZATION

4.1 INTRODUCTION

The physical configuration of the linear thyratron (LT) is amenable to optical characterization by using laser interferometry. The linear geometry provides a long pathlength, and the large optical ports allow viewing of the entire cathode-control grid region. Hook method spectroscopy was applied to the study of excited state densities on the linear thyratron. The detection limit for the density of excited states using this method for our conditions is $\approx 10^{11}$ cm^{-3}. In Section 4.2, the experimental apparatus used to make excited state measurements in the linear thyratron and the hook method are described. Excited state densities for discharges in He and H_2 are presented and discussed in Section 4.3.

4.2 DESCRIPTION OF HOOK METHOD INTERFEROMETER

The hook method interferometer and experimental set-up are sketched in Figure 4-1. A photograph of the experimental apparatus appears in Figure 4-2. The thyratron was mounted on an x-y translation stage in one leg of a Michaelson interferometer. The thyratron could be repositioned with an accuracy of $\approx$0.5 mm. A Michaelson interferometer was chosen in order to increase the pathlength of the probe through the plasma. An optical element to compensate for the windows of the thyratron and to provide a method of tilting the fringes was placed in the other leg of the inteferometer. The interferometer was illuminated by a wide band ($\Delta\lambda \approx 8$ A) nitrogen pumped dye laser (pulse duration $\approx$2 ns) collimated to a spot size of 1 mm using a two-element telescope. The N_2 laser produced ≈ 50 μJ of energy. The resulting fringe pattern was dispersed by a 1-m spectrometer with a 1200 ℓ/mm grating operated in second order. We used an RCA TC2011 vidicon camera as a two-dimensional detector and recorded the fringe patterns on videotape for later

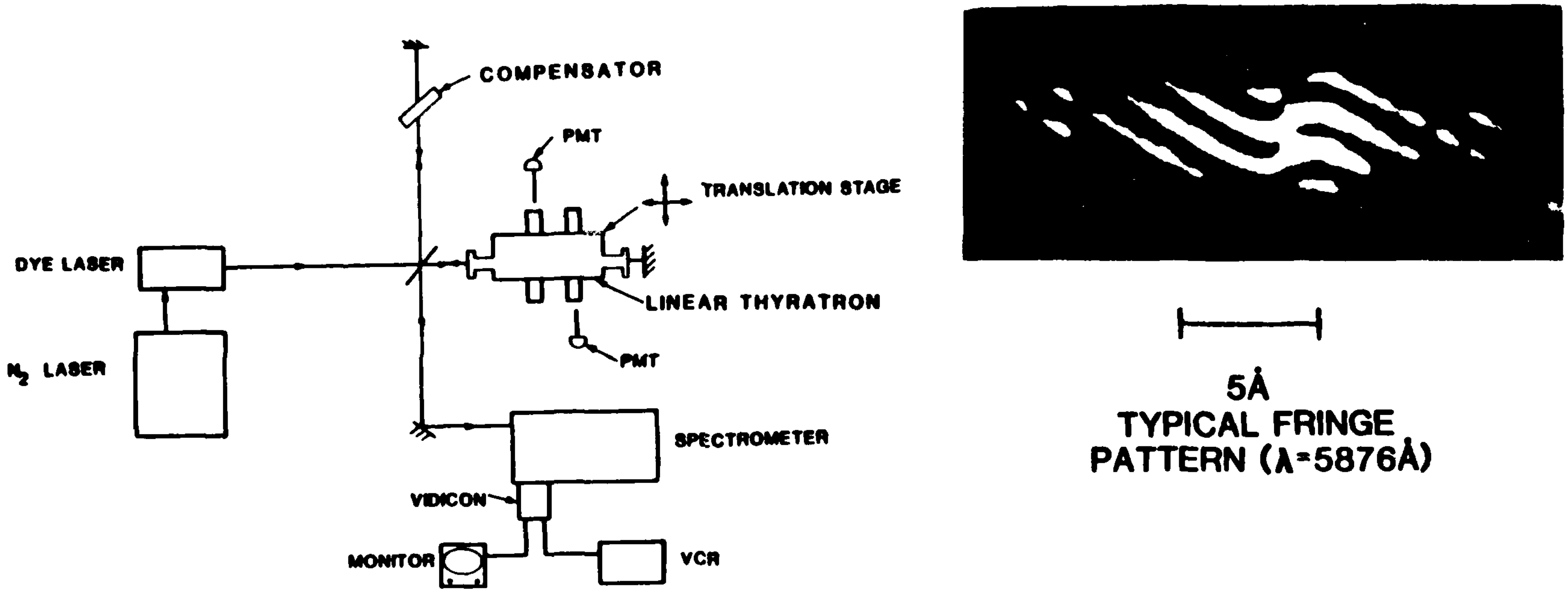

86 10988

Figure 4-1. Schematic of Hook Method.

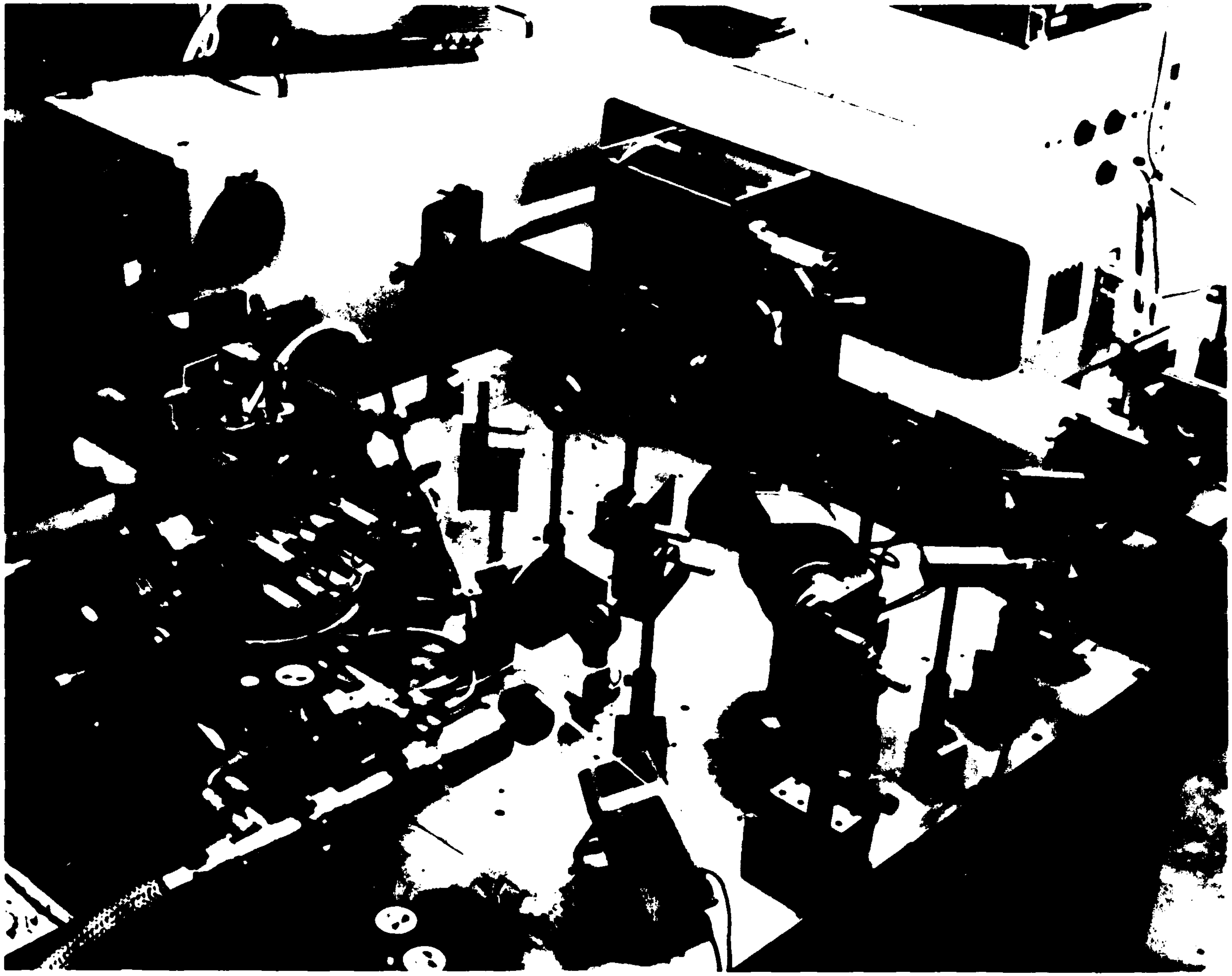

Figure 4-2. Experiment Apparatus showing Lasers, Hook Interferometer, and Spectrometer.

analysis. A 1.0-1.5 neutral density filter was required before the spectrometer to avoid saturation of the vidicon.

The duration of the dye laser is sufficiently short that the interferometer records an "instantaneous" value of the excited state density (actually averaged over 2 ns). A time resolved measurement is obtained by delaying the dye laser with respect to the current pulse on successive firings of the thyratron. The system jitter is at best 5-10 ns, largely due to the jitter of the thyratron. The first indication of the thyratron acting "poorly" is for the jitter to grow to many tens of nanoseconds. When this occurred, the thyratron was flushed a few times with fresh gas, and jitter returned to its lower value. Time and spatial resolution is obtained by setting at a particular spatial location and obtaining interferograms at many delay times, changing the spatial location, and repeating the process. An "x-y" map of excited states for time t_o is obtained by interpolating the time resolved measurements.

A typical fringe pattern obtained from the interferometer is shown in Figure 4-1 and is obtained by tuning the wide band dye laser to overlap the transition of interest. An excited state density is obtained from the fringe pattern by measuring the distance (in wavelength) Δ between the extrema of the "hooks" in the interferograms and applying the relation (Reference 1)

$$N = \frac{\pi k \Delta^2}{r_o \lambda^3 f \ell} \qquad [4.1]$$

where N is the number density of the excited state, f is the oscillator strength of the transition, r_o is the Bohr radius, ℓ is the pathlength, λ is the wavelength of the transition, and k is the order of the interferogram. This order is obtained from $k = p\lambda/\Delta\lambda$, where $\Delta\lambda$ is the wavelength separation between p fringes.

4.3 EXCITED STATE DENSITIES IN THE LINEAR THYRATRON WITH "NON-OPTIMUM" GRIDS AND COMPARISON WITH THEORY

Excited state densities during a discharge pulse were first measured in the prototype thyratron equipped with the small windows. Even though the view of the plasma was somewhat limited (see Figure 3-15), quite useful information was obtained, which was later used to modify the grids of the thyratron. The first measurements were of the 2^3P state in helium at a pressure of 900 μm with the thyratron switching 8 kV. The auxiliary and control grids were pulsed, and a dc simmer current was used with an unheated cathode to minimize jitter. The dye laser was tuned to 5876 A, and the spectrometer was operated in second order.

Current and voltage waveforms for the experimental conditions appear in Figure 4-3. Contour maps of the density of the He 2^3P excited state appear in Figure 4-4. Since the effective lifetime of this state may be long compared to the duration of the current pulse, due in part to radiation trapping, the measured densities are an indication of the time integral of the local excitation rate for populating that state and, by inference, of the current density. In Figure 4-4 at 20 ns, the current appears to flow through the auxiliary grid slot and is directed towards the control grid, but not in the direction of the control grid slot. By 40 ns, current is dominantly directed towards the control grid slot. Note that there are two local regions of excited state maxima: in the auxiliary grid slot and below the control grid slot. In the frames for 60, 80, and 100 ns, we see a widening of the current density and a relatively large current density to the left of the auxiliary grid slot, indicating that a large fraction of the current flowing to the control grid and control grid slot is not originating through the auxiliary grid slot. The peak of the current occurs at ≈100 ns. During the fall of the current, the local maximum in excited state density returns to the region just above the auxiliary grid slot.

We attempted to repeat the measurements for the same conditions while operating with a hot cathode. When operating with a hot cathode, however,

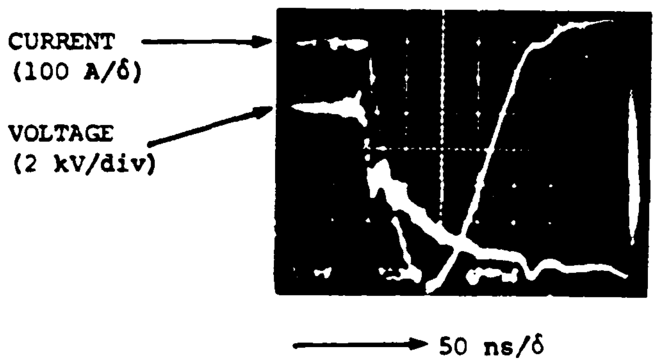

86 11006

Figure 4-3. Current and Voltage Waveforms for Conditions of Hook Spectroscopy Results (He 900 μm).

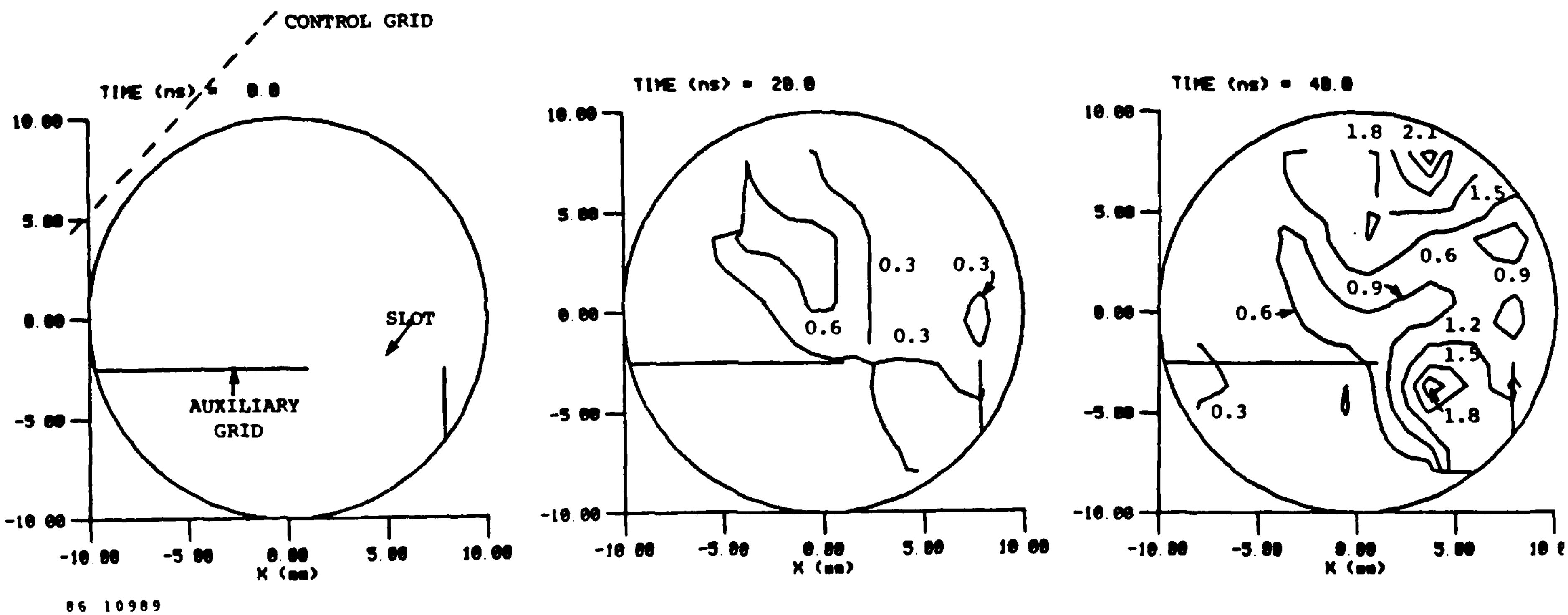

Figure 4-4. He 2^3P Density (10^{12} cm^{-3}) 900 µm He, 8 kV (Cold Cathode).

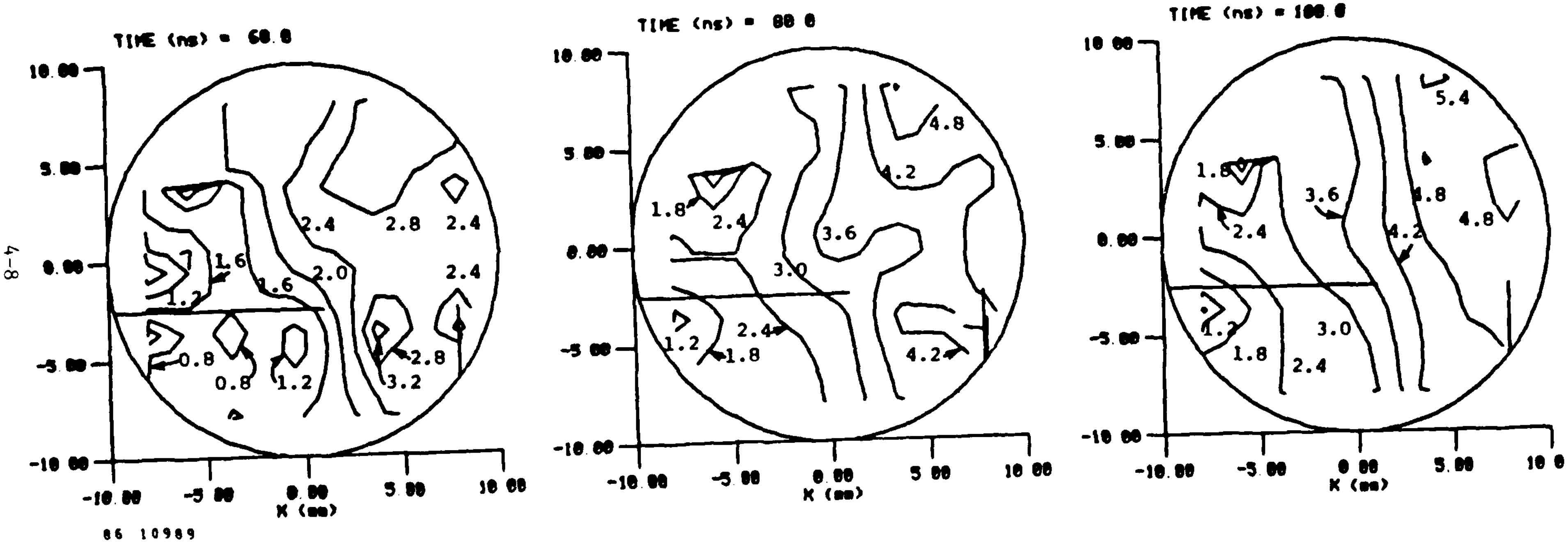

Figure 4-4.(cont.) He 2^3P Density (10^{12} cm^{-3}) 900 μm He, 8 kV

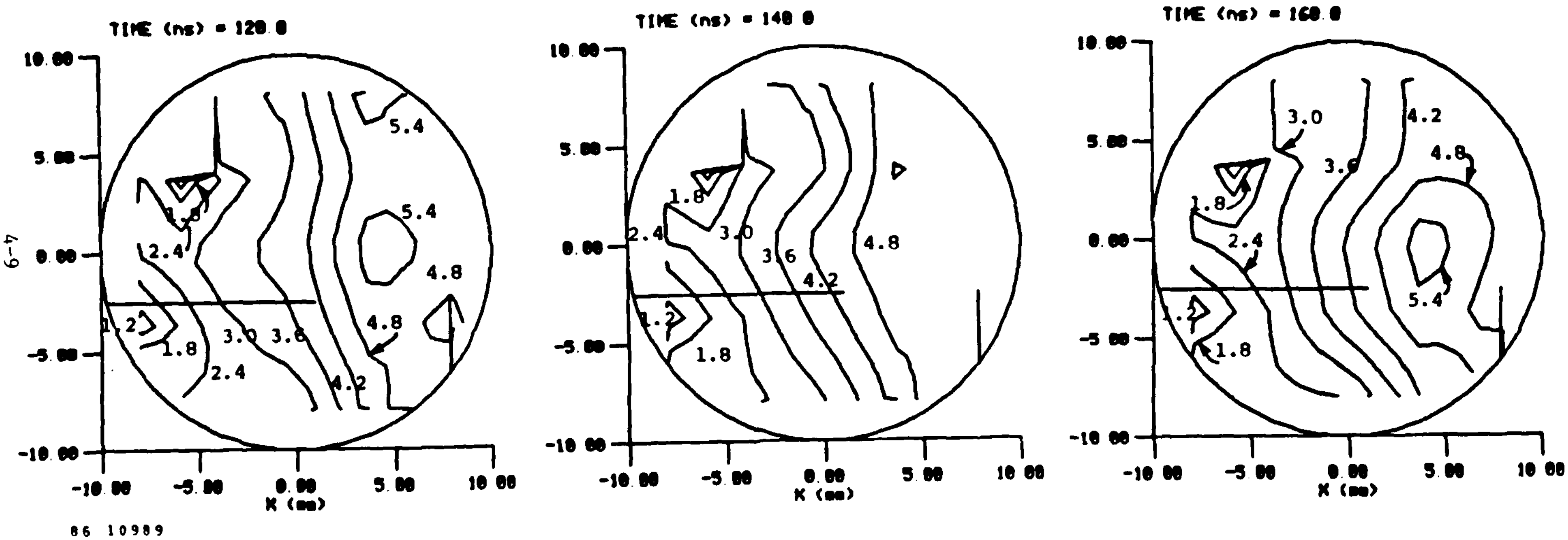

Figure 4-4.(cont.) He 2^3P Density (10^{12} cm^{-3}) 900 μm He, 8 kV

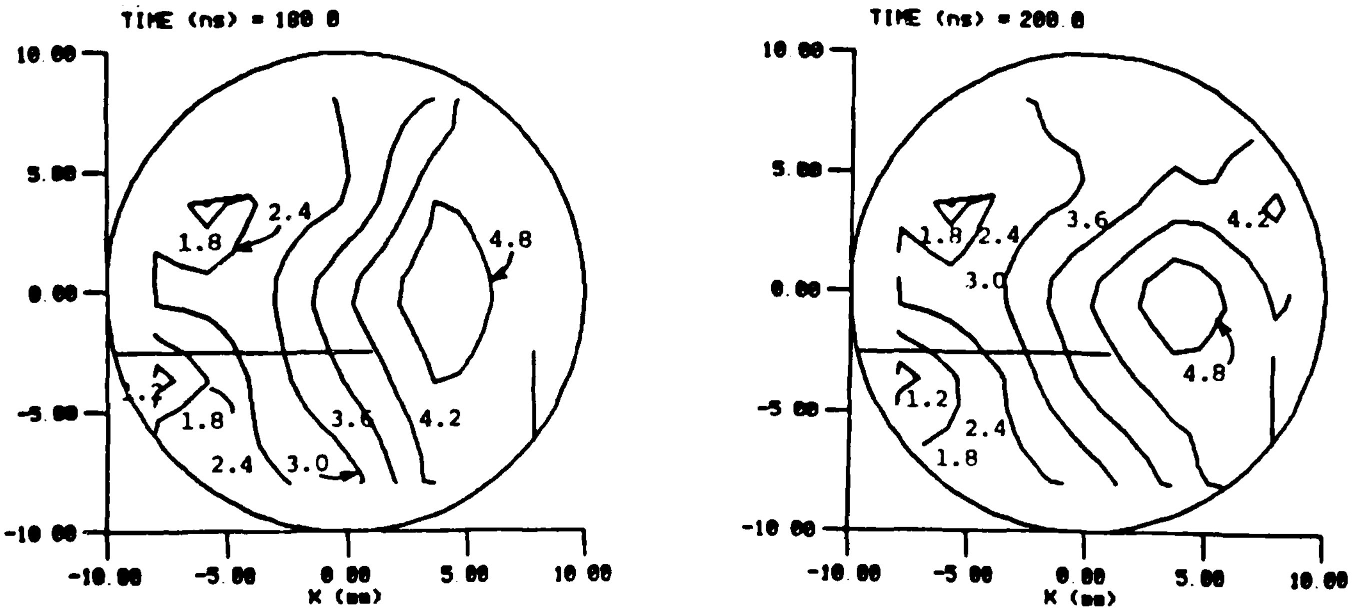

86 10989

Figure 4-4. (cont.) He 2^3P Density (10^{12} cm^{-3}) 900 μm He, 8 kV

jitter was too large to obtain meaningful data. To reduce the jitter to acceptable values (<5-10 ns), we had to raise the helium pressure to ≥1800 μm. The hook spectroscopy measurements were repeated at this pressure with a hot cathode. The experimental setup and operating conditions were otherwise identical to those described above, except that no dc simmer current was used.

Contours of the He 2^3P excited state density for the linear thyratron operating in helium at 1800 μm pressure with a hot cathode appear in Figure 4-5. The density of excited states is approximately equal to those measured with the cold cathode, having a maximum value of approximately 5×10^{12} cm^{-3}. Unlike operating with a cold cathode, there does not appear to be a "striker" between the cathode and control grid that would indicate a breakdown initially in that direction. Breakdown appears to be fairly uniform (t = 20 ns) with some higher density of excited states near the control grid slot. As time progresses (t = 60 ns), regions of higher density appear near the auxiliary grid slot, but in a direction close to the wall of the linear thyratron and not towards the control grid slot. At progressively later times, the density of excited states becomes more uniform and does not display the type of gradients observed with the cold cathode.

The excited state densities plotted in Figures 4-4 and 4-5 are disturbing with respect to the unexpected unformity of the excited states as a function of position within the LT. We would expect a great differentiation in the spatial dependence of the excited states as a consequence of the directed flow of current from the cathode through the control grid slot. This pattern of current flow was not observed. The evidence of anomalous electron emission suggested that additional information could be obtained by using a framing camera to examine plasma emission. That study was described in Section 3.4. The results of that study, combined with the results of the spectroscopic measurements described above, motivated us to change the configuration of the auxiliary grid. It was during this modification that larger windows were installed on the linear thyratron (see Figure 3-16).

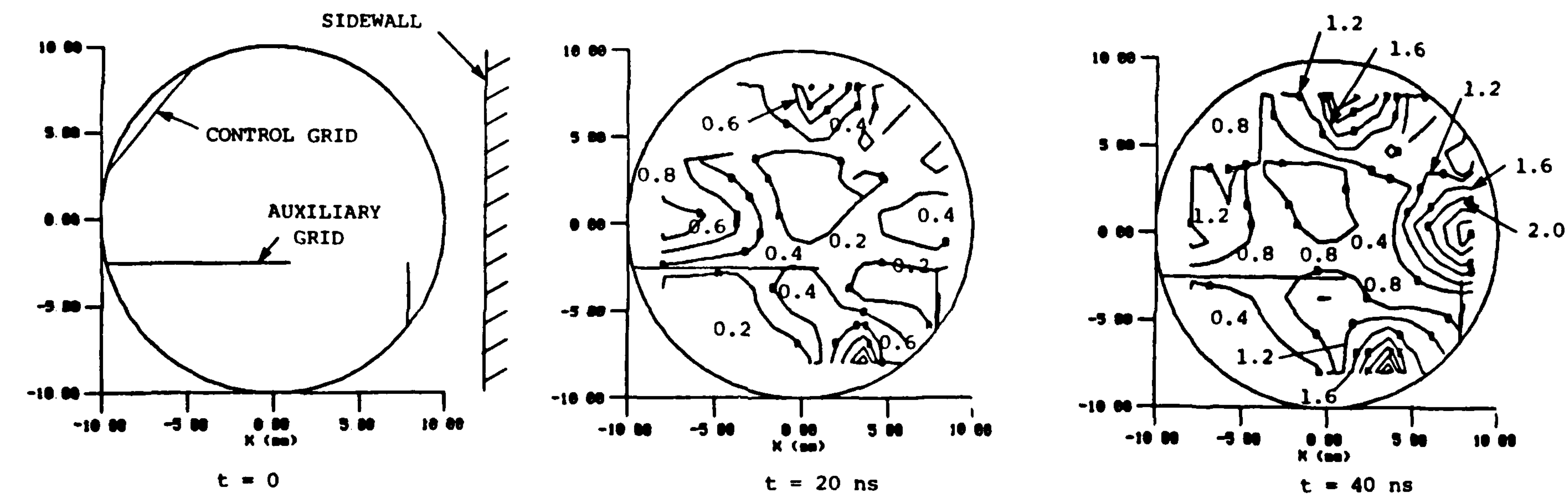

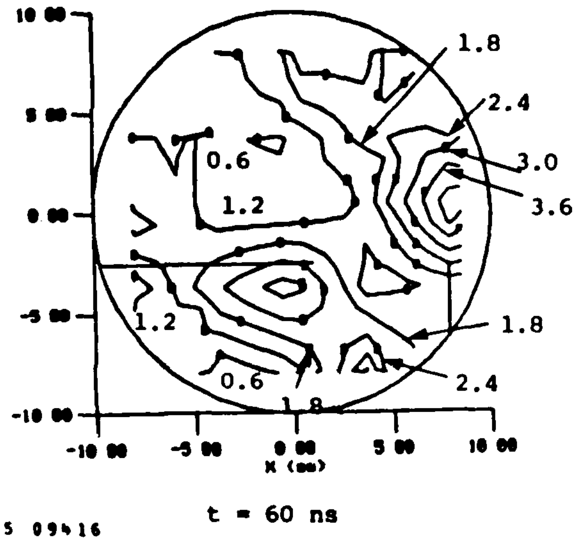

85 09416

Figure 4-5. Hook Method Spectroscopic Measurements for $He2^3P$ Density. Contour values are units of 10^{12} cm^{-3}. Current maximum is at 100 ns. (Hot Cathode)

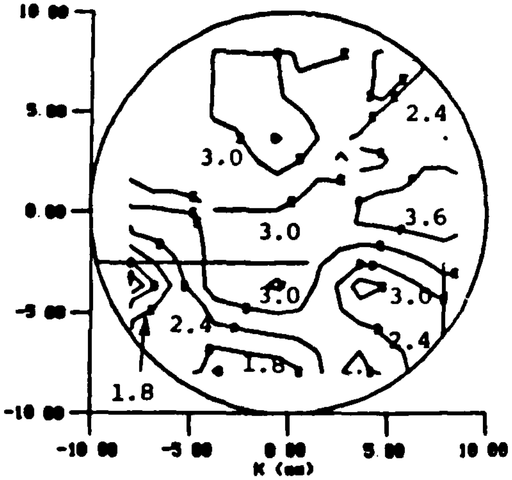

t = 80 ns

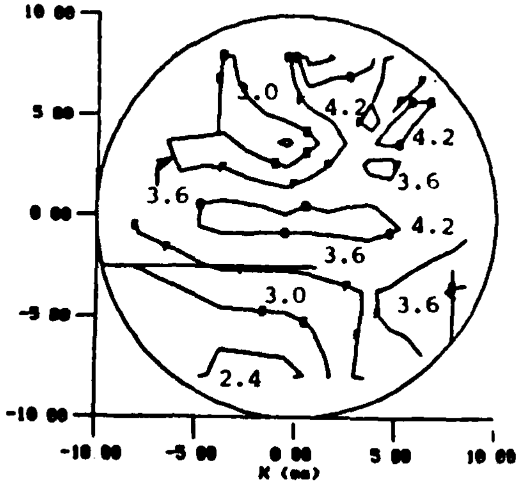

t = 100 ns
(CURRENT MAXIMUM)

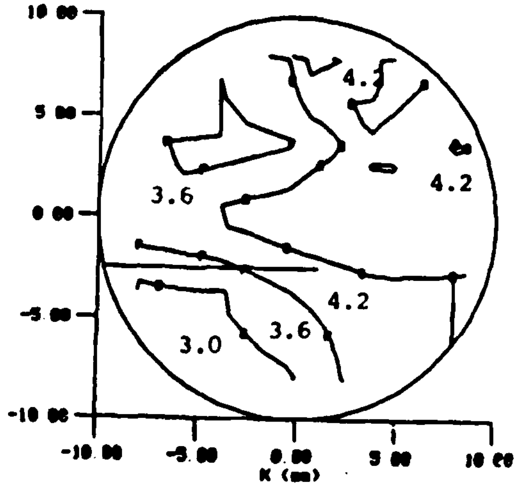

t = 120 ns

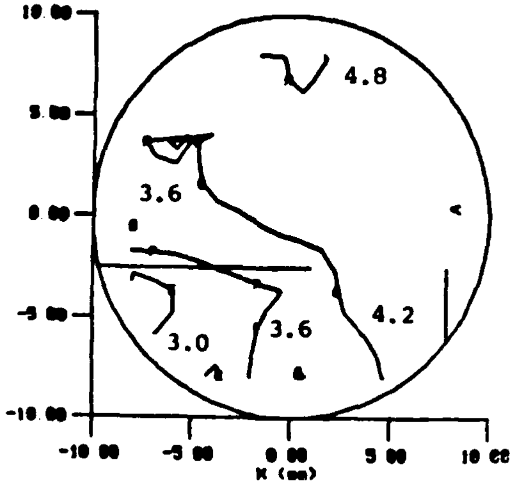

t = 140 ns

85 09417

Figure 4-5 (Cont.) - $He2^3P$ Density ($10^{12}/cm^3$)

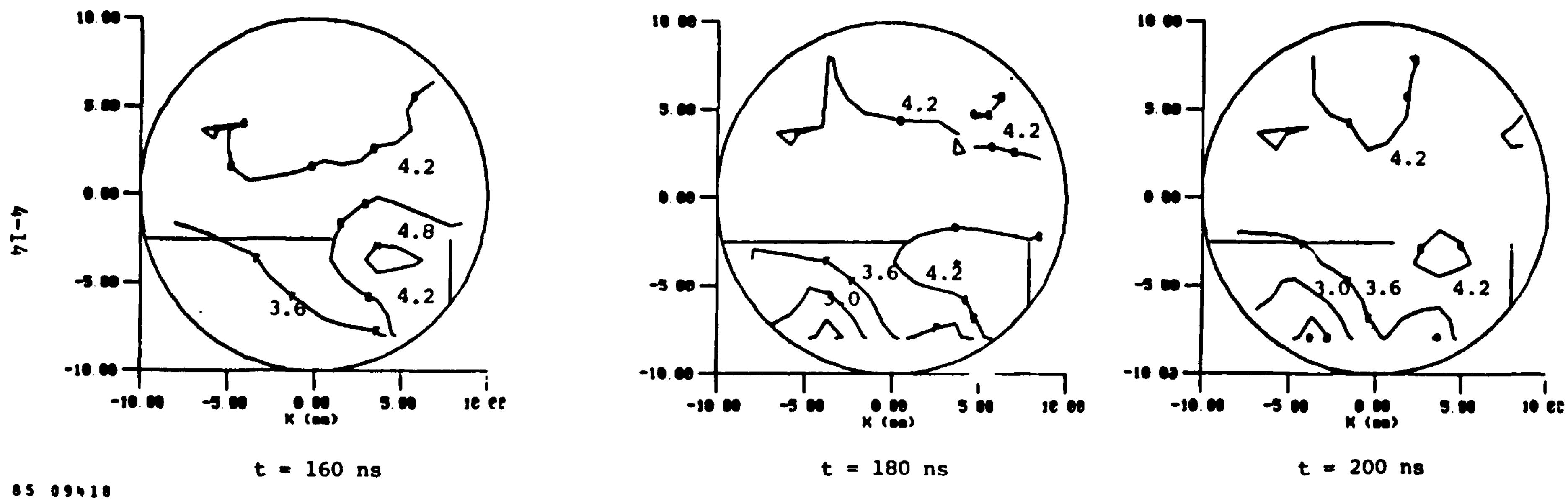

Figure 4-5 (Cont.) - $He2^3P$ Density ($10^{12}/cm^3$)

One conclusion of the study was that electron emission was occurring from the sidewalls of the thyratron. This possibility was investigated by using the linear thyratron simulation code LINTHY2D. In the model, the sidewalls are treated as a conductor at the cathode potential; however, no electron emission is usually allowed to occur there. The effect of electron emission from the sidewalls on the electron density and distribution of excited states was investigated with the model by allowing some fraction of the "cathode" emission to emanate from the sidewalls. For purposes of demonstration, this fraction was arbitrarily chosen to be 0.5. The location for this electron emission from the sidewalls was randomly chosen between the cathode and control grid planes. Electron density without and with electron emission from the sidewalls appears in Figure 4-6, and the He excited state density for the same conditions appears in Figure 4-7. The approximate field of view of the experimental measurements is indicated. The model results with electron emission from the sidewalls are in much better agreement with the experimental measurements than otherwise identical conditions without sidewall emission.

4.4 EXCITED STATE DENSITIES IN THE LINEAR THYRATRON WITH "OPTIMUM" GRIDS

With the new larger windows on the LT, virtually the ENTIRE plasma region could be observed. Measurements of the density of the He 2^3P excited states as a function of time and position were repeated with the low inductance geometry. These results are shown in Figure 4-8. The current and voltage characteristics for these conditions are shown in Figure 3-18 for the low inductance geometry. The maximum excited state density is approximately $6 \times 10^{12}\ cm^{-3}$ and occurs within the baffled region near the control grid slot. The local current density at this time is 900-1000 $A\text{-}cm^{-2}$. Excited state densities behind the auxiliary grid were barely at the detection limit ($<10^{11} cm^{-3}$ maximum value). This indicates that there is no significant amount of current flowing between the wall of the linear thyratron (a conductor at the cathode potential) and the auxiliary grid. Excited state densities are small immediately adjacent to both the lower portion of the control grid and

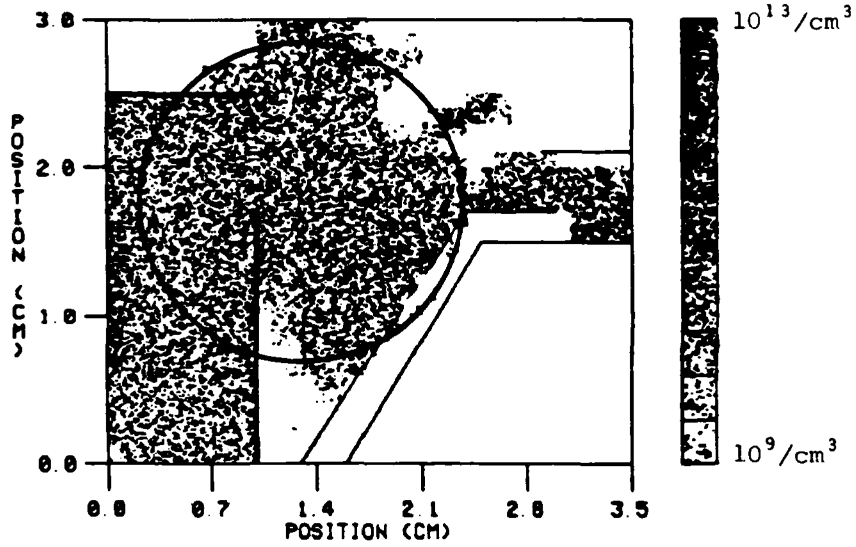

WITHOUT SIDEWALL EMISSION

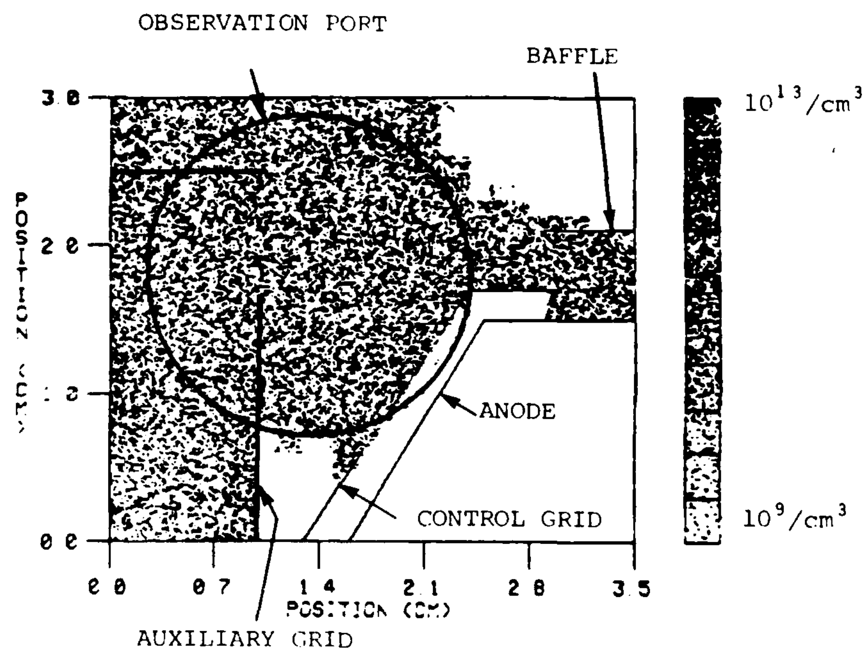

85 09419

WITH SIDEWALL EMISSION

Figure 4-6. LINTHY2D Results for Electron Density.

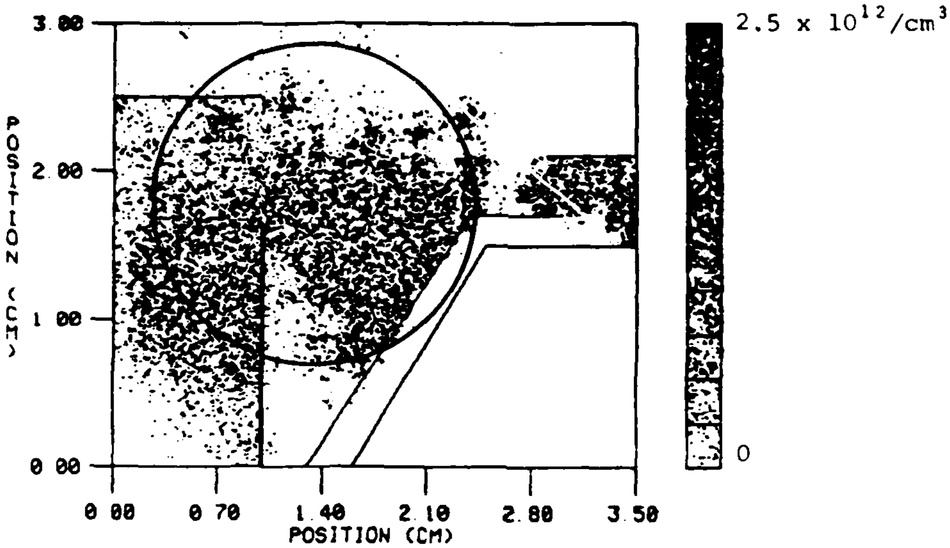

WITHOUT SIDEWALL EMISSION

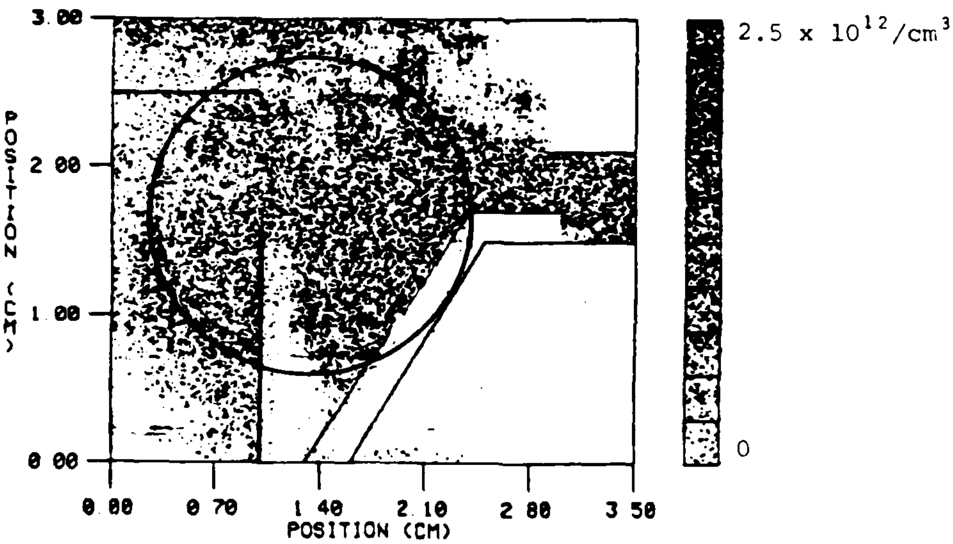

85 09420

WITH SIDEWALL EMISSION

Figure 4-7. LINTHY2D Results for He* Excited State Density

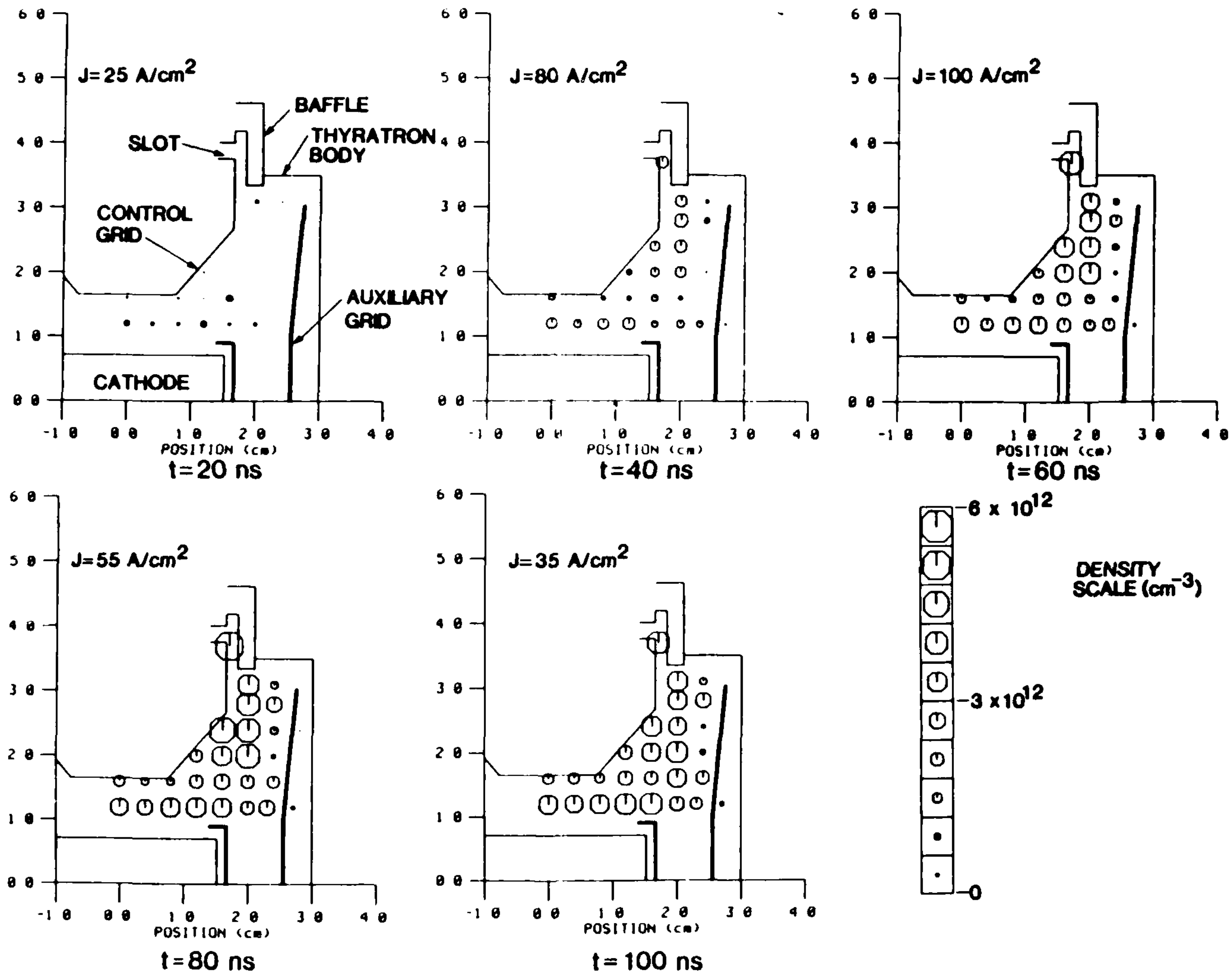

86 10990

Figure 4-8. He 2^3P Density for the Low Inductance Geometry. (8 kV, 900 μm)

near the auxiliary grid. A line of high density of excited states sits above the cathode a distance that approximately corresponds to the negative glow as observed with the framing camera. Since the cathode is operating cold, electron emission is not dominantly thermal and, therefore, one would expect a sheath and negative glow near the cathode. Other than the baffled region near the control grid, the highest density of excited states was observed near the vertex of the control grid, extending down from the baffled region. Results from our plasma simulation model indicate this is a region of locally high space charge.

The delineation between the highly excited region and the relatively lowly excited region is quite sharp, and the time dependence of the excited state densities in the two regions is different. In Figure 4-9, excited state densities are plotted as functions of time for two locations: adjacent to the control grid and ≈0.5 cm away from the control grid (in the direction of the auxiliary grid). The excited state density adjacent to the grid has a higher maximum value and has a time dependence similar to the total current. The offset between the extrema of the excited state density and current is due to the finite lifetime of the excited state. The excited state density further from the grid increases only during the first few tens of nanoseconds. We interpret these results as indicating that the current flows nearly uniformly through the region in front of the control grid slot early during the current pulse when the grid voltages are high. Later during the current pulse when the anode and grid voltages are lower, current flows dominantly near the control grid. Only qualitatively similar results for the time dependence of the excited state density were obtained with the lower current density, high inductance geometry. These results are shown in Figure 4-10. The peak current is 1200 A maximum at 100 ns. There appears to be a more rapid decline from the maximum for the more highly excited region as compared to the less excited region, although the difference is minimal. The effective lifetime of the excited states is longer for the case with lower peak current, implying that the dominant quenching mechanism is by electron collisions.

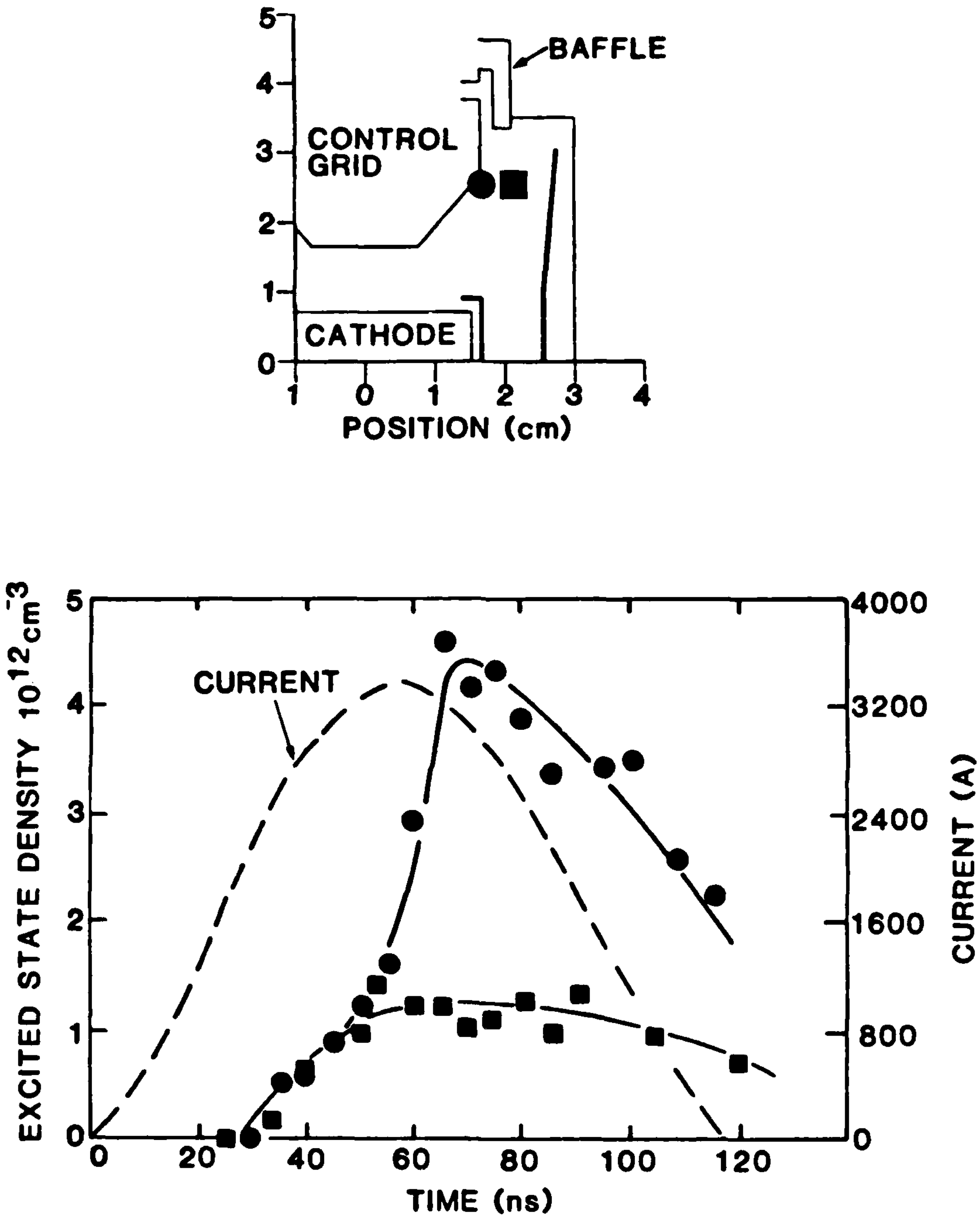

85 09523

Figure 4-9. He 2^3P Density at Locations Adjacent and 0.5 cm from the Control Grid.

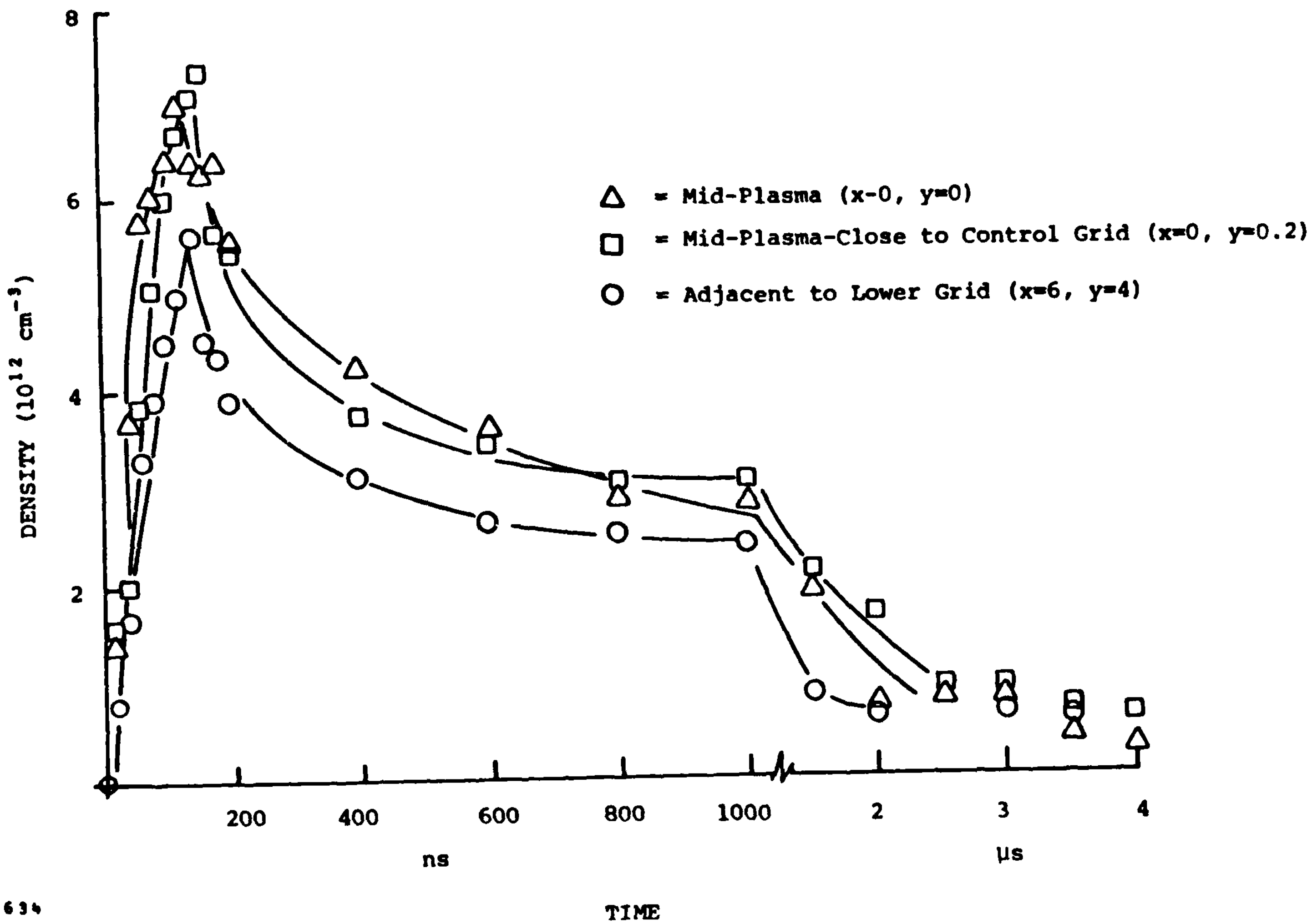

85 09634

Figure 4-10. Time Dependent He 2^3P Densities in the High Inductance Geometry

The radiative lifetime of the transition examined is 15 ns; however, it terminates on a metastable level, making it susceptible to radiation trapping. Locations immediately adjacent to a surface will be less likely to be radiation trapped than in the center of a large volume. This effect, however, does not explain the behavior observed in the high inductance geometry where both locations are far from a wall. The second possibility is that either the radiating level or the metastable level participating in the radiation trapping are being quenched in a non-radiative fashion more quickly in the high current density region as compared to the low current density region. Quenching by electrons can occur by either superelastic collisions or by excitation (or ionization) out of the state. To account for our observations, the rate of quenching must be on the order of $n_e r = 1/50\ \text{ns} = 2 \times 10^7\ \text{s}^{-1}$. For a typical electron quenching rate constant of $5 \times 10^{-8}\ \text{cm}^3\ \text{s}^{-1}$, the electron density would need to be $5 \times 10^{14}\ \text{cm}^{-3}$, which qualitatively agrees with theory.

If we assume that the rate of excitation of the state is proportional to the current, we can show that the effective lifetime of the state is equal to the offset in time between the maximum of the current and the maximum in the density of the excited state (see below). The effective lifetime τ is given by $1/\tau = 1/\tau_r + 1/\tau_c$, where the subscripts denote the radiative and collisional lifetimes. The 2^3P state in He is radiatively coupled only to the 2^3S state with a lifetime of 100 ns. The effective lifetime given by the expression above for the location near the grid is ≈20 ns. Therefore, quenching of the state must be dominantly non-radiative. Away from the grid, the lifetime of the state is ≈70 ns, close to the radiative lifetime. Assuming non-radiative quenching is dominated by electron collisions, the longer lifetime and lower maximum excited state density away from the grid implies a lower current density.

Hook spectroscopy measurements of excited state densities with the thyratron operating in hydrogen were performed. The density of the 2S excited state of atomic hydrogen was measured by operating the interferometer at

6562 A, the H_α transition. This state, denoted H^*, is most likely populated by one of three mechanisms:

$e + H_2 \rightarrow H + H^* + e$	Dissociative Excitation	[4.2]
$e + H \rightarrow H^* + e$	Direct Excitation	[4.3]
$H^{**} \rightarrow H^* + h\nu$	Radiative (or Collisional) Cascade	[4.4]

Due to the finite lifetime of the excited state, the instantaneous density of the state is a function of the time integral of the instantaneous rate of excitation. To first order, the instantaneous rate of excitation is proportional to the local current density. However, any analysis is complicated by the fact that the two dominant rates of excitation, dissociative excitation of H_2 and direct electron impact of H, are linearly proportional and quadratically proportional to the local current density, respectively.

Experimentally measured H 2S excited state densities measured with our hook interferometer are shown in Figure 4-11. Results are plotted as a function of time at three points in the thyratron. The locations of these three points are shown in the schematic at the top right corner. Also plotted in Figure 4-11 is the absolute value of the current through the thyratron. The excited state densities are in the mid-$10^{12} cm^{-3}$. The excited state density near the control grid slot has the larger value, an indication of the current density being higher there as the plasma begins to constrict toward the slot. As the plasma becomes more diffuse nearer the cathode, the excited state density decreases. Note that the excited state densities "rebound" as the current rings after 110 ns. Measurements were also made at a third point, shown by the triangle in the schematic, a few millimeters above the cathode. The excited state density at this point was generally below the detection limit of the interferometer for this transition ($0.1 \times 10^{12} cm^{-3}$). Only a single measurement above the detection limit could be made at this location.

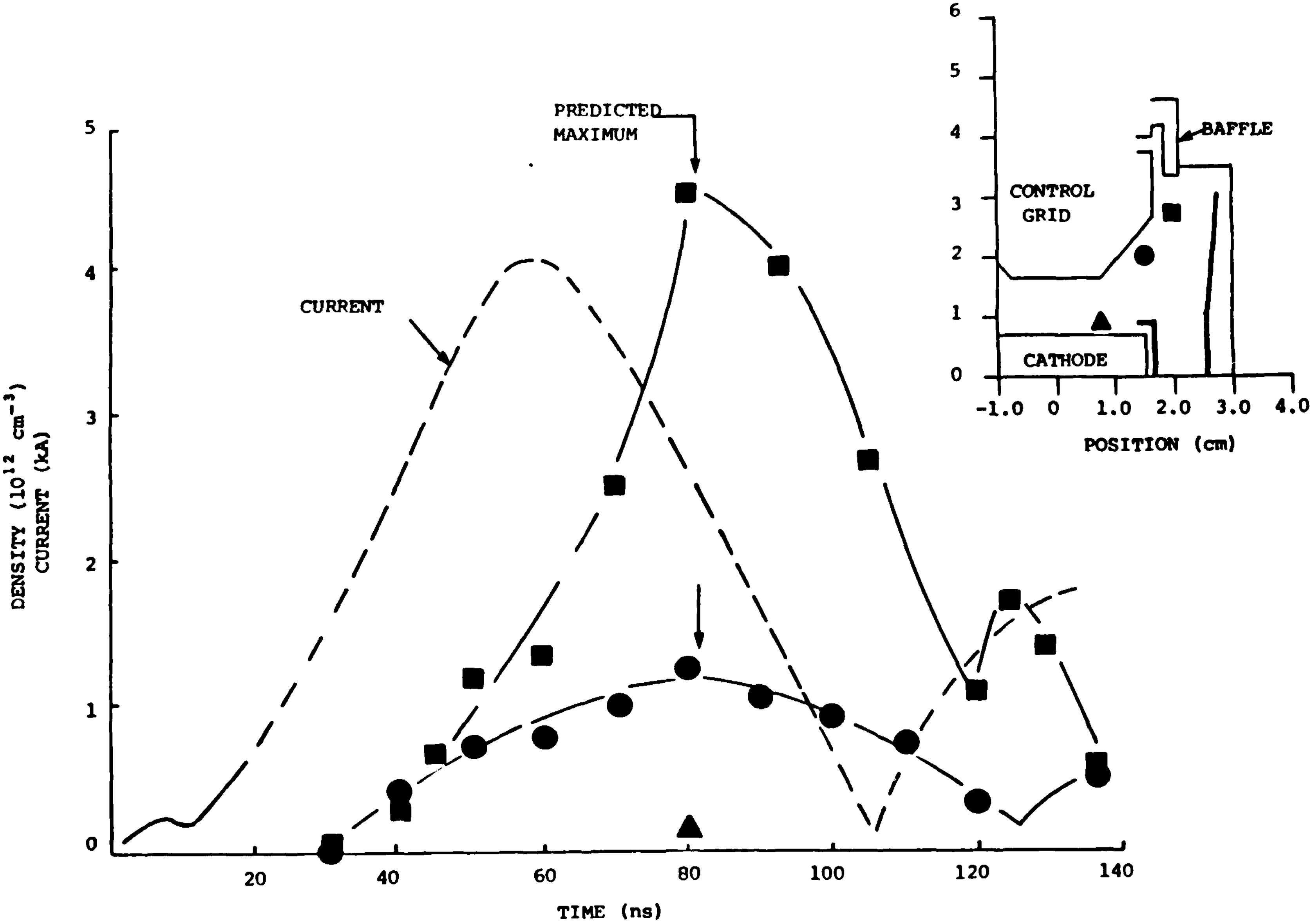

85 09863

Figure 4-11. H(2S) Excited State Density and Current Pulse in Linear Thyratron ($P = 275\ \mu m$, $V_{anode} = 8$ kV). Position of measurements are shown in the schematic at right.

The peak in the measured excited state densities lags behind the peak in the current by approximately 20 ns. A similar time lag was observed in excited state measurements in He. This lag can be understood and predicted with a simple model for the time dependence of the excited state density. Assume that the rate of excitation of the excited state is proportional to the total current and that the excited state has an average lifetime τ. For the first half-cycle of the current pulse, we can approximate that the current $I(t) \approx I_o \sin(\omega t - \Delta t)$, where Δt is an offset from zero, obvious from Figure 4-11. The time rate of change in the density of an excited state N is then

$$\frac{dN}{dt} = A \cdot I_o \sin(\omega t - \Delta t) - \frac{N}{\tau} \qquad [4.5]$$

where A is constant of proportionality between current and excitation rate. Solving Equation [4.5] for N(t) and setting $N(t < \Delta t) = 0$ we obtain

$$N(t) = \frac{AI_o}{\left(\omega^2 + \frac{1}{\tau^2}\right)} \qquad [4.6]$$

$$\left(\frac{1}{\tau} \sin(\omega t - \Delta t) - \omega \cdot \cos(\omega t - \Delta t) + \omega \cdot \exp\left(- \frac{t-\Delta t}{\tau}\right)\right)$$

For a half-sine period of 100 ns ($\omega = 3.14 \times 10^7 s^{-1}$) and $\tau = 22$ ns (radiative lifetime), the excited state density as given in Equation [4.6] has a maximum value at t = 82 ns. This time, shown in Figure 4-11 with arrows, is in good agreement with the experimentally measured time at maximum. This simple model shows that the lag in excited state density with respect to the current pulse is simply a result of the integrating effect of the finite lifetime of the state.

REFERENCES

1. W.C. Marlow, Appl. Opt. 6: 1715 (1967)

Section 5
CURRENT DENSITY MEASUREMENTS

5.1 INTRODUCTION

In its present configuration, the linear thyratron (LT) is an excellent test stand to measure the electron emission capability of dispenser cathodes. We define the maximum current available from a cathode of the type employed here as that current when the discharge makes the transition from a glow to an arc. The evidence of this transition is a sudden drop in the voltage across the control grid-cathode gap. Since the thyratron has numerous optical viewports, it is possible to visually monitor the onset of arcing and thereby unambiguously determine the current density at which arcing occurs by correlating the observation of arcing with the simultaneously measured V-I characteristic. In the past, arcing was determined only by monitoring the control grid voltage during commutation; if the grid voltage dropped suddenly, an arc was said to have occurred. This detection scheme was suspected since an independent (i,e., visual) verification that arcing had occurred could not be made. In these studies, it was not entirely clear that the suddenly observed voltage drop was due to a cathode arc. For example, the voltage drop could have been caused by an arc to a grid or to a heat shield. Having the ability to visually observe the arc enables us to measure when and where an arc forms and to correlate the observation with changes in the V-I characteristics.

5.2 CURRENT DENSITY MEASUREMENTS

To make the current density measurements, the configuration of the LT was not physically changed from that of previous studies. However, the energy storage pulse forming line was replaced with a two- or three-stage PFN with nominal characteristics of $C = 70\ \mu F$ and $\tau = 50\ \mu s$. The additional capacitance was added to the PFN in order to insure sufficient current to reach the arcing limit. A framing camera, observing through one of the large

end windows, was employed to visually record the onset of an arc and to confirm that the arc took place at the cathode surface. The framing camera rate was adjustable and the duration of a single exposure was typically 200-400 ns, depending upon the emission intensity. Once a reliable correlation between visually observed arcing and the simultaneous V-I characteristics was made, a set of framing camera photographs was not taken for every voltage trace recorded. In this manner, the rate of data acquisition was increased. Periodically, upon recording a "suspect" V-I trace, the framing camera was employed to confirm that an arc had taken place.

A framing camera photograph of the control grid-cathode space during a discharge pulse in the LT is shown in Figure 5-1. A hot spot is visible emanating from the center of the cathode. Simultaneously, the voltage across the control grid-cathode space showed a large drop, which we believe confirms that a cathode arc has taken place. A sequence of two framing camera photographs, their timing pulses, and the cathode-grid voltage are shown in Figure 5-2. The top trace of the oscillogram is the grid voltage and the bottom trace shows the timing marks of the camera. The bottom camera exposure corresponds to the leading timing mark and shows a diffuse discharge. In the second camera exposure, taken after the drop in grid voltage, an arc on the cathode can be clearly seen. Thus, we conclude that the grid voltage discontinuity indicates a cathode arc.

After establishing the onset of cathode arcing, we measured the emission capability of our dispenser cathode for different temperatures, gases, and rates of current rise. The current pulse for the higher rate of current rise trials (1×10^{9} and 2×10^{9} A-s^{-1}) was sinusoidal; the current waveform for the lowest rate of current rise (5×10^{8} A-s^{-1}) was made more rectangular by employing a two-section, pulse-forming network. The shapes of the two current waveforms used are shown in Figure 5-3.

Using the method described above, the currents and current densities at which we observed arcing at the cathode as a function of cathode temperature

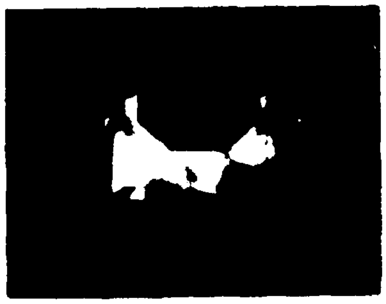

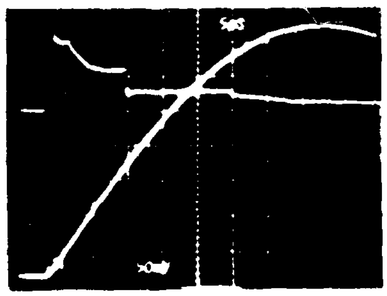

85 09921

Figure 5-1. (a) Framing Camera Photograph of Cathode Arc.
(b) Control Grid Voltage Showing discontinuity of Onset of Arc.

AD-A194 111 LINEAR THYRATRON(U) SPECTRA TECHNOLOGY INC BELLEVUE WA 2/3
M J KUSHNER ET AL. 31 JUL 87 AFWAL-TR-87-2080
F33615-84-C-2474

UNCLASSIFIED F/G 9/1 NL

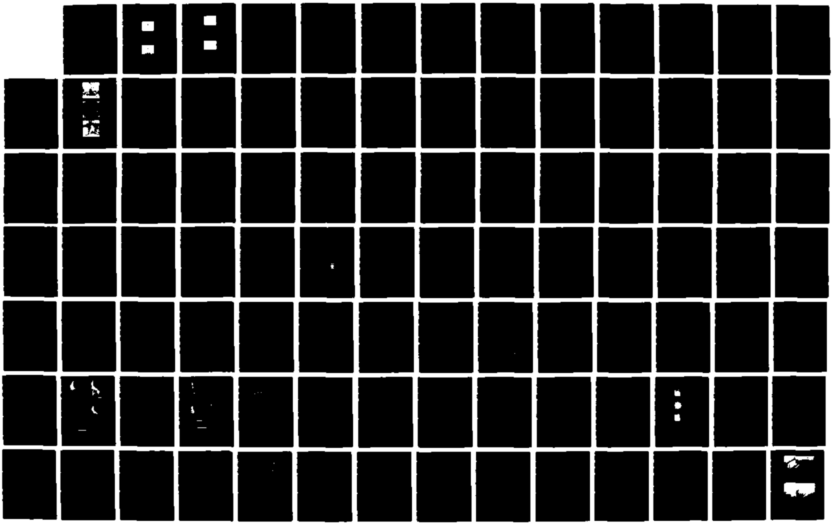

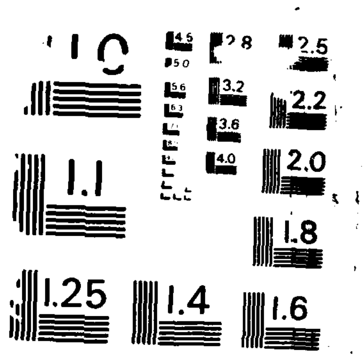

COPY RESOLUTION TEST CHART
NATIONAL BUREAU OF STANDARDS - 1963 -

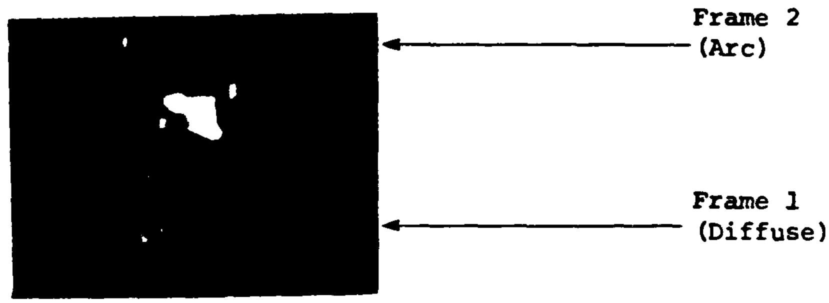

Framing Camera Photographs

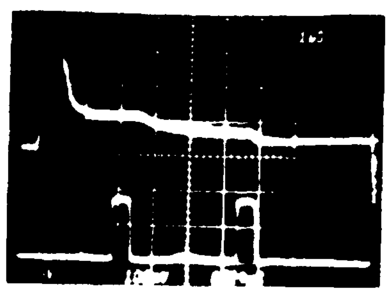

85 09922

Top: Control Grid Voltage (50 V/div)

Bottom: Timing Pulses for Framing Camera Photographs.

Figure 5-2. Framing Camera Photographs Confirm Cathode Arc.

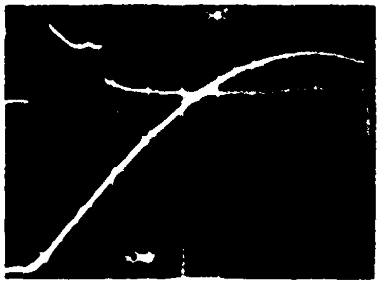

Waveform for 1×10^9, 2×10^9 A/S

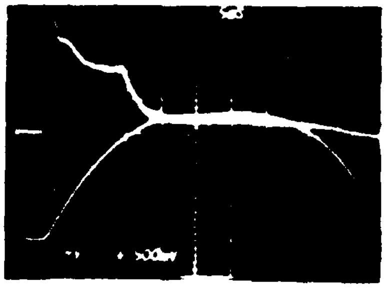

Waveform for $\frac{dI}{dt} = 5 \times 10^8$ A/S

Top: V_{GRID} (50V/DIV)

85 09923 Bottom: CURRENT

Figure 5-3. Current Waveforms for Current Density Measurements.

in hydrogen are plotted in Figure 5-4. These measurements were made at constant pressure. Therefore, the gas density decreases approximately as $1/T_{cathode}$. The current density of the cathode is based on an effective area of 60 cm^2 for our cathode, including the area of the slots. The current density based on the transverse dimensions of the cathode would be twice as large. The arcing current was found to be a function of the rate of rise of the current pulse. In general, the dispenser cathode can support higher peak currents before arcing with higher rates of current rise. A weak temperature dependence was measured, at most a factor of two between 300 K and 1300 K. The lower rates of current rise had a large temperature dependence. The time-to-arcing for the cathode as a function of temperature and rate of current rise is shown in Figure 5-5. For the indicated rates of current rise, the cathode diffusely supports current for 15 μs at most.

The weak temperature dependence of the arcing current implies that thermal electron emission is responsible for only a small fraction of the observed current; that is, a non-thermal mechanism is responsible for a major fraction of the electron emission. The most likely candidate is field emission. However, because the time scale of interest (many microseconds) is long enough for ions to transit the sheath, we cannot currently rule out secondary emission mechanisms. Assume that the non-thermal and thermal emission contributions to the current are additive and that the non-thermal contribution to the current is independent of temperature. Doing so, one can compute an effective "work function" ϵ_w for the cathode by solving

$$I(T) = I_{NT} + I_T \bullet e^{-\frac{\epsilon_w}{kT}}$$

where I_{NT} is the non-thermal contribution to the current and I_T is the thermal contribution. Since there is a different slope for I(T) for each rate of current rise, there is a different "work function" for each rate of current rise. Using the data for $dI/dt = 10^9$ $A\text{-}s^{-1}$, we obtain $I_{NT} = 75$ A/cm^2, $I_T = 167$ A/cm^2 and $\epsilon_w = 0.18$ eV. The fact that the arcing current is sensitive to the rate of current rise implies that there may be some

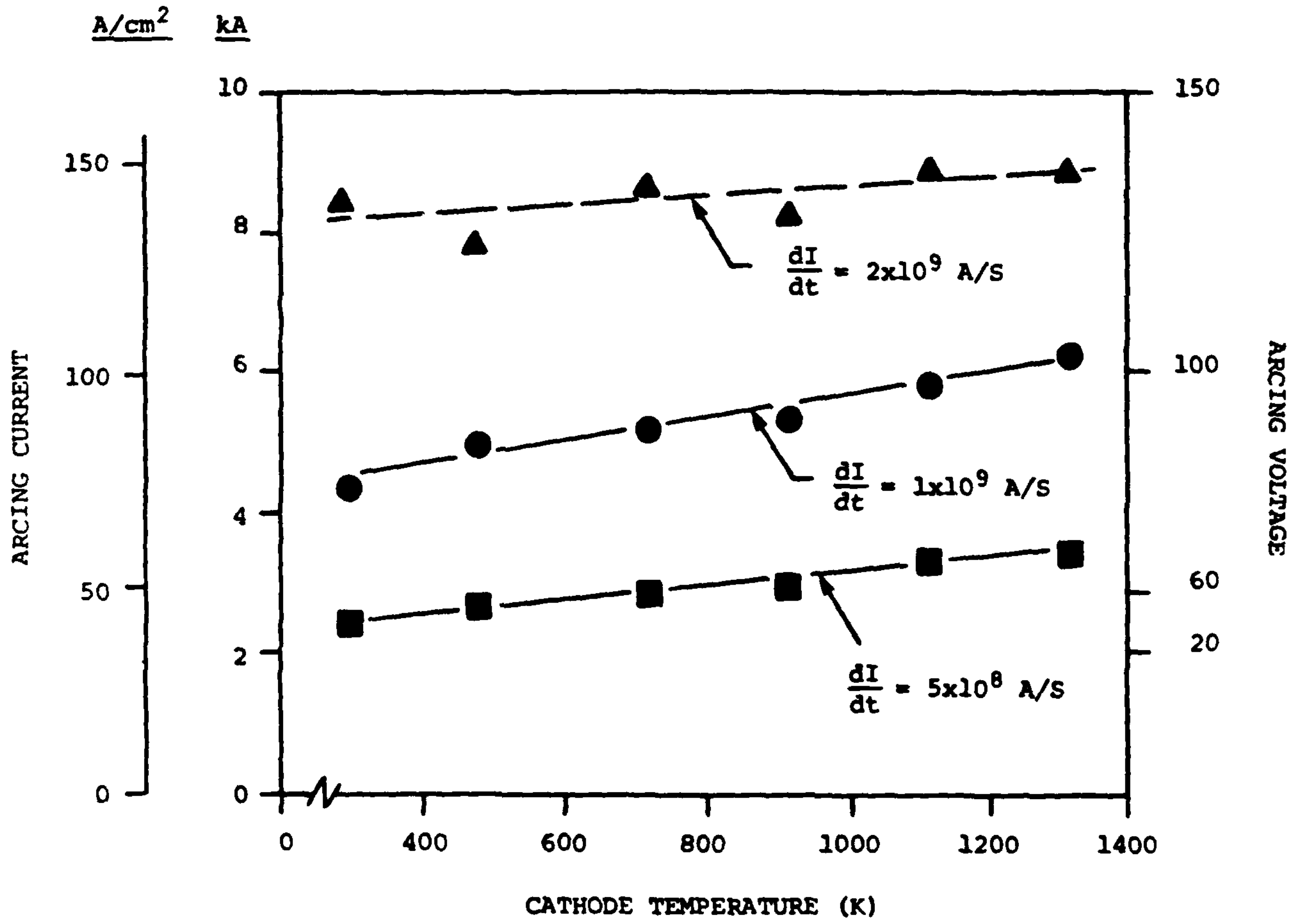

85 09924

Figure 5-4. Cathode Arcing Current vs. Temperature in Hydrogen (300 μm) for Different Levels of dI/dt.

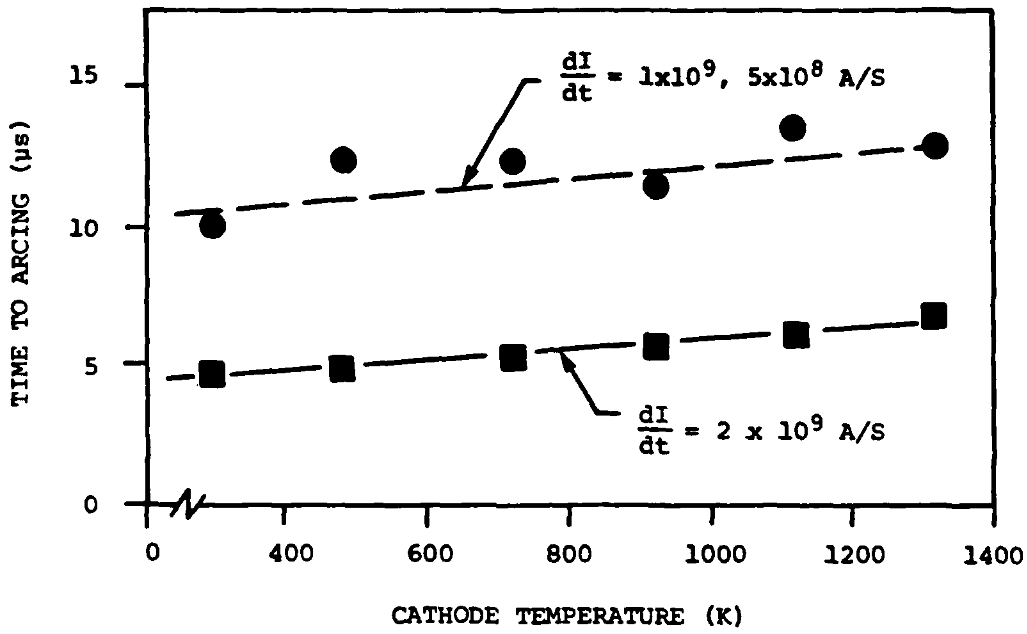

85 09925

Figure 5-5. Time to Cathode Arcing (H_2, 300 μm).

time-dependent heating mechanism of the cathode that also must be considered.

To determine whether the arcing limit of the dispenser cathode is sensitive to gas density in hydrogen, the measurements shown in Figure 5-4 (constant pressure) were repeated at constant gas density. For these trials, it was assumed that the gas temperature was approximately equal to the cathode temperature. The gas pressure of the LT was adjusted to keep gas density constant according to the ideal gas law. The arcing current as a function of cathode temperature at constant gas density is shown in Figure 5-6 for $dI/dt \approx 5 \times 10^{8}$ $A\text{-}s^{-1}$. The results are nearly identical to the data in Figure 5-4 for constant pressure. For constant voltage and current, the electron temperature is most likely inversely proportional to gas density. The fact that we obtained a null result for the change of arcing current as the gas density changes (constant pressure vs. constant density) appears to rule out an electron temperature dependence on arcing current.

The cathode arcing limits in helium and neon also were measured for $dI/dt \approx 5 \times 10^{8}$ $A\text{-}s^{-1}$ and are presented in Figures 5-7 and 5-8. The slopes of these curves are steeper than the hydrogen data, implying that when operating in helium and neon, there is a larger effect of cathode temperature on the arcing current. To the extent that heavier atoms heat (damage, sputter, or otherwise react) with the cathode to a greater degree than do light atoms (provided the ion transit time through the sheath is short compared to the time of interest), then these results are consistent with the transient heating mechanism suggested above. Further analysis must clearly be performed to delineate what emission mechanism is consistent with our data. Clearly, the surface morphology of the cathode will be an important consideration.

In their work on oxide cathodes, the Russian researchers have noted that the level of sparking current is dependent on the potential drop in the cathode region (Reference 1). They argued that arcing current varies directly with cathode potential, so lower voltage drops across the grid-cathode region result in lower arcing current limits. They also noted that arcing was more frequent at the end of the current pulse when dI/dt was a minimum or negative,

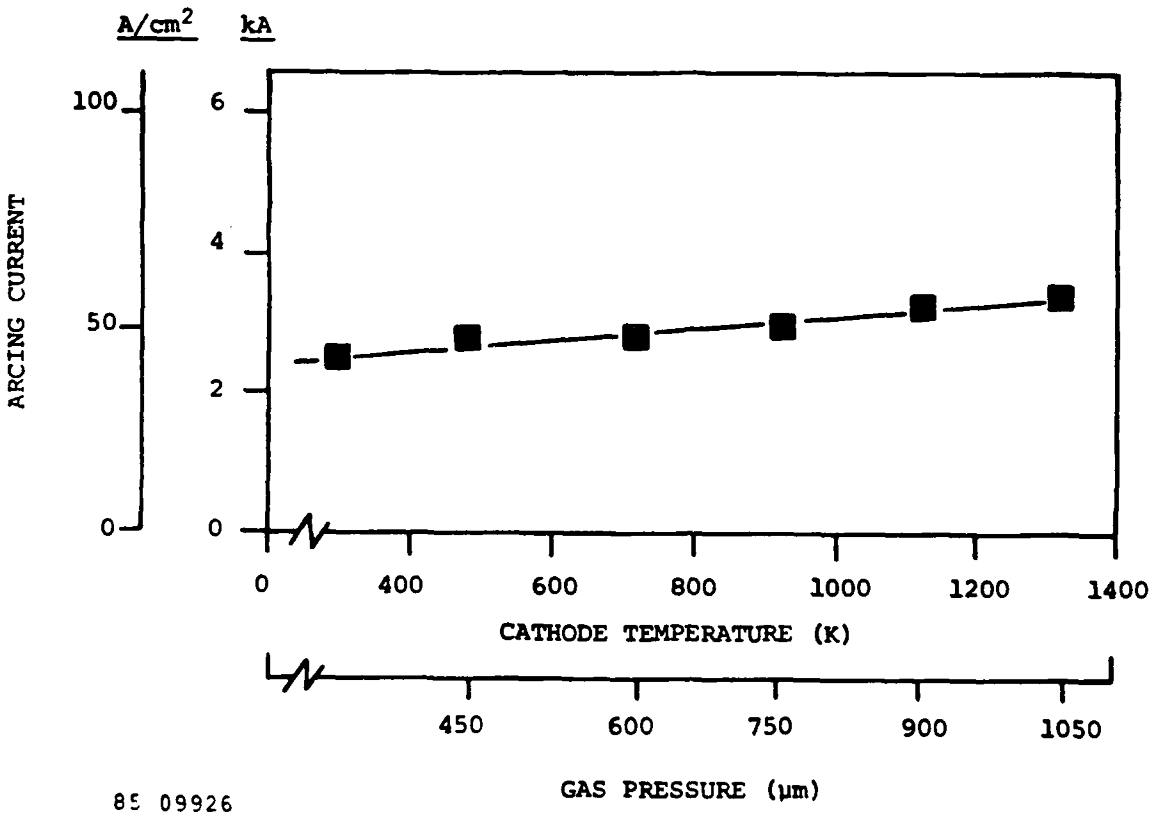

Figure 5-6. Cathode Arcing Current for Constant H_2 Gas Density.

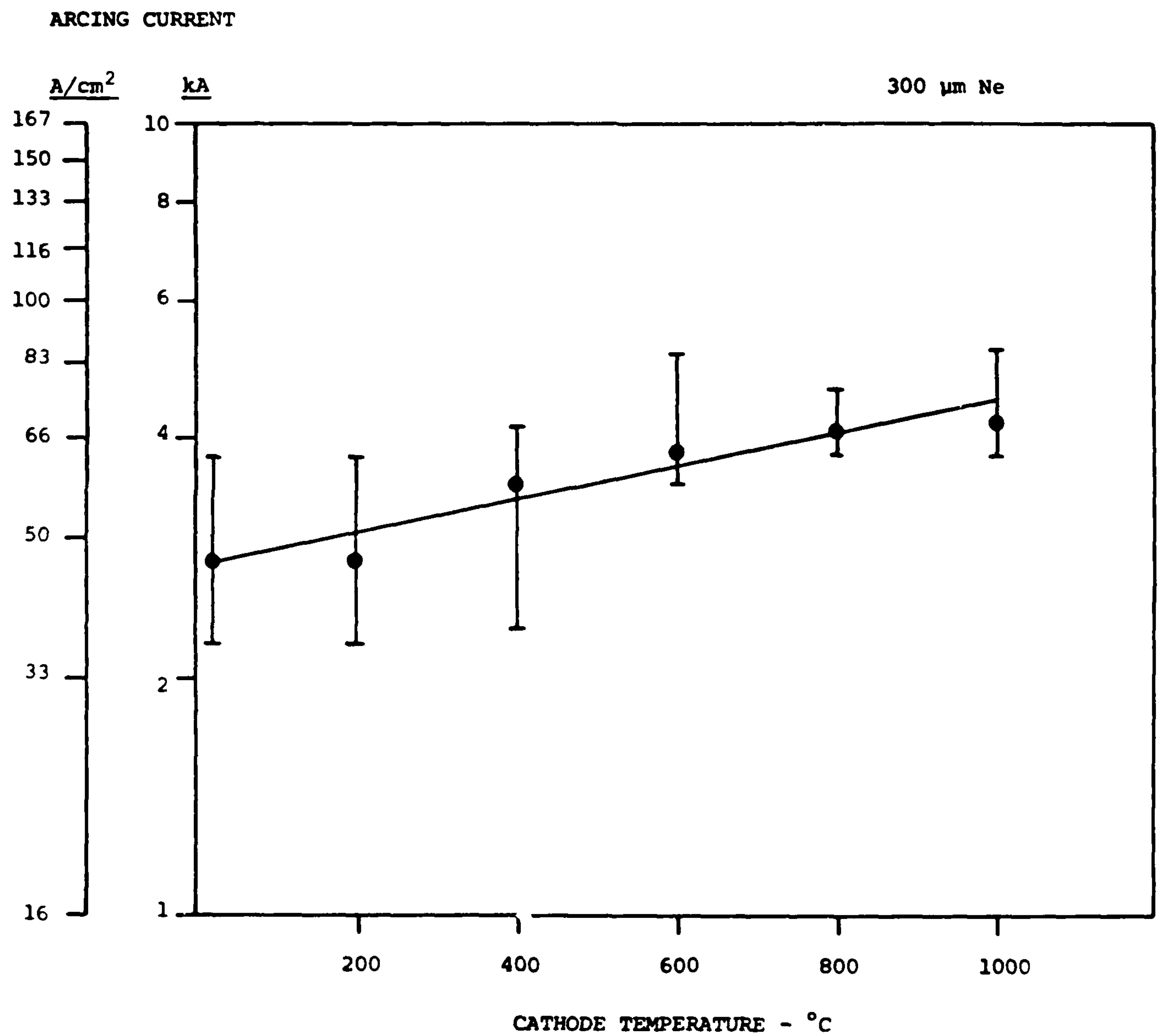

85 09927

Figure 5-7. Arcing Current vs. Cathode Temperature for 300 µm Neon.

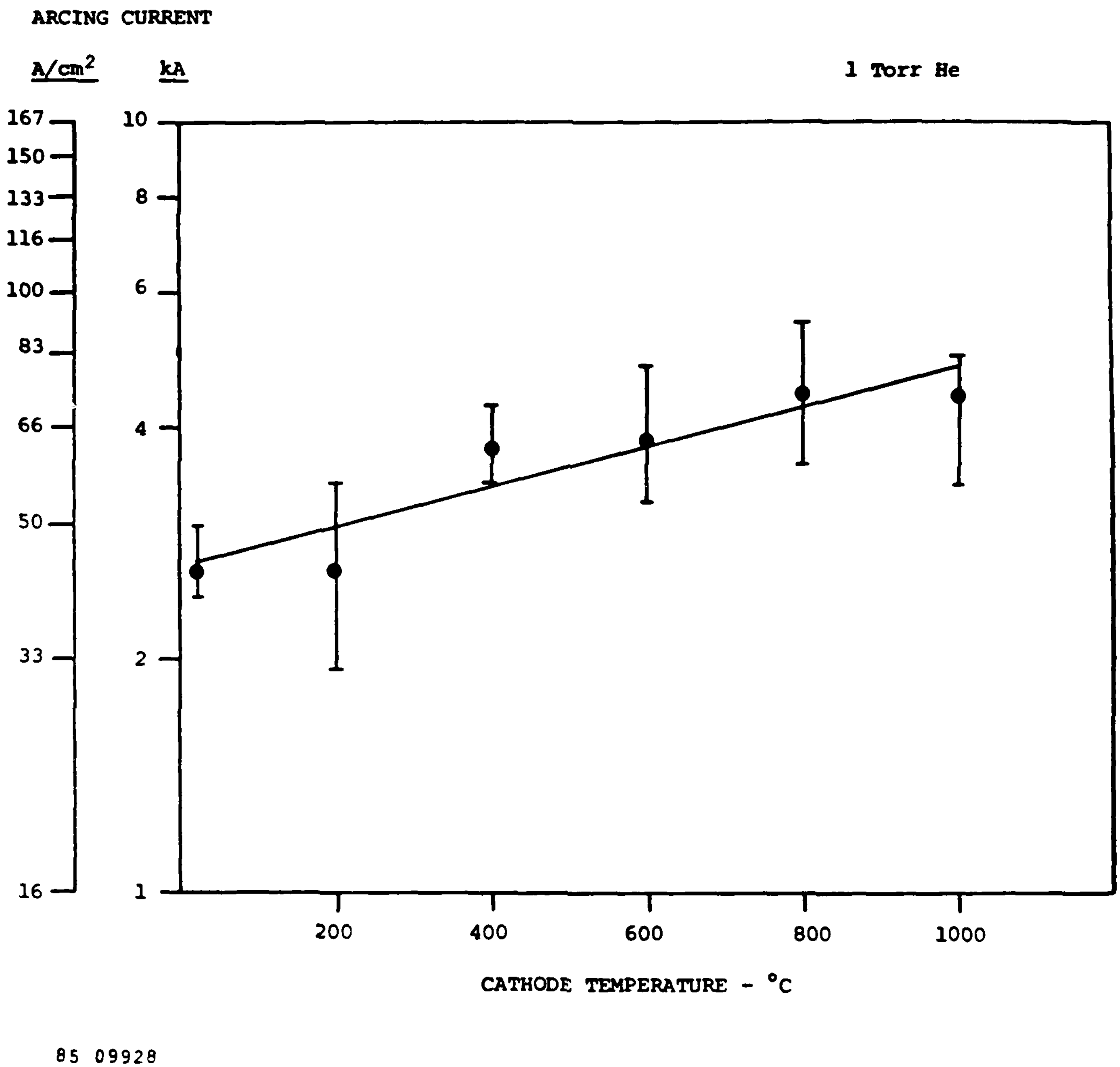

Figure 5-8. Arcing Current vs. Cathode Temperature for 1 Torr Helium.

and grid-cathode potential also was a minimum. A similar trend is observed here for dispenser cathodes. The grid-cathode voltage when arcing occurs for different cathode temperatures is noted in Figure 5-4.

Goldberg et al. reported similar results, as cited in the Russian works for cathode arcing (Reference 2). Cathode arcs were not observed during the rising portion of the current pulse, which implied that field emission or ion bombardment mechanism contributed heavily to the current. Goldberg summarized the work of other investigators by reporting that the rate of current rise is relatively unimportant to the cathode. This conclusion conflicts with our data. Although we have no viable model for low temperature cathode emission at the present time, it appears that dI/dt, cathode potential, and cathode temperature are all related to low-temperature electron emission.

5.3 EMISSION MECHANISMS

From the results discussed above, we found that there is at best a weak dependence on initial cathode temperature for the maximum glow current density sustained by our dispenser cathode. There was, however, a dependence on the rate of current rise. We suggested that the emission mechanism may be initially by field emission and subsequently by thermal emission as dendritic-like structures on the surface were heated by ion bombardment. This suggestion was based on the hypothesized existence of similar dendritic structures on the surface of our cathode, as had been observed on other aged dispenser cathodes (Reference 3).

An estimate can be made for the required size of the dendrites on the surface in order for the transient field emission to thermal emission mechanism to be valid. For field emission of electrons, an electric field emission of ≈1 MV/cm is required, which for our voltages requires a feature size of $\leq$ 10 μm. Assume that the surface of the cathode is covered by cylindrical dendrites of radius r_d, height h_d, and surface density ρ_s. Also assume that the average current density is j, the voltage drop at the cathode is V_c, the heat capacity of the surface material is κ, and current is carried

only by the dendrites. The rate of temperature rise of a dendrite is then

$$\kappa\frac{dT}{dt} = \frac{jV_c}{\rho_s \pi r_d^2 h_d} - \frac{2\sigma\left(T^4 - T_s^4\right)}{r_d} - \frac{\left(T - T_s\right)\alpha}{\frac{\left(2h_d^2\right)^2}{\pi}}$$

where α is the thermal conductivity of the dendrite, σ is the Stefan-Boltzmann constant, and T_s is the ambient surface temperature. The thermal constants for tungsten are $\kappa \approx 2.6$ J-cm^{-3}-K^{-1} and $\alpha \approx 1.64$ cm^2-s^{-1}. For purposes of discussion, choose $j_{max} = 100$ A/cm^2, $V_c = 50$ V, and $h_d/r_d = 6$. The dendrite temperature at the end of a 5-μs current pulse ($j(t) = j_{max}(t/2\mu s)$) as a function of r_d and fractional surface coverage is shown in Figure 5-9. The results are scaled by the parameter $(\kappa/\kappa_c)f$ where κ_c is the heat capacity of crystalline tungsten and f is the fractional surface coverage of the dendrites. The heat capacity of polycrystalline materials is generally lower than crystalline materials. The structure of the dendrite-like material found on aged dispenser cathodes may not be single crystals and, therefore, would have a reduced heat capacity (and thermal conductivity) from their single crystal counterparts. The size of dendrites as measured from the work of Petr and Gundersen[3] is indicated. A final temperature of ≈800 K would be required for significant thermal emission. For these conditions, $(\kappa/\kappa_c) \leq 1\%$ is required for transient heating to be important during a single current pulse. If $\kappa \approx \kappa_c$, then the surface coverage is ≤1% and the subsequent current density violates the Child-Langmuir criteria. Therefore, if transient heating is important, κ must be less than κ_c. These results are for a single shot and for a cold cathode. Obviously, high repetition rate operation and a heated cathode will result in higher dendrite temperatures.

The next logical step would be to make scanning electron microscope (SEM) photographs of our cathode to determine dendrite size and coverage. This procedure would require demounting the cathode or chipping off a piece of it, and both options were deemed too risky (with respect to damaging the cathode) at this time. Therefore, SEM photographs were not obtained for our cathode. However, we did obtain a piece of similar cathode

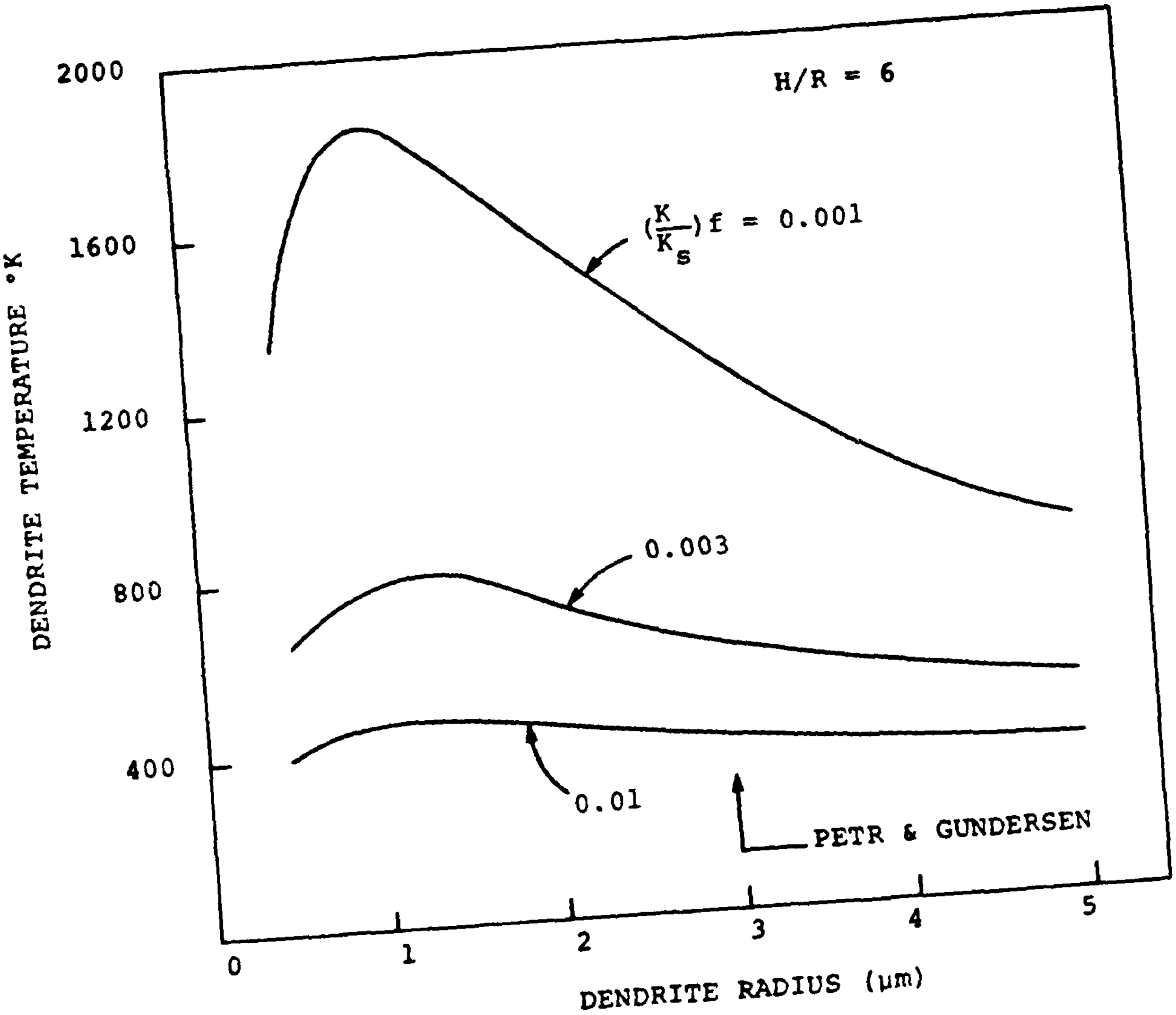

86 10339

Figure 5-9. Calculated Dendrite Temperature at End of 2 μs Current Pulse (100 A/cm^2)

material from the cathode vendor (Spectramat) and took SEM photographs of the surface. This cathode material was <u>not</u> activated nor aged. The surface morphology is the "before" conditions of our cathode and would not be expected to have large dendrite formations. The SEM photographs are shown in Figure 5-10. As expected, there are no dendrites on the surface, as observed by Petr and Gundersen, but there are some surface features. Figure 5-10a shows a typical surface feature with size of 1-2 μm. The surface coverage of these features, as shown in Figure 5-10b, is quite low ($\approx$5%). The surface features consist of both "spikes" and "holes." An enlargement of a "hole" between grains is shown in Figure 5-10c. The diameter of this "hole" is $\approx 2\ \mu m$. SEM examination of our cathode must wait for the end of this program when an autopsy of the tube will be performed.

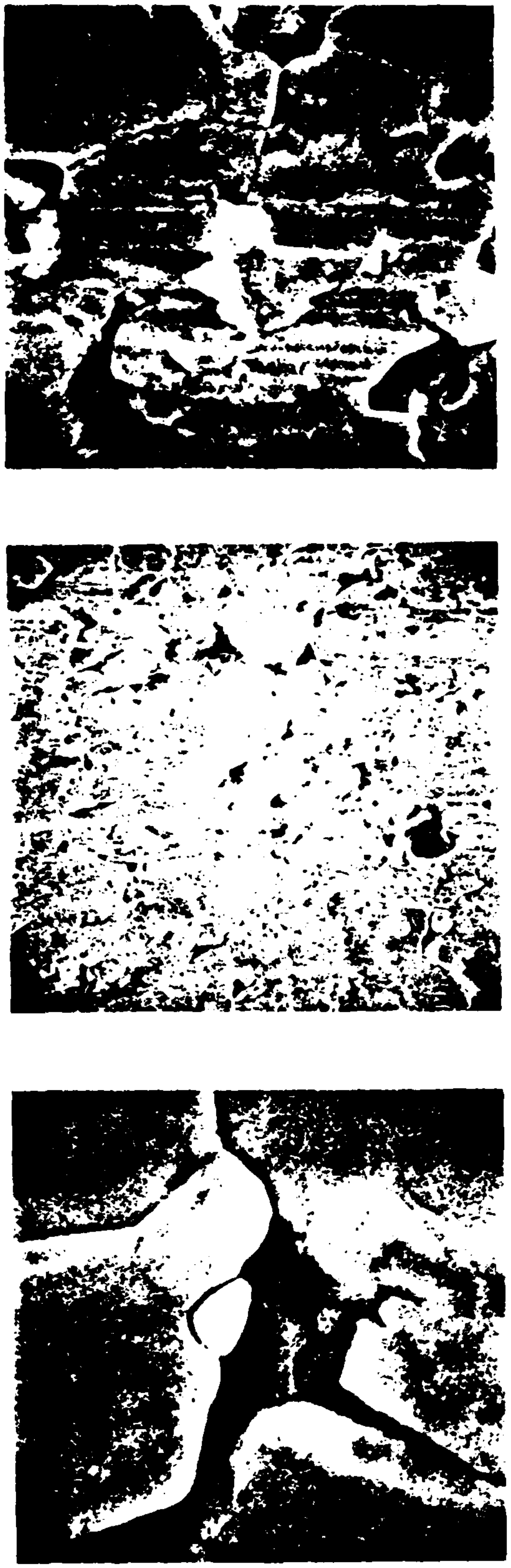

a) 4050x

b) 810x

c) 8400x

Figure 5-10. SEM Photographs of Dispenser Cathode Material

REFERENCES

1. Fogelson, Breusova, and Vagin, **Pulse Hydrogen Thyratrons**, pp. 81-89, translated by SCITRAN, 1482 E. Valley Road, Suite 15, Santa Barbara, California 93108.

2. S. Goldberg et al., **Hydrogen Thyratrons**, Final Report, Signal Corps Contract DA36-039 SC-15372, p. 164, March 1951.

3. R. Petr and M. Gundersen, "Field Emission Cathode for High Power Beams," Laser and Particle Beams 1: 207 (1983)

Section 6

DESIGN OF THE 100 kV MODIFIED LINEAR THYRATRON
CONCEPTUAL DESIGN OF THE SCALED-UP 100 kV THYRATRON

6.1 INTRODUCTION

The motivation for developing the linear thyratron (LT) is, in part, to be able to scale thyratrons to higher currents by simple length scaling. The prototype linear thyratron has provided encouraging results with respect to this scaling. By operating the auxiliary grid with approximately 2 mA/cm^2 of dc current, the cathode-control grid gap will fill with high density plasma along its entire length when pulsed simultaneously (to within 5 ns). Simultaneous and uniform cathode coverage has been obtained in both hydrogen and helium at pressures between 0.3 and 2.0 Torr. The assurance of cathode current uniformity is important since non-uniform coverage may result in local values of current density that exceed the glow-arc transition. These findings indicate that it may be possible to build a significantly longer device with the ability to switch hundreds of kiloamperes.

Future switch requirements specify operating voltages of approximately 100 kV per gap. Commercial thyratrons are available which operate at these voltages; however, they employ gradient grids that divide the total potential across several gaps. Each gap supports $\leq$40 kV, a generally accepted upper holdoff limit for commercial tubes. The use of gradient grids has certain disadvantages: multiple grids increase the length of the thyratron envelope housing, thereby increasing the inductance of the tube; multiple gaps dissipate more energy during commutation than do single gaps; and tube fabrication is greatly complicated when using more than a single gap.

The relatively low value of holdoff per gap (<40 kV) found in commercial tubes does not necessarily result from violations of Paschen's law but results primarily from other material and structural causes. Commercial manufacturers

often use stamped metal parts in the high voltage region, which may or may not have been deburred. This results in sites where local electric field enhancement is excessively high and electron field emission is a problem. Recognising that commercial manufacturers do not tailor electrode edges to avoid excessive electric field enhancement, Mancebo hypothesised that higher holdoff voltages could be obtained by careful contouring of parts in the high-voltage section (Reference 1). Subsequently, Mancebo built several triode thyratrons, taking care to round electrode edges to keep electric field enhancement to less than 10^6 V/cm, and successfully operated his prototype devices at ≈100 kV.

The work of Mancebo demonstrated that single-gap thyratrons can operate reliably at high voltages if design and thyratron manufacturing techniques are adhered to. This philosophy has been applied to a conceputal design for a linear thyratron that will switch voltages of approximately 100 kV and currents of approximately 50-100 kA. Future pulse power requirements are unclear at this time, but it is known that those requirements will exceed the specifications of currently available thyratrons. To establish a set of criteria for this design study, we have selected the following parameters as design goals:

1.	Anode Voltage	100 kV
2.	Anode Current	100 kA
3.	Pulse Width (τ_p)	$0.3\mu s < \tau < 3\mu s$
4.	Burst-mode Repetition Rate	100 Hz-10 kHz
5.	Anode Delay Time Drift ($\Delta\tau_{ad}$)	50 ns
6.	Jitter	5 ns

A conceptual design for a modification of the prototype LT and for a scaled-up LT that will meet these requirements is summarized in the following sections.

6.2 CATHODE SIZING

The conceptual design for the scaled-up linear thyratron calls for use of an unheated dispenser cathode similar to that in our 10-cm-long prototype device, which has been used unheated in several other experimental tubes (References 2,3). Our measurements have shown that unheated cathodes of this type can conservatively support, without arcing, 150 A/cm^2 during microsecond discharge pulse duration. However, lifetime data are lacking. The longest lifetime test for a dispenser cathode has been conducted with a modified EG&G HY-7 thyratron. During this life test, the thyratron has switched up to 40 kV and 40 kA, with a 10-μs pulse length at 100 Hz. The thyratron has been in the field for over 4 years and there is no sign of cathode failure or degradation (Reference 4).

To supply 100 kA of current, the cathode area of the scaled-up linear thyratron must have an effective area of approximately 650 cm^2. The word "effective" is used to distinguish the surface area of a slotted cathode from the product of its transverse dimensions. For a 1-m-long device using a slotted cathode, this implies an active cathode width of ≈6.5 cm/α, where α is the fractional increase in surface area due to the slots. This dimension is consistent with the approximately 8-cm-diameter anode/insulator specified below by thermal considerations. Vendors are able to supply dispenser cathode assemblies of these widths with lengths up to 20 cm. Approximately five such assemblies would be required for the 100-cm device supporting 1 ka/cm.

6.3 HIGH-VOLTAGE INSULATOR

One practical difficulty in fabricating a meter-long thyratron is the high- voltage insulator. Conventional thyratrons use cylindrical insulators whose axis is perpendicular to the cathode emitting surface. The insulator for the present linear thyratron uses a similar geometry where the insulator is a "stretched cylinder" or hollow rectangle (see Figure 6-1). STI has developed techniques to fabricate large ceramic vessels for the walls of the LSX fusion reactor facility at STI by fritting together large pieces of

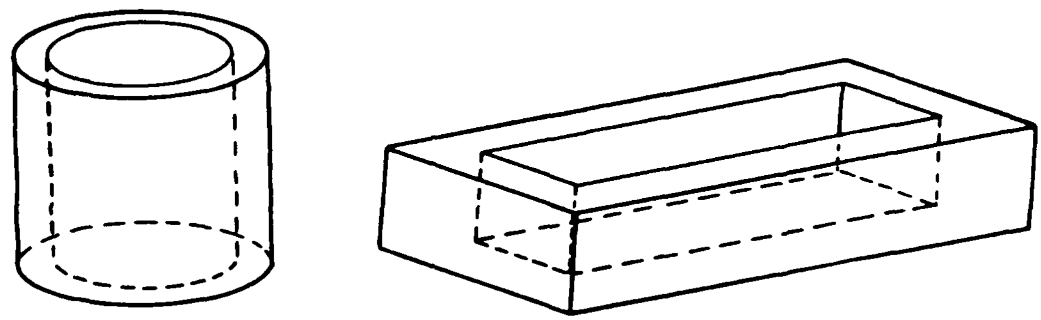

Figure 6-1. Conventional Insulator Geometries.

ceramic or glass (Reference 5). The frit material is electrically and mechanically similar to the host materials being joined so, in principle, it should not degrade the voltage standoff of the insulator. A design verification test of such an insulator has yet to be performed and conventional materials must be considered first. Generally quartz, ceramic, and Pyrex glass can support an electric field at the surface in air of 20 kV/cm and many times that in vacuum (see below).

A schematic of the high-voltage section for a conventional rectangular insulator appears in Figure 6-2. Due to imposed constraints, we will use this geometry for the high-voltage modification of the prototype LT. The electric potential between control grid and anode for a conventional rectangular insulator having a dielectric constant $\epsilon = 5$ is plotted in Figure 6-3. A well-designed high-voltage section will minimize the electric field parallel to and at the surface of the insulator in order to minimize the probability of surface flashover. The parameters that can be varied to minimize the surface electric field are listed in Figure 6-2. We have already discussed the importance of rounding the edges of the control grid and anode to minimize the probability of field emission leading to surface flashover. We specify a minimum radius of curvature of 0.15 cm (60 mil) for the edges of the control grid and anode to insure that the electric field at the edges is $<10_6$ V/cm. The remaining parameters that can be varied to minimize the electric field stress on the insulator are insulator dielectric constant, thickness, gap height (above ground plane), and insulator-anode gap. Parameterizing these values, we found that the surface electric field stress was relatively insensitive to the dielectric thickness and to values of the dielectric constant ϵ greater than 3.0. However, the field stress is sensitive to both the insulator-anode gap (d) and the gap height (h), as shown in Figure 6-4. The field stress increases when the gap approaches either the ground plane (H = 0 cm) or the high-voltage plane (H = 8 cm) due to compression of the lines of electric potential near those planes. The design point for the modified high voltage thyratron is shown in Figure 6-4 as the open circle.

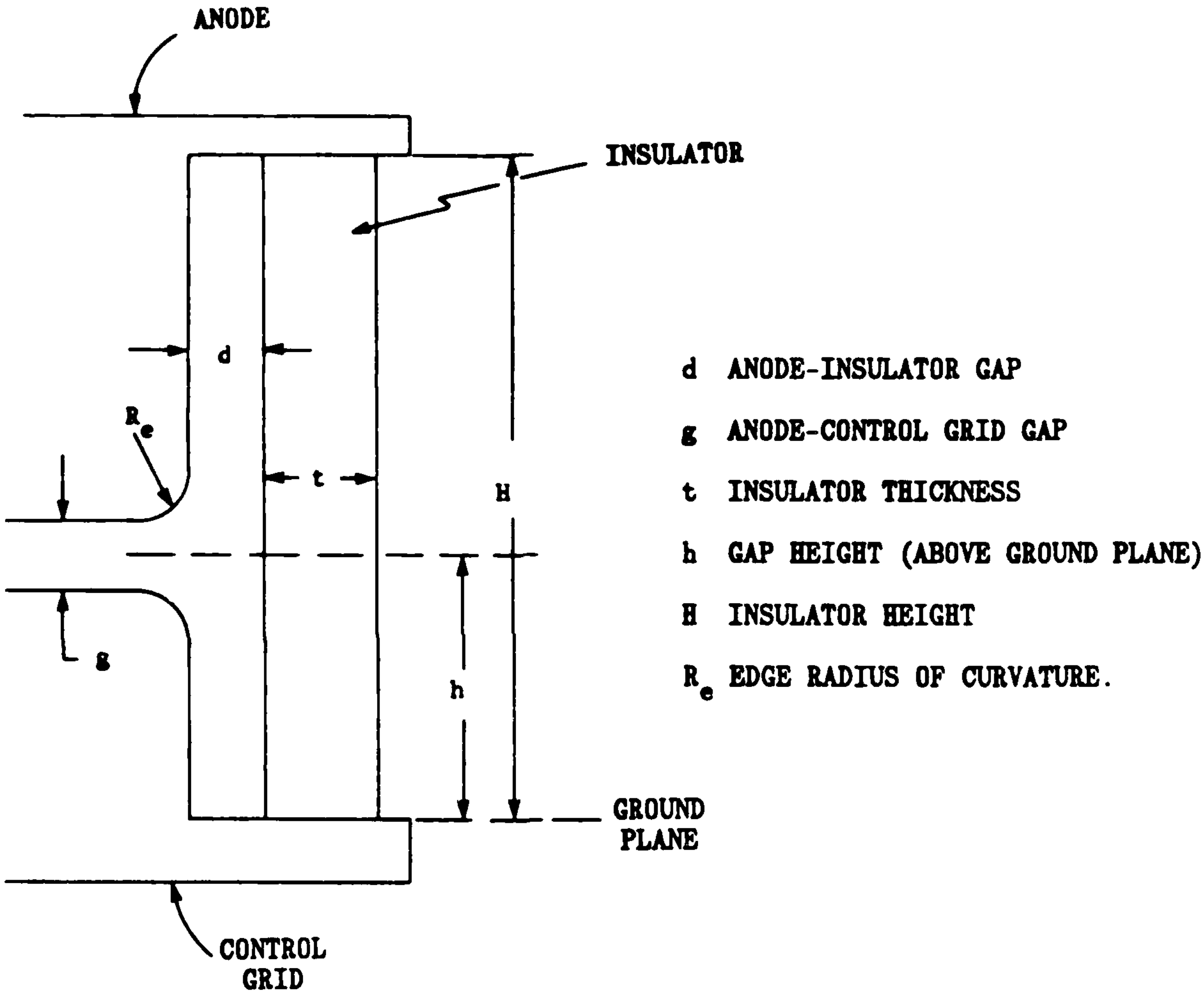

Figure 6-2. Orientation Sketch for Critical Dimension for the Rectangular Geometry Insulator.

86 10977

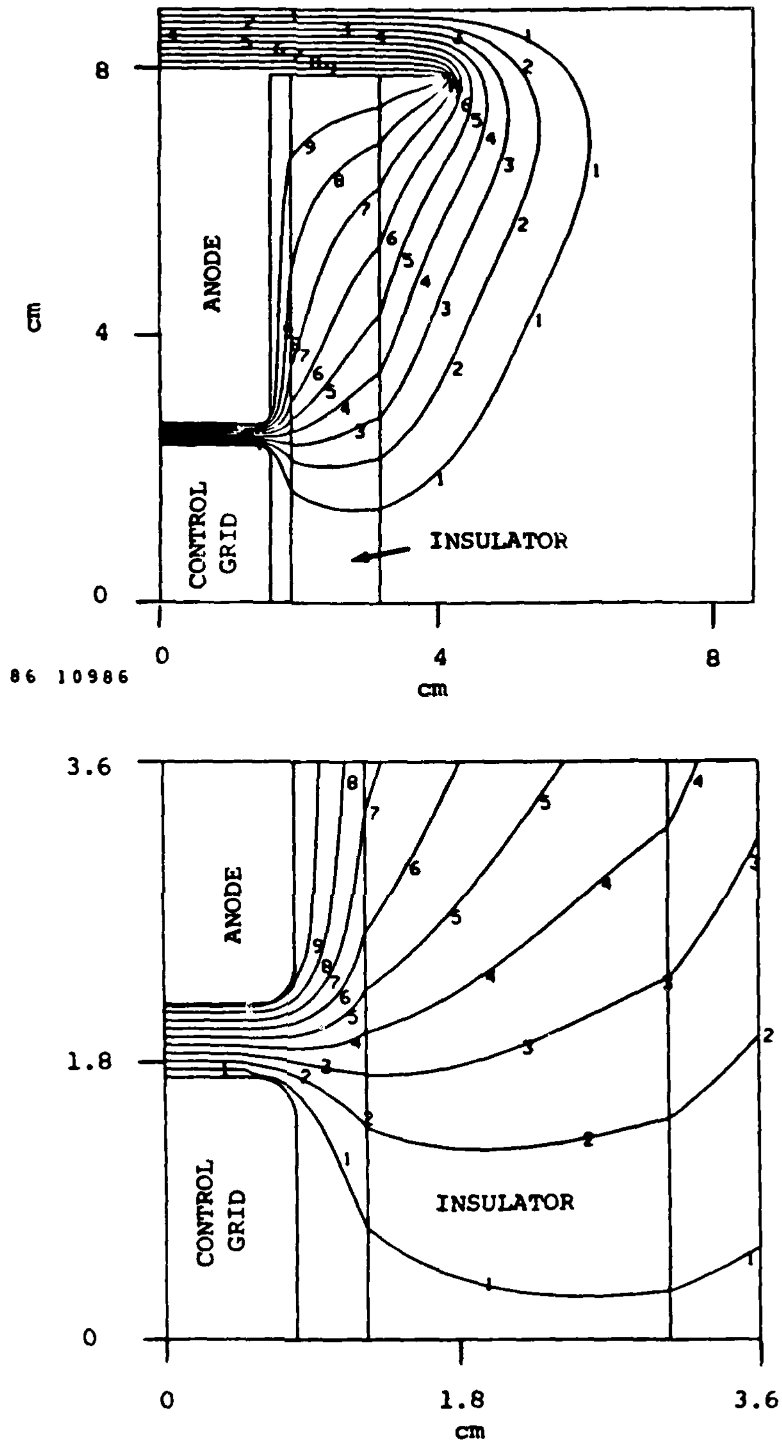

Figure 6-3. Potential Contours for the Rectangular High-Voltage Insulator.

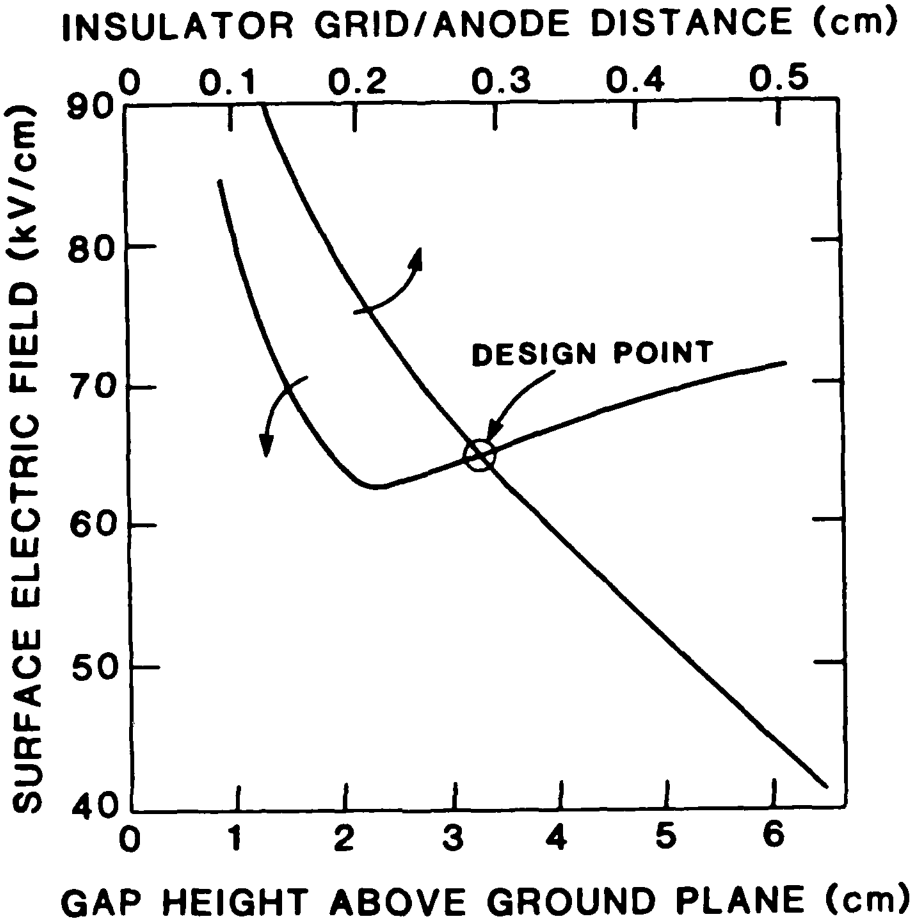

86 10824

Figure 6-4. Maximum Electric Field on the Surface of the High-Voltage Insulator for Gap Height (h) and Anode-Insulator Distance (t).

A new thyratron configuration is required that will minimize the probability for flashover across the high voltage insulator and reduce fabrication costs. A schematic of such a design is shown in Figure 6-5. In this design, the longitudinal axis of the cathode, grids, and anode are aligned coaxially within a cylindrical insulator. In conventional thyratrons that use a cylindrical insulator, the cathode surface is usually perpendicular to the axis of the cylinder. Therefore, to increase the current rating of the thyratron, the diameter of the insulator must be increased. To increase the current rating of the Collinear Cylindrical Linear Thyratron (CCLT), only the height (length) of the cylindrical insulator must be increased. Quartz, Pyrex, and ceramic cylinders measuring up to 20 cm in diameter and 3 m in length are commercially available and minimize fabrication costs and complexity, particularly when compared to the racetrack insulator. Glass- or ceramic-to-metal feedthroughs penetrating both the dorsal and ventral surfaces of the insulator are used to gain electrical access to the cathode, grids, and anodes. For current conduction of $\approx$1 kA/cm of length, the diameter of the anode will be approximately 8 cm and the insulator will be approximately 8.5 cm in diameter. These dimensions are largely determined by thermal dissipation requirements (see Section 6.5).

A similar analysis as undertaken for the rectangular geometry will be required to optimize the potential distributions in the CCLT. Due to the relatively large diameter of the insulator tube, the optimum spacings and radii will be similar. The most important parameter will be the dielectric constant of the chosen insulator. Typical values of the surface flashover strength (pulsed) in air and vacuum for a variety of candidate insulator materials are listed in Table 6-1.

6.4 THE CONTROL GRID SLOT REGION

The design of the control grid baffle region is particularly difficult to optimize. The goals of the control baffle optimization are to maximize holdoff, dI/dt, and "switchability" while minimizing switching losses. Unfortunately, these are contradictory goals. The former goal is obtained by

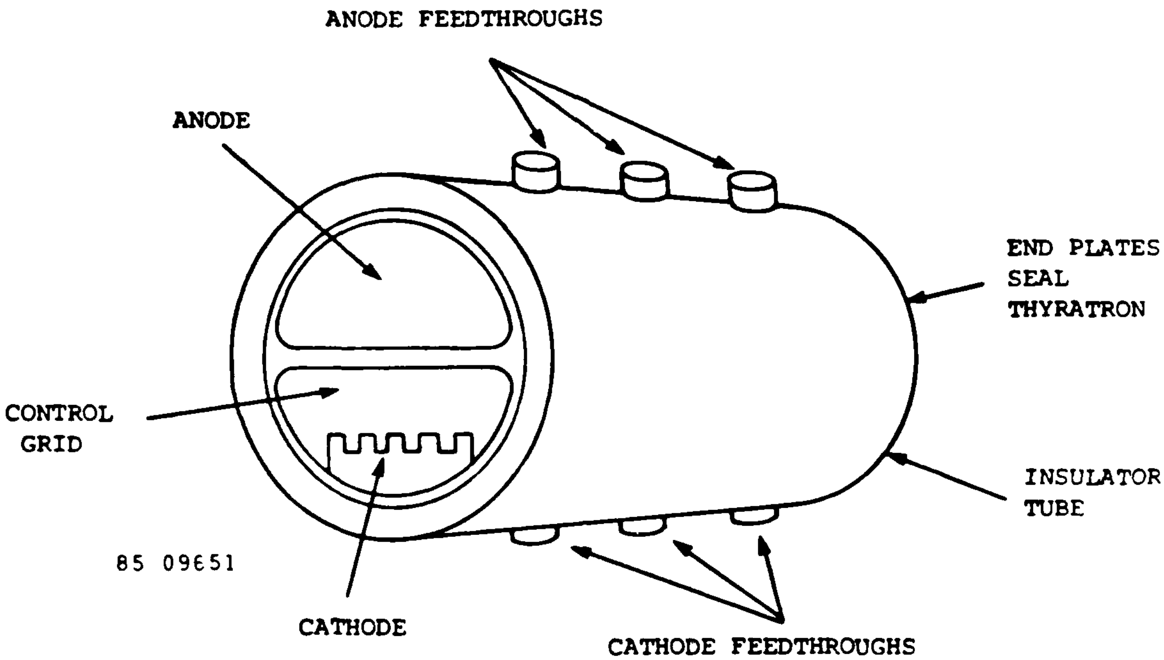

Figure 6-5. Long Cylindrical Thyratron Design Concept Where Insulator Tube Contains Anode, Cathode and Grids.

Table 6-1

SURFACE FLASHOVER STRENGTH (kv/cm)†

Material	Dielectric Constant	Strength	
		Vacuum	Air (1 atm)
Teflon	2.1	103.3	25.0
Plexiglass	3.2	123.0	23.7
Quartz	3.8	86.0	29.0
Pyrex	4.6	111.0	24.5
Macor	5.8	125.0	24.5
Sapphire	12.0	84.0	18.7

† A.S. Pillai and R. Hackam, J. Appl. Phys. 58: 151 (1985)

tight baffling while the latter goals are obtained by loose baffling. The purpose of tight baffling is to reduce, to an acceptable value, the penetration of the anode potential through the control grid slot. The degree of penetration of the electric field is denoted by $\gamma = V_A/V_B$, where V_B is the potential at the edge of the baffle. A minimum requirement is $\gamma = 10^5$. An optimum baffle design is one that obtains this attenuation while maximizing the smallest gap (either the control grid slot or the baffle-control grid) dimension. It is the smallest gap dimension that will in large part determine the resistivity of the control grid-anode gap. In Figure 6-6, we have plotted the electric potential for three baffle configurations: conventional (Figures 6-6a) and modified (Figures 6-6b and c). The contour corresponding to the lowest electric potential corresponds to an anode attenuation of $\gamma = 10^5$. The modified baffle arrangements maintain the necessary attenuation while increasing the minimum gap size.

The attentuation coefficients of several commercial thyratrons and Mancebo's device are listed in Table 6-2 with their maximum holdoff voltage. A lower coefficient means that more of the anode field penetrates into the grid-cathode space, which should result in lower holdoff voltage. The attenuation coefficient for Mancebo's thyratron is significantly lower than the HY-5 (i.e., more field penetration) but it holds off more voltage. The conclusion is that field emission is responsible for the lower voltage holdoff in the HY-5. A tube with careful control of field emission can be more loosely baffled, yet hold off higher voltages than one more tightly baffled but not having adequate electrode contouring.

The proposed high voltage section for the modified high-voltage linear thyratron is sketched in Figure 6-7. The anode attenuation factor was parametrically computed for this configuration to bound an acceptable range of dimensions which yield $\gamma \geq 10^5$. The design point dimensions determined from this survey also are listed in Figure 6-7. A conservative value of $\gamma = 10^{6.5}$ was chosen for the design. A sample of the parametric results appears in Figures 6-8 and 6-9. The attenuation factor increases linearly proportional to increases in either the baffle overlap or the control grid thickness. The

Table 6-2

BAFFLE ATTENUATION COEFFICIENT AND VOLTAGE HOLDOFF

Tube	$\mathcal{I}$	Holdoff Voltage
HY-7†	3×10^{3}	20 kV
HY-1802	5×10^{4}	35 kV
HY-5	7×10^{5}	65 kV
Mancebo	2×10^{6}	100 kV

† Lower Section

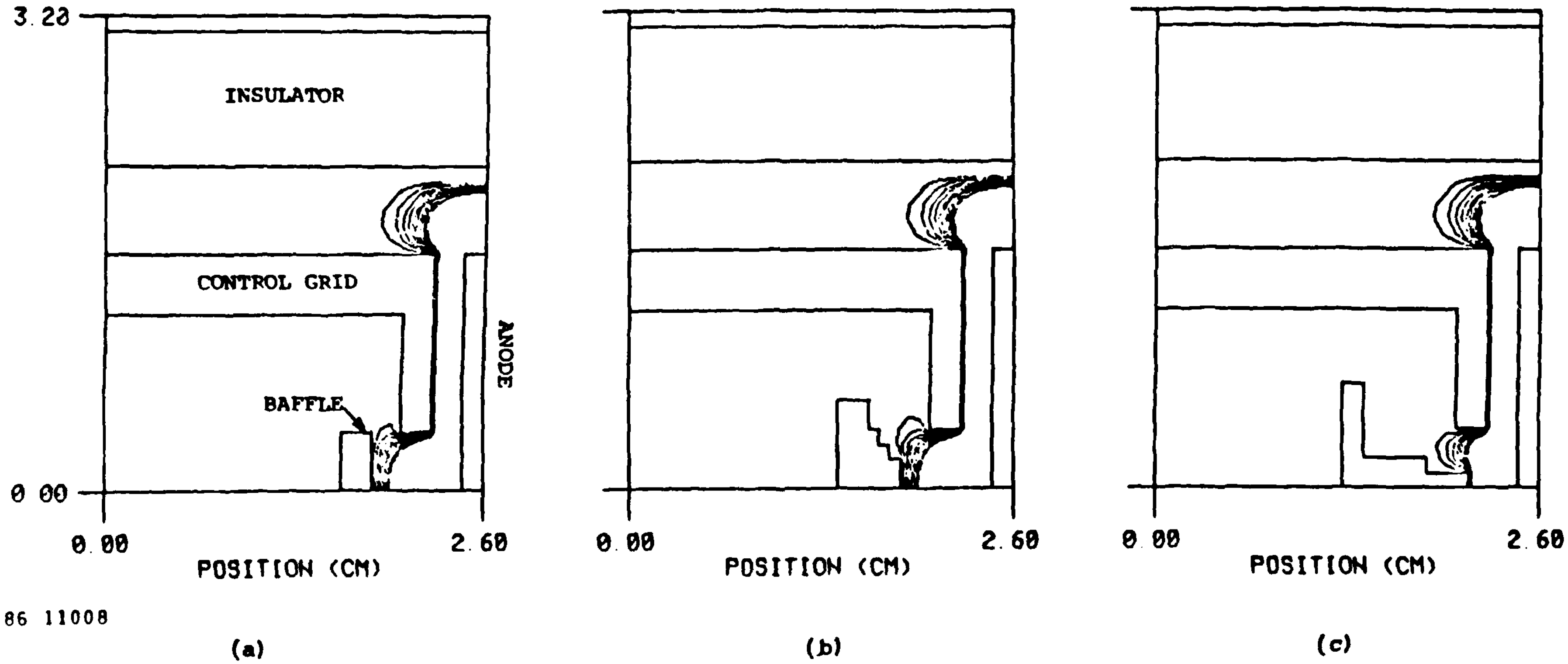

Figure 6-6. Electric Potential Contours in the Control Grid Gap Region for Various Baffle Configurations. The anode attenuation factors range from 10^5 to 10^4. The minimum gap dimension increases from 2a to 2c.

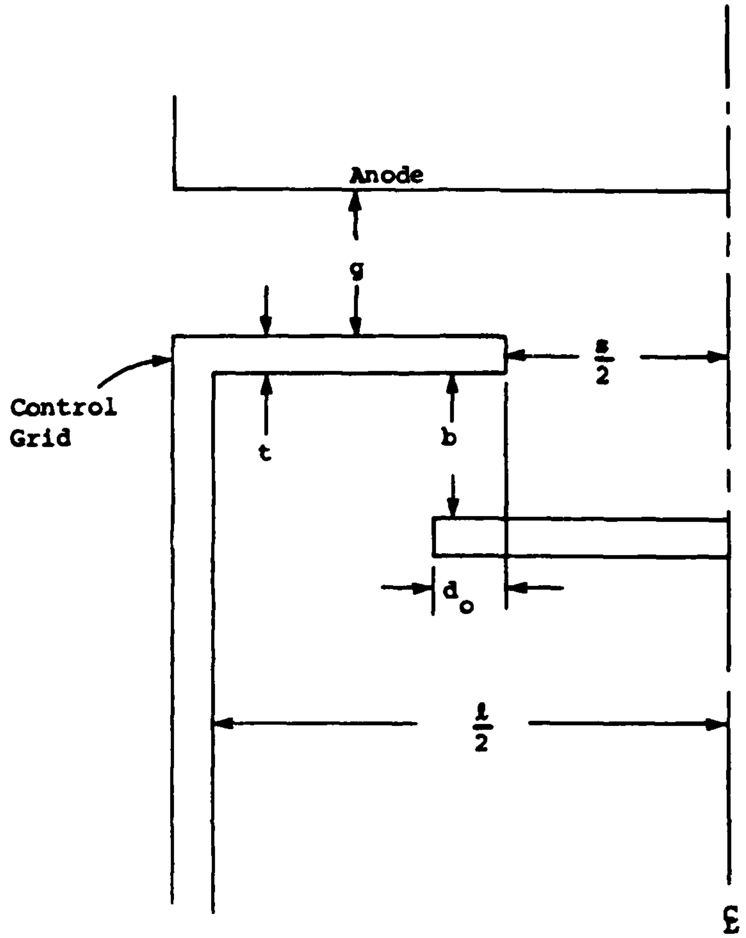

Point Design Dimensions

Symbol	Item	cm
g	Anode-control Grid Gap	0.25
s	Slot	0.25
t	Control Grid Thickness	0.5
b	Baffle Setback	0.2
ℓ	Channel Width	1.6
d_o	Baffle Overlap	0.33

Figure 6-7. Schematic of High-Voltage Section and Legend for Modified Linear Thyratron Dimensions.

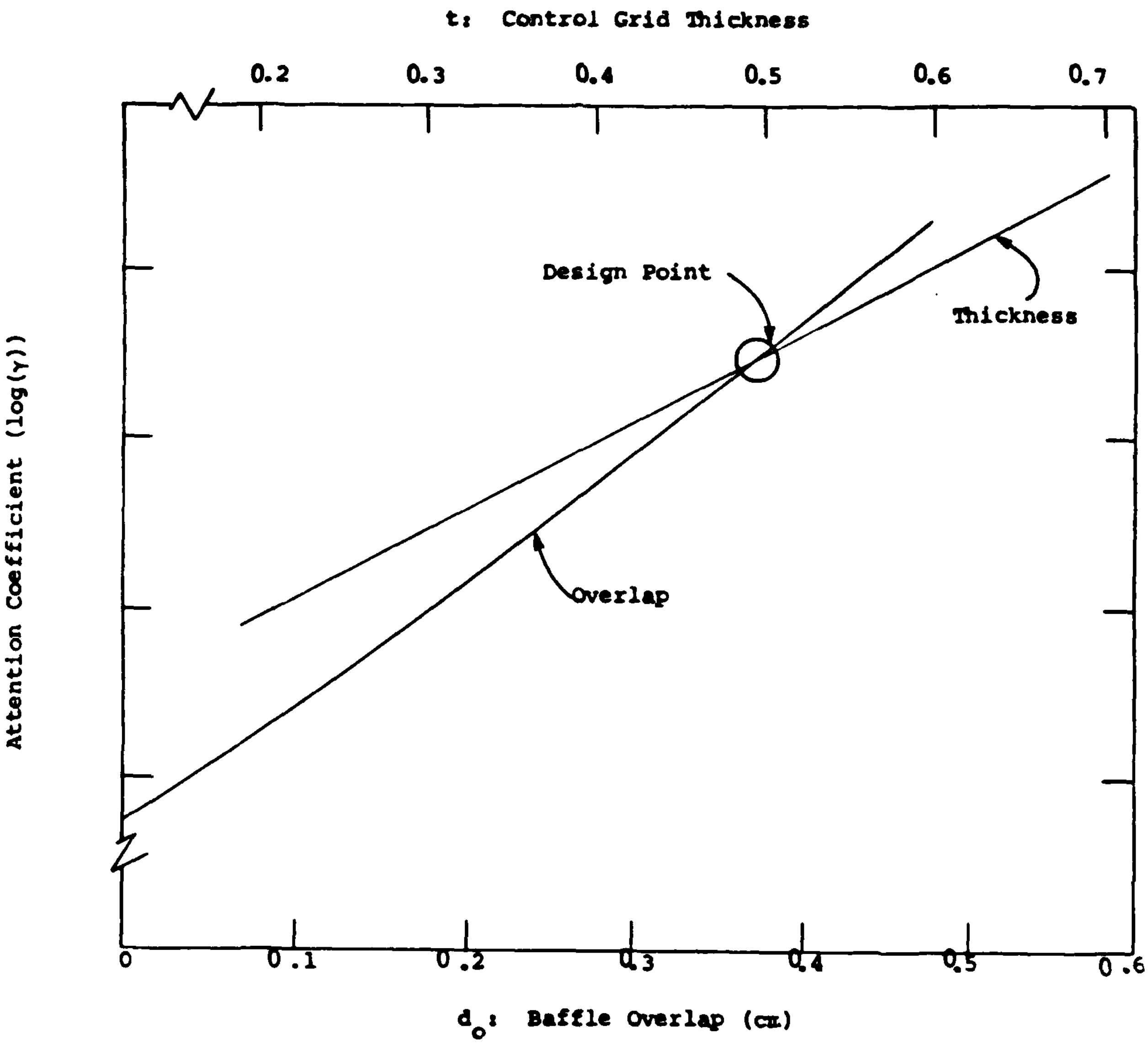

Figure 6-8. Electric Field Penetration Attenuation Factor as a Function of Baffle Overlap (d_o) and Control Grid Thickness (t).

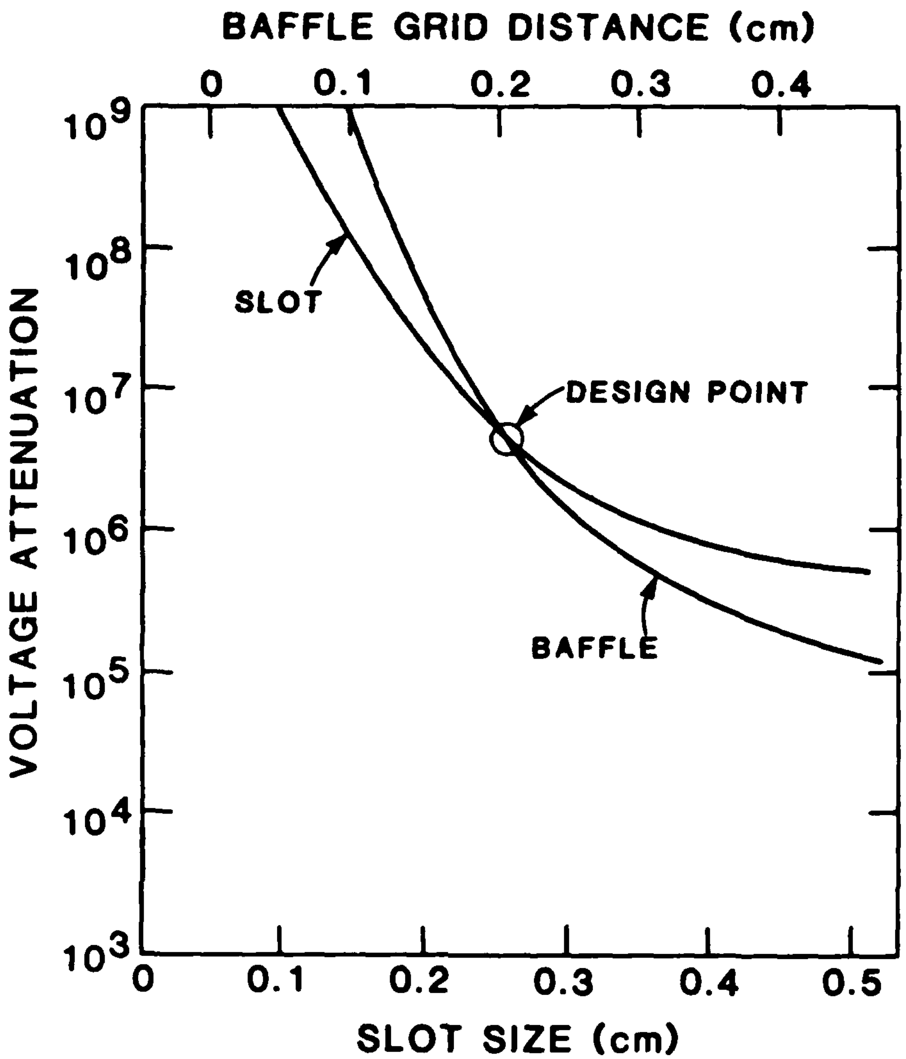

Figure 6-9. Electric Field Penetration Attenuation Factor as a Function of Slot Size (s) and Distance Between Control Grid and Baffle (b).

attenuation factor decreases with increasing baffle offset or slot size, though less than linearly. When the baffle offset or slot size become sufficiently large, field penetration is limited by the baffle overlap.

6.5 THERMAL CONSIDERATIONS

The degree of sophistication of the design for thermal control of the CCLT depends in large part on the average power the device is expected to switch. At this time, we envision the tube operating at 200 Hz for a short burst of many tens of pulses with a repetition rate of a few Hz. Assuming the switching of 100 kV at 100 kA and that the thyratron is 95 percent efficient during commutation, the waste heat in the thyratron will be approximately 30 kW or 300 W/cm. Water-cooling the electrodes should suffice (see below). Both anode delay time drift and jitter are largely a result of anode heating, which changes the local gas pressure in the control grid-anode gap. Generally, the anode delay time $\Delta\tau_{ad}$ can be kept to less than 50 ns if the variation in anode temperature is <200 K. By operating with an unheated cathode, both $\Delta\tau_{ad}$ and jitter are minimized, since the thyratron envelope and grid structures are not additionally heated from this source. (Thyratrons fitted with cold dispenser cathodes and operating with $\Delta\tau_{ad}$ of 40 ns and a jitter of 2 ns (Reference 2) have been reported.)

To determine the cooling requirements for the CCLT, we used the geometry in Figure 6-10. The anode is constructed of flat stainless steel plate of thickness t_s welded to a half cylinder of stainless steel with a diameter d tubing forming the "D" shape shown in the figure. The center of the "D" forms a flow channel for cooling water. The control grid has N slots of width s separated by a distance ℓ. We assume that the anode is uniformly heated in the region illuminated by the control grid slots and that both t_s and w are $<<\ell$.

To insure that the thermal stress on the anode is a minimum, the local surface temperature is a minimum, and that the coolant contact area is a maximum, the face of the anode must be isothermal. This condition is met if the time required to locally heat the metal is less than the characteristic

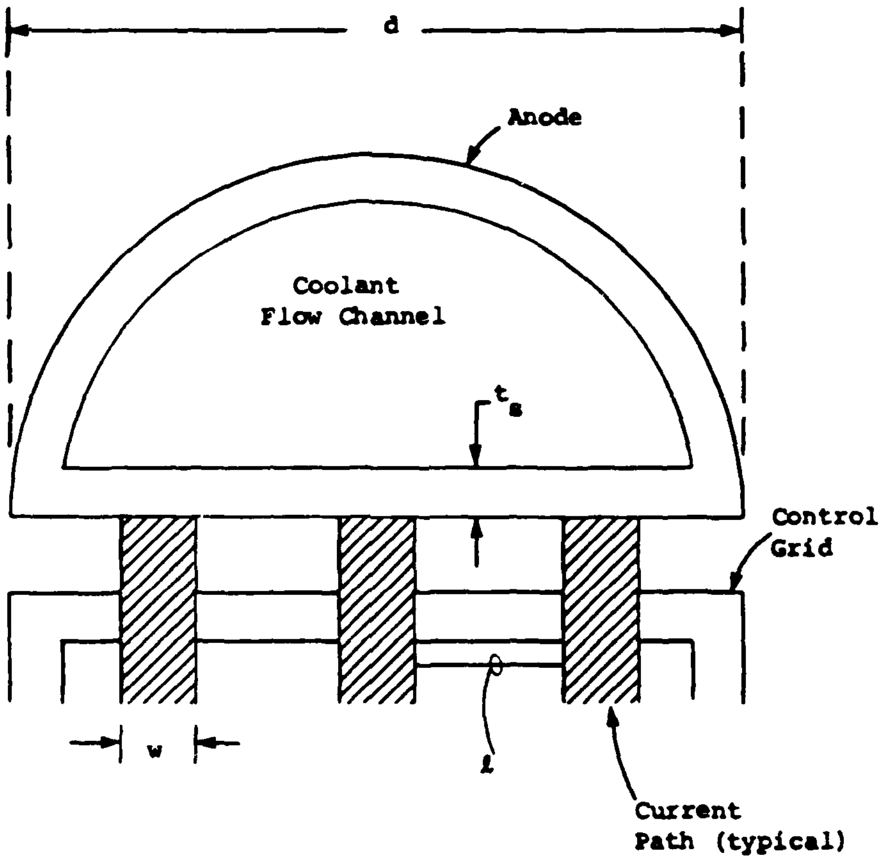

Figure 6-10. Schematic of Anode and High-Voltage Section for the CCLT Showing Current Paths Through the Control Grid.

thermal conduction time; that is

$$\frac{\left(\frac{\ell}{2}\right)^2}{a} << \frac{wt_s cN(\Delta T)}{P} \qquad [6.1]$$

where a is the thermal diffusivity, c is the heat capacity, ΔT is the temperature rise, and P is the linear heating rate of the anode (W/cm). The thermal diffusivity of stainless steel is ≈0.04 cm^2/s and its heat capacity is ≈3.6 J/cm^3-K. Using as a maximum value ΔT = 200 K and P = 300 W/cm and noting that N = D/w and ℓ = D/N, then we must have 2.5 << Dt_s/w^2. The limiting dimensions are approximately given by Dt_s/w^2 = 25. We can further set an limit on w by requiring that the maximum current density through the slots be approximately 1-2 ka/cm^2. For our example, w ≈ (0.5-1.0)/N cm and we choose a mid-range value for our calculations. A scaling map for anode thickness t_s resulting from these specifications is shown in Figure 6-11 where anode thickness is plotted as a function of anode diameter D and number of control grid slots N. Desirable ranges for D and t_s are indicated by the dashed lines, showing that two control grid slots are required. To insure that the flat portion of the anode is isothermal, we choose t_s = 4 mm and D = 8 cm. These parameters yield w = 4-5 mm and ℓ = 4 cm.

We now estimate the flow of water required to limit the temperature rise of the anode to 200 K from ambient, or 500 K. Since the anode is isothermal, we can specify that the inside surface of the flat portion of the anode is at this temperature. The heat flux that must be transferred through this surface is P/D W/cm^2. The heat transfer coefficient for a fluid over a surface is approximately h_c = Nu • k/D where Nu is the Nusselt number and k is the thermal conductivity of the fluid. Assuming laminar flow over a flat plate, Nu ≈ 0.66 $RePr^{0.5}Pr^{0.3}$ where Re is the Reynolds number based on length and Pr is the Prandtl number. Assuming an inlet temperature of 290 K and an outlet temperature of 350 K, the average Prandtl and Reynolds numbers for water are Pr ≈ 4.0 and Re ≈ 135 uL where u is the flow velocity (cm/s) and L is the flow length (L = 100 cm). With k = 0.0064 W/cm-K and u = 200 f/D^2 cm/s (f is the water flow rate in gallons/minute), we have $h_c = 10 \cdot f^{0.5}/D^2$ W/cm^2-K.

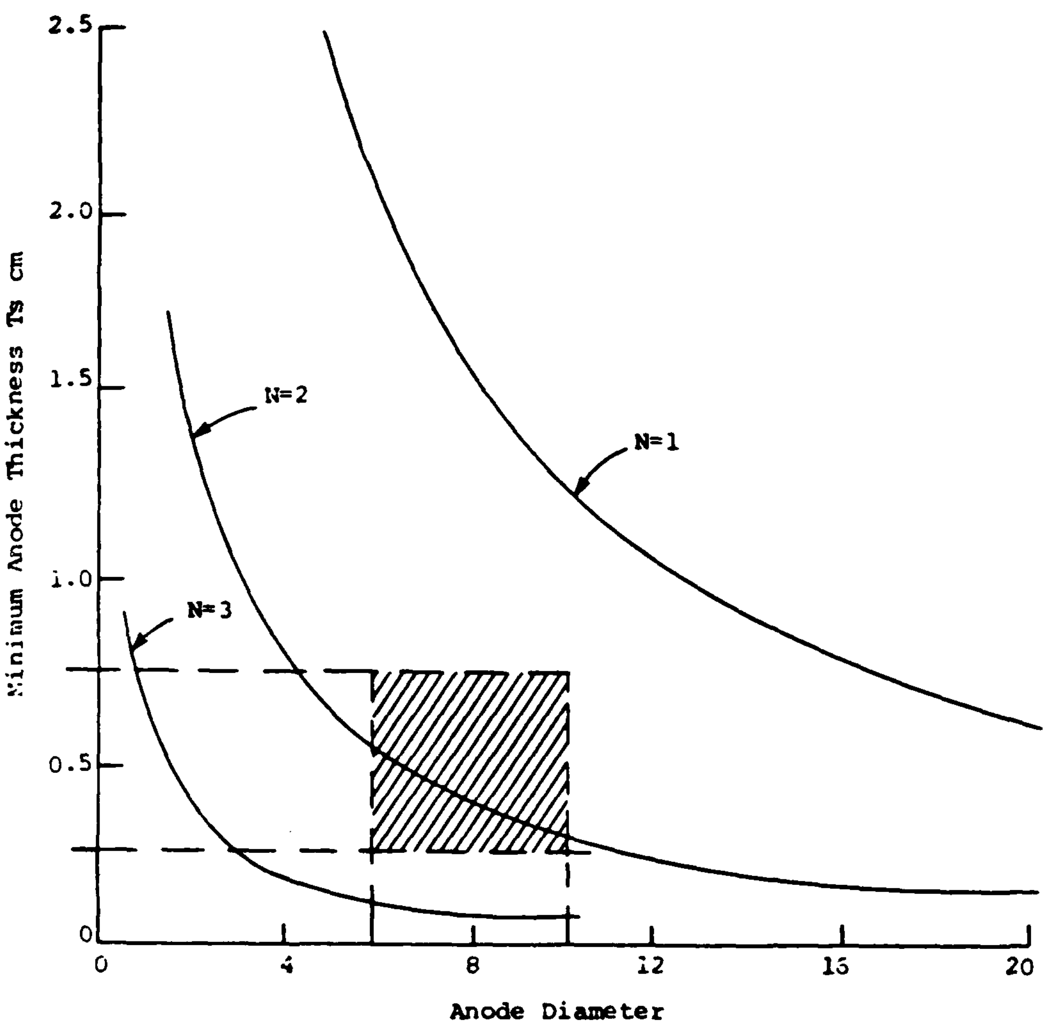

Figure 6-11. Anode Thickness as a Function of Anode Diameter for N Control Grid Slots.

Therefore, the rate of heat transfer yields

$$\frac{P}{D} = \frac{2h_c\left(T_s - T_{ave}\right)}{D} = \frac{20f^{0.5}\left(T_s - T_{ave}\right)}{D^3} \qquad [6.2]$$

$$f = \left[\frac{PD^2}{20\left(T_s - T_{ave}\right)}\right]^2$$

where T_s is the surface temperature (500 K) and T_{ave} is the average water temperature (320 K). With P = 300 W/cm and D = 8 cm, f ≈ 30 gal/minute, a large but not unreasonable value. Note that $f \propto P^2$ so that increasing the efficiency of the thyratron greatly reduces the coolant flow rate.

REFERENCES

1. L. Mancebo, "100-kV Hydrogen Thyratron Without Gradient Grids," IEEE Trans. Elect. Devices ED-18: 920-924 (1971)

2. Long-Life High-Current Thyratrons for Fast Discharge Lasers, Spectra Technology and Impulse Electronics, Final Report, Contract AFWAL-TR-84-2003, March 1984.

3. S. Friedman, R. Petr, J. O'Connell, and J. McGowan, "Instant-Start Cathodes for High Average Power Hydrogen Thyratrons," IEEE 15th Pulse Power Modulator Symposium, pp. 127-132 (IEEE, New York, 1982)

4. S. Schneider, Final Report on Delivery Order No. 0715 between Battelle Columbus Laboratories and S. Schneider, Prepared for Pulse Power Technology Branch, U.S. Army Electronics Technology and Devices Laboratory, Ft. Monmouth, New Jersey, November 1984.

5. Spectra Technology, Inc., "FRC High Flux Formation and Large S Physics Studies: TRX/LSX," Submitted to DOE Office of Fusion Energy, Div. APP, Advanced Fusion Concepts Branch, 28 February 1985.

Section 7

LINEAR THYRATRON PLASMA SIMULATION CODE: LINTHY2D

7.1 INTRODUCTION

The rapid development of thyratrons has traditionally suffered from lack of design and analysis tools. Three phases during thyratron switching require analytical or computational support: holdoff, commutation, and conduction. Computer codes that solve for the electric field exist for analyzing conditions during holdoff, (Reference 1) and recently published discharge kinetics models describe thyratron characteristics during conduction (Reference 2,3). Models previously have not been available to analyse the commutation phase of thyratron switching. This deficiency results from the fact that during commutation the gas pressure ($\lesssim$1 Torr), voltage ($\lesssim$50-100 kV), and electrode spacing ($\lesssim$1 cm) are in a parameter space in which traditional methods of analysis cannot be applied. For example, the geometry is complicated (i.e., non-planar), resulting in a nonuniform electric field; the mean free path of electrons is sometimes comparable to electrode separations; and the relative rate of change in the electric field can be comparable to the rate of plasma formation.

A plasma simulation code has been developed to model the linear thyratron during the holdoff and commutation phases of switching. The purpose of the model is to aid in the analysis of experimental data and to provide a design tool for modifying the linear thyratron and for designing new thyratrons. The plasma simulation code, named LINTHY2D, is a self-consistent 2-1/2-dimensional, time-dependent treatment that is capable of modeling electron avalanche in an arbitrary gas and in an arbitrary geometry. LINTHY2D uses a Monte Carlo particle simulation to model electron transport, and a continuum formulation to model heavy particle transport. An electron multiplication and renormalization technique is used to explicitly model electron avalanche using the particle simulation. A modified null

cross-section technique is used to allow collisions with excited states, ions, and electrons during the avalanche when these densities may change by many orders of magnitude. Poisson's equation is solved to obtain the spatially dependent electric potential. Current and voltage characteristics are obtained by integrating with the plasma simulation models for the external circuits for the auxiliary grid, control grid, and energy storage circuit.

In Sections 7.2-7.8, the plasma simulation model LINTHY2D will be described. The model has been validated by comparison to the experimental current and voltage characteristics for the prototype linear thyratron, and to the distribution of excited states measured by hook spectroscopy. These comparisons will be discussed in Section 7.9. Scaling laws and a discussion of tradeoffs of operating characteristics of thyratrons generated with the results from LINTHY2D are discussed in Sections 7.10-7.11.

7.2 MACROELECTRONS AND RENORMALIZATION

The goal of the plasma simulation is to model the electron avalanche and current flow through a linear thyratron while using a reasonable amount of computing resources. The change in current density during the electron avalanche implies a change in electron density of 10^{5}-10^{14}cm^{-3}. To model this process using Monte-Carlo techniques, particles used in the simulation have an assigned weight corresponding to a specified number of electrons and are called macroelectrons. As the electron avalanche develops, the weights of the macroparticles are renormalized to keep the number of macroelectrons in the simulation to a manageable size. This renormalization procedure, similar to that used by Kline, (Reference 4) is described below.

The simulation begins with N_o macroelectrons released from the cathode, each having a weight W_o (see Figure 7-1). The weights of the electrons are $I/(eN_o\Delta t)$ where I is the instantaneous current and Δt is the length of time over which the N_o electrons are released from the cathode. Trajectories and collisions for these macroelectrons are computed. When an ionization occurs, another macroelectron is added to the simulation with a weight equal to the

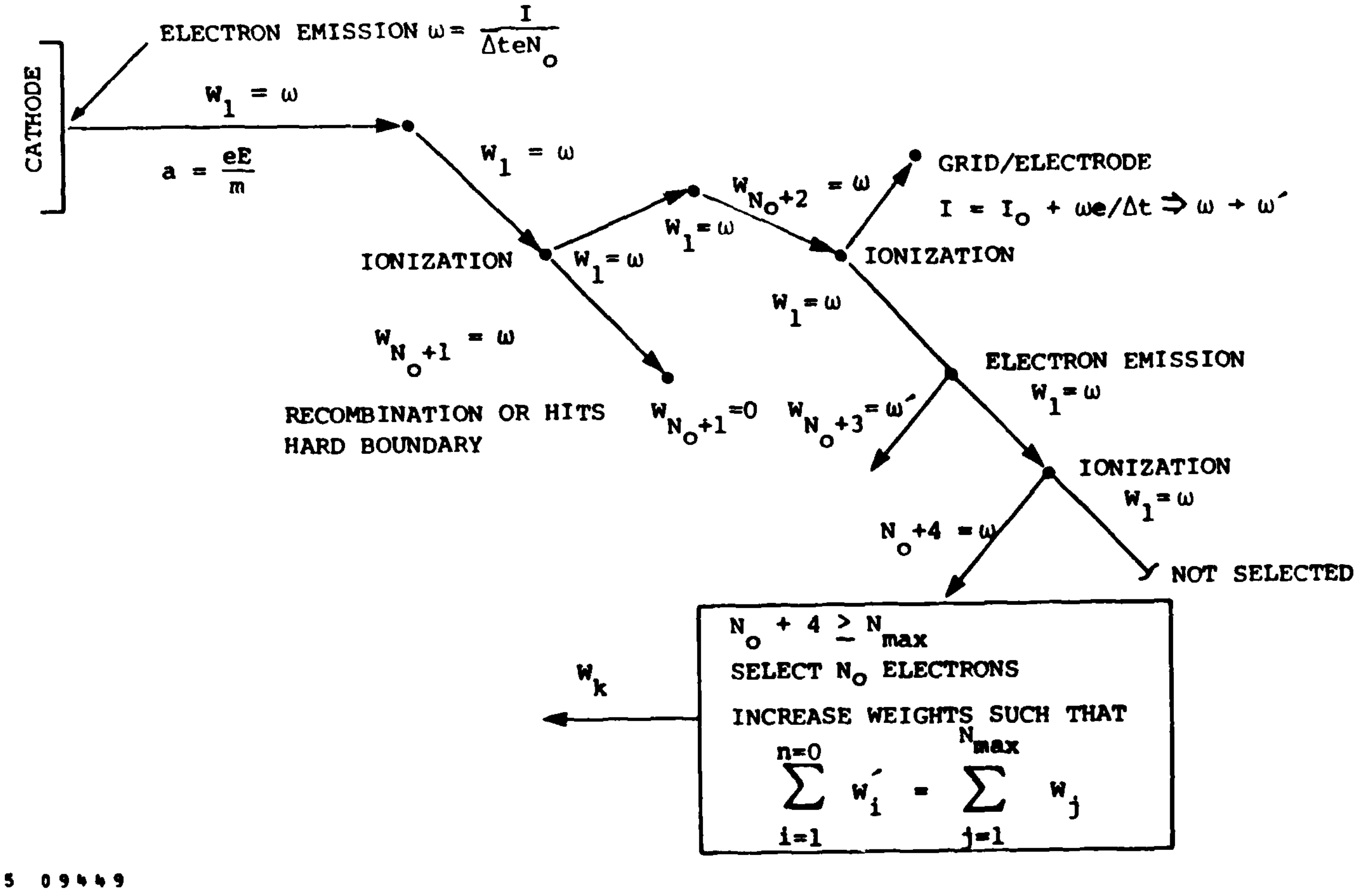

Figure 7-1. Schematic of Electron Multiplication and Renormalization.

weight of the macroelectron that had the ionising collision. Periodically macroelectrons are released from the cathode, not necessarily having weight W_o, thereby increasing the number of macroelectrons in the simulation. If a macroelectron is collected by a grid or electrode, its weight is summed to obtain the grid or electrode current, and the collected macroelectron is removed from the simulation. When the total number of macroelectrons exceeds a pre-selected value N_{max}, the simulation is interrupted for renormalization. The total weight of the macroelectrons is summed. N_o macroelectrons are then randomly selected and their weights are summed. The unselected macroelectrons are removed from the simulation. The ratio of total weight to the weight of the selected electrons yields a renormalization factor. The weight of the selected macroparticles is multiplied by this factor, thereby insuring conservation of charge. The simulation then proceeds with fewer but heavier macroelectrons. The normalization procedure is separately performed within different regions of the thyratron to insure that the distribution of total charge in each region is not significantly perturbed by the renormalization process. The number of macroelectrons fluctuates between N_o and N_{max} during the simulation. Typically these values are 4,000 and 12,000, respectively.

The electron density is obtained by summing the weights of the macroelectrons within a given computational cell. The electron density is then $\sum W_i/\Delta V$, where ΔV is the volume of the cell. To improve upon statistics and smooth the electron density, the macroelectrons are assumed to have a finite size and shape (Reference 5). The contribution of a macroelectron to the electron density in a particular cell is proportional to the fractional overlap of the finite particle into that cell. The macroelectron is typically a parallelepiped having dimensions equal in size to the computational cell.

7.3 EXTENDED NULL CROSS-SECTION TECHNIQUE

During Monte Carlo simulations of electron collisions in electric discharges, it is often convenient for all electrons to appear to have the same collision frequency. This is accomplished by use of a null cross section (Reference 6). In using the null cross-section technique, the maximum

electron collision frequency for the energy range of interest, ν_{max}, is determined (see Figure 7-2). For each electron energy, a null cross section is calculated such that when this cross section is added to the real collision cross sections, the resulting collision frequency is equal to ν_{max}. During the simulation, a collision is said to occur during a time Δt if for a random number r_1 $(0 < r_1 < 1)$, $\Delta t \geq -\ell n(r_1)/\nu_{max}$. If this inequality holds, another random number r_2 is selected. A real collision is said to occur if $r_2 \leq \nu_a/\nu_{max}$, where ν_a is the real collision frequency; that is, the electron collision frequency in the absence of the null cross section. However, if $r_2 > \nu_a/\nu_{max}$, a null collision has occurred and the particle proceeds unhindered. If the collision is real, the specific type of collision (e.g., elastic collision, electronic excitation) is determined by selection of a third random number, r_3. The i^{th} collision is said to occur if $\nu_{i-1} < r_3 \cdot \nu_a \leq \nu_i$, where ν_i is the collision frequency associated with the i^{th} possible collision at the energy of interest.

During an electron avalanche in a device such as the linear thyratron, the relative densities of the species with which the electrons collide can change significantly as a function of either position or time. This change in density results from electron collisions exciting or ionising the gas. Therefore, the electron collision frequency and the type and number of possible collisions also change as a function of position and time. For example, near the slot in the control grid of the thyratron, the fractional excitation and ionisation can approach 0.1, making collisions with excited states, ions, and electrons important processes. When initially calculating the ν_j and ν_{max}, the densities of excited states and ions are zero. As the density of collision partners changes, many evaluations of cross sections might be required to revise the ν_j and ν_{max} appropriately. To circumvent this problem, a new extended null-cross section technique was developed.

The extended null cross-section technique is implemented by including cross sections for collisions with all anticipated collision partners in the initial computation of the ν_j and ν_{max} (see Figure 7-3). To do so, we must estimate the maximum possible density that each of the collision partners

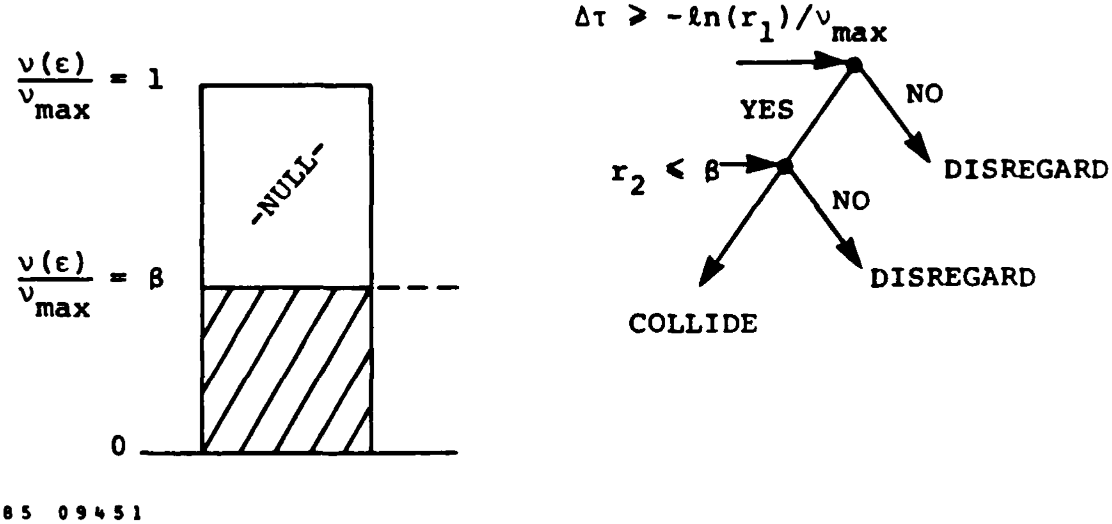

Figure 7-2. Schematic of Conventional Null Cross-Section Technique. r is a random number (0<r>1) and ν is an electron collision frequency.

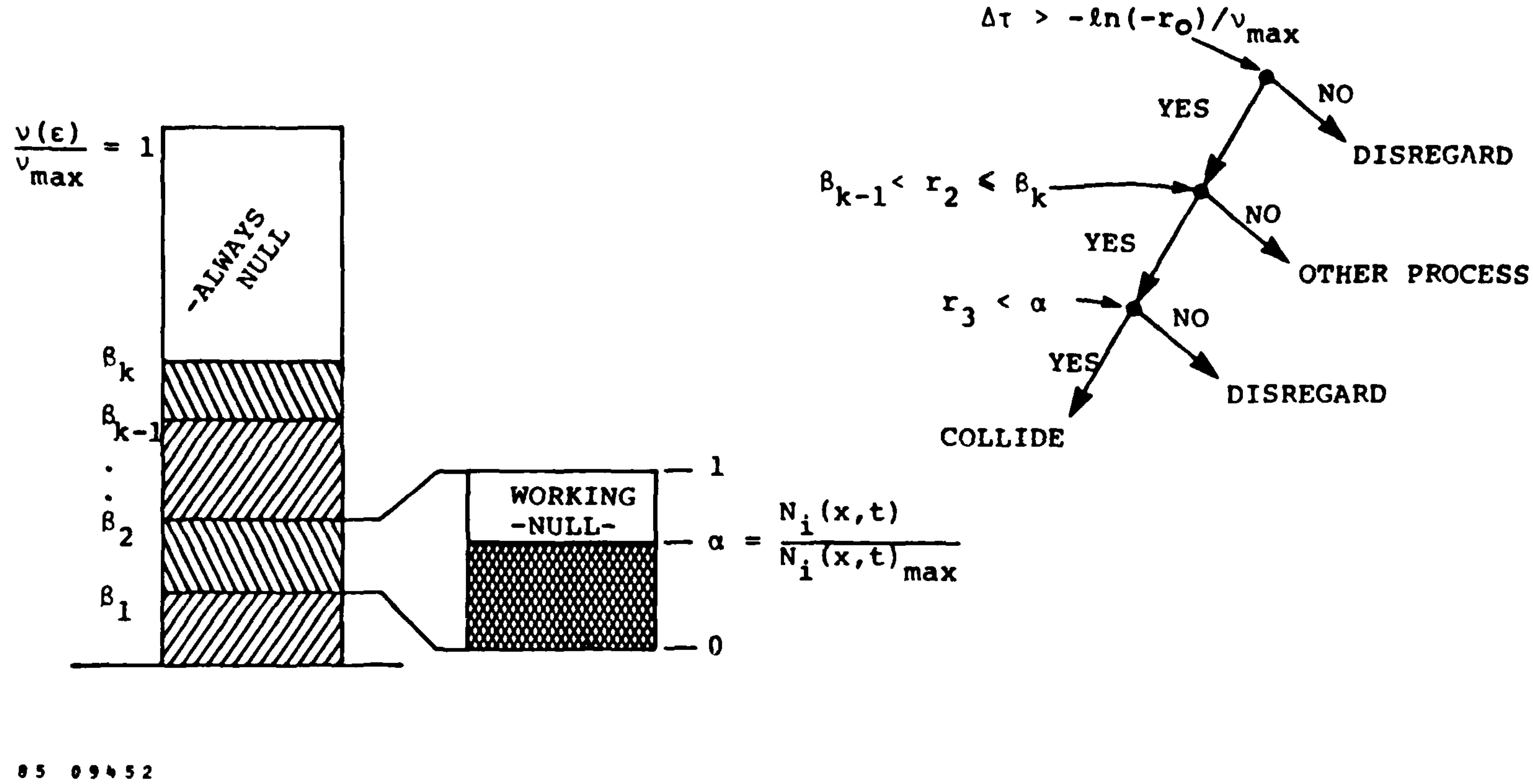

Figure 7-3. Schematic of Extended Null Cross-Section. r is a random number (0<r>1). ν is an electron collision frequency.

might have during the electron avalanche. The maximum collision frequency for each energy, ν_{max}, then consists of the sum of the collision frequencies, with all species as calculated with the maximum anticipated density of that particular species, and a collision frequency that is always null, ν_{null}. As described at the beginning of this section, the null collision frequency serves the purpose of making the effective collision frequency at all energies the same. Now the null collision frequency includes the maximum anticipated density of all collision partners. At any particular spatial location or time, the "real" collision frequency for collision j with species k is simply $\nu_{jk} = \nu_{jk}^{max} \cdot N_k(x,t)/N_k^{max}$, where $N_k(x,t)$ is the instantaneous density of species k, N_k^{max} is its maximum anticipated value, and ν_{jk}^{max} is the maximum anticipated collision frequency for process j with species k. The remaining portion of ν_{jk}^{max}, $\nu_{jk}^{max} \cdot (1 - N_k(x,t)/N_k^{max})$, is treated as being null and is added to ν_{null}. Using this technique, only a single evaluation of cross sections and collision frequencies need be performed. Actual time and spatially dependent "real" collision frequencies are obtained by a simple scaling of the local density of collision partners to their maximum anticipated value.

The procedure for determining whether a particular collision has occurred proceeds by the selection of a sequence of random numbers r_i $(0 < r_i < 1)$:

r_1:	$\Delta t \geq r_1/\nu_{max}$	$\rightarrow$	A "collision" occurs
r_2:	$r_2 \leq \nu_a/\nu_{max}$	$\rightarrow$	A real collision occurs
r_3:	$\nu_{j-1,k} < r_3 \leq \nu_{jk}$	$\rightarrow$	"Collision" type j, species k occurs
r_4:	$r_4 \leq N_k(x,t)/N_k^{max}$	$\rightarrow$	A real collision with species k occurs

By appropriate normalization of the collision frequencies and number densities, we can use a single random r for all the r_1 through r_4 described above.

7.4 EXCITATION PROCESSES AND CROSS SECTIONS

In the simulation of electron avalanches in noble gases, four states of the gas were included: the ground state, a single total excited state, and singly and doubly ionized atoms (see Figure 7-4). The following electron impact excitation reactions were used:

$e + M^{(*)} \rightarrow M^{(*)} + e$	electron-neutral elastic scattering
$e + M^{+} \rightarrow M^{+} + e$	electron-ion elastic scattering
$e + e_{ave} \rightarrow e_{ave}\ e$	electron-electron scattering
$e + M \rightarrow M^{*} + e$	electronic excitation
$e + M^{*} \rightarrow M + e$	electronic superelastic relaxation
$e + M \rightarrow M^{+}\ e + e_s$	ionization
$e + M \rightarrow M^{2+}\ e + 2e_s$	double ionization
$e + M^{*} \rightarrow M^{+}\ e + e_s$	excitated state ionization
$e + M^{+} \rightarrow M^{*}$ $e + M^{++} \rightarrow M^{+}$	radiative recombination
$2e + M^{+} \rightarrow M^{*} + e$ $2e + M^{++} \rightarrow M^{+} + e$	collisional radiative recombination

In the reactions above, M is the ground state of the noble gas, M^{*} is the

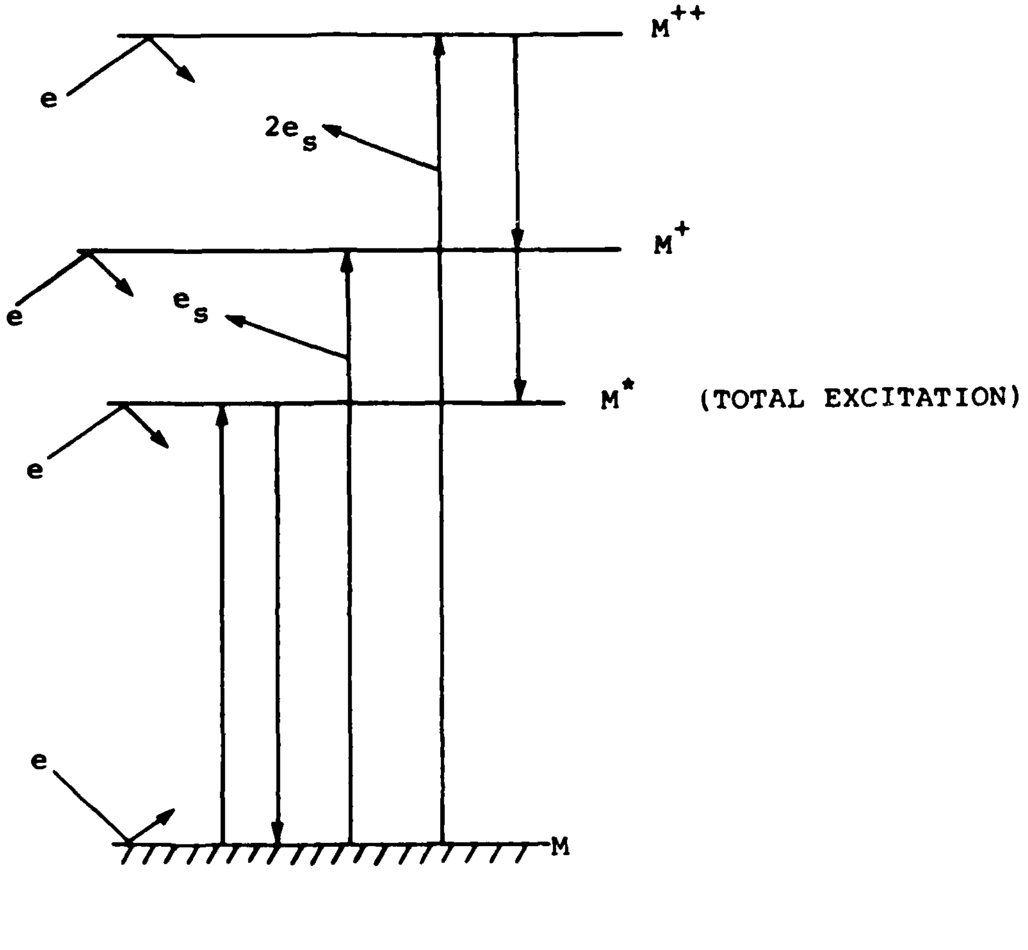

Figure 7-4. Schematic of Electron Impact Processes in Model.

total excited state, and M^+ and M^{2+} are the singly and doubly ionized atom, respectively. The subscripted electron, e_s, denotes the secondary electron in an ionization. The "average" electron is denoted by e_{ave} and will be discussed below. The inclusion of charged particle collisions is particularly important because the plasma can become highly ionised (≈0.1) near the control grid slot during conduction. At such times, the current density is locally constrained by electron-ion collisions.

Calculations were performed for electron avalanche through helium. Neutral elastic scattering cross sections for He were obtained from the compilation by Hayashi (Reference 7). The cross sections for elastic scattering from charged species, both electrons and ions, were obtained in analytic form from Mitchner and Kruger (Reference 8).

$$\sigma_{ee} = \sigma_{eI} = 4\pi b_o^2 \ell n \left(1 + \left(\frac{\lambda_D}{b_o}\right)^2 \right)^{1/2} \qquad [7\text{-}1]$$

where the subscripts ee and eI are for electron-electron and electron-ion collisions, respectively. λ_D is the Debye length and b_o is the impact parameter for 90° collisions

$$\lambda_D = \left(\frac{\epsilon_o k T_e}{n_e e^2}\right)^{1/2}, \qquad b_o = \frac{e^2/4\pi\epsilon_o}{m_e v_e^2} \qquad [7\text{-}2]$$

The electron mass and velocity are m_e and v_e, respectively. To evaluate this cross section and the collision frequency with charged particles, the electron temperature (T_e), electron density (n_e), and ion density are required. The ion density is obtained from solution of the heavy particle conservation equations, discussed in Section 7.5. The electron density and temperature are obtained in the following manner. During the simulation, the spatially dependent electron density is periodically calculated by summing a sequence of "snapshots" of the location of the macroelectrons taken at pre-set intervals. An effective electron temperature also is computed in this manner by setting $T_e = 2\epsilon/3k$ where ϵ is the average electron energy. The most recently summed

values for electron density and temperature are then used to calculate σ_{ee} and σ_{ei}. A range of n_e and T_e must be estimated before the simulation in order to provide sufficient working null space in the ee and eI collision frequencies. When an ee collision occurs, the collision partner is assumed to be the average electron; that is, an electron with a velocity randomly selected from a Maxwellian with temperature T_e. In this manner, the electron distribution, in the absence of other collisions, will relax to a Maxwellian.

When available, the total excitation cross section of the atom was used to compute the rate of excitation of the lumped excited state M^*. The sum of the 2^1P and 3^1P excitation cross sections was used for helium (References 9, 10). The superelastic cross section was calculated from the excitation cross section by detailed balance. Cross sections for ionization of the ground state atoms for electron energy $\leq$ 1000 eV were obtained from Rapp and Englander-Golden (Reference 11). The fraction of the ground state ionization cross section attributable to double ionization was obtained from Stephens et al. for helium (Reference 12). The semi-empirical cross sections of Vriens were used for ionization of the excited state (Reference 13). Cross sections used for these calculations for helium appear in Figure 7-5.

Each cross section was assigned a degree of anisotropy with respect to the angular distribution of the scattered electron. The electron was assumed to scatter isotropically in the azimuthal direction. That is, the azimuthal scattering angle is $\phi = r \cdot 2\pi$, $0 < r < 1$. The probability for scattering through the polar angle θ was assumed to have the form

$$p(\theta) \propto \cos^m\left(\frac{\theta}{2}\right). \qquad [7\text{-}3]$$

When $m = 0$, the scattering is isotropic; when >> 1, the scattering is dominantly forward. A plot of $p(\theta)d\theta$ appears in Figure 7-6 for different values of m. The randomly distributed scattering angle θ_s is obtained from Equation [7-3] by normalizing the differential scattering probability to unity for scattering in the range $0 \leq \theta_s\ \pi$, and inverting the integral (Reference 14). The scattering angle is then given by

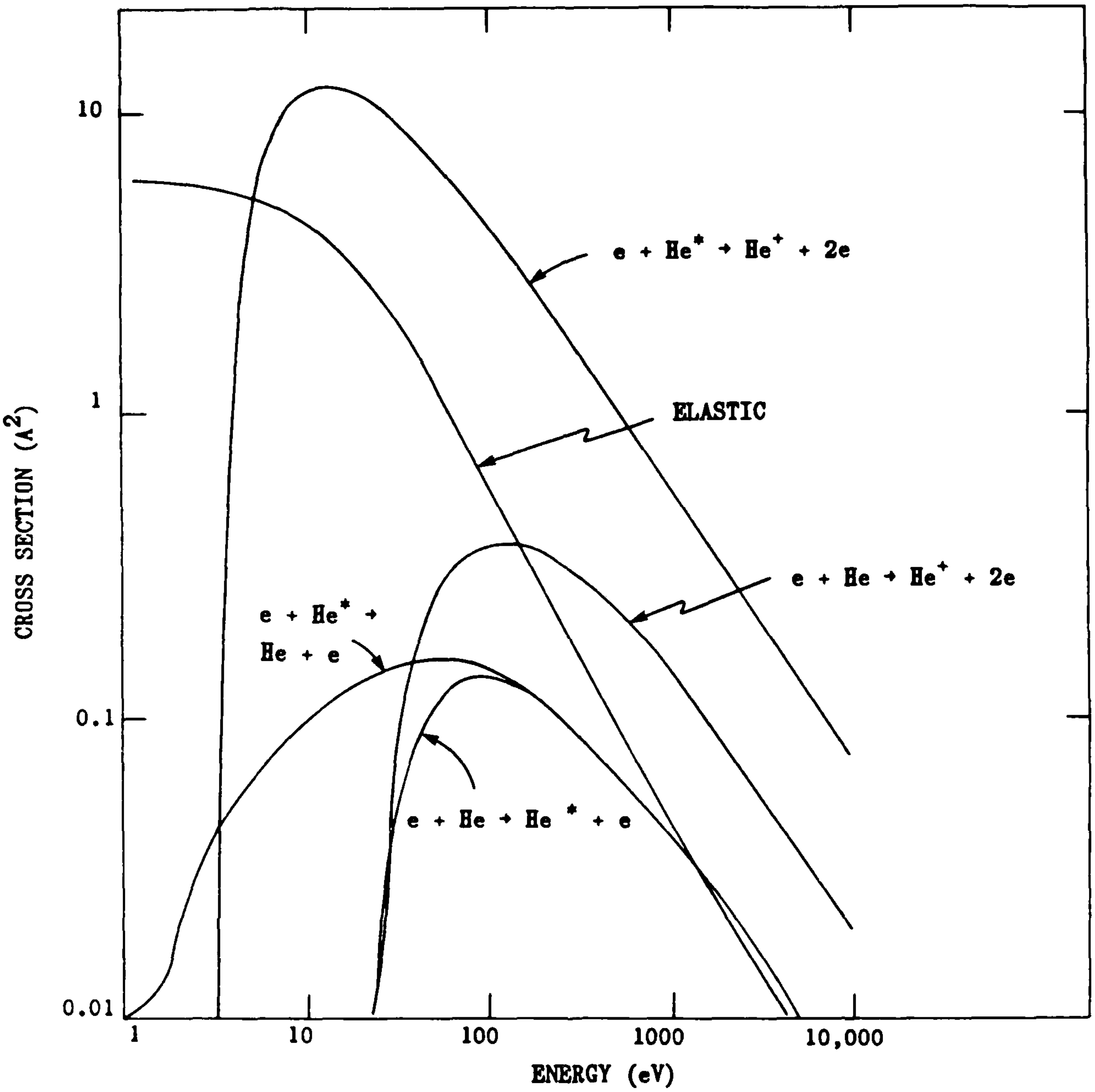

Figure 7-5. Electron Impact Cross Sections for He Used in the Simulation.

86 10978

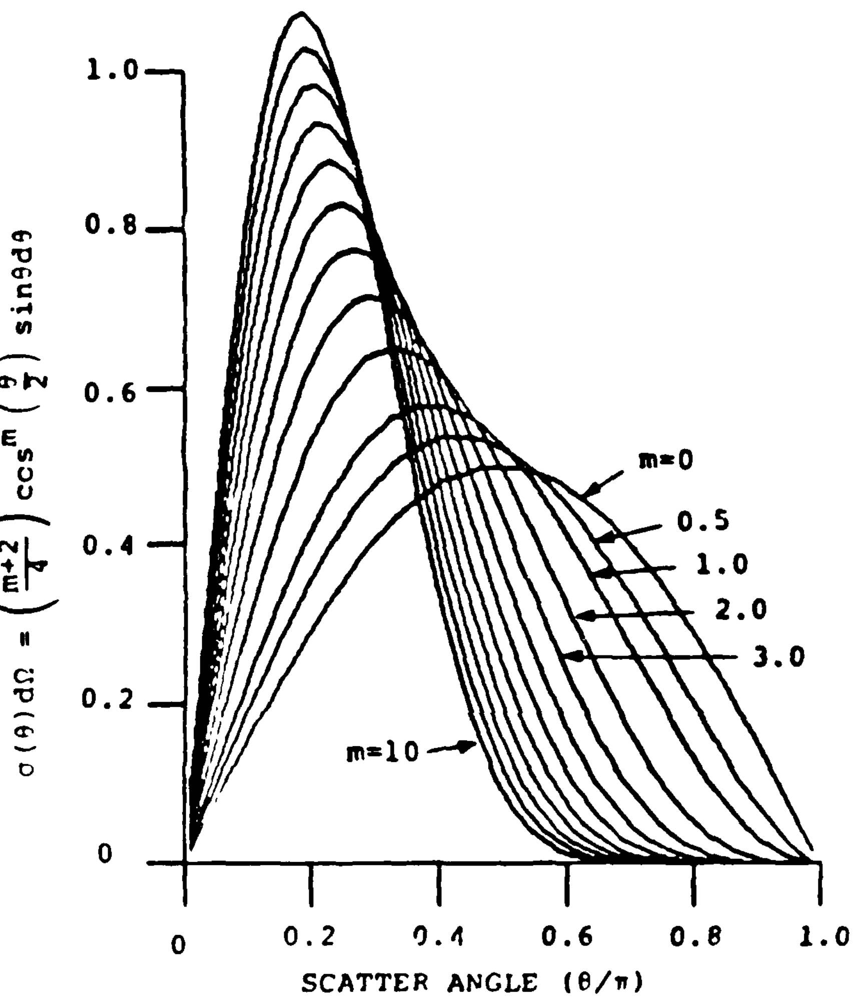

86 10955

Figure 7-6. **Fraction of Electrons Scattering into Polar Angle θ for Different Isotrophy Factors m (m = Isostropic, m>>1 Forward Scattered).**

The quantity plotted is $\sigma(\theta)d\Omega = (\frac{M+2}{4})\cos^m(\frac{\theta}{2})\sin\theta d\theta$
$= p(\theta)\sin\theta d\theta$

$$\theta_s = 2\cos^{-1}\left((1 - r)^{\frac{1}{(m + 2)}}\right) \qquad [7\text{-}4]$$

where r is a random number between 0 and 1. The value of $m \approx 3$ was typically used when information on the differential form of the cross section was not available. Otherwise, an approximation to the experimental value was used; that is, m is energy dependent. Adjustment of m was used in order to convert from "momentum transfer" cross sections to the "elastic" cross sections required for Monte Carlo simulations and to match computed swarm data to experiment. This conversion is accomplished by

$$\frac{\sigma_{MT}}{\sigma_{EL}} = 2\left(1 - \left(\frac{m + 2}{m + 4}\right)\right) \qquad [7\text{-}5]$$

To obtain the velocity components of the scattered particle, we choose a coordinate system whose z-axis is aligned with the direction of propagation of the particle, $|\vec{V}| = (0,0,V_z)$. Call this coordinate system the collision system and call the coordinate system used for the simulation the basis system. The velocity components of the scattered particle in the collision system are simply ($V'\cos\phi\sin\theta$, $V'\sin\phi\sin\theta$, $V'\cos\theta$), where V' is the speed of the particle after the collision; that is, after the energy loss (or gain) experienced by the particle is accounted for. The polar and azimuthal scattering angles θ and ϕ are defined above. To obtain the coordinates of the scattered particle in the basis system, we must first obtain the Eularian angles α and β of the initial velocity $|\vec{V}|$ in the basis system and compute the transformation matrix which yields the coordinates in the system to which one is transforming. Doing so, the velocity components of the scattered particle are

$$V'_x = V'\bullet(-\cos\alpha\bullet\sin\theta\bullet\sin\phi + \cos\beta\bullet\sin\alpha\bullet\sin\theta\bullet\cos\phi + \sin\beta\bullet\sin\alpha\bullet\cos\theta) \qquad [7\text{-}6]$$

$$V'_y = V'\bullet(\sin\alpha\bullet\sin\theta\bullet\sin\phi + \cos\beta\bullet\cos\alpha\bullet\sin\theta\bullet\cos\phi)$$

$$V'_z = V'\bullet(-\sin\beta\bullet\sin\theta\bullet\cos\phi + \cos\beta\bullet\cos\theta)$$

To verify the selection of cross sections, ionization coefficients and drift velocities were computed with the plasma simulation code for constant E/N and compared to experimental data. An example of this verification for helium appears in Figure 7-7.

7.5 HEAVY PARTICLE CONSERVATION EQUATIONS

The time duration for voltage collapse and electron avalanche in the devices of interest is $\lesssim 100$ ns. During this short time, heavy particles (ions and excited neutral atoms) do not move appreciable distances, even in the regions of intense electric fields. The mobility of ions is reduced by resonant charge exchange reactions, thereby limiting their drift velocity to moderate values. Given these conditions, the motion of the ions and excited states of the neutral gas can be described by continuum transport equations. The density of ions and excited states obtained in this fashion are coupled to the particle simulation for the electrons through the change in collision frequency of electrons for a particular process resulting from changes in the density of collision partners, through the charge density appearing in Poisson's equation, and through the rate constant for collisions appearing as the source term in the ion and excited state conservation equations.

The conservation equations solved for heavy particle type j having number density N_j, mass M_j and charge Z_j are

$$\text{Momentum:} \quad \frac{\partial\left(u_j N_j\right)}{\partial t} = -\nabla \cdot u_j u_j N_j + \frac{Z_j eE}{M_j} - N_j u_j \nu_{CE} \qquad [7\text{-}7]$$

$$\text{Continuity:} \quad \frac{\partial N_j}{\partial t} = -\nabla \cdot u_j N_j + S_j(x,t) + D_j \nabla^2 N_j - \frac{N_j}{\tau} \qquad [7\text{-}8]$$

where u_j is the velocity of particle type j, E is the local electric field, D_j is the diffusion constant, S_j is the source function for electron impact collisions exciting species j, ν_{CE} is the collision frequency for charge exchange, and τ is an effective lifetime, applicable only to excited states of neutral atoms. Since we are considering only a single mono-atomic gas, charge

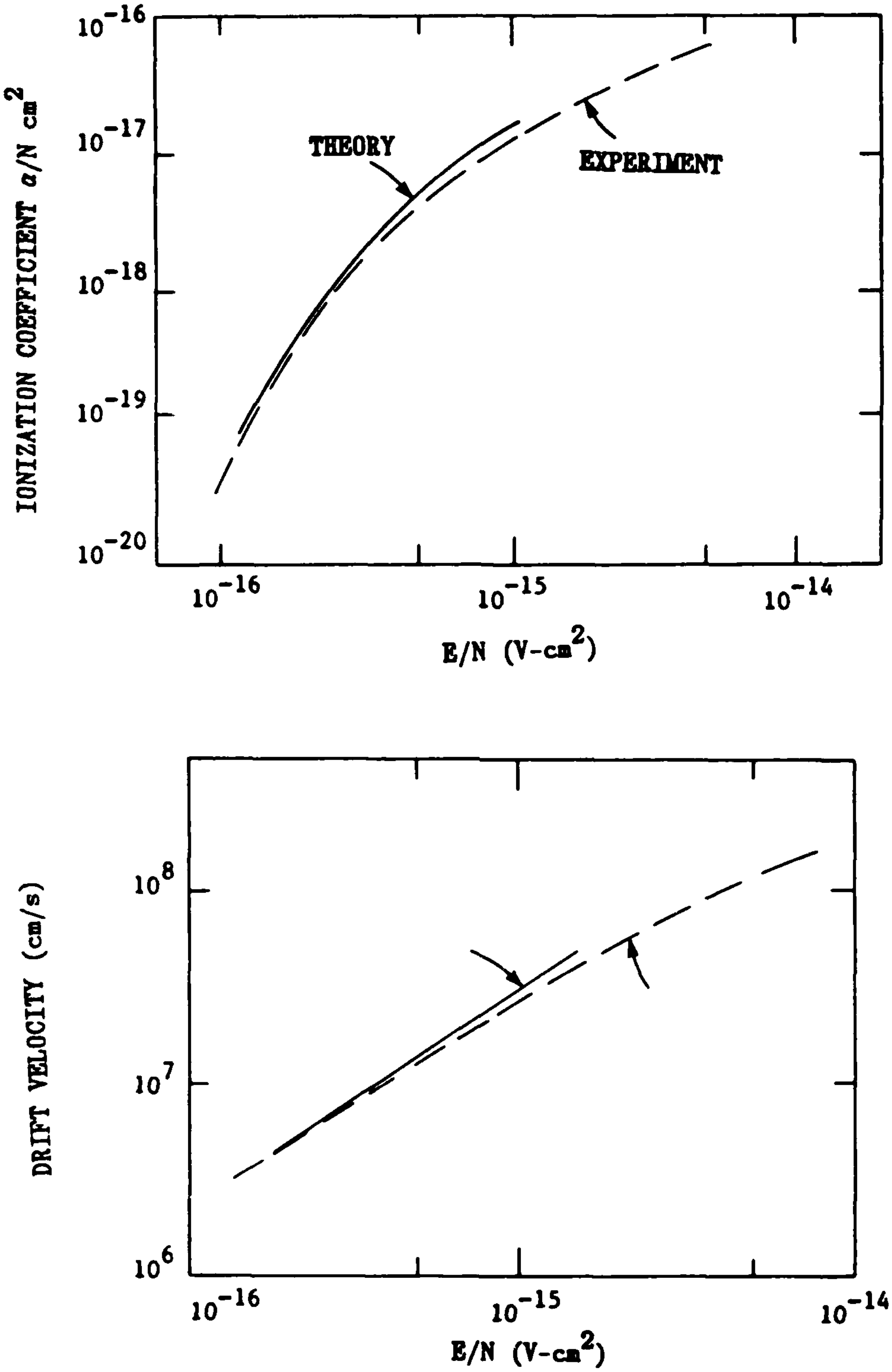

Figure 7-7. Verification of Cross Sections by Comparing Computed Ionization Coefficient and Drift Velocity to Experiment (Experiments: J. Dulton, J. Phys. Chem. Ref. Data 4, 577, 1975).

exchange is resonant and, therefore, appears only as a momentum damping mechanism and not in the source term for ions. We assumed the momentum kept by the neutral particle after a charge exchange is isotropically distributed in the bath of neutral particles. Therefore, the momentum conservation equation is not applied to neutral particles. The conservation equations for neutral excited states consist only of the source, diffusion, and lifetime terms of Eq. 7-8.

The resonant charge exchange cross section for collisions between He^+-He were obtained from the semi-emperical calculations of Duman and Smirnov (Reference 15). Diffusion constants for charged particles were derived from the mobility of the particles obtained from the compilation of Ellis, Pai, and McDaniel.[16] An effective ion temperature, required to compute the mobility, is defined as $T_{eff} = T + M_j|u_j|^2/3k$, where T is the actual gas temperature and k is Boltzmann's constant.

The source function $S_j(x,y,t)$ is the net rate of formation of species j resulting from electron collisions. This rate is obtained directly from the electron particle simulation in the following manner. The heavy particle conservation equations are updated only after time intervals Δt_H, which are long compared to $1/\nu_{max}$; typically $\Delta t_H \approx 0.5$ ns. During each interval Δt_H, the number of electron collisions are summed for each type of collision at every spatial point of interest. At the end of the interval Δt_H, the source term for electron collisions of type k with species j at location (x,y) is

$$S_{jk}\left(x,y,t+\Delta t_h\right) = \frac{\sum_i W_i}{\Delta t_H \Delta V} \qquad [7\text{-}9]$$

where the sum is for macroelectrons i with weight W_i having had collisions of type k during Δt_H in the volume element ΔV centered on (x,y). By using the sum of collisions as the source term, charge is conserved since the ion density is incremented only if an actual electron impact ionization collision has occurred. An alternative method for determining the source term is to

directly compute the rate coefficient from the instantaneously derived electron distribution function, as summed over the interval Δt_H. The latter method only conserves charge in the limit of very large numbers of macroelectrons; that is, in the continuum limit.

The boundary conditions for the momentum and continuity equations are that the ion momentum and density are zero at all solid boundaries. The flux of ions colliding with the cathode is summed over Δt_H and secondary electrons are released from the cathode consistent with the flux of ions and a specified secondary emission coefficient. Similarly, the flux of electrons colliding with, for example, the anode is summed and secondary electron emission is included by releasing electrons from that surface. For secondary electron emission by electrons, emission is modeled by having the impinging electron reflect from the surface with a lower weight than when incident. The weight of the reflecting electron is $w = w_o\delta$, where δ is the energy dependent secondary electron coefficient and w_o is the weight of the incident electron. δ may be replaced by the probability density distribution for secondary emission if it is known.

7.6 SOLUTION OF POISSON'S EQUATION

The local electric potential Φ and electric field E within the plasma is obtained by solution of Poisson's equation

$$-\nabla\cdot\epsilon E = \nabla\cdot\epsilon\nabla\Phi = \frac{\gamma\rho}{\epsilon_o} \qquad [7\text{-}10]$$

where ϵ is the local dielectric constant, ρ is the local charge density and γ is a factor discussed below. When ϵ is constant and spatially uniform, the left-hand side of Eq. 7-10 reduces to $\epsilon\nabla^2\Phi$. We use this form of Eq. 7-10 except as discussed below. The charge density is obtained directly from the simulation. The electron density is obtained by summing the local density of macroparticles during a series of "snapshots" of the particle distribution. The ion density is obtained from the solution of the ion continuity equation. During the simulation poisson's equation is solved every time interval Δt

after updating of the circuit equations. The boundary conditions for solution of Poisson's equation at the surfaces of the auxiliary grid, control grid, and anode are given by the values of the electric potential of those surfaces obtained from the circuit equations.

The method used for solution of Poisson's equation is Successive Over Relaxation (SOR) (Reference 17). The SOR method is a discrete iterative numerical technique for solving second order partial differential equations. A simple one-dimensional example will be discussed and the extension to a two-dimensional unequal mesh outlined.

Define the value of variable u at mesh point j as u_j. In discrete notation,

$$\frac{\partial^2 u_j}{\partial^2 x} = \frac{u_{j+1} - 2u_j + u_{j-1}}{\Delta x^2} \qquad [7\text{-}11]$$

where Δx is the distance between equally spaced mesh points. Using this form in Poisson's equation and solving for u_j^k, we obtain

$$u_j^k = \frac{1}{2}\left(\left(u_{j+1}^k + u_{j-1}^k\right) - \Delta x^2 S_j\right) \qquad [7\text{-}12]$$

where S_j is the effective source function (i.e. ρ/ϵ_o) and the superscript denotes the value of u for the k_{th} iteration. The current value of u_j may not satisfy Eq. 12. The correction to u_j is the difference between its current value and its value as given by Eq. 7-12.

$$\begin{aligned} u_j^{k+1} &= x_j^k + \omega\left(\frac{1}{2}\left(\left(u_{j+1}^k + u_{j-1}^k\right) - \Delta x^2 S_j\right) - x_j^k\right) \qquad [7\text{-}13] \\ &= x_j^k(1 - \omega) + \frac{\omega}{2}\left(\left(u_{j+1}^k + u_{j-1}^k\right) - \Delta x^2 S_j\right) \end{aligned}$$

where ω is the weight of the correction. The term SOR comes from the fact that $\omega > 1$; that is, we overcorrect the solution. Typically $\omega \approx 1.75$. Poisson's equation is solved by successively iterating Eq. 7-13 using the most recently updated values of u_j on the right-hand side.

The method can be generally extended to a two-dimensional rectangular mesh using either nearest neighbors (5-point kernal) or next nearest neighbors (9-point kernal) when calculating the 2-D equivalent to Eq. 7-13. We define u_{ij} as the value of u at the i^{th} grid point in the x direction having grid spacing Δx and the j^{th} grid point in the y direction having grid spacing Δy. Further, we define α and β and the relative weights of the next nearest neighbors in the x and y directions, respectively; that is, $\alpha = \beta = 0$ means that we use only a 5-point kernal while $\alpha = \beta = 1$ means we use a full 9-point kernal. The 2-D analogy to Eq. 7-13 is then

$$u_{ij}^{k+1} = x_{ij}^{k}(1 - \omega) + \frac{\omega}{2\left(\Delta x^2 + \Delta y^2\right)} \cdot \tag{7-14}$$

$$\frac{\Delta y^2}{1 + \alpha}\left(u_{i+1,j}^{k} + u_{i-1,j}^{k}\right) + \frac{\Delta x^2}{1 + \beta}\left(u_{i,j+1}^{k} + u_{i,j-1}^{k}\right) +$$

$$\frac{1}{2}\left(u_{i+1,j+1}^{k} + u_{i+1,j-1}^{k} + u_{i-1,j-1}^{k} + u_{i-1,j+1}^{k}\right) \cdot$$

$$\left(\frac{\alpha \Delta y^2}{(1 + \alpha)} + \frac{\beta \Delta x^2}{(1 + \beta)} - \Delta x^2 \Delta y^2 S_{ij}\right)$$

When practical, we attempted to use a square mesh ($\Delta x = \Delta y$). Typical values for the weighting factors were $\alpha = \beta = 0.25$. The application of Eq. 7-14 to solution of Poisson's Equation (Eq. 10) is obtained by setting $u_{ij} \equiv \Phi_{ij}$ and $S_{ij} \equiv \gamma \rho_{ij} / (\epsilon_o \epsilon_{ij})$.

In Eq. 7-10, the charge density is multiplied by the factor γ. Due to the statistical nature of the Monte-Carlo method, there are fluctuations in the charge density ρ that are unphysical. These fluctuations are reduced by numerically smoothing the computed charge density. However, further reductions in ρ, were found to be necessary. The factor $\gamma < 1$ accomplishes this reduction. Typical values of γ are 0.01-0.1. Thus, the solution obtained is not an exact solution of Poisson's equation for the electric potential, rather the solution is "pushed" in the correct direction by the sign and magnitude of the charge density.

When dielectrics are present within the thyratron, the dielectric constant in Eq. 7-10 is no longer uniform. For these conditions, ϵ must be explicitly included in Eq. 7-10, which can also be written as

$$\epsilon\nabla^2\phi + \nabla\epsilon\bullet\nabla\phi = \frac{\eta\rho}{\epsilon_o} \qquad [7\text{-}15]$$

The additional term in Eq. 7-15 (the second term on the left-hand side) is incorporated into Eq. 7-14 by adding the following expression ($u_{ij} \equiv \phi_{ij}$):

$$\phi_{ij}^{k+1} = \bullet\bullet\bullet\bullet\bullet + \frac{\omega\left(\Delta x^2 \Delta y^2\right)}{2\epsilon_{ij}\left(\Delta x^2 + \Delta y^2\right)} \bullet \left(\frac{\partial\epsilon_{ij}}{\partial x}\frac{\partial\phi_{ij}}{\partial x} + \frac{\partial\epsilon_{ij}}{\partial y}\frac{\partial\phi_{ij}}{\partial y}\right) \qquad [7\text{-}16]$$

For a 9-point numerical molecule, the partial derivative for a variable A is written as

$$\frac{\partial A_{ij}}{\partial x} = \frac{1}{2\Delta x(1 + \alpha)} \bullet \left(A_{i+1,j} - A_{i-1,j}\right) + \frac{\alpha}{2\Delta x(1 + \alpha)} \bullet \left(\left(A_{i+1,j+1} + A_{i+1,j-1}\right) - \left(A_{i-1,j+1} + A_{i-1,j-1}\right)\right) \qquad [7\text{-}17]$$

$$\frac{\partial A_{ij}}{\partial y} = \frac{1}{2\Delta y(1 + \beta)} \bullet \left(A_{i,j+1} - A_{i,j-1}\right) + \frac{\beta}{2\Delta y(1 + \beta)} \bullet \left(\left(A_{i+1,j+1} + A_{i-1,j+1}\right) - \left(A_{i+1,j-1} + A_{i-1,j-1}\right)\right)$$

The components of the local electric field at the center of the computational cells are obtained from the values of the potentials at the cell vertices from the following expressions:

$$E_{ij}^{x} = \frac{1}{2\Delta x} \bullet \left(\left(\phi_{i+1,j+1} + \phi_{i+1,j}\right) - \left(\phi_{i,j+1} + \phi_{i,j}\right)\right) \qquad [7\text{-}18]$$

$$E_{ij}^{y} = \frac{1}{2\Delta y} \bullet \left(\left(\phi_{i+1,j+1} + \phi_{i,j+1}\right) - \left(\phi_{i+1,j} + \phi_{i,j}\right)\right)$$

An example of the electric potential computed in the fashion described above for a geometry considered for the 100-kV scale-up of the prototype linear thyratron is shown in Figure 7-8. Note the penetration of potential lines from the anode through the control grid slot.

7.7 CIRCUIT MODEL

The linear thyratron, having a tetrode geometry, utilises three electrical circuits: one each to drive the auxiliary and control grids, and the energy storage circuit, which is the circuit being switched by the thyratron. Typical thyratron operation might have a dc priming current between the cathode and auxiliary grid. Upon a trigger signal, the auxiliary grid is pulsed to a few kilovolts to breakdown the control grid-auxiliary grid region and fill it with plasma. The control grid may be initially at a negative voltage to prevent pre-fire. Coincident to or at some time delay after triggering of the auxiliary grid, the control grid is also pulsed to a few kilovolts (positive), thereby breaking down the cathode-control grid gap and drawing plasma into the vicinity of the control grid slot. As the voltage collapses between the control grid and cathode, potential lines from the anode penetrate through the control grid slot, attracting electrons from out of the cathode-control grid region into the control grid-anode gap. Current flows through the control grid slot, closing the switch.

In conventional discharge models, the plasma is treated as simply a time-dependent resistor within the circuit. The resistance of the plasma is obtained by $R = L/(\sigma A)$, where σ is the conductivity of the plasma, L is the series length of the plasma, and A is its cross-sectional area. This definition of resistance is not easily applied to a thyratron because there are no unambiguous definitions of σ, L, or A. As a result, two models for the resistance of the plasma as a circuit element were used: a "conventional" resistor and a resistive current source.

The circuit model used in the simulation is shown schematically in Figure 7-9. Conventional rate equations are used to describe the flow of

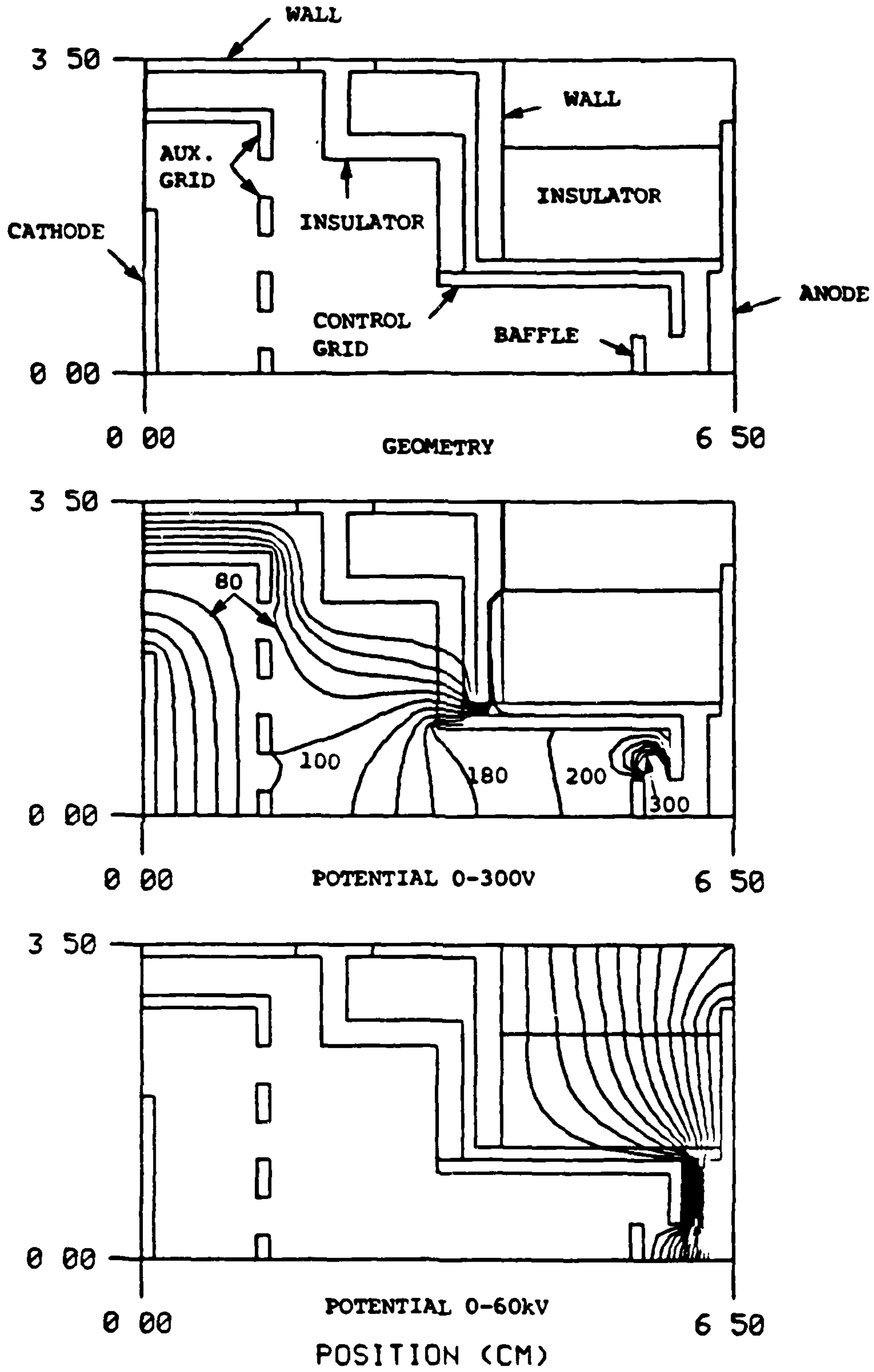

86 10984

Figure 7-8. Geometry and Electric Potential for Modified Linear Thyratron. Auxiliary grid potential = 100V, control grid potential = 200V, anode potential = 60kV.

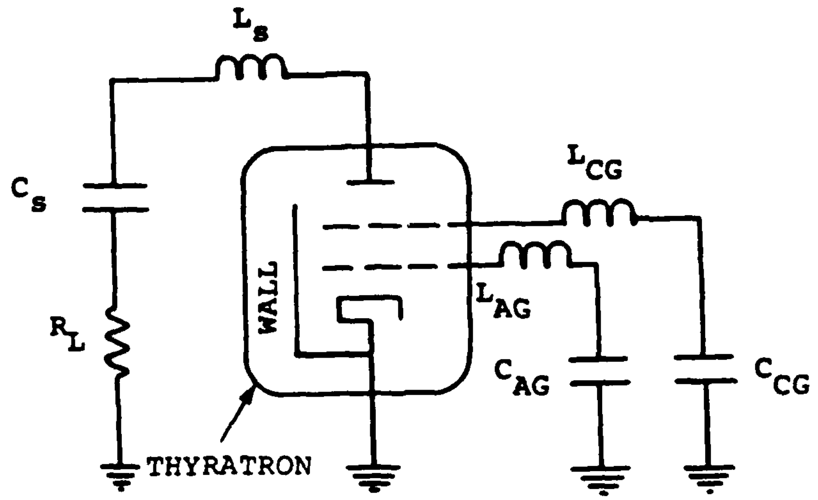

85 09456

Figure 7-9. Schematic of the Circuit Model for the Auxiliary Grid (AG), Control Grid (CG) and Switching (s) Circuits. R_L is the load (resistor).

current and change of voltage in the discrete or lumped circuit elements in each of the three external circuits. The simulation begins by having the anode at the maximum hold-off voltage. The auxiliary and control grids are either pulsed in some programmed manner or are specified to be at some maximum voltage. Macroelectrons are released from the cathode having a weight that corresponds to a current density of a few milliamps-cm^{-2}. The simulation proceeds for a time Δt. When treating the plasma as a current source, during Δt the weights of all the macroelectrons collected by a particular grid or electrode are summed. After Δt the current flowing through, for example, the control grid circuit, is $I_{CG} = (\sum eW_i)/\Delta t$, where the sum is overall macroelectrons collected by the control grid. Given that this current is now flowing through the control grid circuit, the change in voltage across each of the circuit elements can be computed. With these changes in voltage, the potential of the control grid can be computed using Kirchoff's Law. The current through each of the three discharge circuits is summed, yielding the total cathode current I_C. This value is then used to specify the weight of the macroelectrons released from the cathode during the next time interval, $W = I_C\Delta t/(eN_o)$, where N_o is the number of macroelectrons released.

When treating the plasma as a "conventional" resistor, one or more current paths from cathode to anode are specified. During the calculation for each time interval Δt, the electron density and electron collisions along the paths are summed. The resistance for current flow along the chosen paths is then computed from the integral

$$R = \int \frac{m_e \nu_c}{e^2 n_e A} \cdot dl \qquad [7\text{-}19]$$

Using this method requires at least one iteration of the calculation to confirm that the chosen current paths are indeed the most probable.

Certain "real-time" adjustments must be made in the currents computed in this fashion due to the discrete incremental changes made in voltages. One must insure that the current flowing through a particular circuit is less than

the value limited by the load resistor in that circuit and that the rate of current rise is less than the inductively limited value.

7.8 INPUT OF GEOMETRY, MATERIAL PROPERTIES, AND RESISTANCE PATHS

In order to make the plasma simulation code LINTHY2D a useful design tool, it must be "user friendly;" that is, the user must be able to easily change the input parameters. Scaler parameters are input through a NAMELIST file. The 2-D geometry of the thyratron (i.e. the location, shape, size, and identity of the various grid structures) is input through a pre-processor within the code that reads a "geometrical" input file and translates that file into the desired thyratron geometry. An example of this input file appears in Figure 7-10 and corresponds to the geometry appearing in Figure 7-8. The input is an ASCII file with rows and columns corresponding to the rows and columns of cell-centered grid points used in the simulation. The number in a particular location identifies the type of material that appears there. The following scheme is used.

Number	Material
0	Gas
1	Control Grid
2	Anode
3	Auxiliary Grid
4	Cathode
5	Non-Electron emitting Metal at Cathode Potential
6	Insulator (with specified dieletric constant)
7-9	Current Paths
A,B,C	Regions Surrounding Cathode, Auxiliary Grid, and Control Grid respectively in which sheaths may be found.

```
5555555555556666665555555555000000000000000000      CONTROL GRID=1
0000000000000066000000000055000000000000000000      ANODE=2
0000000000000066000000000055000000000000000000      AUXILIARY GRID=3
0000000000000066000000000055000000000000000000      CATHODE=4
3333333333000066000000000055000000000000000000      GROUND PLANE=5
0000000003000066000000000055000000000000000002      INSULATOR=6
0000000003000066666666666055000000000000000002      RESISTANCE PATHS=7-9
0000000003000066666666666055666666666666666662      SHEATHS=A,B,C
0000000000000000000000066055666666666666666662
0000000000000000000000066055666666666666666662 10
0000000000000000000000066055666666666666666662
0000000003000000000000066055666666666666666662
4000000003000000000000066055666666666666666662
4000000003000000000000066055666666666666666662
4007000000000000000000066055666666666666666662
4000777770000000000000066055666666666666666662
4000000007777770000000066000000000000000000002
4000000003000007770000011111111111111111110022
4000000003000000007770000000000000000000010022
4008888803000000000077777777777777777770010022 20
4000000888888888888888888888888888888887010022
4000000000000000000000000009999999999998710022
4000009999999999999999999990000000000010000022
4009999003000000000000000000000000000010000022
4000000003000000000000000000000000000010000022 25
|       |         |         |         |     |
1       10        20        30        40    46
```

Figure 7-10. Input File Used to Generate the Geometry Shown in Figure 7-8.

7.9 COMPARISON OF PLASMA SIMULATION RESULTS WITH EXPERIMENT

Validation of the plasma simulation code LINTHY2D was performed by comparing computed results with experimental data for both "macroscopic" (e.g. voltage and current waveforms) and "microscopic" (e.g. distribution of excited states) quantities.

Comparison of the results from LINTHY2D for voltage and current with experiment is shown in Figure 7-11 for the low and high inductance geometries used in the experiment. In both cases, the initial anode voltage is 8 kV and the gas pressure is 1.2 Torr He. The agreement is qualitatively good. The oscillations in the theoretical voltage in Figure 7-11b result from oscillations in the resistance of the plasma combined with having the current be inductively limited. The sudden decrease in plasma impedance that occurs upon switching results in a lowering of the E/N in the cathode-grid space. The lowering of E/N manifests a decrease in the rate of gas phase ionization, although the loss rate of electrons, does not change proportionally. Since the current is inductively limited and will not change as rapidly as does the voltage, to maintain current continuity the voltage drop across the thyratron plasma must increase in order to increase the rate of ionization. Ionization in the thyratron during commutation occurs largely between the cathode and control grid. Therefore the oscillation in voltage occurs largely between the cathode and control grid.

The computed electron density for the conditions of Figure 7-11b is shown in Figure 7-12 for a selection of times during the current pulse. As expected, the electron density increases with increasing current. The distribution of electrons is quite non-uniform. A large density of electrons occurs in the vicinity of the vertex of the control grid and near the slot and baffle. This is a region of relatively high space charge and high potential due, in part, to the penetration of potential lines through the control grid slot after the breakdown of the cathode-grid space.

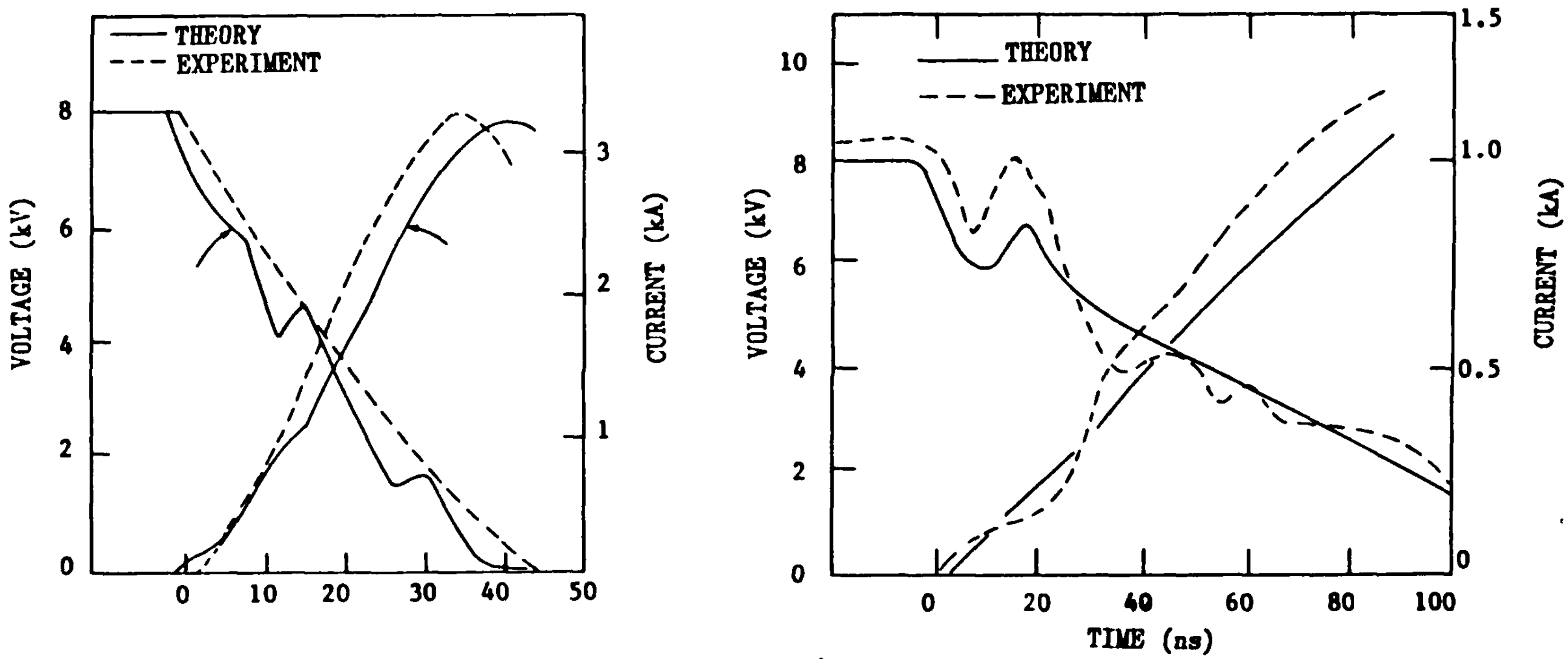

Figure 7-11. Voltage and Current Waveforms (Experiment and Theory for (a) Low and (b) High Inductance Geometries).

8610979

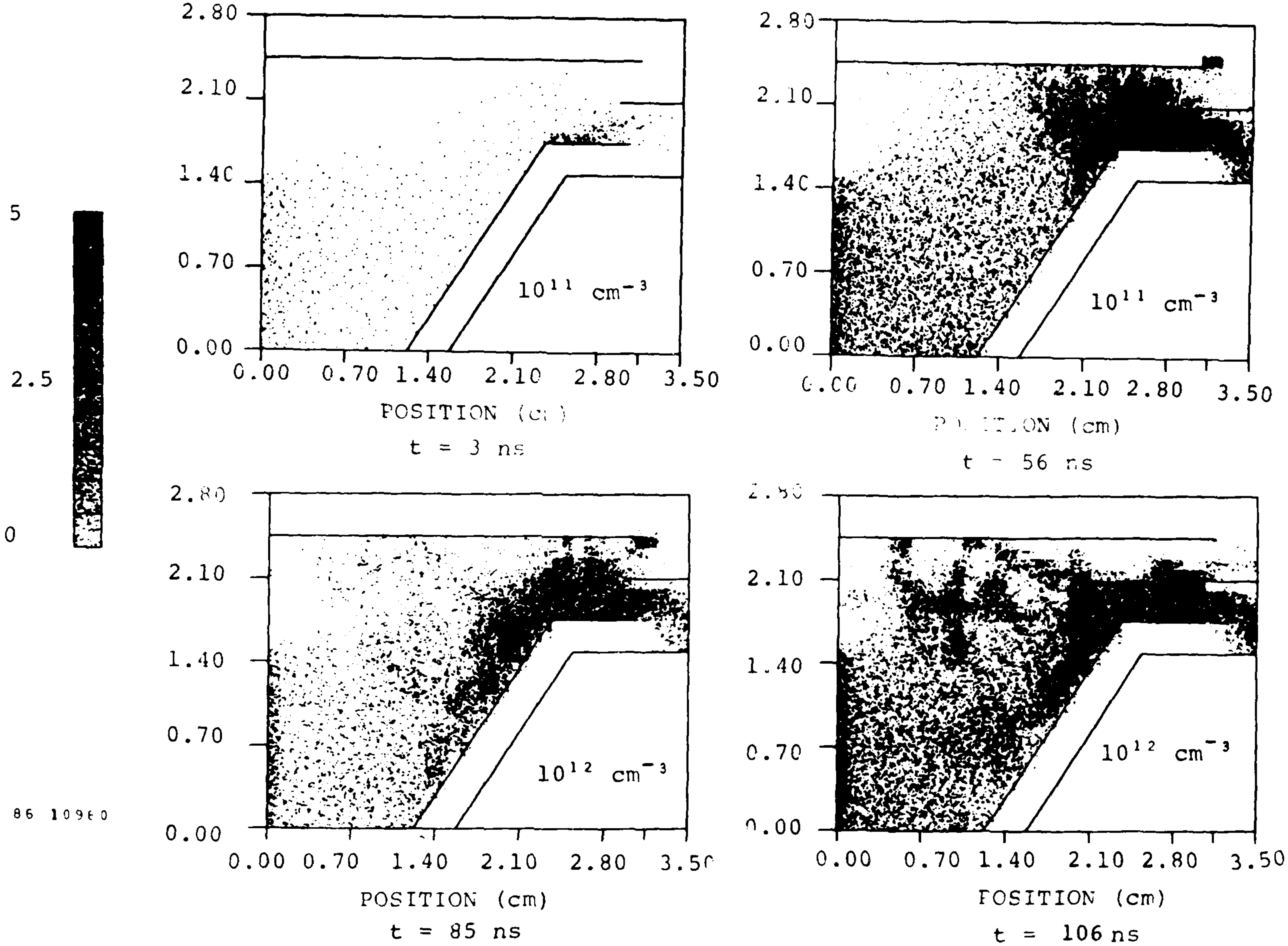

Figure 7-12. **Electron Density for the High Inductance Geometry (He, 1.2 Torr). (See Figure 7-13 for grid identification.)**

The distribution of electron energies for the case at t=100 ns is shown in Figure 7-13. The two regions where the density of electrons in the lowest energy group (0-30 eV) is high are near the cathode and in the approach to the control grid slot. The low-energy electrons near the cathode are simply thermal electrons which have only recently been emitted and which have not yet been accelerated. Note that the model assumes that electron emission from the cathode is thermal. The cathode "surface" is, therefore, the extent of the virtual cathode. The high density of thermal electrons near the control grid vertex and near the slot result from a number of causes such as emission or reflection of electrons from the control grid; a high rate of ionization resulting in a large density of low energy secondary electrons; and a high density of ions, which increase the electron collision frequency. The next group of electrons with higher energy (30-100 eV) represent those electrons accelerated away from the cathode and electrons accelerated from the thermal group near the vertex and into the control grid slot. Finally, the last two high energy groups of electrons are found only in the control grid slot and in the anode-grid gap where the electric potential is high. Note that current to the anode (i.e., electrons which traverse the control grid-anode) gap is almost entirely due to electrons attracted through the control grid slot by penetration of the anode potential through the slot. The amount of ionization that occurs in the control grid-anode slot is minimal.

A comparison between experiment and theory for the distribution of excited states in the linear thyratron is shown in Figure 7-14. The conditions are for the low inductance geometry at 60 ns. The qualitative agreement is good, showing a maximum in excited state density in the slot, near the vertex, and just above the cathode. Further discussion on the distribution of excited states appears in Section 4.

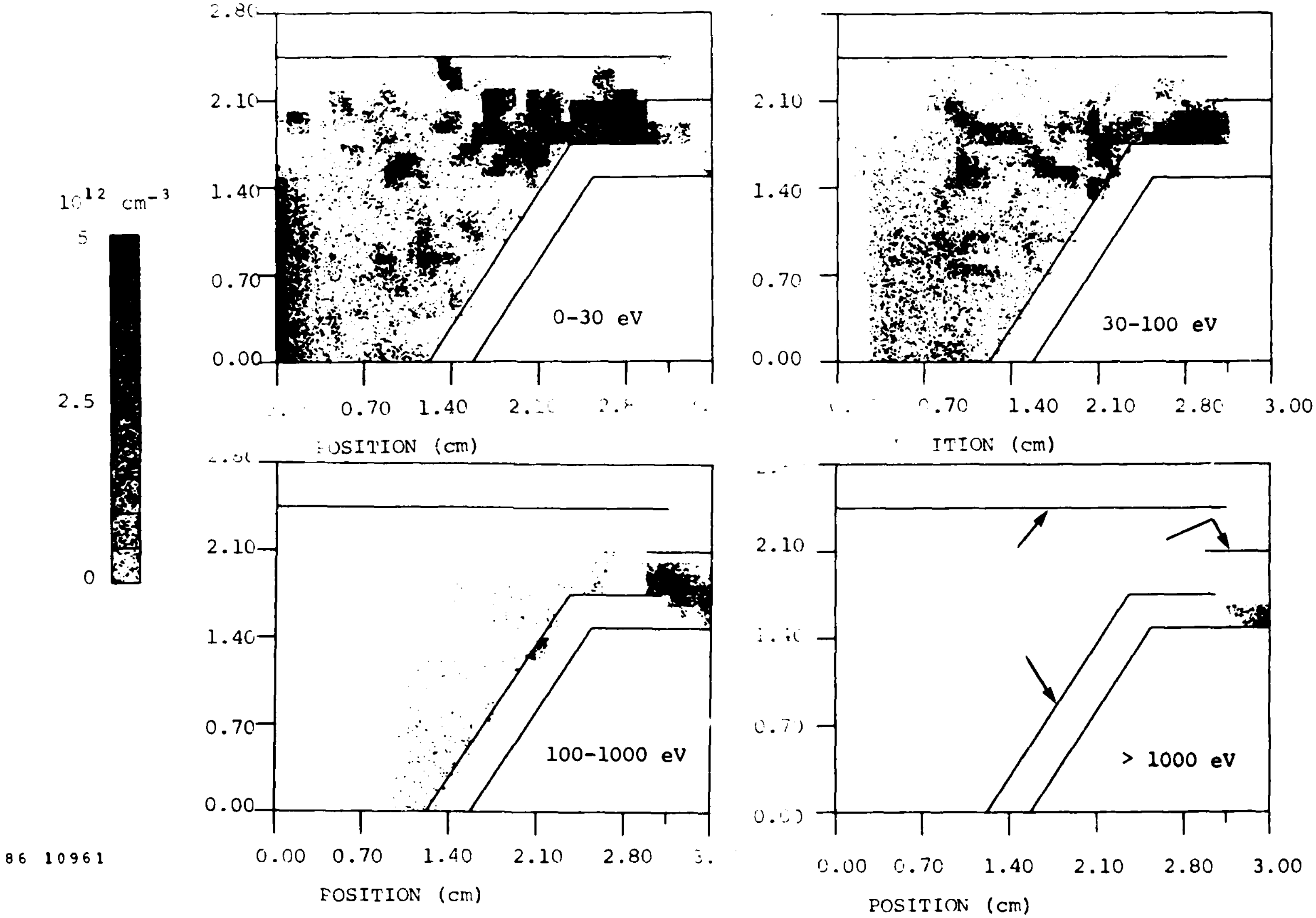

Figure 7-13. **Simulation of Electron Energy Distribution for t = 100-ns. The anode is at 2.4 kV and the control grid is at 115V (He, 1.2 Torr).**

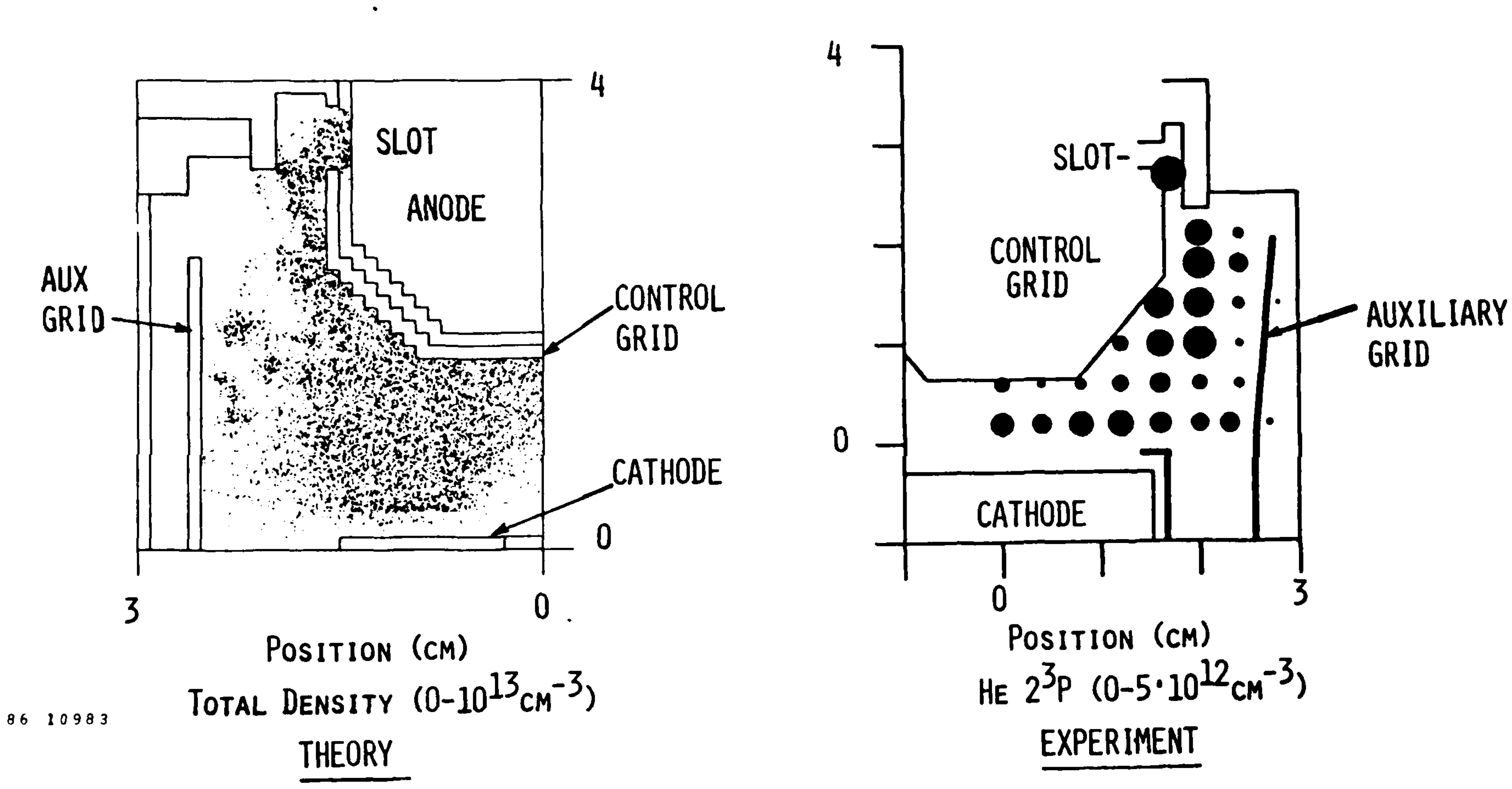

Figure 7-14. Comparison of Theory and Experiment for the Distribution of Excited He States.

7.10 THE TRADEOFF BETWEEN HOLDOFF AND SWITCHING SPEED

In this section, we will demonstrate the use of the plasma simulation code LINTHY2D for designing thyratrons and defining their operating characteristics. This demonstration will consist of using LINTHY2D in evaluating the design tradeoff between high-voltage holdoff and switching speed.

Since thyratrons operate on the near side of the Paschen curve, high-voltage holdoff is increased by decreasing the product P•D, where P is the gas pressure and D is the separation between the electrodes of interest, typically the control grid and the anode. Pre-fire can occur by either exceeding the voltage specified by P•D, by field emission at sharp edges, or by leakage current from the cathode. Field emission becomes increasingly more important as the dimension D becomes smaller because structural components near the cathode slot and baffle must become thinner, thereby reducing the radius of curvature at the edges of the baffle or slot. For sufficiently high holdoff voltages, this reduction in radius of curvature can lead to electric field enhancement and subsequent field emission of electrons.

Leakage current is a statistically occurring short between the cathode and anode, resulting from a random flux of electrons originating near the cathode. Most thyratrons operate with a hot thermionically emitting cathode, and many operate with a dc simmer current between the cathode and an auxiliary grid. In either case, there is a copious supply of electrons that must be confined to a region close to the cathode and away from the control grid slot prior to triggering. When operating without a dc simmer current the negative space charge field at the surface of the cathode is sufficient to confine the majority of emitted electrons. However, statistically there will be some small fraction of electrons energetic enough to penetrate the local space charge field at the cathode surface, or from the cathode auxiliary grid space in the case of a dc simmer current, and drift towards the control grid slot. These electrons can then be drawn to the anode through the control grid slot by fringing electric fields which penetrate through the control grid slot from

the high potential anode.

To prevent electrons from entering the control grid-anode gap, the control grid slot should be tightly baffled with a shield (having the control grid potential) placed in front of the control grid slot. The shield, or baffle, prevents anode potential from penetrating into the cathode-control grid gap. A negative bias can be applied to the control grid to achieve the same goal. Both of these remedies decrease the speed at which the thyratron can subsequently be switched. To minimise the switching time, the control grid slot should be loosely baffled to allow the anode potential to penetrate the slot, and the control grid should be at the maximum possible voltage (that is, at a voltage just below the cathode-control grid gap breakdown voltage). Both of these criteria are inconsistent with high-voltage holdoff. Clearly, a tradeoff must be performed between voltage holdoff (preventing pre-fire) and switching speed.

To examine the tradeoff between holdoff and switching speed, LINTHY2D was used in two modes. In the first mode, we calculated the value of the negative (dc) control grid bias necessary to insure that there is no leakage current to the anode. The value was examined as a function of the degree of baffling of the control grid slot and the anode voltage. The leakage current was computed by "releasing" electrons from the cathode and following their trajectories. The control grid bias for which none of the electrons released from the cathode are collected by the anode is defined as the bias for which pre-fire is prevented. In the second mode, LINTHY2D was used to fully simulate the electron avalanche during breakdown of the cathode-control grid slot. A switching time was calculated by determining the time required for the current to obtain the specified value ΔI.

The thyratron geometry for which this tradeoff was performed is shown in Figure 7-15. The thyratron was operated with 250 μm of helium, uses the linear geometry 10 cm in depth, and is symmetric across the lower plane of the figure. The model thyratron is a tetrode having a screen auxiliary grid. The single control grid slot is shielded by the baffle as shown. The variable for

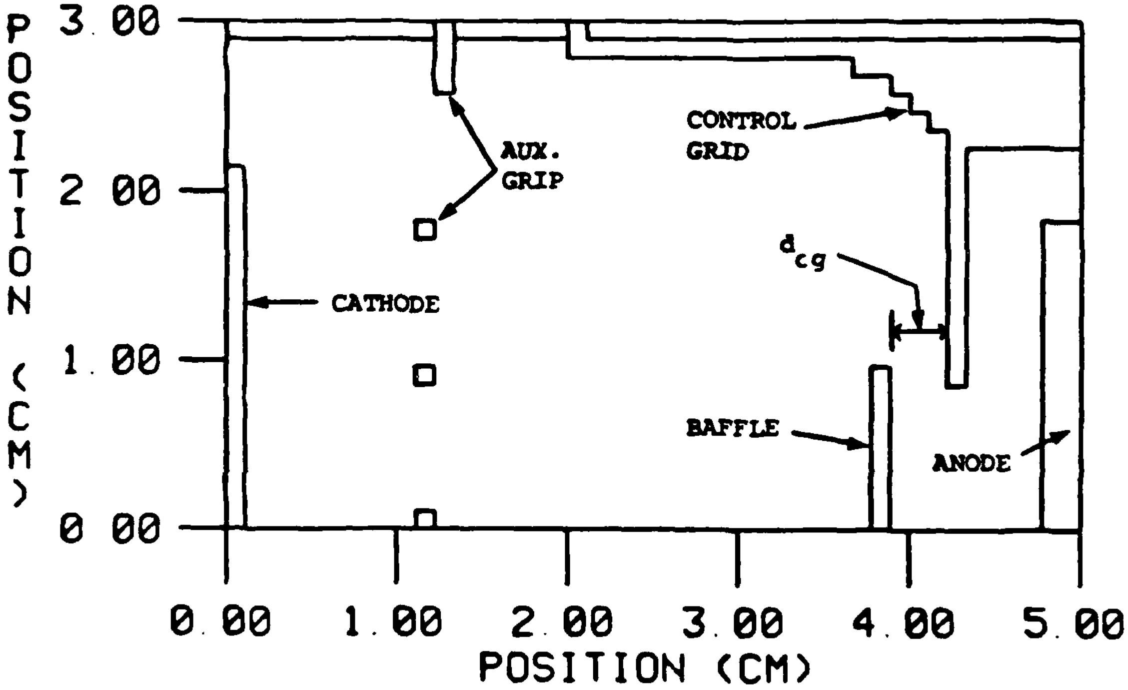

85 09930

Figure 7-15. Geometry for Model Thyratron Used in Holdoff Study.

this exercise is the separation between the control grid and the baffle, defined as the gap size d_{cg}. The smaller this dimension, the more tightly the control grid slot is baffled.

The computed leakage current is the fraction of the electrons released at the cathode that are collected by the anode. These currents are plotted in Figure 7-16 as a function of negative dc control grid bias (V_{dc}) for three values of d_{cg}. The anode voltage is 100 kV. The fringing electric potential penetrating the control grid slot for a selection of d_{cg} and V_{dc} is shown in Figure 7-17. Plots of the probability density for electrons escaping from the cathode for V_{dc} = -150 V and three values of gap size d_{cg} appear in Figure 7-18. Clearly, the more tightly baffled geometry requires a smaller value of V_{dc} to insure there is no leakage current to the anode, a consequence of the smaller penetrating electric potential through the slot from the anode with the tight baffle. In the absence of a dc bias, the fringing fields from the anode attract a significant fraction of the electrons even under tightly baffled conditions. The value of V_{dc} required to insure no leakage current as a function of gap size and anode voltage is shown in Figure 7-19. At high holdoff voltages and as the gap size increases, a larger than linear increase in V_{dc} is required to insure there is no leakage current.

The trade-off between gap size and switching speed is next discussed. We define the absolute switching speed, τ_a, as the time after pulsing the control grid at which a specified current is reached. Since the rate of current rise may be inductively limited, τ_a contains a contribution from both the holdoff voltage and the geometrical inductance. To normalize these contributions, a reduced dimensionless switching speed τ_r is defined as

$$\tau_r = \frac{\tau_a}{\left[\Delta I / \left(\frac{dI}{dt}\right)_L\right]}, \quad \left(\frac{dI}{dt}\right)_L = \frac{V_H}{L_g} \qquad [7\text{-}20]$$

where ΔI is the specified current denoting switching, V_H is the holdoff voltage, L_g is the geometrical inductance, and $(dI/dt)_L$ is the inductively

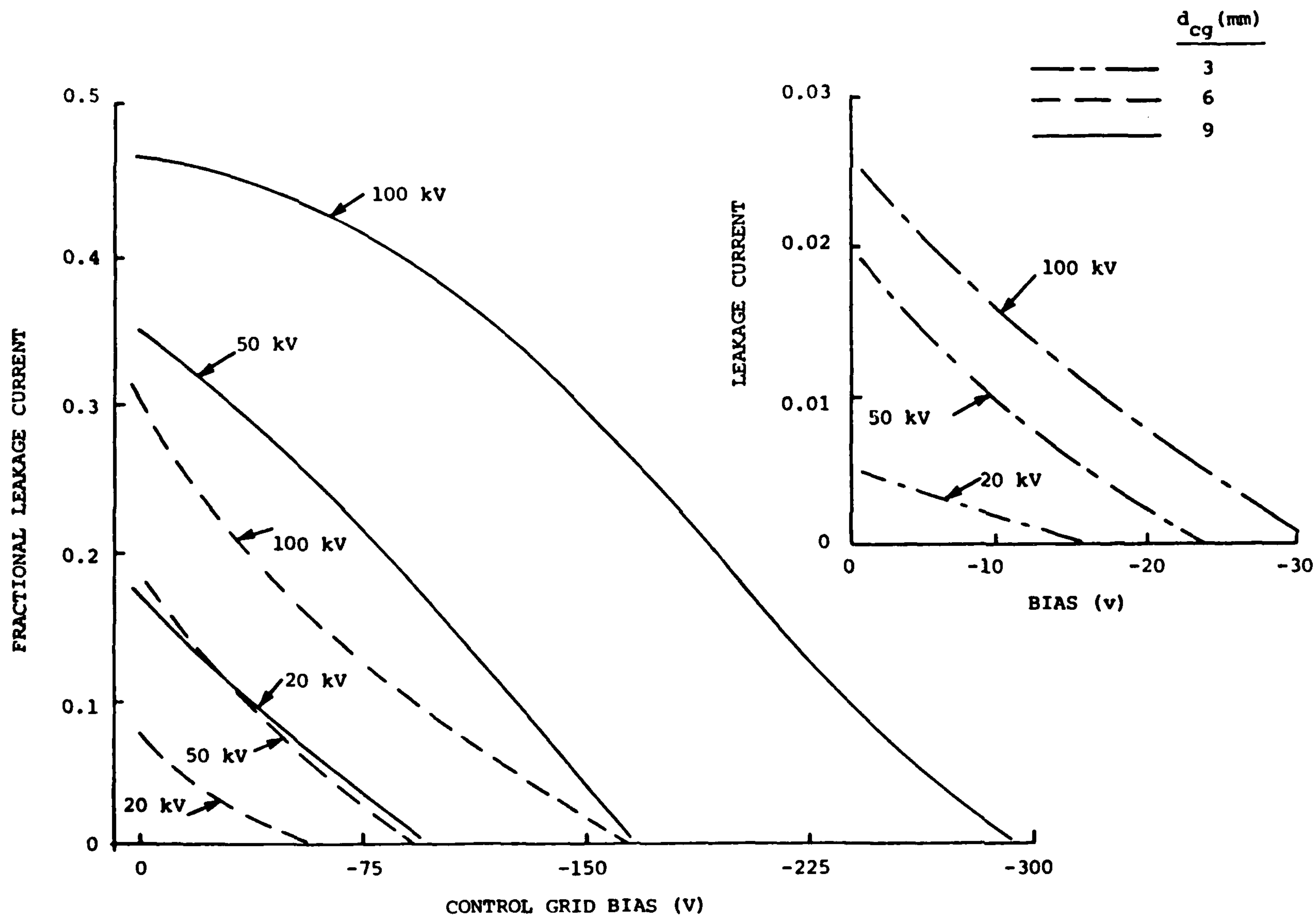

85 09997

Figure 7-16. Fractional Leakage Current for Geometry in Fig. 7-14 for Various Anode Voltages and Gap Sizes (d_{cg} is Noted in Legend in Upper Right).

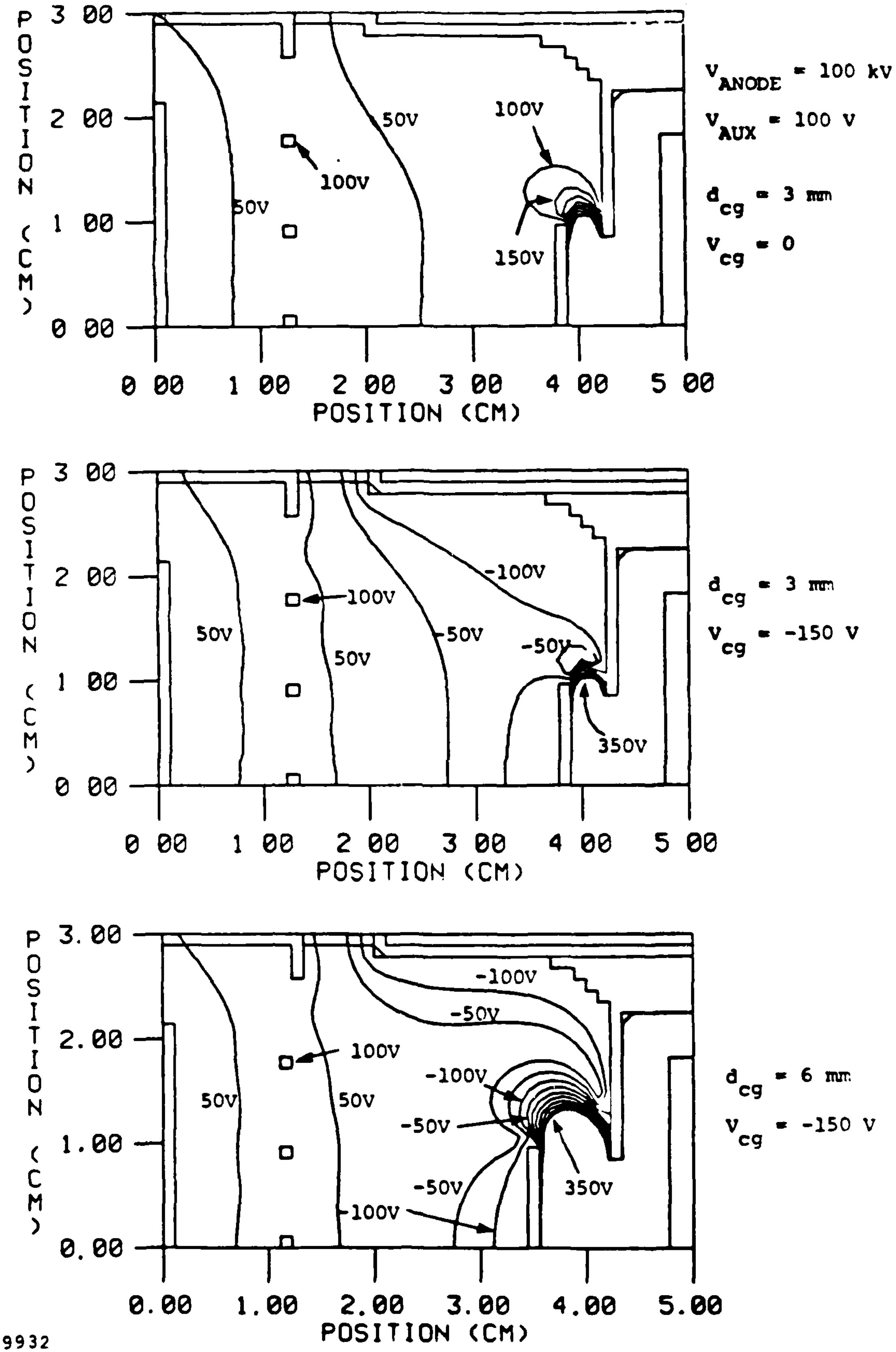

85 09932

Figure 7-17. Fringing Electric Potentials for a Selection of Gap Sizes and Control Grid Bias.

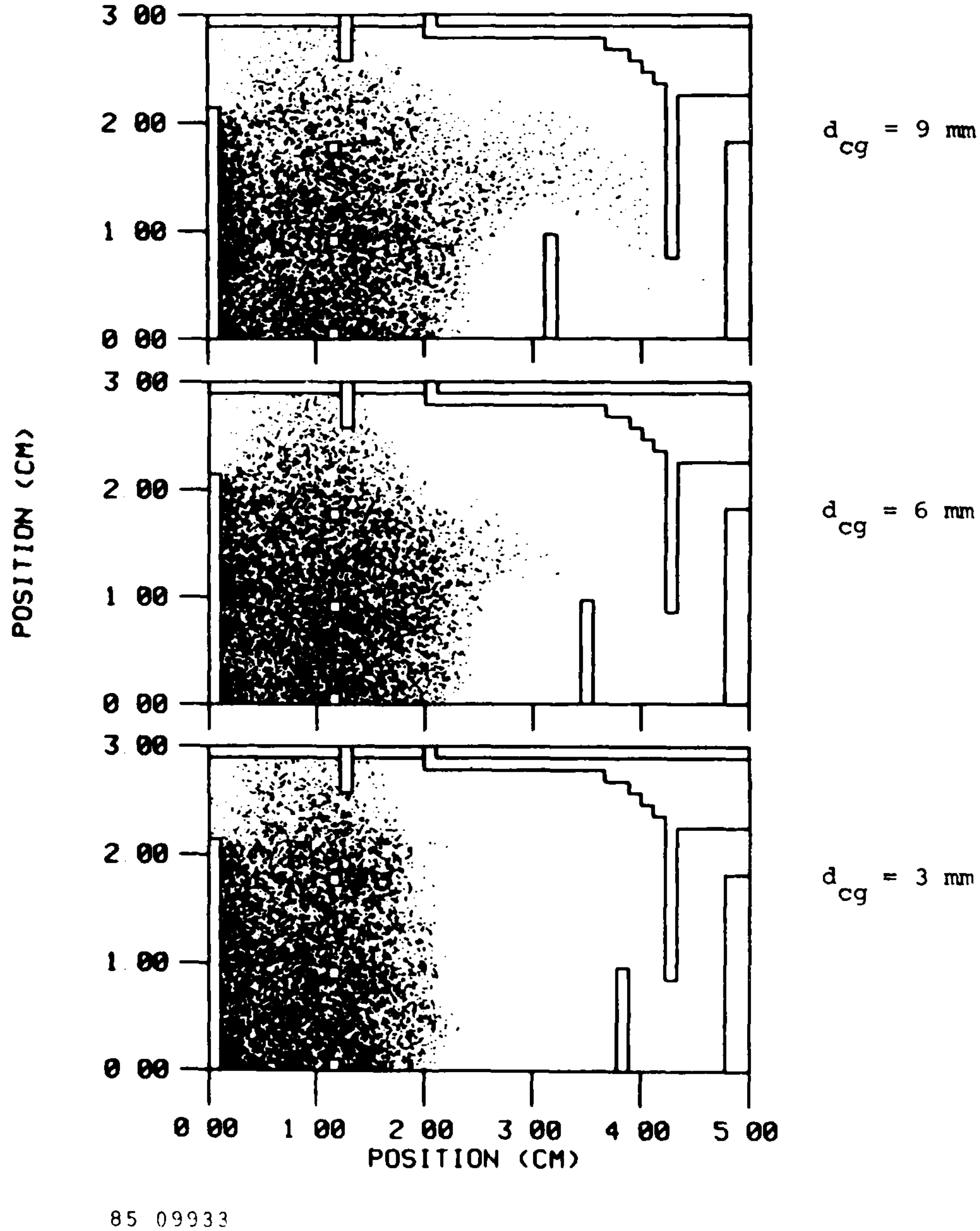

Figure 7-18. Probability Density for Elctrons Escaping from the Cathode for V_{ANODE} = 100 kV. The control gird bias is -150V.

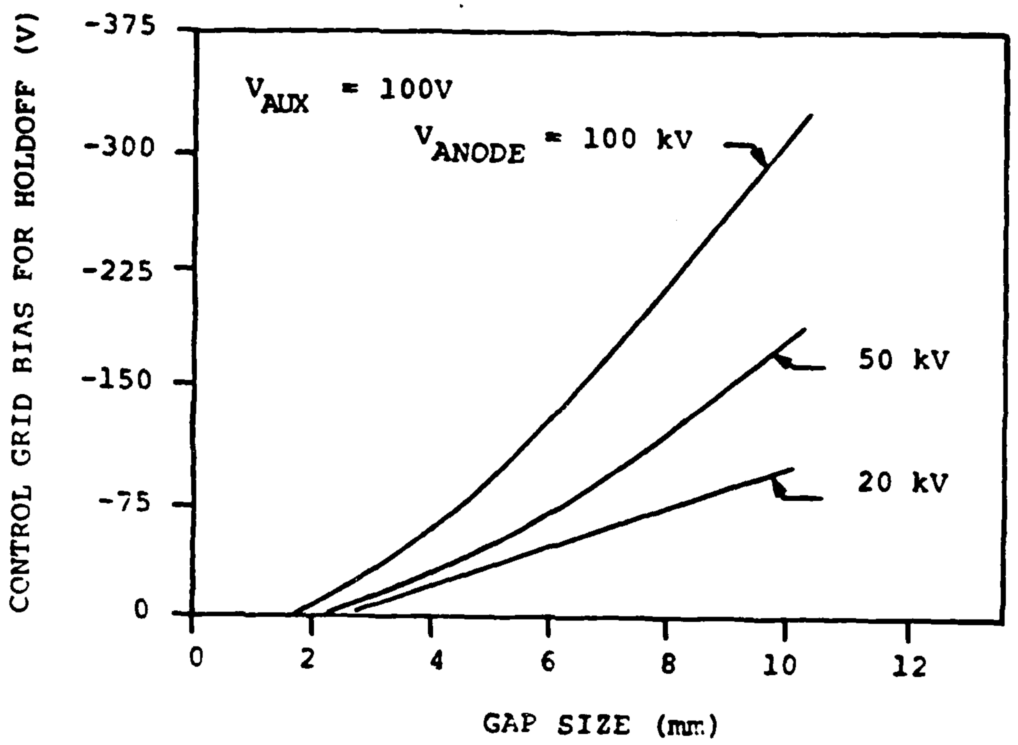

85 09915

Figure 7-19. Control Grid Bias Required for no Leakage Current for the Geometry of Figure A (He, 250 μm).

limited rate of current rise. τ_r is the factor by which the inductively limited rate of current rise must be multiplied to yield the actual switching time. For the discussion below, $\Delta I = 2$ kA and $L_g = 75$ nH.

Absolute switching time, τ_a for $V_H = 65$ kV is plotted in Figure 7-20 as a function of gap size. The switching time decreases with increasing gap size. The actual points computed with LINTHY2D are plotted in this figure and show the statistical scatter of the method. The results shown in other figures are hand-drawn smoothed lines through a similar distribution of individual simulation points. The dimensionless switching speed τ_r for a selection of gap sizes as a function of holdoff voltage V_H is shown in Figure 7-21. For these conditions, the relative change in switching speed between gaps of different sizes is approximately constant. τ_r decreases with decreasing V_H; however, for sufficiently small V_H, τ_r reaches a constant value. This implies that the non-inductive component to the switching speed (e.g. avalanche and plasma spreading time) is relatively constant for $V_H < 40$ kV. The decrease in τ_r is largely a function of the increase in the inductive rate of current rise as V_H decreases. For sufficiently low V_H (< 40 kV), the rate of avalanche and plasma spreading also decreases as V_H decreases, and does so in such a manner as to keep τ_r nearly constant.

7.11 SCALE UP OF THE LINEAR THYRATRON TO 100 kV

The prototype linear thyratron was modified to operate at $\leq$100 kV. These modifications and the performance of the modified LT are discussed in Section 8. LINTHY2D was used to investigate the operating characteristics of the modified linear thyratron. For the prototype LT to operate at 100 kV, the control grid-anode gap must be isolated within an insulated region in order to reduce the possibility of insulator flashover and field emission. The circumstances of the existing LT geometry require that the feedthroughs to the control grid remain in their present location. The result is that the control grid slot is immersed in a region of near equipotential. An alternate, but mechanically more complex geometry requires additional modification of the control grid to increase the electric field in the approach to the control

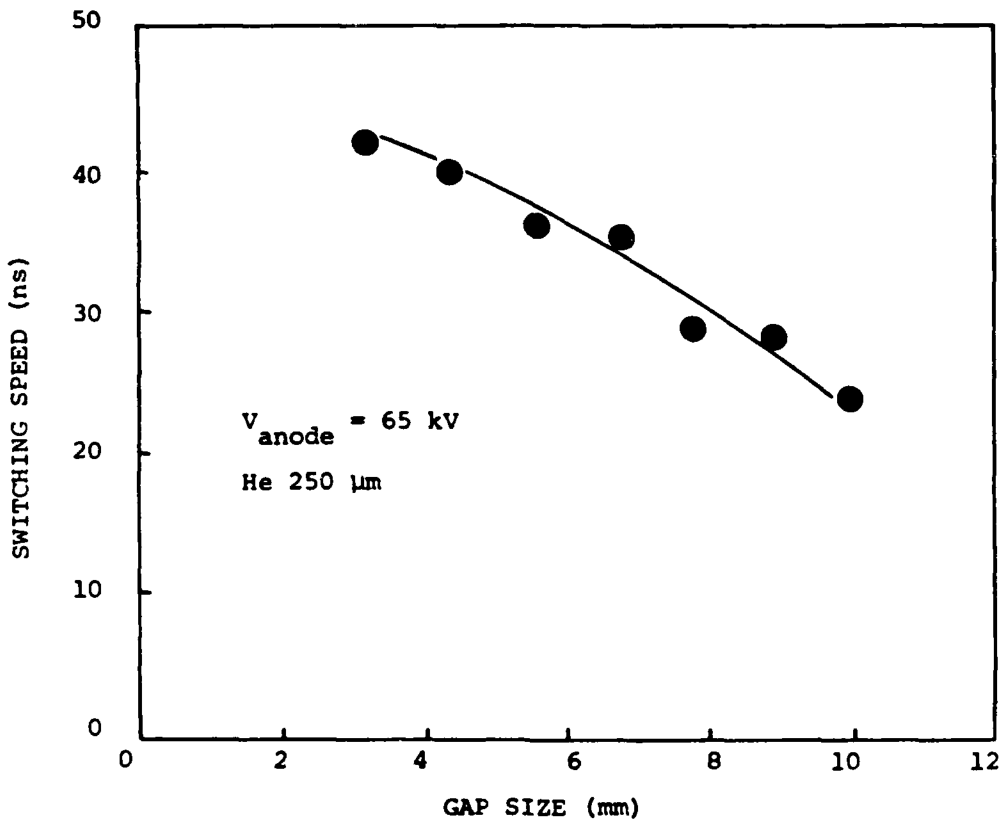

85 09996

Figure 7-20. Absolute Switching Speed (ΔI = 2 kA)

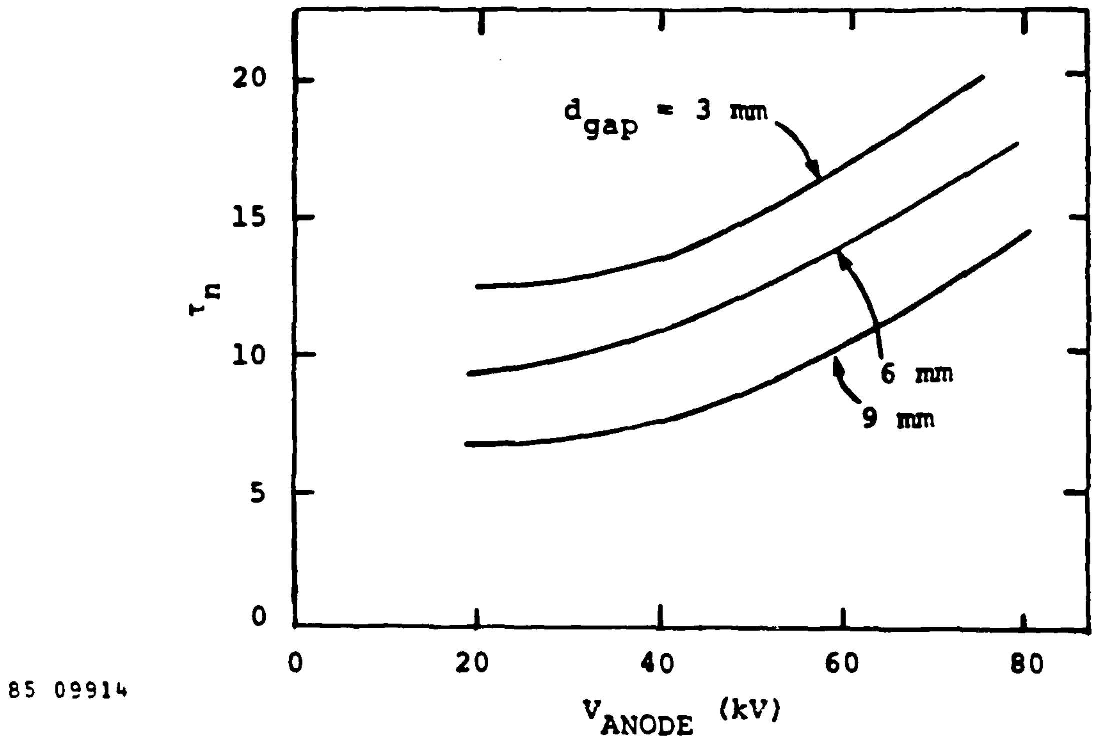

Figure 7-21. Normalized Switching Time as a Function of Gap Size and Anode Voltage. Control grid is pulsed to 200V.

grid slots. These two geometries are called LT-1 and LT-2 respectively (see Figure 7-22). In geometry LT-2, the supporting structure for the control grid, a conductor in LT-1, is replaced by an insulator. The auxiliary grid is widened to include a mesh covering the cathode. By virture of these modifications, the current drawn by the control grid is channeled towards the control grid slot instead of being preferentially collected by the supporting structure.

Performance of the modified linear thyratron using the two geometries discussed above was simulated using LINTHY2D. Results from those simulations are shown in Figure 7-23 where plots of the electron density appear as a function of position and time. The design modification in LT-2 succeeds in channeling current in the desired direction. As a result, the switching speed is increased as shown in the simulated voltage and current characteristics appearing in Figure 7-24. Since the control grid area is reduced and the cathode-control grid distance is effectively increased in LT-2, the control grid voltage is also higher. This results in a hotter plasma, as shown by the electron distribution functions in Figure 7-25. The hotter plasma contributes to a faster switching speed by increasing the rate of electron avalanche. The jitter is also lower with LT-2. A comparison between experiment and theory for current in the LT-1 geometry appears in Figure 7-26.

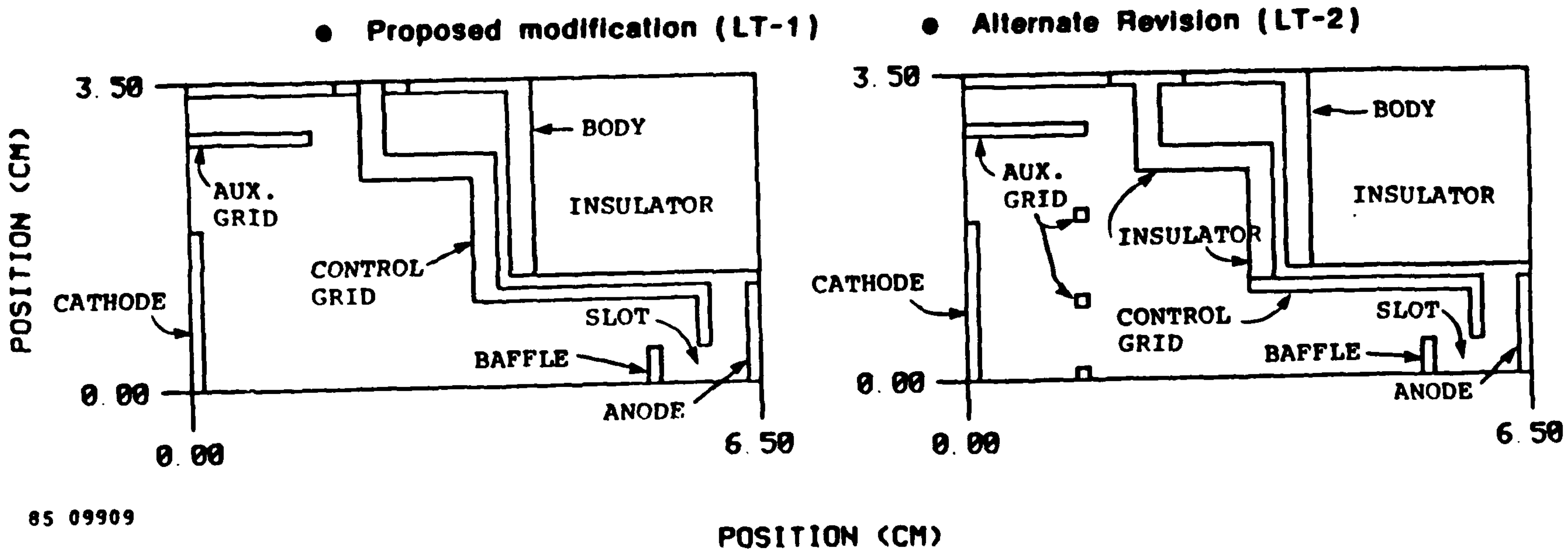

Figure 7-22. Geometries LT-1 and LT-2 as Simulated in LINTHY2D.

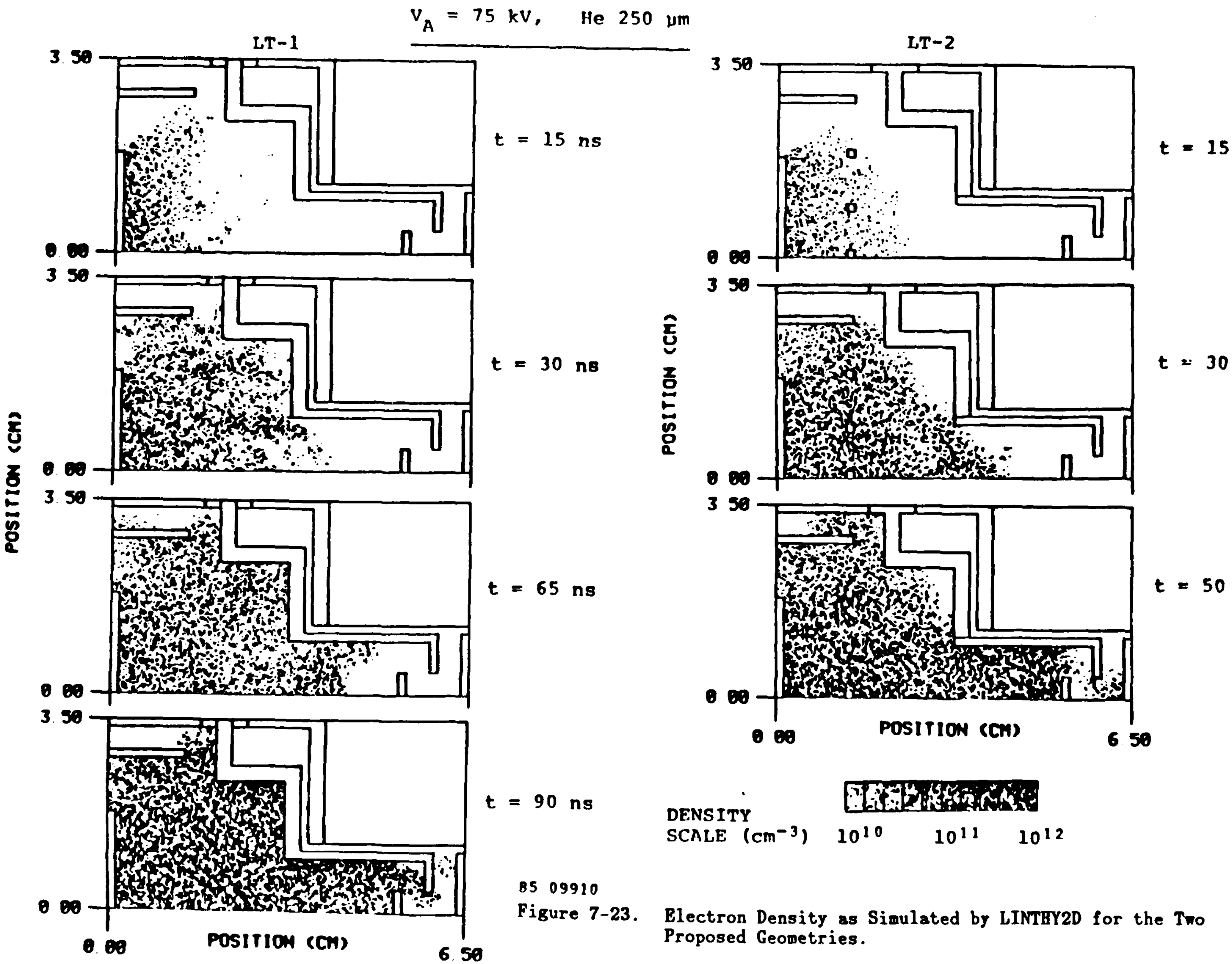

85 09910

Figure 7-23. Electron Density as Simulated by LINTHY2D for the Two Proposed Geometries.

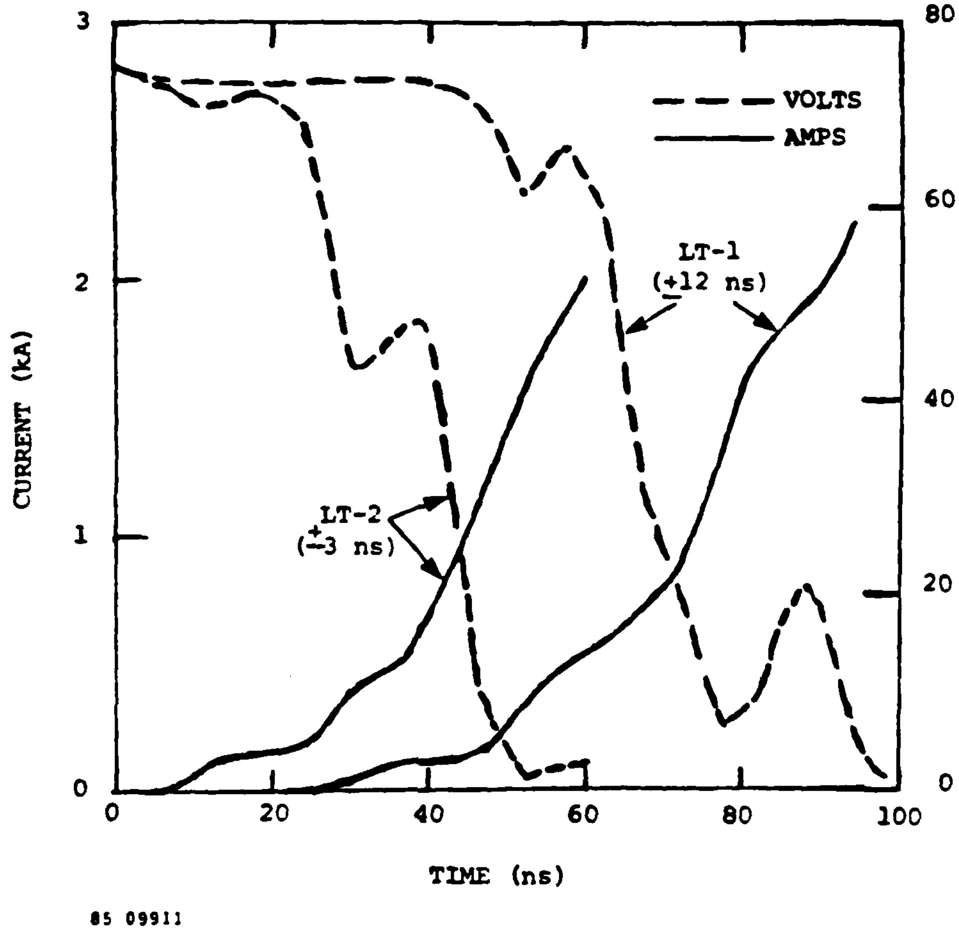

Figure 7-24. Predicted Current and Voltage Characteristics and Jitter for the Two Proposed Geometries LT-1 and LT-2.

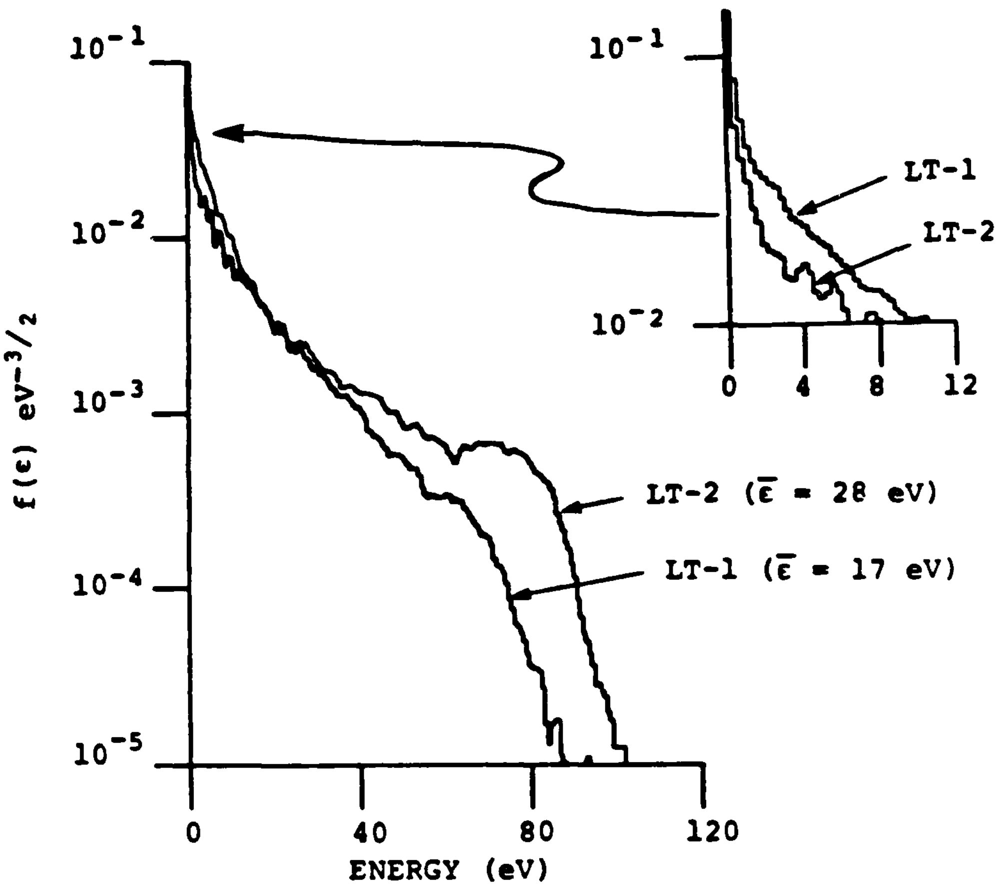

85 09912

Figure 7-25. Electron Distribution Functions at t = 15 ns for the Geometries LT-1 and LT-2. The geometries LT-2 results in a hotter plasma due primarily to a higher control grid voltage.

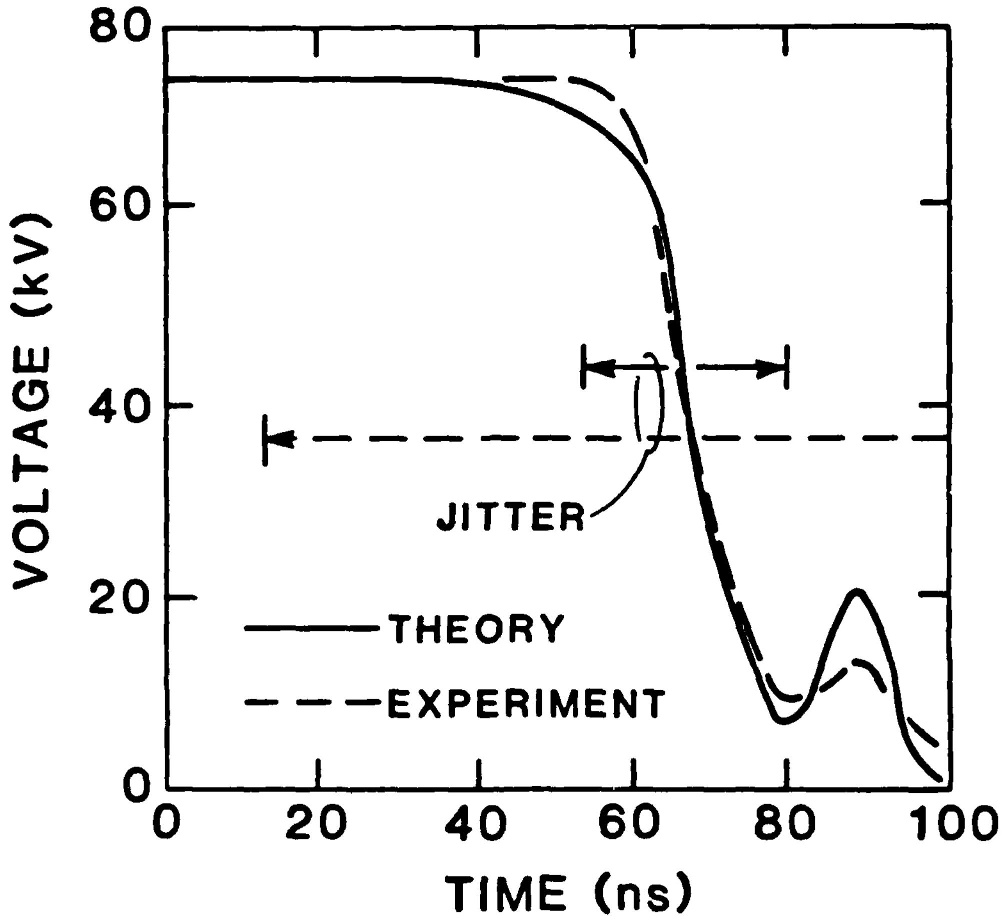

86 10825

Figure 7-26. Comparison of Theory and Experiment for Voltage Waveform with Geometry LT-1. (Charging voltage 75 kV, 250 μm He.)

REFERENCES

1. P.J. Roach, S. Steinberg, H.J. Happ, and W.M. Moeny, "3-D Electric Field Solutions in Boundary-Fitted Coordinates," Proceedings of 4th IEEE Pulsed Power Conference, T.H. Martin and M.F. Rose, eds., (Texas Tech Press, Lubbock, Texas, 1983), pgs. 465-466.
2. B.M. Penetrante and E.E. Kunhardt, J. Appl. Phys. 59, 3383 (1986).
3. J.A. Kunc, and M.A. Gundersen, IEEE Trans. Plasma Sci. PS-10, 315 (1982).
4. L.E. Kline and J.G. Siambis, Phys. Rev. A 5, 794 (1972).
5. C.K. Birdsall and A.B. Langdon, Plasma Physics via Computer Simulation, (McGraw Hill, New York, 1985), pgs. 19-22.
6. S.L. Lin and J.N. Bardsley, J. Chem. Phys. 66, 435 (1977).
7. M. Hayashi, "Recommended Values of Transport Cross Sections for Elastic and Total Collision Cross Section for Electrons in Atomic and Molecular Gases," Nagoya Institute of Technology, IPPJ-AM-19, 1981.
8. M. Mitchner and C.H. Kruger, Partially Ionized Gases (Wiley, New York, 1973), pgs. 54-62.
9. W.C. Fon, K.A. Barrington, P.G. Burke and A.E. Kingston, J. Phys. B. 14, 2921 (1981).
10. F.G. Donaldson, M.A. Hender, and J.W. McConkey, J. Phys. B. 5, 1482 (1972).
11. D. Rapp and P. Englander-Golden, J. Chem. Phys. 43, 1464 (1965).
12. K. Stephens, H. Helm, T.D. Mark, J. Chem. Phys. 73, 3763 (1980).
13. L. Vriens, Phys. Lett. 8, 260 (1964).
14. G.L. Graglia, Physica 92C, 91 (1977).
15. E.L. Duman and B.L. Smirnov, High Temperature 12, 431 (1974).
16. H.W. Ellis, R.Y. Pai, and E.W. McDaniel, At. Nuc. Data Tables 17, 177-210 (1976).
17. W.F. Ames, Numerical Methods for Partial Differential Equations (Academic, New York, 1977), pgs. 119-125.

Section 8
HIGH-VOLTAGE OPERATION WITH THE MODIFIED LINEAR THYRATRON

8.1 INTRODUCTION

The purpose of the experimental, theoretical, and design studies of the linear thyratron described in previous sections has been to increase our understanding of thyratron operation in order to improve its performance. In this section, we describe modifications made to the linear thyratron to maximize its high-voltage holdoff, and we describe its high-voltage performance. The goals of these modifications were to operate the linear thyratron at ≤100 kV, and in a burst mode at 200 Hz. This goal was essentially met by demonstrating performance at ≤95 kV, with bursts of 5 pulses at 200 Hz, and by demonstrating recovery with a pulse separation of ≥3.5 ms.

The modifications and performance of the linear thyratron described in this section should not be considered the optimum performance specifications for the linear concept. The performance specifications obtained with the modified linear thyratron were limited by design constraints resulting from the original configuration of the thyratron. As discussed in previous sections, there exist alternate geometries for which linear thyratron performance could exceed that described below.

8.2 HIGH-VOLTAGE PULSER

A 100 kV power supply was designed and built to pulse charge the pulse forming line (PFN) that was switched by the modified linear thyratron. An electrical schematic of the 100-kV power supply and schematics of the voltage and current waveforms at various points in the circuit appear in Figure 8-1. A capacitor bank (C1) is dc charged to a maximum of 10 kV. This capacitor is charged in a few seconds and therefore must be sized large enough to supply current for many successive charges of the PFN during burst mode operation. Upon triggering an F-195 thyratron,

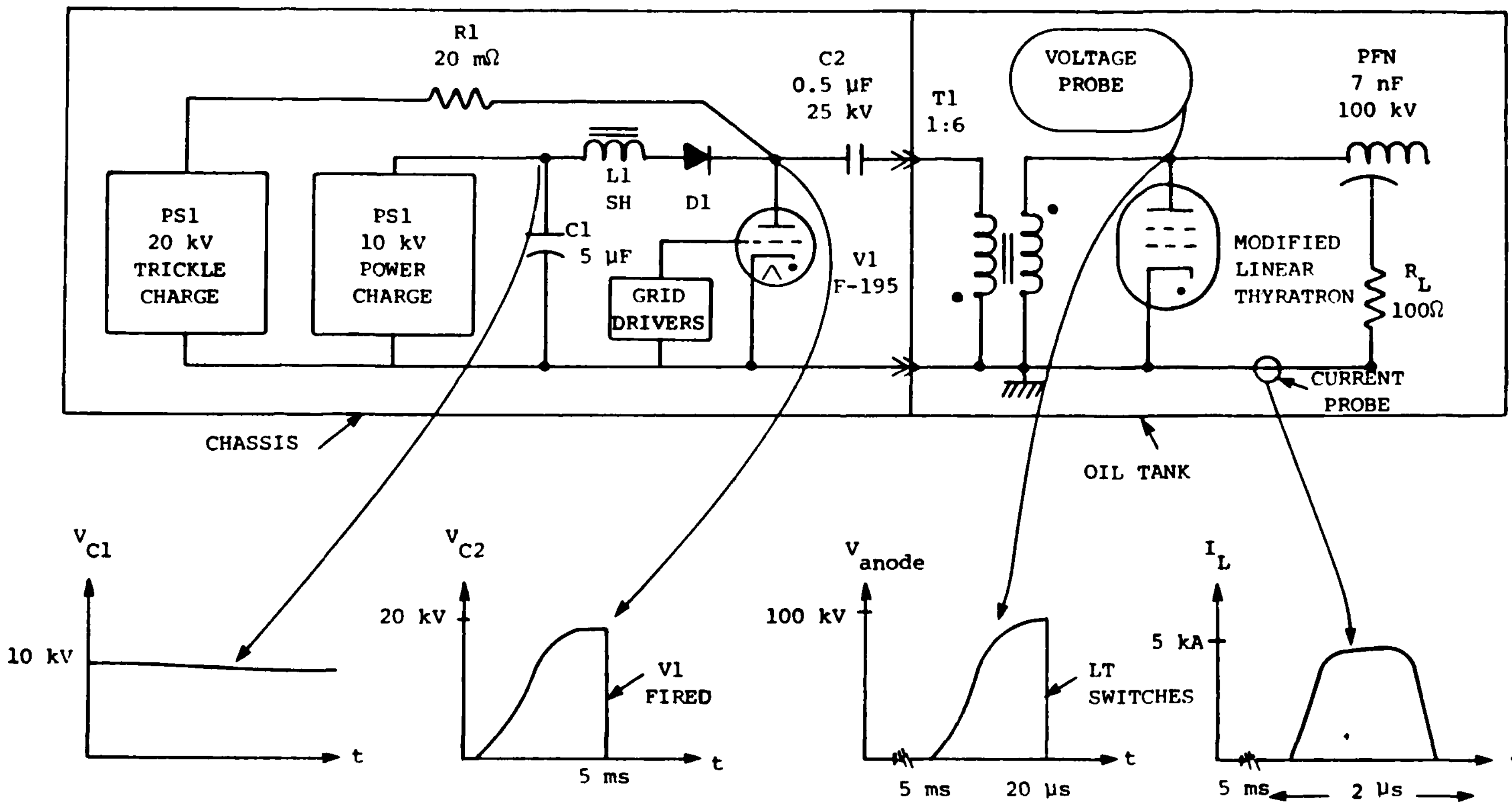

85 09995

Figure 8-1. Schematic of High-Voltage Modulator and It's Associatd Waveforms.

capacitor C1 is partially discharged through an inductor L1 (doubling the voltage), and a 1:6 iron core transformer thereby pulse charges the 3-stage 7 nF PFN up to 100 kV. The charging time to maximum voltage is approximately 15 μs. Therefore, the thyratron must hold off ≥90% of the maximum charging voltage for >5 μs. The PFN is subsequently switched by the modified linear thyratron and discharged through a 10-100 Ω load resistor.

The charging and switching voltage of the thyratron is monitored with a 50-kΩ resistive voltage divider which bleeds off approximately 10 percent of the charging current during the charging cycle. A capacitive voltage divider was initially used and later abandoned due to excessive noise. A Pearson current transformer monitors the current through the thyratron.

8.3 LINEAR THYRATRON AND LABORATORY MODIFICATIONS

In accordance with the design criteria described in preceeding sections, the existing linear thyratron was modified for operation at higher voltages with a goal of 100 kV. A schematic of the modified linear thyratron appears in Figure 8-2. Photographs of the subassemblies for the linear thyratron appear in Figure 8-3. The control grid assembly is shown in Figure 8-3a. The parts are (from left to right) the control grid, a plug for the control grid slot, the control grid baffle, and a mounting collar. The anode is shown in Figure 8-3b and the teflon high-voltage insulator is shown in Figure 8-3c. A partial assembly photograph of the linear thyratron is shown in Figure 8-3d. This sub-assembly of the linear thyratron excludes the lower flange upon which the cathode assembly is mounted. The windows, insulator, and anode are not in place. The control grid is shown protruding from the case of the thyratron. A teflon mounting collar is shown at the base of the control grid. The purpose of the mounting collar is to insure proper spacing between the control grid and the insulator. The top four feedthroughs are for the control grid. Schematics of the parts for the control grid appear in Figure 8-4. The fully assembled linear thyratron is shown in Figure 1-5.

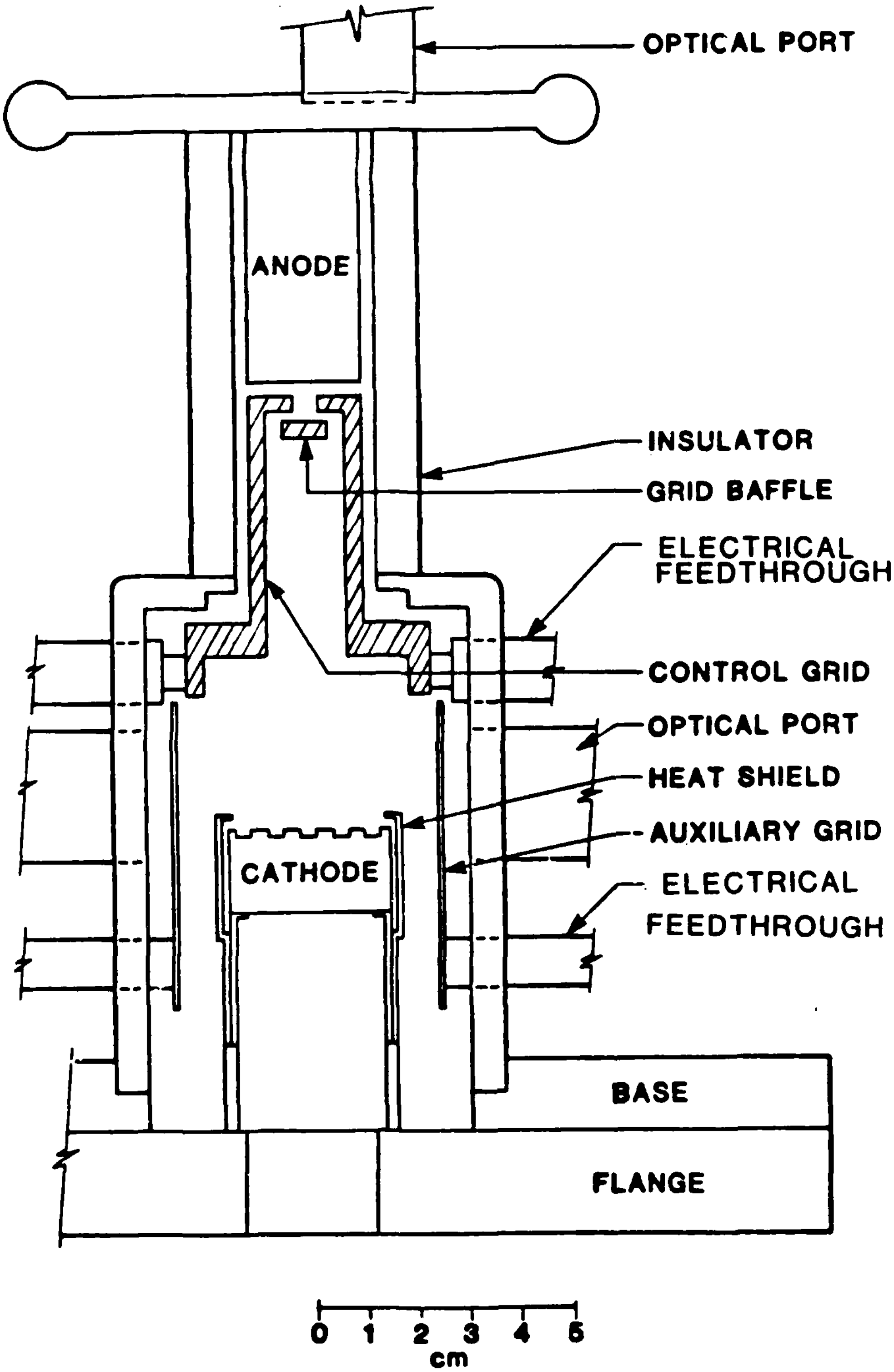

Figure 8-2. Schematic of the Modified Linear Thyratron.

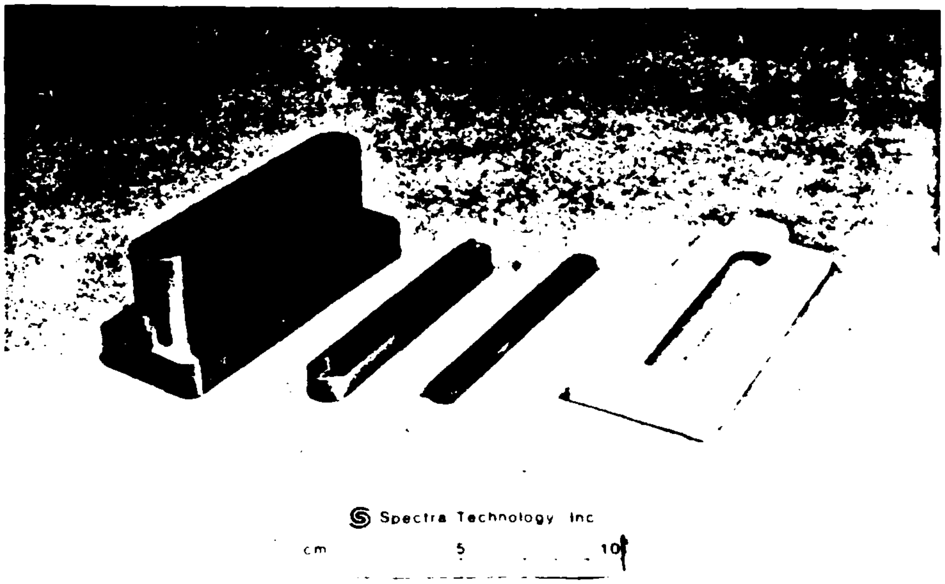

a) Left to Right) Control Grid, Control Grid Slot Plug, Control Grid Slot Baffle and Mounting Collar

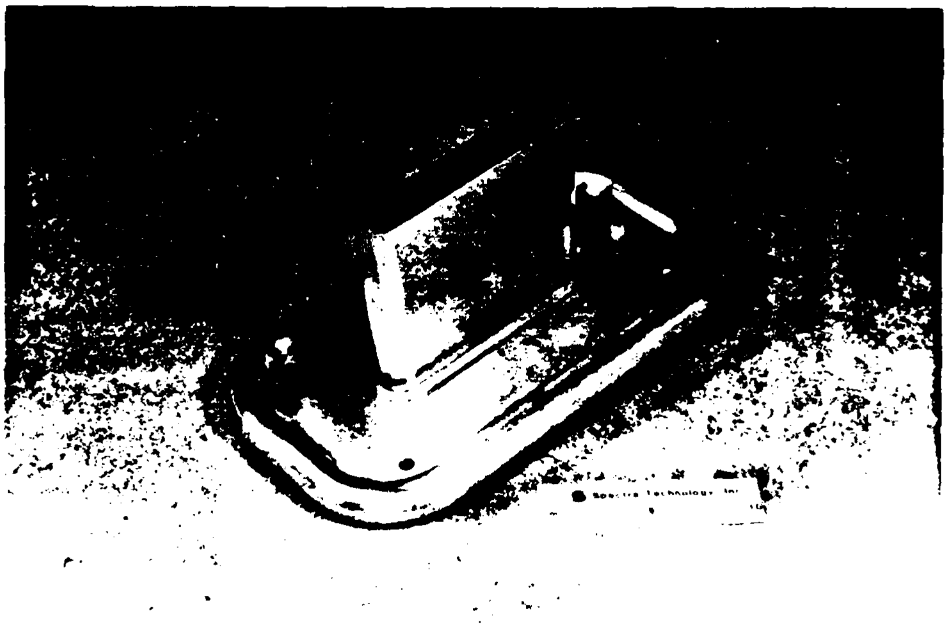

86 11009

b) Anode Assembly

Figure 8-3. Linear Thyratron Grid and Anode Components

AD-A194 111   LINEAR THYRATRON(U) SPECTRA TECHNOLOGY INC BELLEVUE WA   3/3
M J KUSHNER ET AL. 31 JUL 87 AFWAL-TR-87-2000
F33615-84-C-2474

UNCLASSIFIED   F/G 9/1   NL

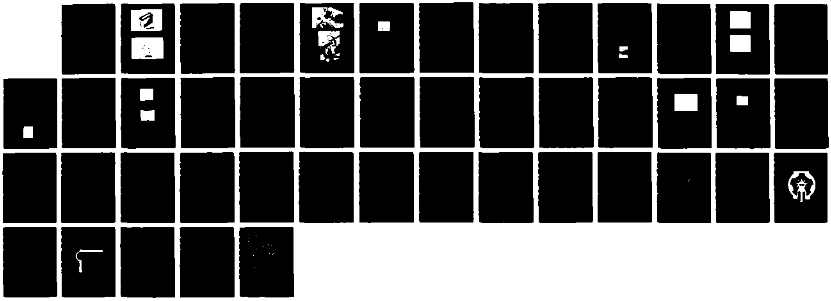

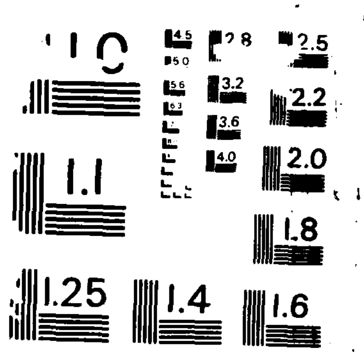

COPY RESOLUTION TEST CHART
NATIONAL BUREAU OF STANDARDS-1963

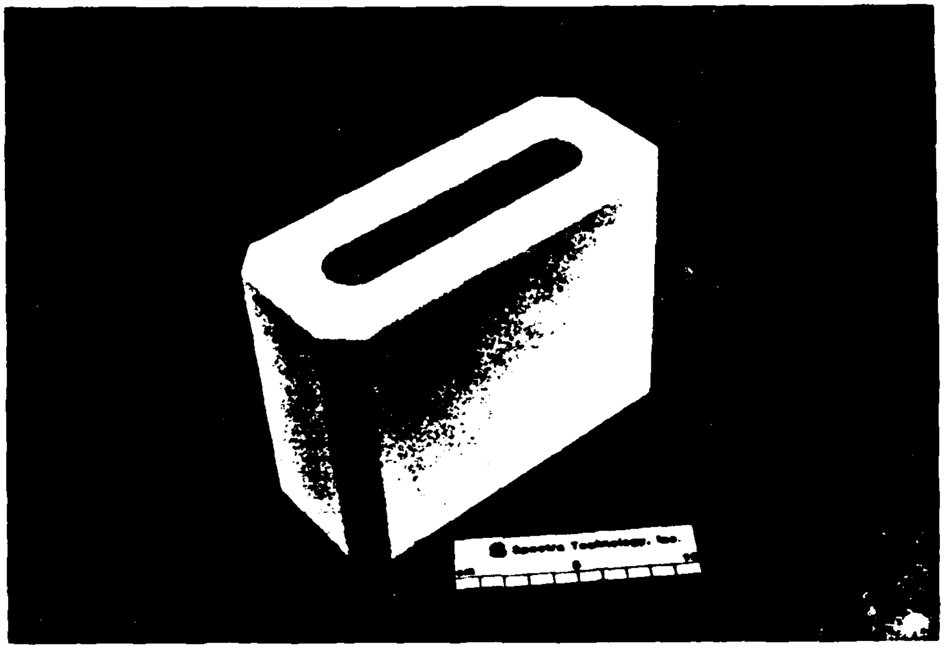

c) High Voltage Insulator

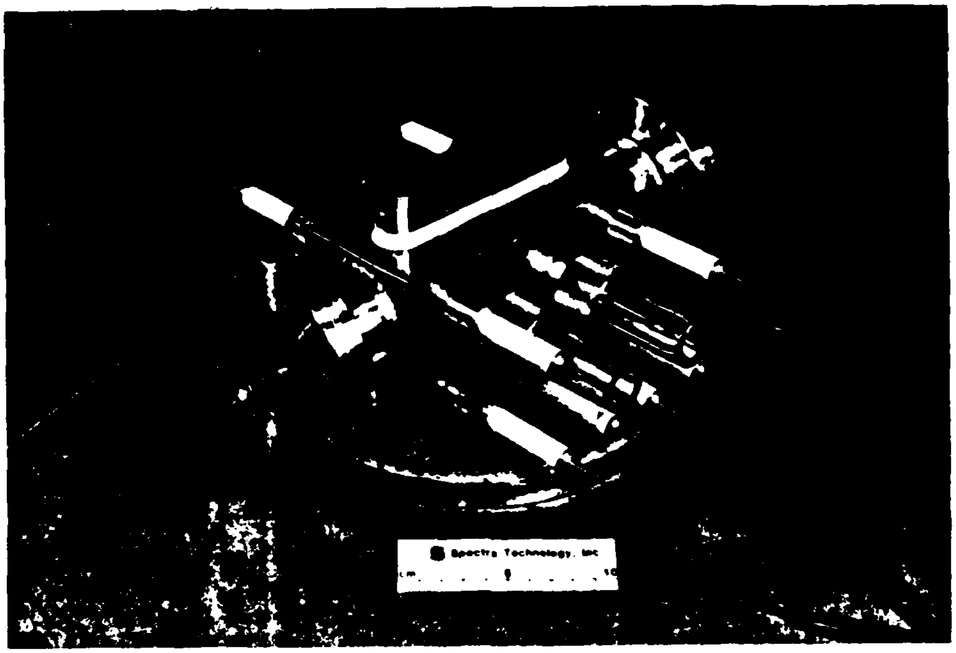

86 11210

d) Partial Assembly of Linear Thyratron

Figure 8-1. Continued. Linear Thyratron Insulator and Partial Assembly Photographs

8715483

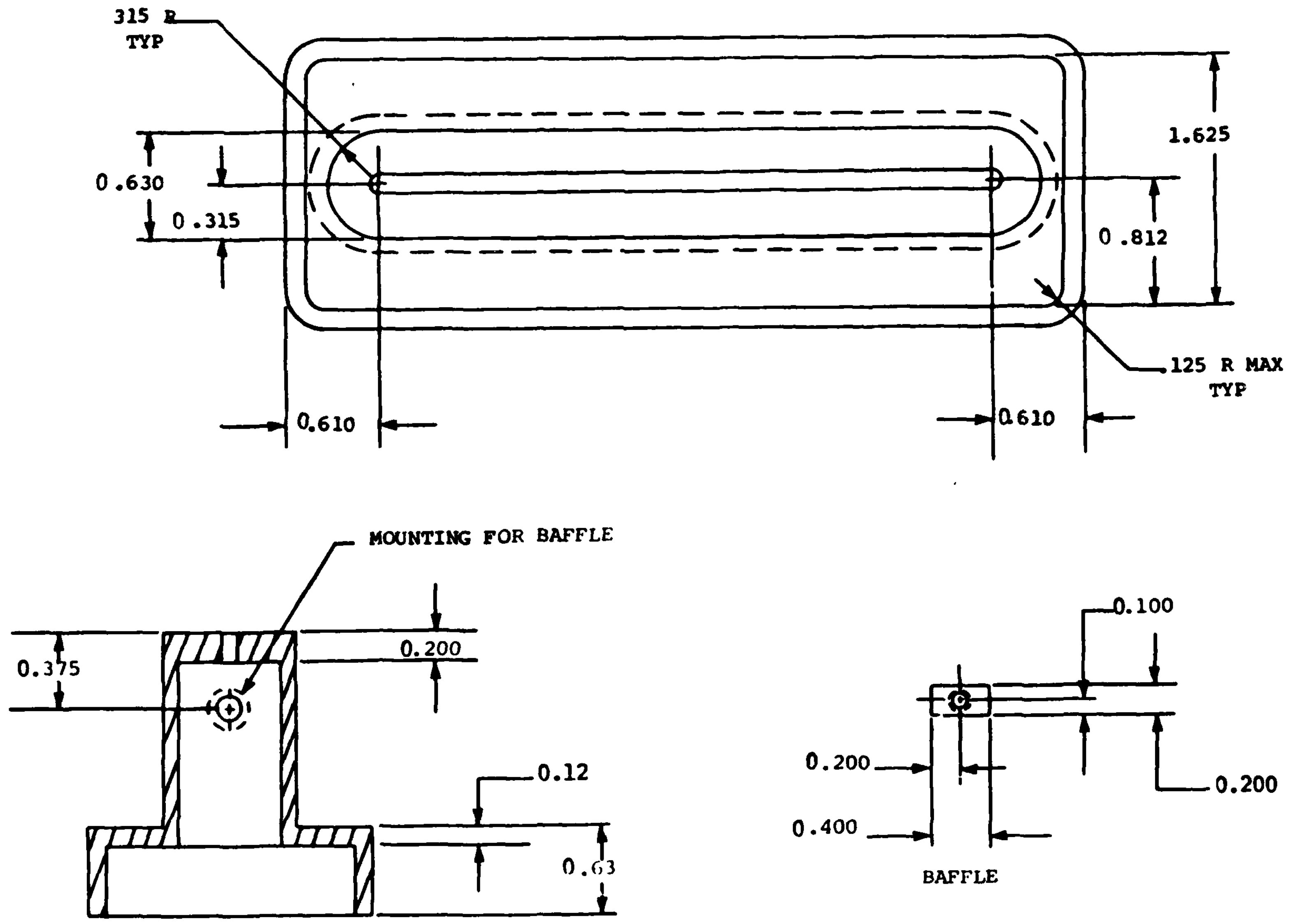

Figure 8.4. Details for the Control Grid (Dimensions are in Inches)

The laboratory setup is shown in Figure 8-5. The oil tank is internally separated into two sections; one for the 100-kV step-up transformer and one for the pulse forming line. The compartments can be separately filled with oil. A cover for the oil tank (not shown) vacuum seals the tank to enable the interior to be evacuated. The transformer and oil were separately "degassed" by evacuating the tank to a pressure of <100 mTorr for >72 hours. The oil was then backfilled into the transformer compartment. The transformer was subsequently kept under oil for the remainder of the study. The linear thyratron is mounted upside down to enable the high voltage section to be immersed in oil without also immersing the electrical feedthroughs, windows, and vacuum connections. Metallic cups were built to fit around the large end windows to enable oil immersion to approximately half the window height while still allowing one to view the interior. The linear thyratron is connected to a 10-cm diffusion pump by the 5-cm tubing approximately 1.5 m in length. The diffusion pump is continuously cold trapped to -50 C. The background pressure, as measured by an ion gauge located on the pump side of the 5-cm tubing is typically 4×10^{-8} Torr.

8.4 PRELIMINARY SWITCHING TRIALS WITH THE MODIFIED LINEAR THYRATRON

Initial testing of the modified linear thyratron was performed in hydrogen and consisted of charging the PFN, switching the thyratron, and checking for pre-fires at a repetition rate of ≈1 Hz. The thyratron was operated while simultaneously pulsing the auxiliary and control grids (voltage 2-4 kV) and without a dc auxiliary grid current. For these trials, the high-voltage insulator was made of Teflon. Triggering occurred at the peak of the PFN charging cycle (≈15 μs). Typical traces of the charging and switching cycles for the modified linear thyratron is shown in Figure 8-6. The left trace (5'kV/div, 5 μs/div) is of the anode voltage of the thyratron. The right trace (100 A/div, 500 ns/div) is of the current through the load.

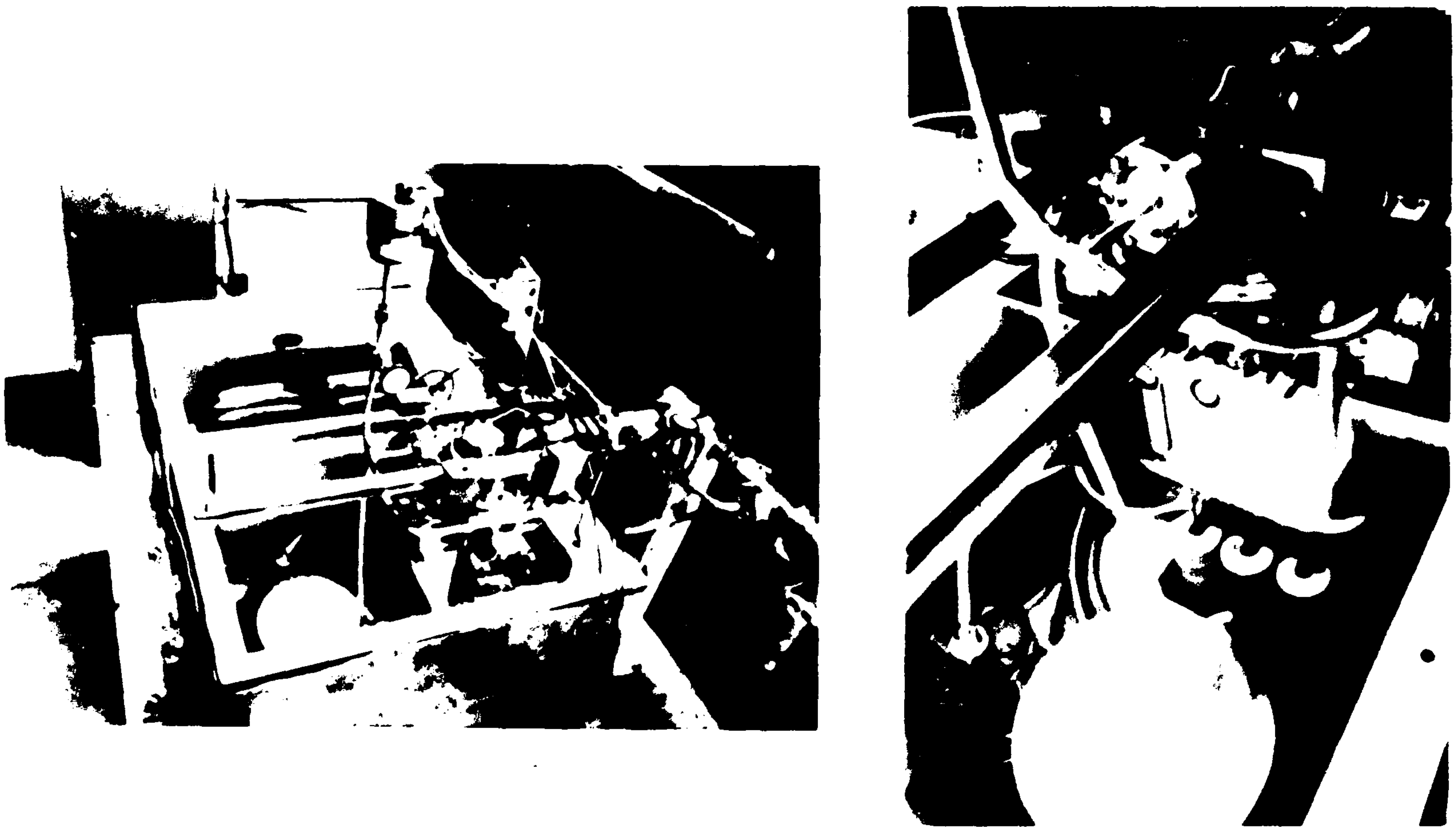

Figure 8-5. Laboratory Setup Showing the Modified Linear Thyratron Mount in the Oil Tank.

86 10490

86 10992

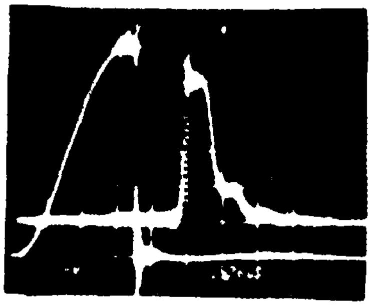

Left: **Anode Charging Voltage** (5 kV/div, 5 μs/div)

Right: **Current** (100 A/div, 500 ns/div)

Figure 8-6. Typical V-I Traces for High-Voltage Operation of Modified Linear Thyratron. (30 kV max, H_2, 150 μm)

Initial trials with the modified linear thyratron were only marginally successful. The maximum holdoff voltage in hydrogen (150 μn) was ≈17.5 kV. Prefiring was observed to consist of arcing at the outer edge of the control grid-anode gap and preferentially on one side of the thyratron. We measured the holdoff voltage in vacuum and obtained nearly identical results, leading us to suspect field emission as the source of prefiring. The thyratron was disassembled and examined. The control grid showed evidence of arcing only along its edges. A small amount of damage was noted on the insulator adjacent to the arc spots. Upon measuring the dimensions of the grid parts, we found that the edges of the control grid and anode had not been machined to specified radii. The measured radii were <10 mil; the specified radii were 60 mil. The control grid-anode gap was measured to be 60 ± 10 mils, also below specifications (100 ± 5 mils). The small edge radii for the control grid and anode resulted in excessive field enhancement. The gap being too narrow resulted in excessive electric field penetration through the control grid slot. Both effects contributed to prefiring. The thyratron parts were returned to the machine shop. The edges of the control grid and anode were machined to radii of 60 mil and the control grid-anode gap was widened to 100 mils. The thyratron was reassembled. The orientation of the insulator was turned by 180° to move the damaged portion away from the control grid-anode gap.

Subsequent testing of the thyratron hydrogen was initially more successful. A dc simmer current was used between the auxiliary grid and the cathode for these trials. Without further conditioning, we switched 48 kV (H_2, 150 μm) at a repetition rate of 1 Hz. After accumulating ≈100 shots, though, the holdoff voltage of the thyratron monotonically decreased. Attempts to further condition the thyratron by purposely operating at low voltage failed. When holdoff voltage fell to below 20 kV, the thyratron was disassembled and examined. There appeared to be no physical damage to either the control grid or the insulator, although the insulator was slightly discolored at the level of the control grid-anode gap. The anode had isolated arc spots. The surfaces of the control grid and anode were wiped with a white cloth and were clean with the exception

of the surface of the anode facing the control grid. This surface was covered with a thin film, which appeared black on the cloth. The film was not analysed; however, we found the film only on the anode. Thus, we felt this resulted from negatively charged fluorocarbon ions generated from outgassing or plasma induced desorption from the Teflon insulator. The Teflon insulator was replaced with one identically shaped made of Macor ceramic.

8.5 HIGH-VOLTAGE OPERATION OF THE MODIFIED LINEAR THYRATRON

The results for high-voltage operation of the modified linear thyratron reported here will be exclusively for operation in hydrogen and helium. In general, holdoff in helium was superior to that in hydrogen for a given pressure; however, we were able to reliably switch the thyratron in helium only at relatively high pressures ($\lesssim$500 μn) and corresponding low holdoff voltages (< 50 kV) with the standard control grid pulser. For example, holdoff and switching at 35 kV in helium was obtained at the Paschen limited pressure of 550 μm. For operation in hydrogen, the same performance required a pressure of 225 μm. The inability to switch in He at low pressure was circumvented by building a second control grid pulser operating at $\lesssim$15 kV. Switching could then be obtain in He at pressures $\lesssim$200 mu\n at voltages of $\lesssim$85 kV. The higher control grid pulser voltage was necessary due to the large cathode-control grid gap. This is, in principle, a problem solved by modifying the cathode-control grid region to operate on a more favorable portion of Paschen's curve.

Thyratron operation was evaluated by the ability to both holdoff and reliably switch a desired voltage. No attempt was made to maximize dI/dt switched by the thyratron. Unsuccessful operation occured when the thyratron prefired at a voltage less than the peak of the charging cycle or the thyratron could not be switched on command. The former is a "failure" because the tube did not hold off voltage for the entire charging cycle but could conceivably be a "success" for a shorter charging period. Unless otherwise noted, the auxiliary grid was operated with a reverse dc simmer

current. That is, the dc voltage on the auxiliary grid was negative with respect to the cathode. This mode of operation was required for dc discharge stability by having the auxiliary grid act as a hollow cathode. The control and auxiliary grids were simultaneously pulsed with voltages of 2.5-5.0 kV in hydrogen. The control grid was operated at 5-15 kV in helium.

The maximum switching voltage for operation in H_2 is shown in Figure 8-7 as a function of gas pressure. Current and voltage waveforms for operation at 80 kV are also shown in Figure 8-7. The thyratron was reliably operated in the 90-95 kV range. The maximum dI/dt was 1.8×10^{10} A-s^{-1} although we did not attempt to maximize this value by minimizing inductance in the discharge circuit. The voltage fall time for this range of switching voltage is shown in Figure 8-8. The voltage fall time for gas discharge switches operating on the near side of Paschen's curve typically increases with increasing holdoff voltage. This trend is qualitatively followed in these results; however, there appears to be a fast and a slow branch for the voltage fall time. The separate branches indicate some type of bimodal switching behavior. Examples of voltage waveforms for the fast and slow branches are shown in Figure 8-9. The current rise times are also short and long respectively. This behavior cannot presently be explained, but may result from fluctuations observed in the spatial distribution of the dc simmer discharge. The fast branch could also be a "switched" prefire; that is, a discharge which resembles an arc more than a glow and therefore is more rapid. We assume that a prefire is more like an arc than a glow. At sufficiently high voltage where the prefire becomes more probable, it may be possible to "trigger" a prefire in the same fashion that one triggers a glow discharge.

The failure mode for switching at high voltages and low pressures (<150 μm H_2) was both from prefire and the inability to switch the tube on command. To obtain reliable switching a dc simmer current between the auxiliary grid and the cathode was required. To obtain a reliable dc simmer current, the auxiliary grid had to be negative with respect to the

- 100 μm H_2

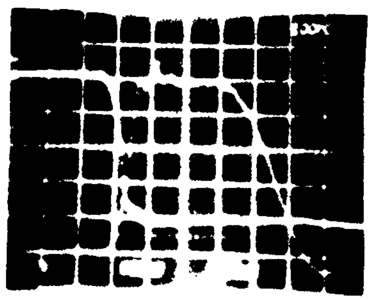

- Voltage (20 kV/Div) - Left
- Current (300 A/Div) - Right
- 100 ns/Div

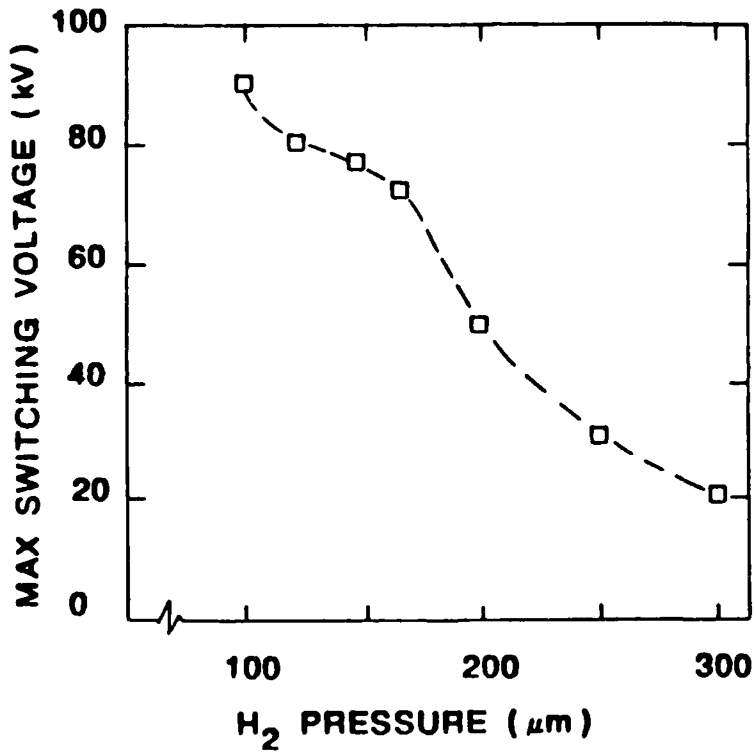

Figure 8-7. Maximum Switching Voltage and I-V Characteristics for Operation in H_2.

86 10420

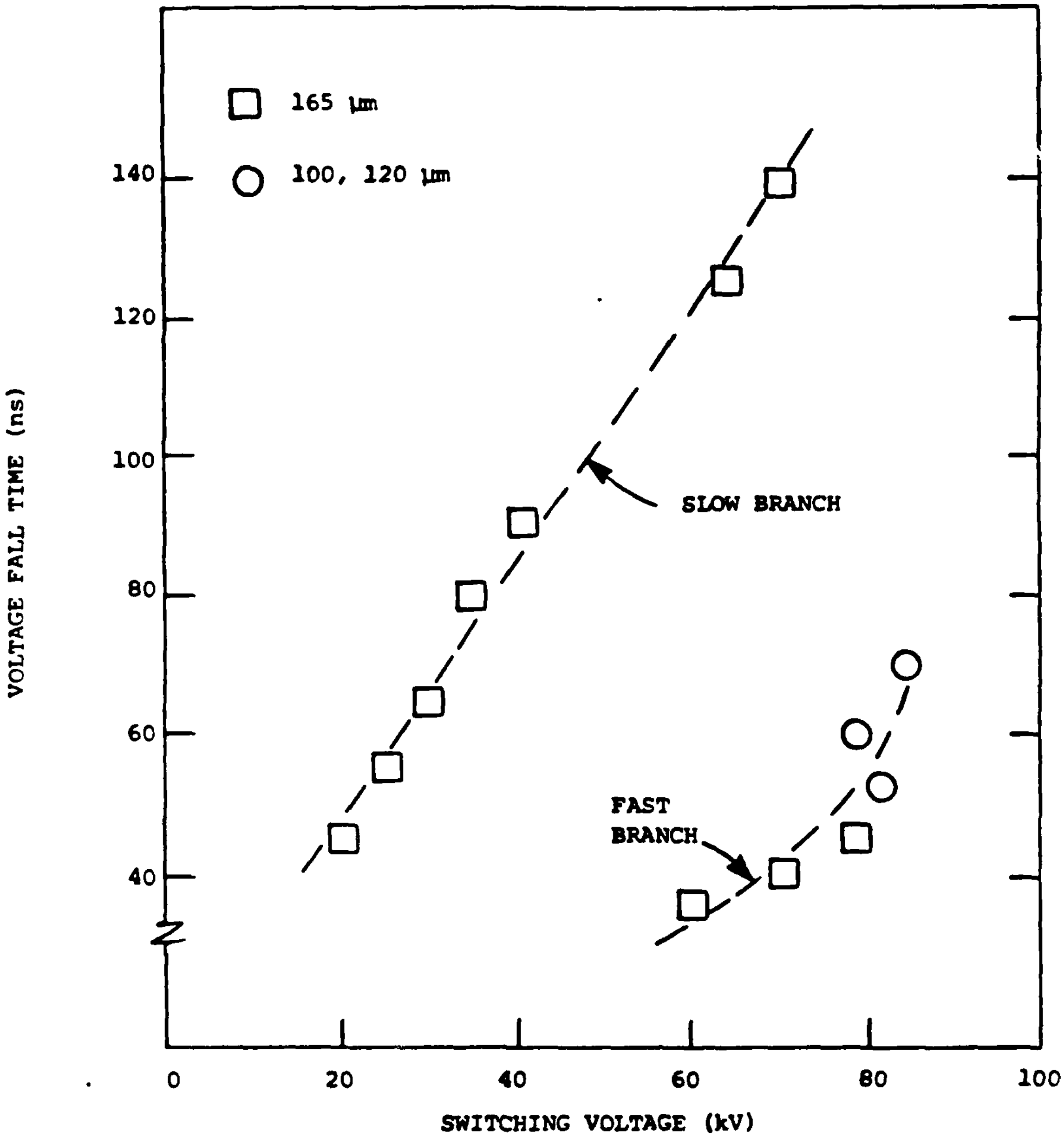

86 13509

Figure 8-8. Voltage Fall Time as a Function of Switching Voltage for Operation in H_2.

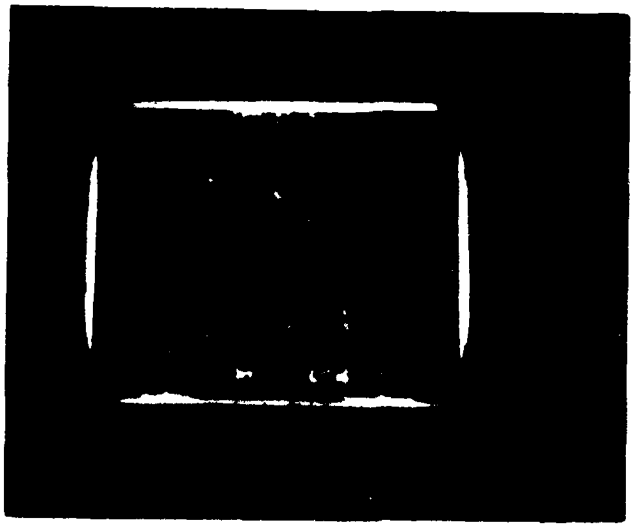

(a) 120 μm H_2

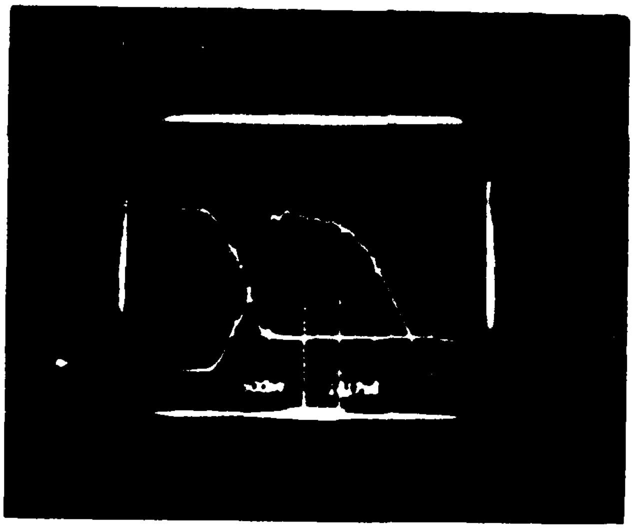

(b) 167 μm H_2

86 10980

Figure 8-9. I-V Characteristics for Switching in H_2 Showing (a) Fast and (b) Slow Behavior. (Voltage left trace, current right trace; 20 kV/div, 250A/div, 100 ns/div.)

"cathode," thereby acting like a hollow cathode. The thickness of the cathode dark space for each of the parallel opposing auxiliary grids increased with decreasing gas pressure. At sufficiently low pressure the opposing cathode dark spaces met and the dc discharge could no longer be sustained. At this time triggering became more difficult.

Holdoff failure due to prefire results from exceeding the Paschen breakdown voltage for a given p•d product. When prefire occurs at a given voltage, the gas pressure must be reduced. This mode of operation was pursued until the dc simmer current could no longer be sustained. In the absence of triggering, pulsed holdoff for the duration of the charging cycle could not be obtained at voltages greater than 95 kV in hydrogen. We operated the control grid with a negative dc bias of $\geq$-200 V to determine whether prefire was a result of potential penetration through the control grid slot or as a result of exceeding the Paschen limit. We did not increase holdoff voltage with the negative dc bias, thereby suggesting that prefire is a result of exceeding the Paschen limit.

Similar high-voltage switching performance was obtained when operating in helium. The maximum switching voltage for operation in He is shown in Figure 8-10 as a function of gas pressure. A voltage waveforms for operation at 75 kV is also shown in Figure 8-10. The thyratron was reliably operated only in the 75-85 kV range, less than in hydrogen.

The gas pressure for a given switching voltage is higher when using helium than when operating in H_2, thereby suggesting that higher voltage operation could be ultimately achieved in helium. The voltage trials in He were conducted chronologically after those in hydrogen and therefore we suspected that we had accumulated damage to the thyratron. The linear thyratron was disassembled and inspected. Arc marks were found on the edges of the control grid however damage was minimal. We did, however, measure the control-grid anode gap and found that it was 150 mills compared to the 100 mills measured during the hydrogen trials. We determined that the control grid had slipped in the teflon mounting collar at some previous

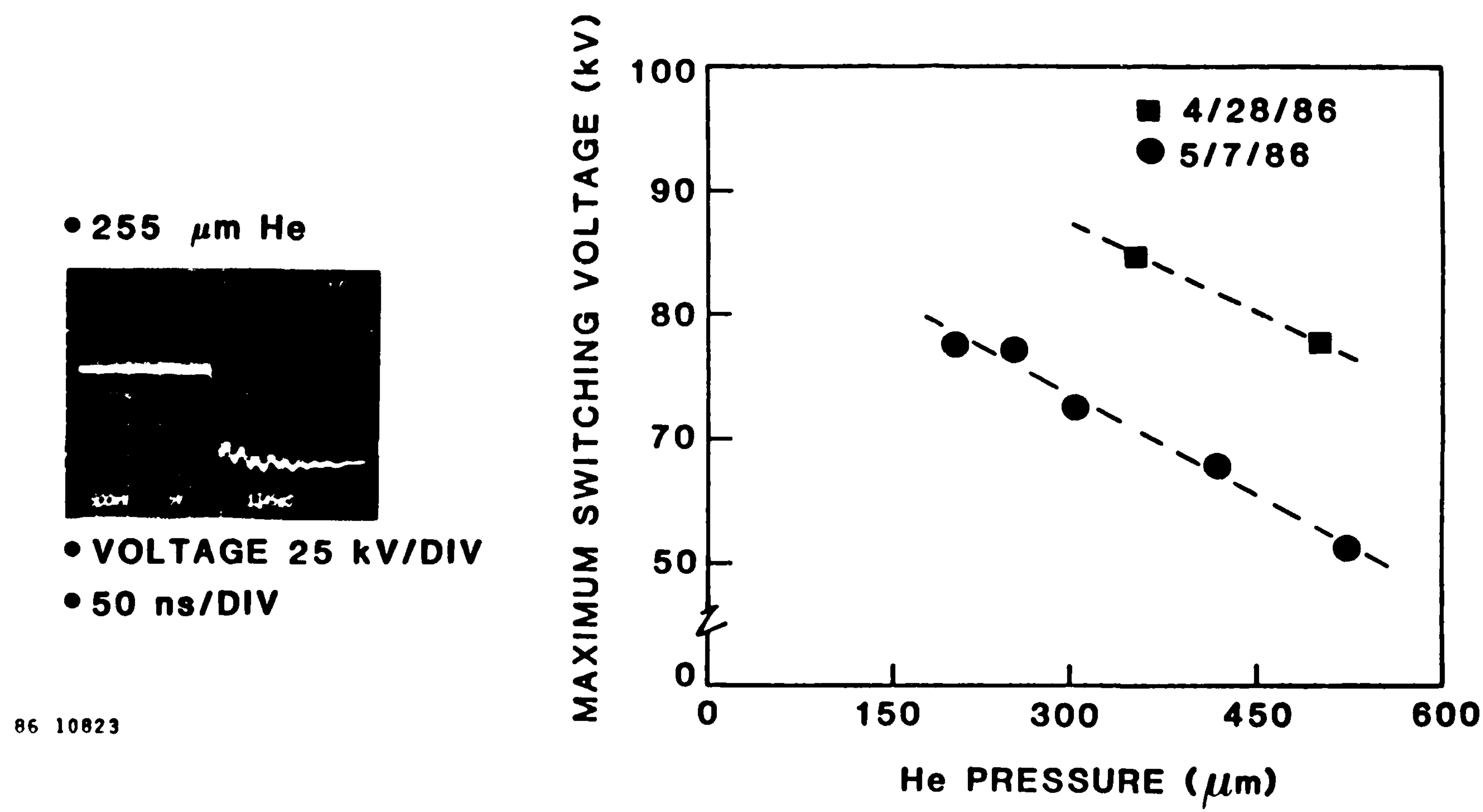

Figure 8-10. Maximum Switching Voltage and Voltage Waveform for Operation with He.

time, thereby increasing the control grid-anode gap, and reducing the holdoff voltage. Upon inspection of the data, this slipping must have occured near the end of our hydrogen trials and certainly before the helium trials. In subsequent modifications of the linear thyratron we will redesign the mounting collar to prevent such slipping.

8.6 DUAL PULSE HIGH-VOLTAGE OPERATION

High repetition rate operation of the linear thyratron requires the thyratron to recover to its prepulse nonconducting condition during the interpulse afterglow period and to holdoff the desired charging voltage until switched by command. The voltage drop across a well behaved recovered thyratron prior to switching is the open circuit voltage across the load and equal to the charging voltage of the PFN. If the thyratron fails to recover in the desired time, then the PFN is terminated by a finite resistance during the charging period and the voltage drop across the thyratron is less than the open circuit voltage. An indication of the recovery of the thyratron is therefore V_H/V_C, where V_H is the "holdoff" voltage across the thyratron on a subsequent charging cycle at the desired triggering time, and V_C is the charging voltage of the initial pulse. A qualitative requisite for recovery is that $V_H/V_C > 0.95$. The typical failure mode for the modified linear thyratron during repetitive pulse operation is to have $V_H/V_C < 1.0$. Inadequate recovery may also result from prefiring of the thyratron on subsequent charging cycles. This type of recovery failure was <u>not</u> observed with the modified linear thyratron.

Voltage waveforms demonstrating successful and unsuccessful recovery of the thyratron for a pulse separations of 5 ms (200 Hz) and 2 ms (500 Hz) respectively are shown in Figure 8-11. The conditions are V_C = 45 kV for H_2 at 100 μm. The first pulse is that shown being switched at the peak of the charging cycle. The second pulse is not switched and shows damped LC ringing at the resonant frequency of the charging circuit.

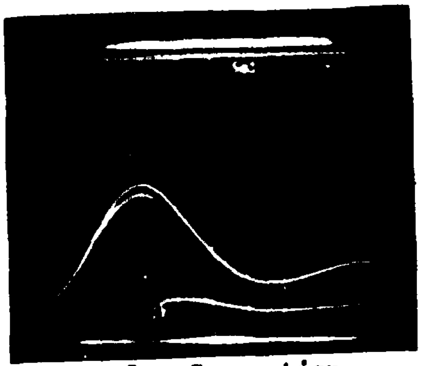

5-ms Pulse Separation
(a)

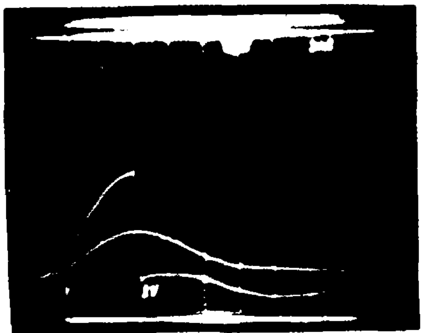

2-ms Pulse Separation
(b)

(5 μs/DIV, 10kV/div)

Figure 8-11. Dual Pulse Operation Showing (a) Successful Recovery at 5-ms Pulse Separation and (b) Unsuccessful Recovery at 2-ms Separation.

Note that the second charging cycle for the fully recovered case in Figure 8-11 has a peak voltage approximately 10 percent higher than the first. The higher voltage on the second charging cycle is logically a result of there being charge left on the PFN from the first pulse when the second pulse begins to charge. In this case, the initial voltage should register as an offset in the base line of the voltage at the start of the charging cycle, which is not the case. The resistive damping of the charging voltage has an e-folding period of ≈25 μs which, for a 5-ms pulse separation, would also imply a negligible voltage left on the PFN. The origin of the higher second pulse voltage is therefore presently unexplained. This voltage could detrimentally impact the recovery of the thyratron, as will be discussed below.

Recovery with $V_H/V_C = 1.0$ was obtained in hydrogen for pulse separations of ≥ 5-ms (equivalent repetition rates of ≤ 200 Hz) for all combinations of voltages and pressures investigated (30-80 kV, 85-200 μm). Recovery began to degrade for pulse separations of less than 5 ms as shown in Figure 8-12. The degradation in recovery with decreasing pulse separation is the same for a large range of charging voltage and pressure. The limit for recovery ($V_H/V_C \geq 0.95$) in the present device is for a pulse separation of ≈3.5-ms (≈300 Hz).

Recovery is obtained by the gas relaxing to its predischarge state. By relaxing we mean that the plasma has recombined and that the gas density, perturbed due to gas heating, has returned to its prepulse value. If the gas density does not not uniformly return to its prepulse condition, then recovery can degrade by a violation of Paschen's law. If the plasma remains hot, recovery can degrade by a reduction in recombination rates. (Two body recombination has a temperature dependence of $T_e^{-0.5}$ whereas three body recombination has a dependence of $T_e^{-4.5}$.) Recombination can also proceed by diffusion and heterogeneous processes at the wall.

A simple set of rate equations can be written for recovery in hydrogen plasmas based on the processes listed in Table 8-1. Since the

Table 8-1

REACTIONS AND RATE CONSTANTS FOR RECOVERY IN AN H_2 PLASMA

Reaction	Rate Constant†
$e + H_3^+ \rightarrow H + H_2$	2.5(-8)
$e + H^+ \rightarrow H$	4.2(-12)
$e + e + H^+ \rightarrow H + e$	1.0(-19)
$e + H_2^+ \rightarrow 2H$	2.5(-8)
$H_2^+ + H_2 \rightarrow H_3^+ + H$	2.0(-9)
$H^+ + H_2 + M \rightarrow H_3^+ + M$	3.0(-29)
$H^+ \xrightarrow{W} 0.5 \cdot H_2$	$250/(P(f_D + 0.06*(1-f_D) + 2300f_I))$
$H_2^+ \xrightarrow{W} H_2$	$1440/(P(f_D + 4(1-f_D) + 18500f_I))$
$H_3^+ \xrightarrow{W} 1.5 \cdot H_2$	$1180/(P(f_D + 0.5*(1-f_D) + 32000f_I))$

† Rate constants are in units of cm^3s^{-1} and cm^6s^{-1} at room temperature.

$\xrightarrow{W}$ denotes heterogeneous recombination at the wall with diffusion constant (cm^2s^{-1}), as noted, where P is the gas pressure (Torr), f_D is the fractional dissociation and f_I is the fractional ionization.

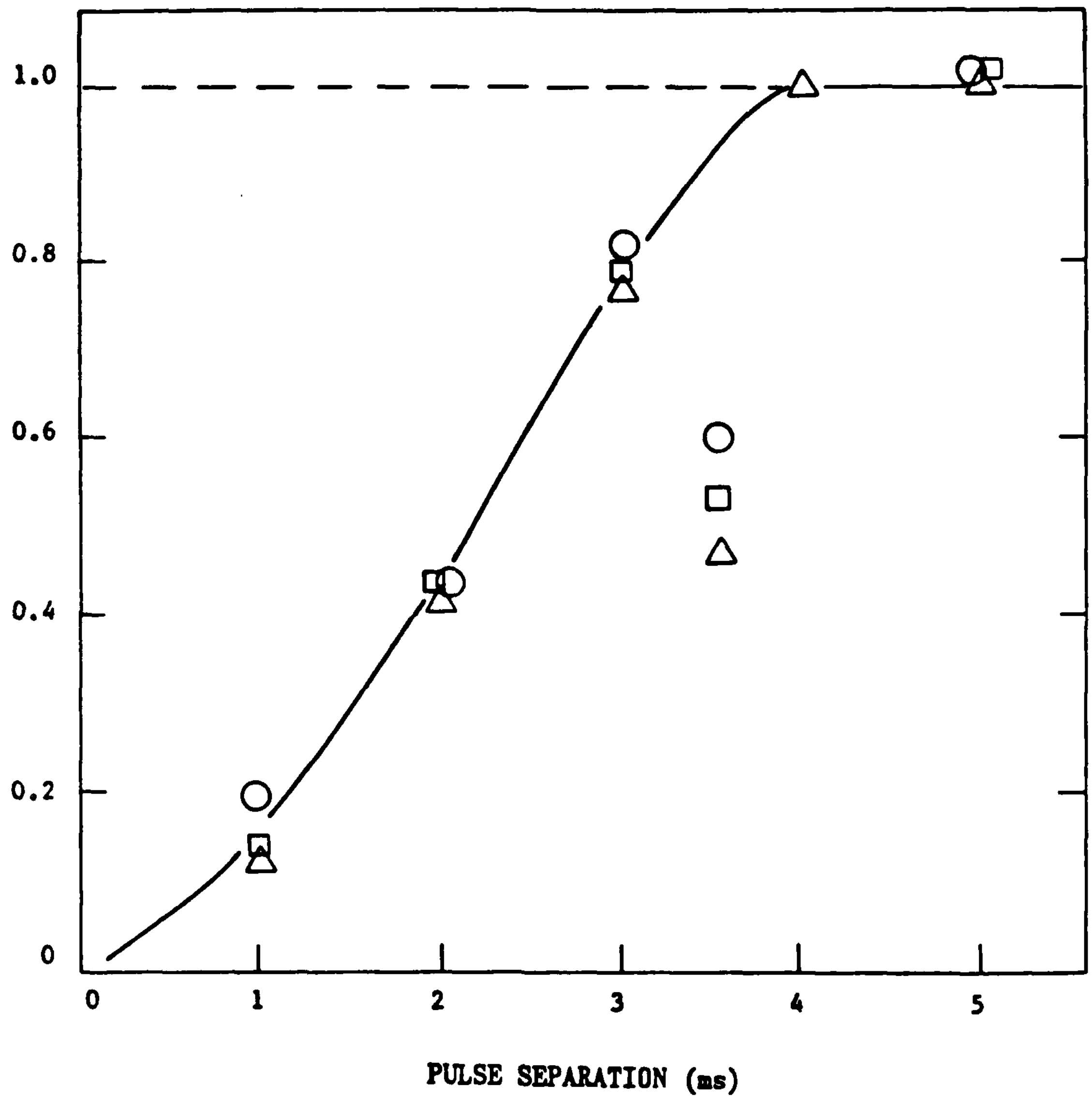

Figure 8-12. Recovery Voltage as a Faction of Charging Voltage as a Function of Pulse Separation for Operation in H_2.

86 10970

cooling rate for electrons in a hydrogen afterglow is on the order of MeV/s, the electrons thermalise to the gas temperature within tens of microseconds. The rates in the table are therefore for room temperature.

In the absence of diffusion, the densities of charged species in a hydrogen afterglow, as computed for the processes in Table 8-1, are plotted in Figure 8-13. The gas pressure is 0.150 Torr, and the initial conditions are a fractional ionisation of 0.001 and a fraction dissociation of 0.1. Late in the afterglow the positive ion is exclusively H_3^+. Significant recovery is obtained only for times >10 ms. Clearly, recombination by diffusion is required for rapid recovery. To this extent, the rapid conversion of positive ions to H_3^+ is beneficial since the diffusion constant for H_3^+, in the absence of charge exchange collisions, is higher than either H^+ or H_2^+.

Now including diffusion, the recovery time is plotted in Figure 8-14 as a function of wall separation. Recovery time is defined as the time required for the electron density to fall below $10^5 cm^{-3}$. Recovery is less than 1 ms requires a wall separation of <3 cm. The control grid-anode gap is 2.5 mm whereas the wall separation in the cathode-control grid gap is 1.5-4 cm. Although the plasma within the control grid-anode gap may be fully recovered in tens of microseconds, it is possible that the plasma within the control grid is not fully recovered for many milliseconds. The penetration of electric potential through the control grid slot when voltage is applied to the anode may then draw plasma from within the control grid into the gap, thereby preventing holdoff.

We mentioned above that the charging voltage on the second pulse is always 10 percent higher than on the first. The origin of this additional voltage is presently unknown. If a voltage is dropped across the thyratron for a substantial fraction of the interpulse period, the plasma temperature may remain high and recombination processes could be impeded. To the extent that recovery is dominated by diffusion, an elevated temperature should not degrade recovery unless the temperature is high enough to

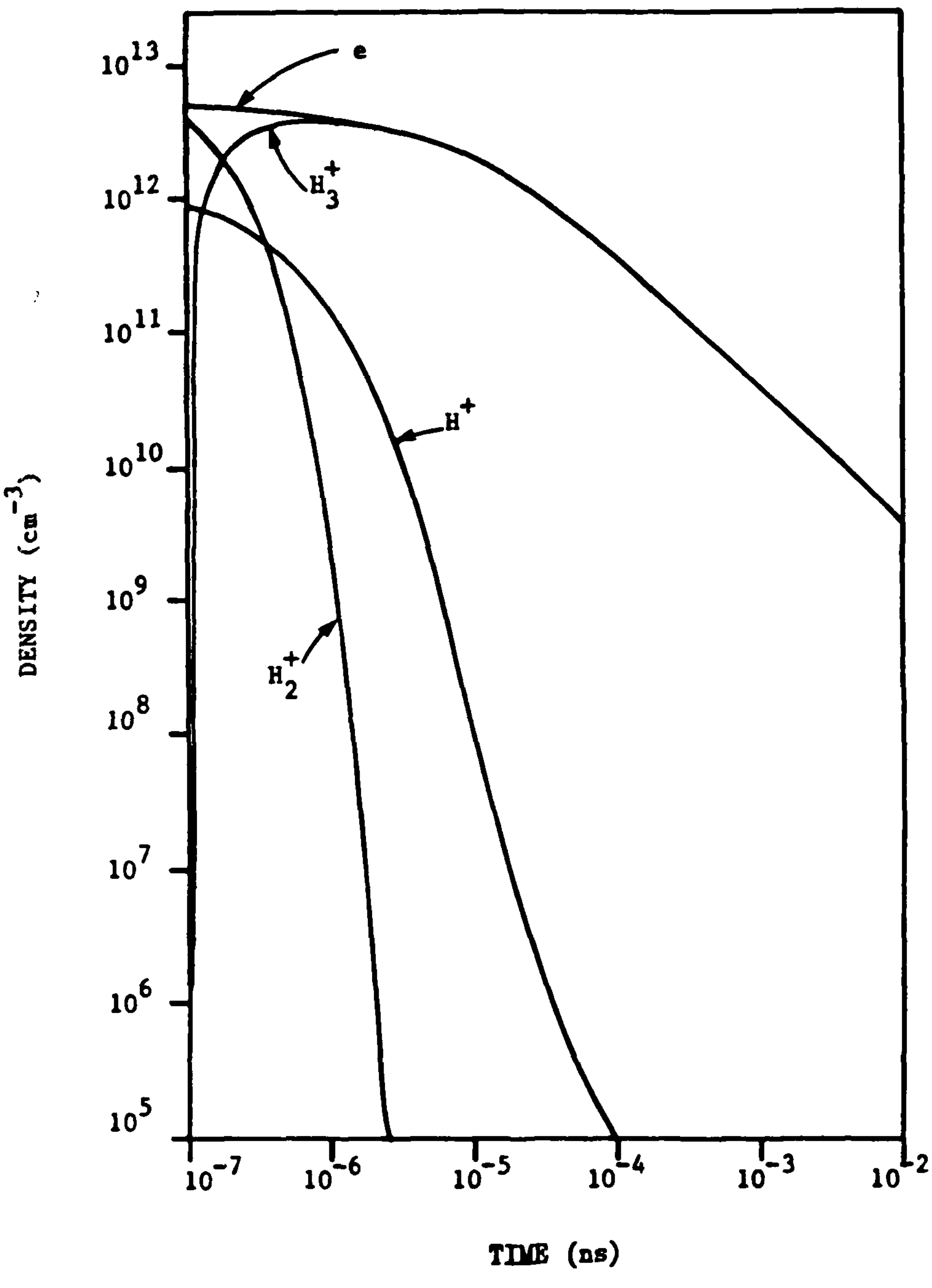

Figure 8-13. Electron and Ion Densities in the Absence of Diffusion in a Thyratron Plasma Afterglow.

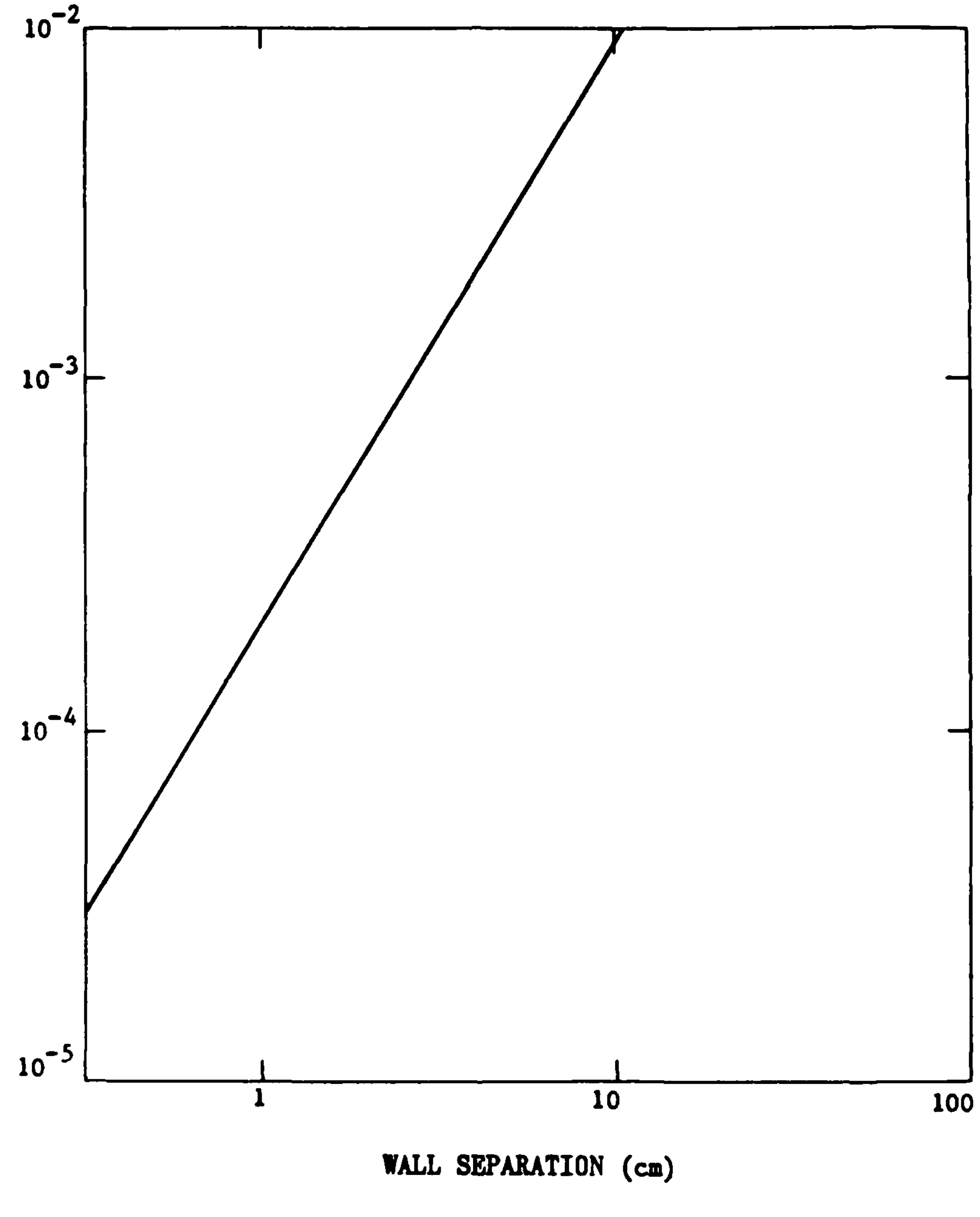

Figure 8-14. Thyratron Recovery Time as a Function of Wall Separation.

86 10969

sustain ionisation. We have determined the electron temperature and applied electric field required to sustain ionisation equal to a specified fraction of the rate of diffusion for a 1-cm wall separation (P = 0.15 Torr). This electric field is plotted in Figure 8-15. We have assumed an ambipolar enhanced rate of diffusion for the electron temperature. To significantly lengthen the recovery time (i.e. $R_{Ionisation}/R_{Diffusion} \approx 1.0$) the voltage drop need only be 50 V/cm. Therefore a small residual potential on the PFN could be responsible for the long recovery time measured for the modified thyratron.

Given the figures in the preceding paragraph, we remeasured the voltage across the thyratron with a long time base, looking for voltages of tens to hundreds of volts to determine whether high repetition rate operation was being degraded by residual voltage across the thyratron. A sample of the results is plotted in Figure 8-16 where we see voltage spikes of a few hundred volts occurring up to 3 ms after triggering. The origin of these voltage spikes is energy stored in the large step-up transformer which then "leaks" out with the appropriate LC time constant long after the discharge pulse is over. Voltage of this magnitude impressed across the thyratron is sufficient to slow down recovery in the manner described above. Note that the degradation in recovery at a pulse separation of 3 ms (see Figure 8-12) corresponds to the cessation of voltage spikes at 3 ms shown in Figure 8-16.

8.7 BURST MODE HIGH-VOLTAGE OPERATION

The modified linear thyratron was operated with a burst of five pulses to examine its recovery capability. For all conditions for which recovery and triggering were obtained for two pulses, recovery and switching could be obtained for five pulses; that is, five pulse burst mode performance was obtained for pulse separation down to 5 ms (200 Hz). An example of switching a burst of five pulses appears in Figure 8-17. The charging voltage is 60 kV, H_2 pressure is 180 μm, and the pulse separation is 10 ms. The drop in voltage on successive pulses is not related to

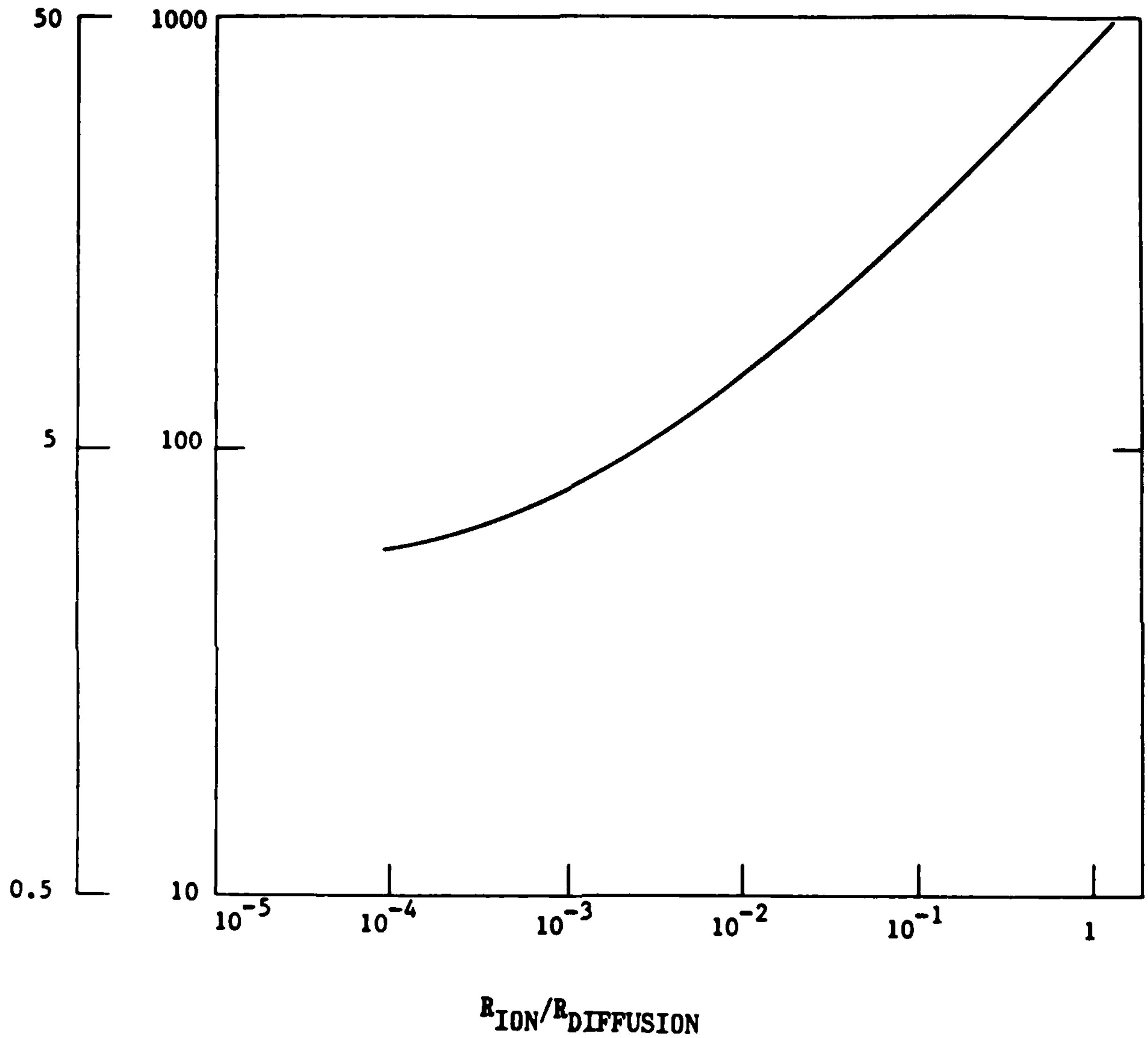

Figure 8-15. Electric Field Required to Obtain an Ionization Rate (R ion) that is a Specified Fraction of the Rate of Diffusion (R diffusion).

86 10968

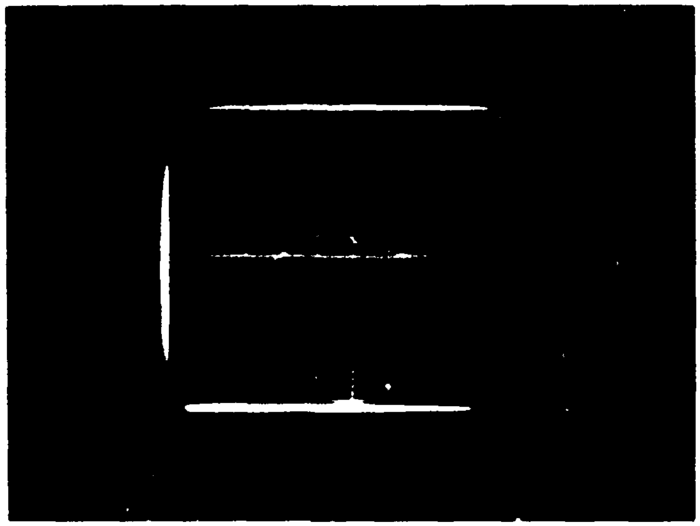

86 10981

Figure 8-16. Post Discharge Voltage Spikes Impressed
Across the Linear Thyratron.
(200V/DIV, 1 ms/DIV).

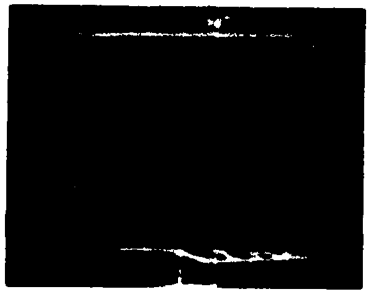

Figure 8-17. Burst Mode Switching at 60 kV in 180 μm Hz. 5 pulses are being switched with a separation of 10 ms.

recovery but is a result of a decreasing voltage on the pulser storage capacitor.

Section 9
HIGH REPETITION RATE AND SWITCHING RATE OPERATION WITH THE FINAL LINEAR THYRATRON MODIFICATION

9.1 INTRODUCTION

This section describes the final modifications made to the linear thyratron and the results achieved. Also, a conceptual design for a radial discharge linear thyratron is presented. The goals of this final phase were to achieve, simultaneously, the switching of 100 kV with $dI/dt > 10^{11}$ A/s in a burst mode at > 2 kHz. Apart from the switching voltage, which was limited to 60 kV, these goals were met.

The modifications to the modulator circuit required to meet the desired 2-kHz rep rate were greater than originally anticipated and became a substantial drain on the program. Consequently, the experimental scope of this phase was limited and it was not possible to perform an "autopsy" of the thyratron, including the dispenser cathode, at the end of the program.

9.2 LINEAR THYRATRON MODIFICATIONS

Figure 9-1 shows the final linear thyratron modification. The most obvious modification is the lower location of the anode-control grid gap in the insulator. The intention is to decrease the length of the low field drift region in the control grid and improve the switching time. Lowering the gap has the disadvantage of raising electric field stresses across the dielectric surface and at the triple point where the insulator rests on the LT body. These regions were carefully modeled with the PANDIRA electro-magnetostatic codes to limit the field stresses across dielectric surfaces to <100 kV/cm and on conductor surfaces to <1 MV/cm.

Further modifications increased the slot width to 0.15 inch, radiused the slot corners with a 0.03 inch radius. The baffling was reduced by

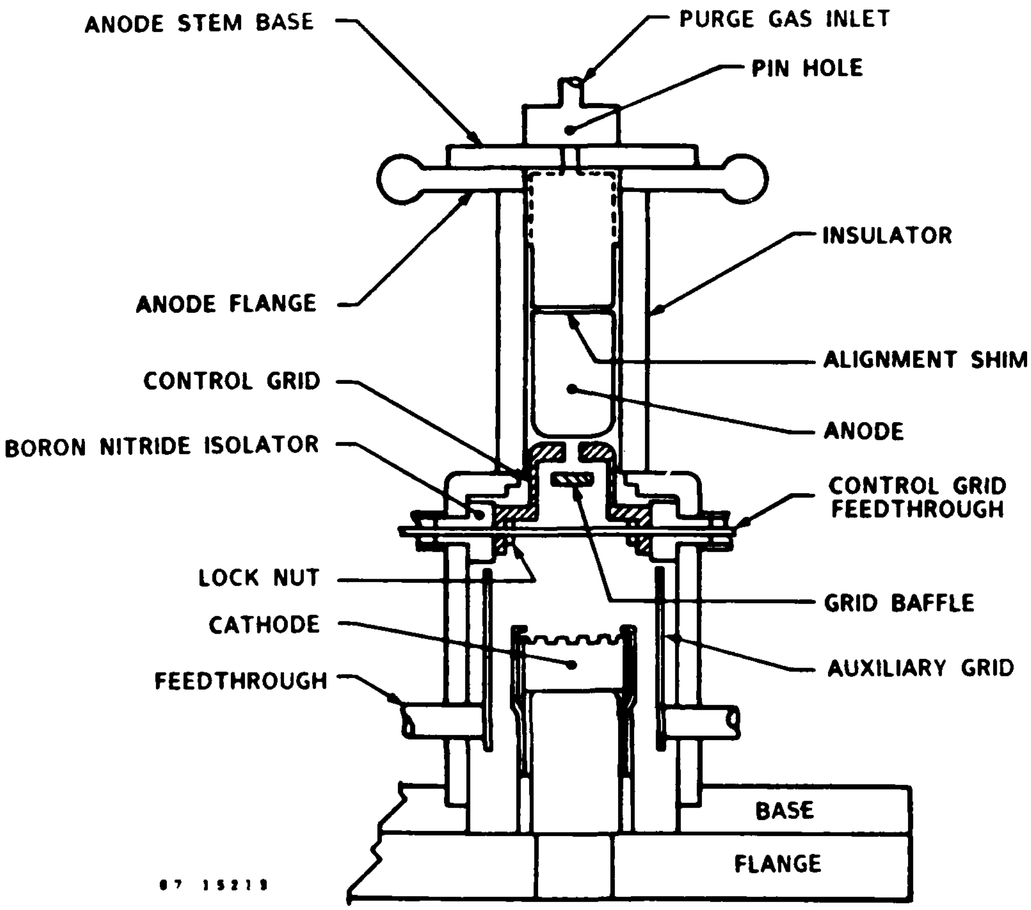

Figure 9-1. Schematic Final Linear Thyratron Geometry.

increasing the baffle-slot gap to 0.18 inch while maintaining the relative position of the lower side of the baffle (ie. making the baffle thinner). The side wall of the control grid was also thinned to 0.03 inch to further reduce both the baffling and the extent of the drift region. The analysis predicted that a negative bias voltage of 200-400 V on the control grid would be necessary to reduce high voltage field penetration into the baffle-slot region because of the looser baffling. Otherwise the high-voltage hold-off would be impaired. These modifications are intended to improve switching time, while maintaining voltage holdoff. The anode stem is split to allow shimming and enable the anode and control grid faces to be aligned to better than 0.002 inch, or 2 percent of the gap. The anode flange has been stiffened and the top portion of the anode stem is hand finished to give a slip fit into the insulator. This ensures a uniform anode-dielectric gap around the anode stem. The final modification added a 0.025 inch radius diamond pinhole to the anode to allow purging of the anode-control grid-slot-insulator regions at a few sccm. Gas is fed to the pinhole through a coiled glass tube for high-voltage holdoff.

Assembly begins with accurately locating the control grid and baffle within the LT body and then placing the insulator around the control grid. When the control grid-insulator spacing is set, the anode flange is attached to hold the insulator in place, and the anode stem is attached through the flange. The whole assembly is then attached to the cathode flange. This procedure allows tight tolerances to be held for all critical dimensions, with emphasis on parallelism rather than absolute dimensions.

All the internal metal pieces are stainless steel. While this is adequate for most purposes, a molybdenum plated anode tip and, perhaps, control grid would be preferable, as damage to both these surfaces was observed in the previously modified LT.

9.2.1 Modulator Modifications

In order to meet the goals of this phase it was necessary to rebuild the modulator and grid trigger circuits. The previous modulator was designed for ≤200 Hz operation at <100 kV compared with >2 kHz at ≥100 kV in this phase. Figure 9.2 shows the modified modulator circuit in its high rep rate and high-voltage configurations. The pulse transformer from the previous phase was designed for 200 Hz and could not be replaced. The control grid and auxiliary grid trigger circuits were modified for 15 kV output at up to 5 kHz for the desired burst of 5 pulses.

It was necessary to add the saturable inductor to enable the modulator thyratron to recover and yet operate at high rep rate. Even with the saturable inductor, the modulator is limited to 1 kHz in its standard configuration (Figure 9-2a). For higher rep rates the modulator switch hangs up and dumps the storage capacitor. This configuration is capable of delivering up to 120 kV to the LT circuit, however.

In order to improve the rep rate the circuit was modified to that shown in Figure 9-2b. This configuration uses the transformer to help the modulator switch recover and enables operation to slightly greater than 3 kHz. Unfortunately, this configuration floats the primary of the pulse transformer at high voltage and requires reversal of either the primary or secondary leads to maintain the correct output polarity to the LT circuit. This places high and low-voltage windings in close proximity to each other and to the transformer core and breakdown occurs at any output greater than 60kV. This breakdown hangs up the switch and dumps the storage capacitor through the shorted transformer. Large negative voltage transients are observed in the secondary.

It was while inadvertently discovering this failure mode that the LT may have been damaged, as discussed later. The LT circuit is a RLC circuit with the inductor winding removed from the circuit to reduce circuit limitations on both current switching times and peak currents. The stray inductance is still significant and the circuit is slightly underdamped.

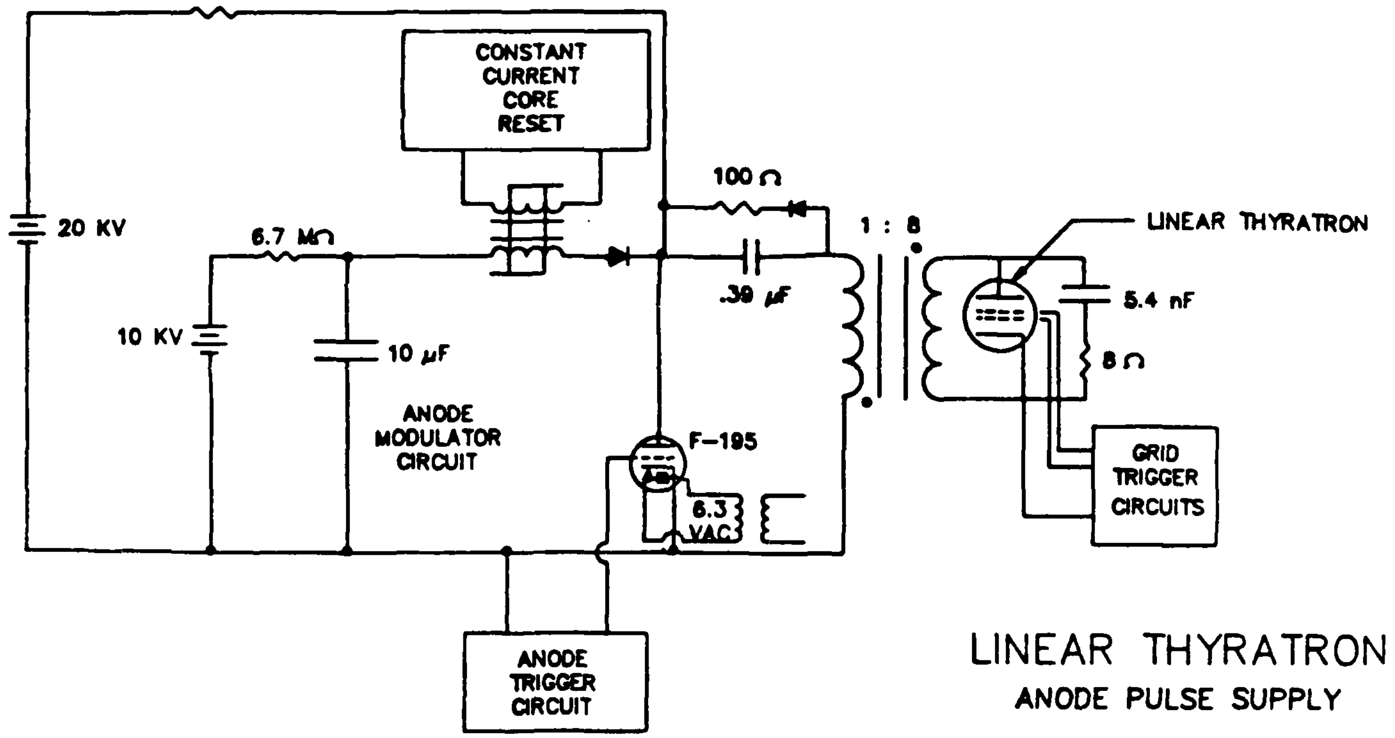

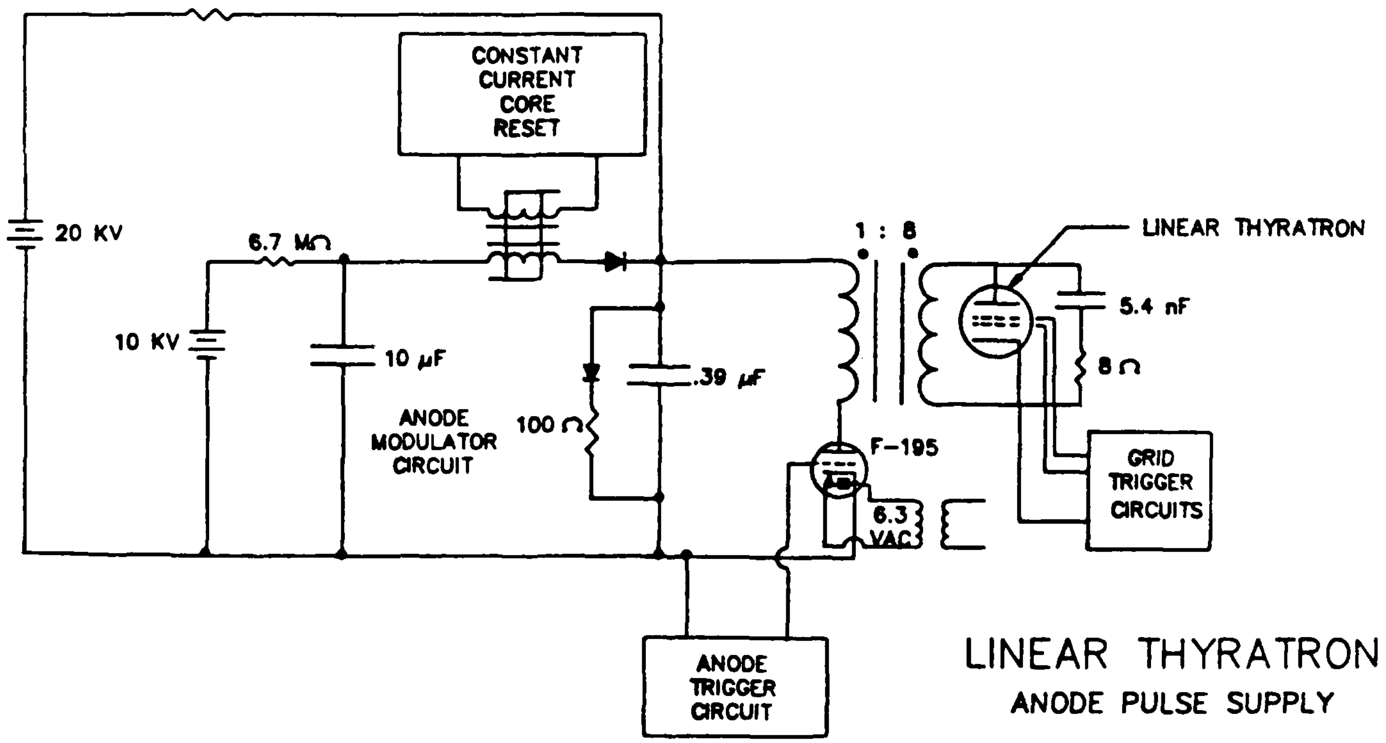

Figure 9-2. Modulator Circuit for (a) 0-120 kV, (b) 0-3 kHz Testing.

9.3 EXPERIMENTAL RESULTS

9.3.1 Voltage Holdoff

The modified LT was first tested up to 50 kV in air to ensure that the system was completely vacuum tight and operational. This was when the rep rate limit of the circuit of Figure 9-2A was discovered and modified to that of Figure 9-2b. The LT was then immersed in oil and tested at higher voltage. At 60 kV the LT appeared to be prefiring, independent of gas type or pressure. Every time this apparent prefire occurred, however, the modulator switch would hang up, as previously mentioned. A prefiring LT would not cause this to happen and it was discovered that the pulse transformer was breaking down internally. The LT is not designed for the large negative voltage and current transients which occurred and may have been damaged. Even when the modulator was reconfigured for high-voltage operation, the LT would not hold off more than 60 kV.

There is another possible explanation for the lower than expected voltage capability of the LT. Windows at the ends of the LT body allow observation and diagnosis of the cathode-control grid region. When LT prefire is due to Paschen breakdown, a discharge is observed in the cathode-control grid region. At the 60 kV breakdown limit, this discharge is not seen. Light is observed from the side of the control grid, indicating that the breakdown path is down the control grid-insulator gap to the LT body. The breakdown occurs at the same location every time.

The machined hole in the macor insulator is not completely symmetrical, and varies in width by as much as 0.01 inch. This, coupled with the possibility that the insulator may not have been accurately placed around the control grid, may lead to regions of the control grid-insulator gap being significantly wider than the 0.030 inch design, which was also the value assumed in the modeling. A wider gap would allow the high field region to penetrate further down the gap than designed, decreasing the holdoff capability.

A combination of reverse current damage and field penetration into the control grid-insulator gap would explain a large part of the limited holdoff capability. The stainless steel anode and control grid are particularly prone to arc damage and sputtering under these conditions. If the anode-control grid gap were deeper into the insulator, this problem would be decreased, at the expense of switching rate.

Once the LT has been immersed in oil, it is a delicate and time consuming procedure to dismantle it without risking serious poisoning of the dispenser cathode. The program expired before an "autopsy" could be performed. Until this can be done, the preceding observations must be considered conjecture, and the LT to be a 60 kV switch until proven otherwise.

9.3.2 Paschen Breakdown

Figure 9-3 shows the measured voltage holdoff limits as a function of gas pressure for H_2, He and a mixture of 60 percent H_2 and 40 percent He. The pure gas data were obtained with the purge flow on. This was not possible with the mixture and limited the number of shots which could be taken. These data are compared with the results from the previous phase. For voltages below 60 kV,the new LT performs better than the previous device. This is due to the care taken in holding critical dimensions as closely as possible, and to the radiusing of the control grid slot corners.

The addition of even small amounts of H_2 into He appears to degrade the holdoff capabilities of the LT below the He values. No "magic" mixture was observed to yield superior performance. This is not totally conclusive since mixtures were only investigated in a cursory manner and in non-optimum conditions.

The data shown in Figure 9-3 required a 300-V negative grid bias because of the wide slot and loose baffling. Flow of a few sccm greatly improved shot to shot repeatability, and allowed the data to be acquired on a more or less

8715468

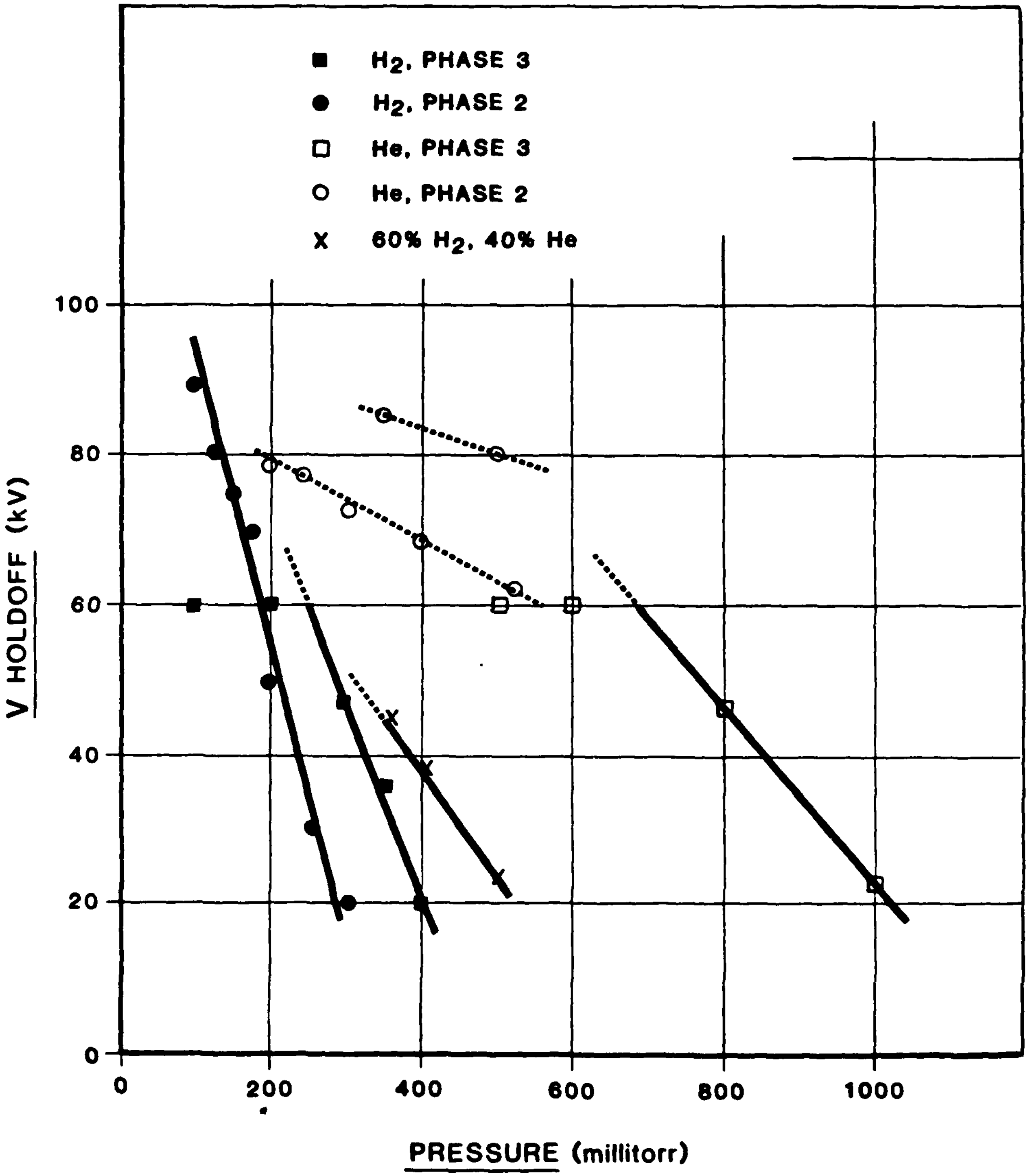

Figure 9-3. LT Holdoff Voltage as a Function of Gas Pressure for the Modified LT's.

continuous basis, rather than the frequent flush and fill required in the previous Phase.

9.3.3 Switching Rates

One of the major goals of this phase was to demonstrate respectable current and voltage switching rates, even for this highly non-optimum geometry. Firgure 9-4 shows current and voltage traces in 100 mTorr He with a negative 300-V grid bias and 50-kV charge voltage. The leading edges of the traces were difficult to resolve due to the writing speed of the oscilloscope, but showed more clearly on the Polaroid negative. The current trace rises to 1 kA in 10 ns for a dI/dt of 10^{11} A/s. The current monitor is a Pearson probe, model 100. The specifications for this probe give a rise time of 20 ns for a square wave pulse. Furthermore, the same minimum rise time is observed in both H_2 and He for a range of pressures. The value of 10^{11} A/s is therefore diagnostically limited and is a lower bound for the maximum dI/dt.

The voltage trace drops to 7 kV in 40 ns for a dV/dt of 10^{12} V/s. As the voltage is decreased further below the holdoff limit the switching rates decrease. The highest switching rates are only observed after the LT has been run for a while. When the system is first turned on the switching rates are very low. Figure 9-5 shows an example when the device is first turned on with 100 mTorr H_2 and 44 kV. In this case $dI/dt = 7X10^9$ A s and $dV/dt = 5X10^{11}$ V/s.

The dispenser cathode has been removed at least 10 times from the various versions of the LT and has been run cold for many thousands of shots. The likelihood of poisoning and/or depletion of the cathode is high. If the LT is run at about 1 Hz for a few minutes with a gas purge flow and the voltage gradually increased, then it operates repeatably and reliably.

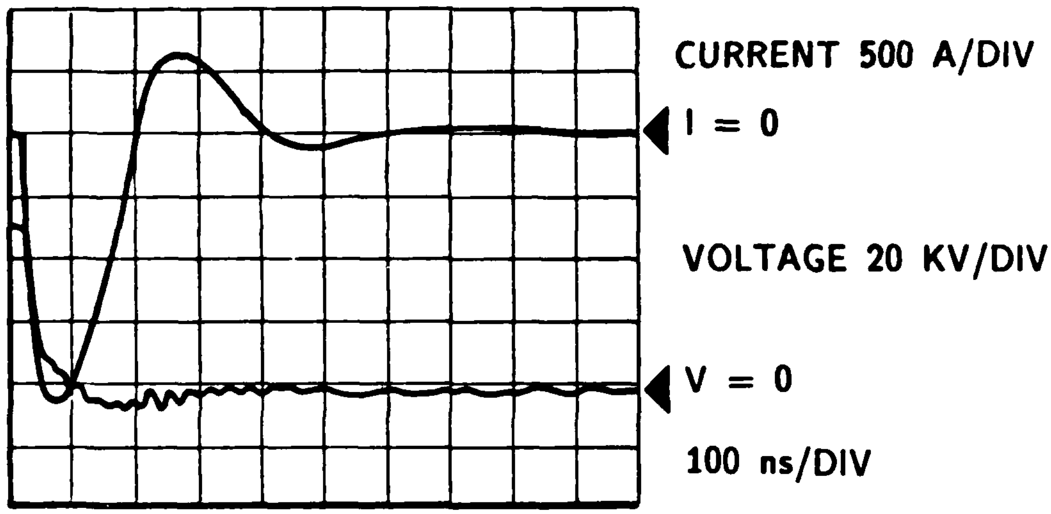

Figure 9-4. VI Switching Characteristics.

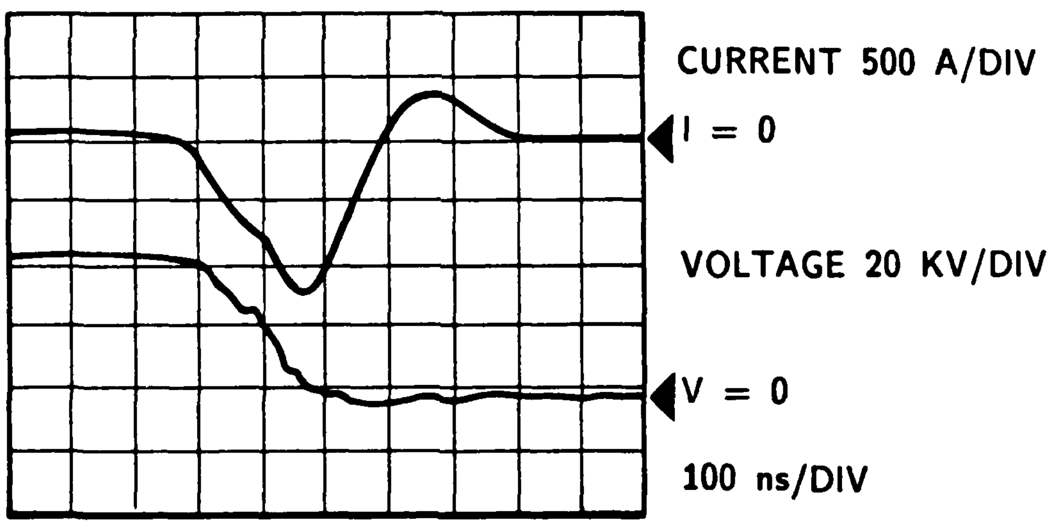

Figure 9-5. Startup Switching Characteristics.

9.3.4 Rep Rate and Switching Power

The LT was tested up to 60 kV to over 3 kHz. Figure 9-6 shows a burst of 5 shots at 3 kHz with a 34-kV charge. the variation in voltage is due to both droop in the storage capacitor and partial saturation of the pulse transformer core. At rep rates slightly greater than 3 kHz, the modulator switch hangs up. The first shot is at higher voltage and its current trace does not appear. The current traces show ≈100 ns jitter between the second and last shots, with the middle two almost indistinguishable. The jitter is mostly due to the different voltages at which each pulse was switched.

The same rep rate limit was observed up to 60 kV, but the jitter becomes much worse and saturation of the transformer core leads to erratic traces making clean data difficult to obtain. These limits are modulator governed, and the rep rate capability of the LT has not been fully tested or demonstrated.

With a 5.4-nF capacitance at 60 kV, the switched energy is 9.7 J/pulse and at a 3-kHz the mean switched power is 29 kW. These values could be raised by increasing the capacitance. The energy per pulse and pulse length limits of the LT are unknown.

The highest switched current was 2.25 KA at 60 kV in 100 mTorr He. This corresponds to a peak instantaneous switching power of 135 MW. There are no signs of saturation by either the cathode or the control grid slot in either He or H_2 and the ultimate current capability of the LT has not been reached.

9.4 A RADIAL DISCHARGE LINEAR THYRATRON CONCEPTUAL DESIGN

The Radial Discharge Linear Thyratron (RDLT) is a novel concept for a high current, high voltage, linear thyratron. The RDLT uses the linear thyratron approach of increasing current switching capability by increasing length, but has several advantages over the existing rectangular geometry. The radial geometry allows several thyratrons to be placed in parallel in a

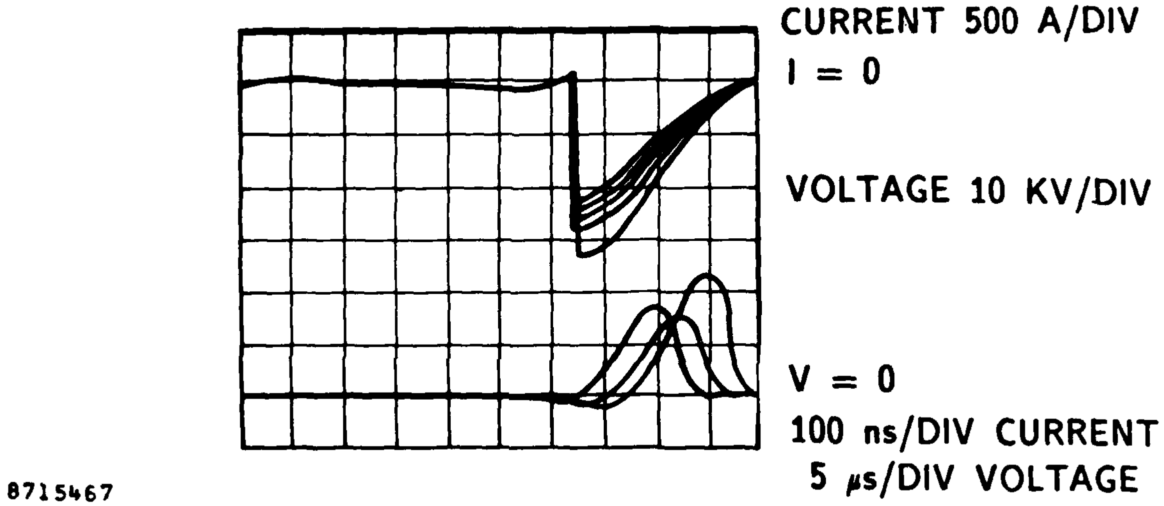

Figure 9-6. VI Traces for a Burst of 5 Pulses at 3 kHz in 800μ Thyratron.

volume similar to that occupied by one rectangular thyratron. This yields a several-fold increase in switching current capability. The electric field distributions in a radial geometry allow for looser baffling of the control grid slot and lower surface field enhancements due to the corners in the slot, enabling faster switching times and higher switching voltages. The radial geometry also yields a larger cathode surface area than anode surface area, making efficient use of the high anode current densities. The result is a compact switch with higher switching current (lower impedance), higher switching voltage, lower inductance and faster switching times than can be achieved in a rectangular geometry for the same switch length.

Figure 9-7 is a schematic illustration of the RDLT concept. The use of four separate discharge regions are a suggestion. It may only be reasonable to use three, or it may be possible to use five or more or to have a continuous discharge. This will depend on the overall dimensions chosen. The concept, however, remains unaltered. It should be possible to run the dispenser cathodes cold, and there will be no problem related to having some of them 'upside down'. From a design and fabrication point of view, an end-fed geometry would be preferable, but the resultant inductance penalty is too great.

The baffle profiles and simmer current geometry shown are suggestions to help the switching time by bringing the simmer current close to, but still shielding, the control grid slot - baffle region (CGSB). The simmer cathode is effectively an auxiliary grid. It will probably be necessary to bias the control grid to ensure adequate shielding of the CGBS. When the control grid is triggered, the sharp baffle corners will focus the discharge towards the CGSB and help reduce the switching time. The inverse radius dependence of the electric field in the radial geometry of the cathode - control grid region will enhance this effect. The control grid vanes ensure that each CGSB 'sees' only its own cathode. If this approach does not work, it may be necessary to use a more conventional baffling and auxiliary grid system.

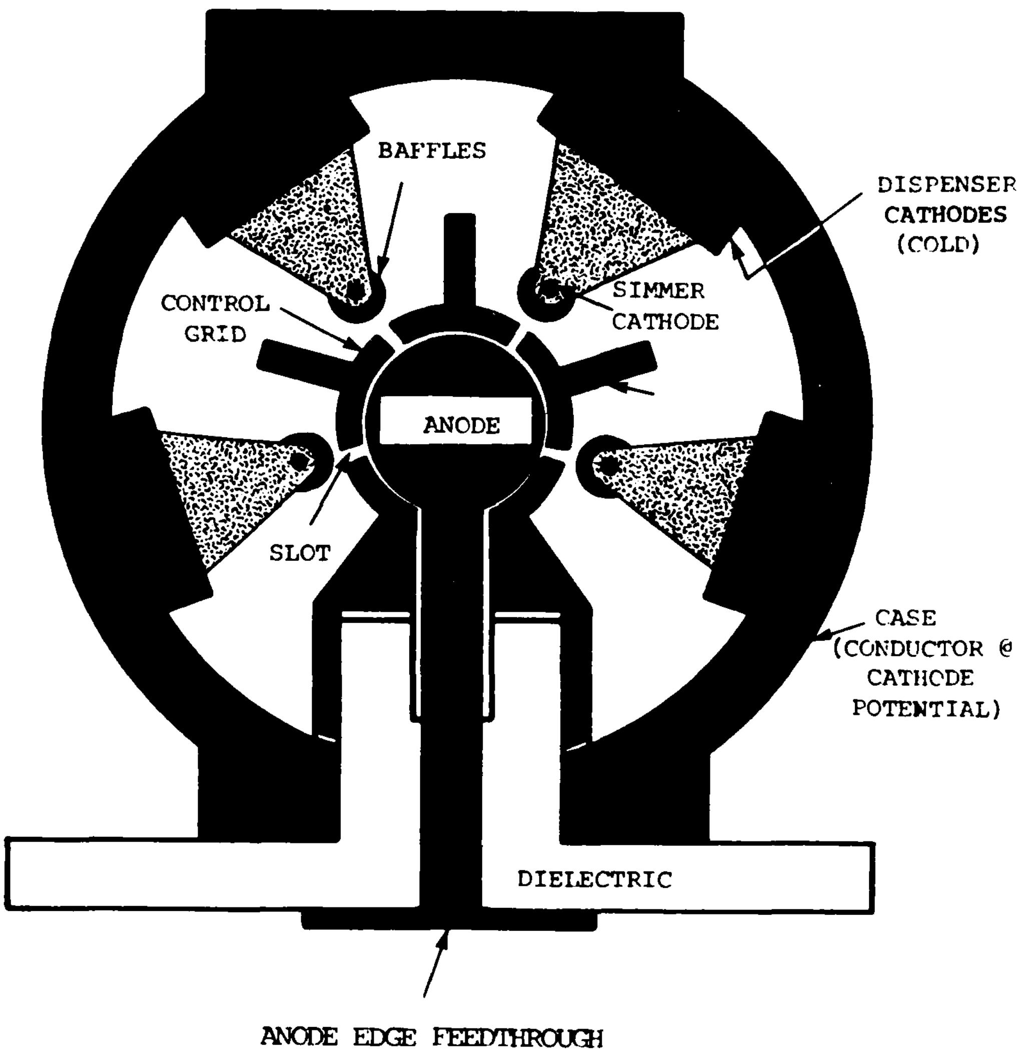

86 10855

Figure 1. Conceptual Design of a Radial Discharge Linear Thyratron

The inverse radius e-field dependence in that anode - control grid region can be used for two purposes. The field penetration into the CGSB is significantly lowered, allowing for looser baffling of the slot. Looser baffling will decrease switching time and switch impedance and inductance. This is a further reason for the suggested baffle profile. When a constant potential surface is rounded towards a greater radius in a radial geometry, the resultant e-field enhancements are lower than would occur when the same rounding is done in a rectangular geometry. Consequently, the field enhancements at the slot corners are lower in a radial geometry than in a rectangular geometry. This will reduce problems due to field emission from the control grid slot corners and improve switching voltage.

The edge fed geometry enables easy attachment to transmission lines and the stacking of several RDLT's in series. The case is at cathode potential, enabling the RDLT to be mounted close to the experiment for most applications, or even directly to the experiment for some applications.

Because of its higher volume and area efficiencies, the RDLT will have significantly lower inductance per unit length than the rectangular geometry and much lower inductance per amp switched. The ability to use looser baffling will also help reduce the inductance and increase switching current capability. Some of the current paths in the RDLT will have slightly higher inductance than others, and it may be necessary to baffle some slots more tightly than others to compensate for this in very high dI/dt applications.

Cooling both the case (cathodes) and the anode will be relatively simple. Gas can be fed into the control grid - anode gap to purge this region and help lifetime issues. The mechanics of the edge feedthrough will take considerable thought, but termination in the axial direction will not be too difficult, as illustrated in Figure 9-8.

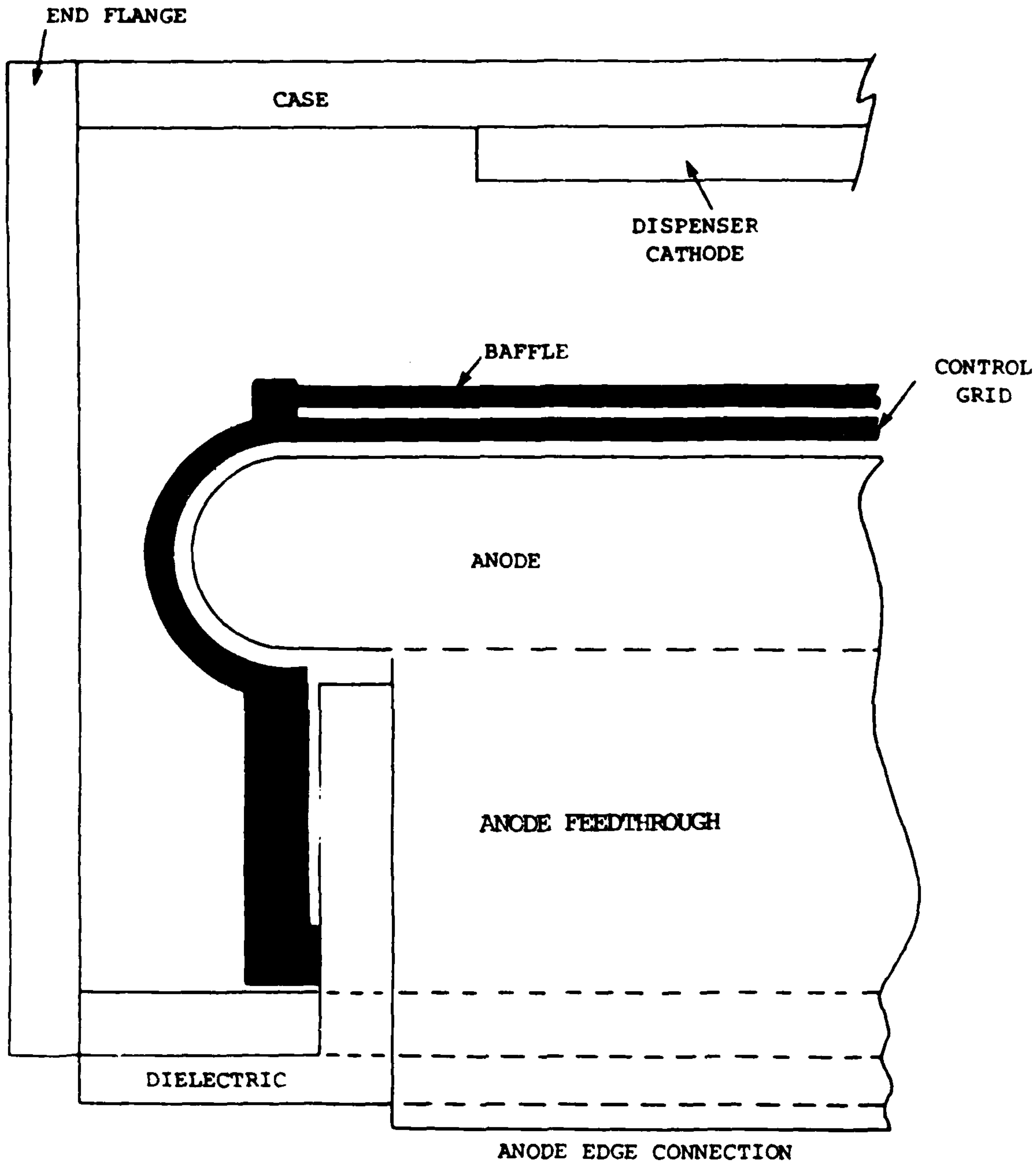

86 10856

Figure 9-8. Conceptual Scheme to Terminate RDLT.

9.5 SUMMARY

This phase of the LT program has demonstrated the value of electrode and grid profiling and field modeling in optimizing thyratron performance. The linear geometry has some intrinsic advantages which have been discussed previously. It also has the benefit of being truly two dimensional in geometry, lending itself to easy diagnosis. The knowledge learned over the phases of this program is equally applicable to conventional geometries.

Even though the desired holdoff of 100 kV was not reached, the goals of >2 kHz with dI/dt $>10^{11}$ A/s and dV/dt $>10^{12}$ V/s were achieved in a very non-optimum geometry with switching voltages up to 60 kV and a single gap. The low holdoff voltage is probably due to both damage caused by modulator failure in early testing and an uneven control grid-insulator gap.

An obvious extension of this program is to build a thyratron for optimum compactness and performance rather than ease of diagnosis, using the results of the LT program. The switch may have a rectangular, conventional, CCLT or RDLT geometry, depending upon the desired performance characteristics.

U.S.Government Printing Office: 1988 548-054/80804

END
DATE
FILMED
DTIC
JULY 88